MODELLING INCLUSION POTENCY AND SIMULTANEOUS TRANSFORMATION KINETICS IN STEELS

By

Stephen John Jones

Queens' College

Cambridge

A dissertation submitted for the degree of

Doctor of Philosophy,

at the University of Cambridge,

September 1996

Preface

This dissertation is submitted for the degree of Doctor of Philosophy at the University of Cambridge. The research described in this dissertation was conducted under the supervision of Dr. H. K. D. H. Bhadeshia in the Department of Materials Science and Metallurgy, Cambridge, between October 1993 and September 1996. This work is to the best of my knowledge original, except where acknowledgment and reference is made to previous work. Neither this, nor any substantially similar dissertation has been or is being submitted for any degree, diploma or other qualification at this, or any other university. This dissertation contains less than 60,000 words.

Stephen John Jones

September 1996

Acknowledgments

Abstract

This work deals with the modelling of microstructural development in steel welds as a function of their chemical composition, welding conditions and non-metallic inclusion content. Theory has been developed to deal with a variety of phase transformations that occur when austenite is cooled into a regime where it is not stable. This theory is quite general and has wide applicability, for example, to wrought as well as welded steels. The thesis begins with a review of the mechanisms of transformation in steels and a description of existing kinetic theory, with emphasis on the welding process including the role of non-metallic inclusions.

It was discovered at an early stage that conventional 'Johnson–Mehl–Avrami' theory for estimating the evolution of microstructure has limitations since it is formulated for reactions occurring in isolation. Transformations in practice frequently occur simultaneously, with the variety of product phases interacting and consequently influencing the course of reaction. To deal with this problem, the Avrami approach has been developed to enable better modelling of the decomposition of austenite into a variety of transformation products, including allotriomorphic and idiomorphic ferrite, Widmanstätten ferrite, bainite, acicular ferrite and pearlite. This general theory is in fact applicable to any transformation system. It has been possible, using this modified theory, to explain a number of published experimental data on transformations in steels, including the recent innovation of inoculating wrought steels with particles to provide heterogeneous nucleation sites additional to the austenite grain surfaces.

The many ways in which non-metallic inclusions influence the nucleation of ferrite have, for the first time, been incorporated quantitatively into a model which permits the importance of different mechanisms to be assessed, and their interactions monitored. It has been possible to demonstrate that frequent claims about 'critical inclusion size', or other claims about particular mechanisms, cannot be sustained in general since inclusion effects often depend on a combination of factors.

Experimental studies on steel line-pipe welds have revealed that the phase designated 'acicular ferrite' is intragranularly nucleated bainite. It appears to grow without diffusion at temperatures below the thermodynamically calculated bainite start temperature. The effect of trace additions of boron on the formation of austenite during heating has been characterised. As expected, the boron retards the transformation during heating, though the effects diminish as transformation progresses since the rate of transformation is extremely rapid at high temperatures. The transformation from austenite in boron containing steels has revealed systematic variations during repeated experiments, variations which are not yet fully understood.

Contents

CHAPTER ONE

The Physical Metallurgy of Steel Welds

This chapter provides an introduction to this thesis. It includes a brief description of the fusion welding of steels and submerged-arc welding in particular. The nature of the austenite to ferrite phase transformation in wrought and welded steels is also discussed.

1.1 Welding

Fusion welding is the joining of materials, usually metals or plastics, by raising the temperature of the joint so that melting occurs which allows a strong bond to form upon solidification. The fusion welding of steel involves the deposition of a small quantity of molten steel within a space between the components to be joined. The joint is formed when the steel solidifies.

The welded joint can be divided into two essential metallurgical regions (Figure 1.1). The fusion zone (weld metal) consists of both the deposited steel and those parts of the parent plate (*i.e.* the steel components that were joined) that were melted during welding. The other major part of the welded joint is the heat-affected zone (HAZ), which consists of those parts of the parent plate where the energy input during welding changes the microstructure without melting the steel. A consequence of this complexity is that as the weld cools to room temperature a series of phase transformations occur in both the fusion zone and the HAZ. This project is concerned with the modelling of solid-state transformations in the fusion zone, so as to predict the final microstructure obtained at ambient temperatures. However, many of the ideas and models developed in this thesis are applicable to materials in general.
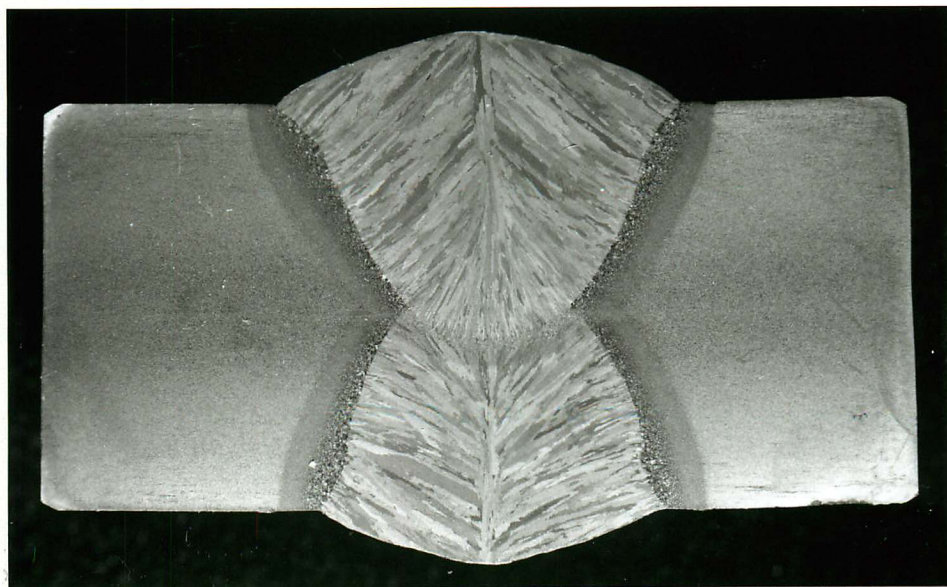
Figure 1.1 Photomicrograph of a submerged-arc weld deposit. One pass was made on each side of the weld. The plate is 19 mm thick.

The joining of two large components often requires the application of a sequence of weld deposits which further complicates the microstructure (Figure 1.2). In such multi-run welds the fusion zone is categorised into two parts, the as-deposited or primary microstructure and the reheated or secondary microstructure. The latter represents regions reheated to cause significant further microstructural change. The reheated zone may contain regions fully or
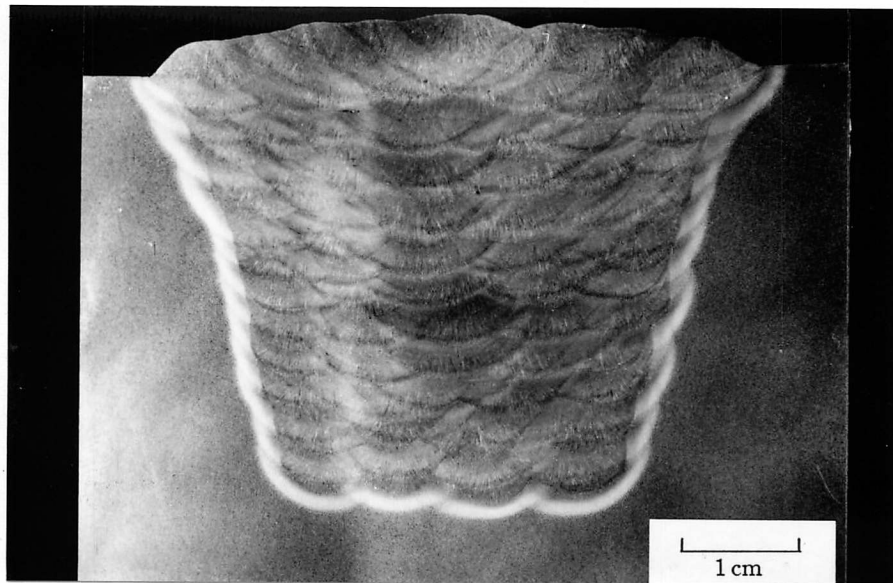
Figure 1.2 Photomicrograph of a multi-run weld (Reed, 1990).

partially reaustenitised and regions which are only tempered.

1.2 Arc Welding

In arc welding a high energy electrical arc, consisting of ionised atoms and free electrons, is created between an electrode and the piece to be welded. The very high temperatures reached in the arc ($\simeq$ 10000 °C) cause a molten weld pool to form, which is protected from the atmosphere by a shielding system. In several forms of arc welding the electrode is actually designed to melt in the arc, thereby entering the weld pool to form a new alloy (Easterling, 1992).

Submerged-arc welding was developed to increase productivity and automation (Svensson, 1994). Very high currents can be used, permitting greater welding speeds whilst maintaining reproducibility and thus quality (Figure 1.3). A hopper precedes the arc, laying a powdered flux along the intended weld line. The flux is usually composed of various silicates and metal oxides, which melt during the welding process to form a protective layer between the atmosphere and the molten weld pool. The welding wire is submerged in this layer of flux and the arc is ignited. The as-deposited weld metal is formed from the welding wire, the parent material and trace additions from the flux. By carefully controlling the composition of the welding wire, the parent plate and the flux, together with the cooling rate, it is possible to control the microstructure and mechanical properties of the weld.

1.3 Phase Transformations in Steels and the Fusion Zone

The astonishing versatility of steel is due primarily to the two allotropes of iron found
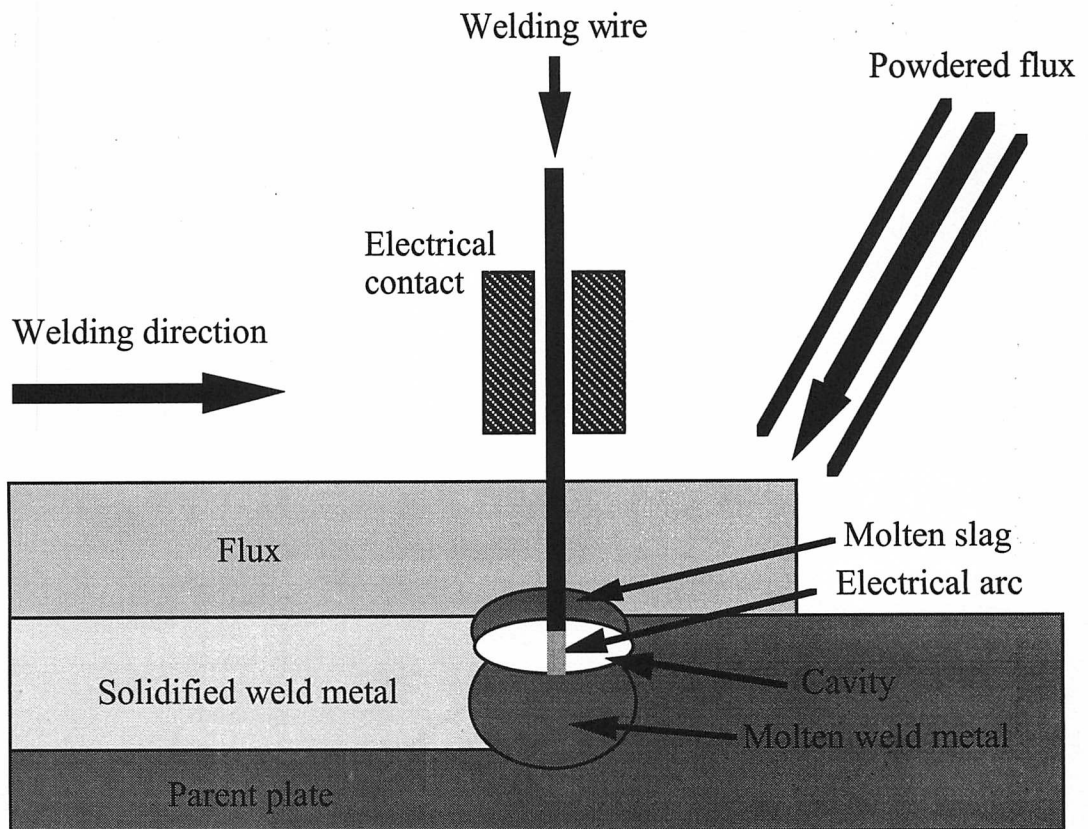
Figure 1.3 Schematic of the submerged-arc welding process.

at atmospheric pressure. This offers an enormous range of microstructural possibilities. Pure iron experiences two changes in crystal structure after solidification. The first phase to form on cooling is body centred cubic (b.c.c.) δ-ferrite at 1548 °C, followed at 1394 °C by face centred cubic (f.c.c.) γ-austenite. Cooling below 911 °C then causes a retransformation to the b.c.c. structure called α-ferrite, which remains stable to ambient temperatures. Phase transformations in low alloy steels are similar to those in pure iron. However, with appropriate alloying the f.c.c. γ-austenite becomes more stable than the b.c.c. δ-ferrite, and can be the first phase to form upon solidification. The austenite to α-ferrite phase transformation is of vital industrial importance because it controls the room temperature microstructure, and thereby the mechanical properties.

Steel microstructures (Figure 1.4) can be classified according to the mechanism by which they form; reconstructive or displacive (Bhadeshia, 1992). Reconstructive transformations involve the diffusional flow of solute and solvent atoms to create a new lattice structure. The reconstructive transformation product of primary interest in low-alloy steel welds is allotriomorphic ferrite, although idiomorphic ferrite and pearlite can form in some welds. Displacive

4

transformations occur at greater undercoolings when the thermodynamic driving force is sufficiently large to permit a homogeneous deformation of the austenite lattice. The following displacive transformation products are found in steels; Widmanstätten ferrite, bainite, acicular ferrite and martensite. At high temperature the thermodynamic driving force for transformation is small so that Widmanstätten ferrite grows by a displacive mechanism in which carbon atoms are partitioned. When the thermodynamic driving force is very large, martensite forms without any diffusion. At intermediate temperatures bainite and acicular ferrite form. These two transformations, which are fundamentally the same, occur in two stages, an initial displacive and diffusionless transformation event is followed by carbon diffusion. In low-alloy steel weld metals Widmanstätten ferrite and acicular ferrite are usually the dominant displacive transformation products. A small amount of austenite may also be retained at room temperature.

In order to attain high toughness and strength it is necessary to maximise the volume fraction of acicular ferrite which nucleates intragranularly. This is thought to be controlled by the nucleation potency of small non-metallic inclusions which form in the weld pool prior to solidification, providing that other factors such as the weld metal composition, austenite grain size and cooling rate are favourable.

1.3.1 Reconstructive Transformations

Reconstructive ferrite is the first phase to form from austenite on cooling below the Ae_3 temperature (where α-ferrite first becomes thermodynamically stable), when the thermodynamic driving force is low and diffusivity is high. All the solute and solvent atoms diffuse to minimise the strain energy. If the transformation is controlled by diffusion, approximate thermodynamic equilibrium is maintained at the interface; this is referred to as 'local equilibrium' at the interface. In a system such as Fe–X–C, where X indicates a substitutional solute, the diffusivity of carbon is several orders of magnitude greater than that of the substitutional atoms. To maintain the balance of flux for all species, two situations (Figure 1.5) arise, both of which are consistent with local equilibrium at the interface (reviewed by Bhadeshia, 1985b):

(1) At low thermodynamic driving forces and hence small supersaturations, a tie line can be chosen that ensures that the carbon concentration in the austenite at the interface is approximately equal to that in the austenite remote from the interface. This reduces the concentration gradient for carbon diffusion to almost zero allowing the substitutional solute X to keep pace. This is known as partitioning local equilibrium (PLE) because there is a substantial redistribution of X.

┌─────────────────────────────┬─────────────────────────────┐
RECONSTRUCTIVE

Diffusion of all atoms during nucleation and growth.
Sluggish below about 850 K.

DISPLACIVE

Invariant-plane strain shape deformation with large shear component.
No iron or substitutional solute diffusion.
Thin plate shape.

ALLOTRIOMORPHIC FERRITE

IDIOMORPHIC FERRITE

WIDMANSTÄTTEN FERRITE

Carbon diffusion during paraequilibrium nucleation & growth.

MASSIVE FERRITE

No change in bulk composition.

BAINITE & ACICULAR FERRITE

Carbon diffusion during paraequilibrium nucleation. No diffusion during growth.

PEARLITE

Cooperative growth of ferrite & cementite.

MARTENSITE

Diffusionless nucleation & growth.

Figure 1.4 Chart showing the characteristics of the various phase transformations in steels (Bhadeshia, 1992).

(2) As the thermodynamic driving force and hence supersaturation increases, a second mode of ensuring mass balance becomes possible. This involves choosing a tie line such that the substitutional concentration in the ferrite is virtually identical to that in the austenite. This results in a large concentration gradient of X, permitting it to keep pace with carbon diffusion. This is termed negligible partitioning local equilibrium (NPLE) because the concentration of X in ferrite is virtually identical to the alloy as a whole.

At sufficiently low temperatures the diffusion distance for X approaches atomic dimen-

sions and the concept of local equilibrium at the interface breaks down. Transformation then proceeds by paraequilibrium, which is a constrained equilibrium when the ratio of iron to substitutional solute atoms remains constant everywhere, but subject to that constraint, the carbon achieves uniformity of chemical potential.

In the rapidly cooling weld deposit it seems a reasonable assumption that ferrite grows by a paraequilibrium transformation (Bhadeshia *et al.*, 1985). The rate of transformation can be controlled by the speed at which carbon atoms are partitioned into the residual austenite ahead of the α-γ interface. As carbon atoms accumulate ahead of the transformation interface the growth rate slows down parabolically with time as the diffusion distance increases (Christian, 1975). Reconstructive or pro-eutectoid ferrite nucleates heterogeneously in steels and is found to grow in two morphologies:

(1) Allotriomorphic ferrite nucleates heterogeneously, at austenite grain boundaries (Figure 1.6). Growth is able to proceed rapidly along the boundaries where diffusivity is high. However, in weld deposits the final volume fraction of allotriomorphic ferrite is limited by the rapidly decreasing temperature and solute build-up in the residual austenite (Easterling, 1992). The prior-austenite boundaries are then decorated with layers of allotriomorphic ferrite, which offer relatively easy paths for crack propagation. In order to maximise toughness the final volume fraction of allotriomorphic ferrite should be minimised, but, a small volume fraction is desirable because it reduces susceptibility to embrittlement of the prior-austenite grain boundaries (Bhadeshia and Svensson, 1993).

(2) Idiomorphic ferrite nucleates intragranularly to form equiaxed grains (Figure 1.6). It does not form in significant quantities in modern weld metals because the cooling rate is too rapid to allow extensive nucleation at intragranular sites such as non-metallic inclusions which offer a relatively high activation energy barrier to nucleation in comparison with the austenite grain surface.

Pearlite (Figure 1.6) also forms via a reconstructive mechanism. This lamellar mixture of ferrite and cementite (Fe_3C) nucleates at the austenite grain surface, the allotriomorphic ferrite-austenite interface or on inclusions. Nucleation of cementite is thermodynamically possible when the carbon concentration of the untransformed austenite reaches that of the austenite-cementite (A_{cm}) phase boundary. Modern steel welds contain a very low concentration of carbon which means that only a small quantity of degenerate pearlite forms in the rapidly cooling weld deposit. However, lamellar pearlite may form in the later stages of transformation
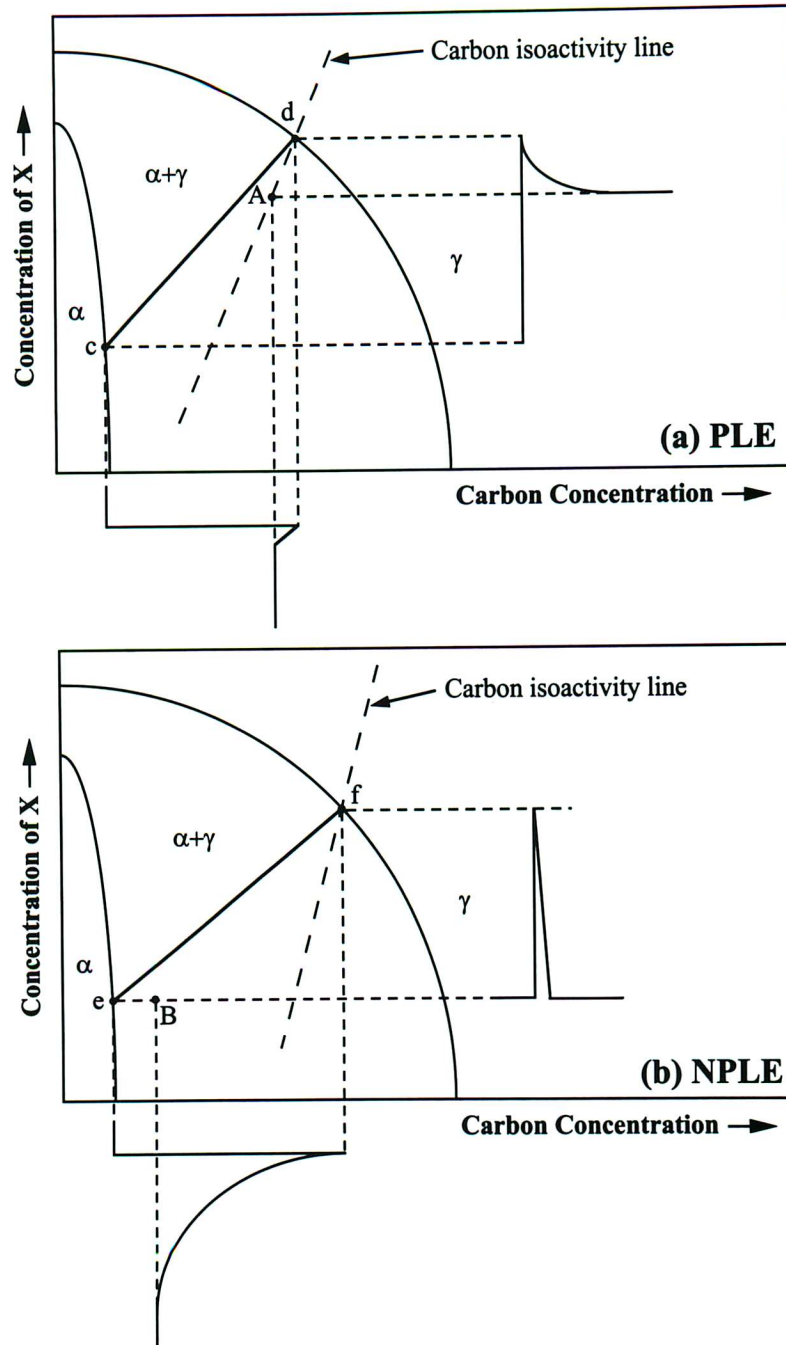
Figure 1.5 Schematic isothermal sections of the ternary Fe–X–C phase diagram which show ferrite growth occurring with local equilibrium at the α-γ interface (adapted from Bhadeshia, 1985b); (a) growth at low supersaturations (PLE) with bulk redistribution of Mn; (b) growth at high supersaturations (NPLE) with negligible partitioning of Mn during transformation. The mean alloy compositions are designated 'A' and 'B' in each case. cd and ef are tie lines (which satisfy conditions pertaining to the conservation of mass and the diffusive fluxes of X and C) appropriate to PLE and NPLE respectively.

if the cooling rate is slow enough to allow significant carbon enrichment of the untransformed austenite (Easterling, 1992).
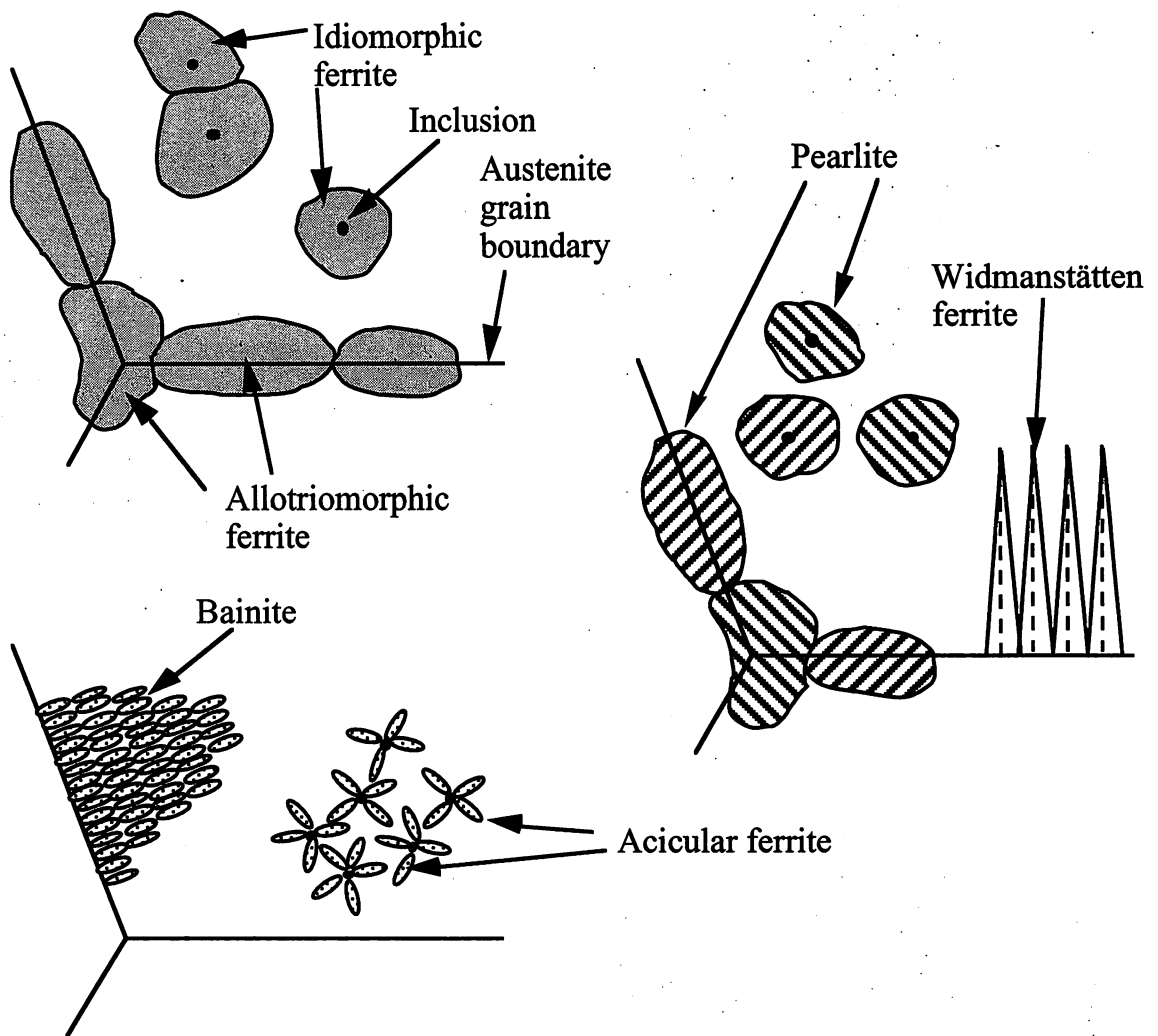
Figure 1.6 Schematic of various steel microstructures.

1.3.2 Widmanstätten Ferrite

As diffusion becomes more difficult displacive transformations are kinetically favoured. Widmanstätten ferrite is the first such displacive transformation product to form during continuous cooling, nucleating on either allotriomorphic ferrite or at the austenite grain surfaces. Widmanstätten ferrite growth causes an invariant-plane strain (IPS) shape change which leaves a plane undistorted and unrotated (Watson and McDougall, 1973). Therefore, an atomic correspondence exists between the iron and substitutional elements in the parent and product lattices. However, the diffusion of interstitial carbon atoms is a thermodynamic necessity and carbon atoms partition to an extent which maintains a uniform chemical potential everywhere.

The transformation is therefore a paraequilibrium reaction (Bhadeshia, 1992), with the growth rate controlled by the diffusion of carbon in the austenite. Zener (1946) suggested that the plate tip shape ensures that the carbon is rejected into the austenite at the sides of the plate, so that the growth rate is constant during isothermal transformation.

The growth mechanism of Widmanstätten ferrite involves the simultaneous formation of two plates to form a strain accommodating pair (Bhadeshia, 1981). Therefore, the strain energy associated with the transformation is relatively small ($\simeq 50$ J mole^{-1}). This allows displacive transformation to occur at high temperatures (the Widmanstätten ferrite start temperature, W_S, is the highest temperature at which growth is thermodynamically possible) where the driving force is significantly less than that strain energy due to the formation of a single displacive plate (Bhadeshia, 1992). Widmanstätten ferrite has a distinctive wedge morphology, because the strain accommodating pairs of plates appear as one under the optical microscope (Figure 1.6). Unfortunately, parallel packets of these wedges form, which provide little hindrance to crack propagation, making it detrimental to toughness (Bodnar and Hansen, 1994b; Bhadeshia, 1996).

1.3.3 Bainite and Acicular Ferrite

As the undercooling below the Ae_3 temperature increases, a diffusionless transformation to b.c.c. ferrite becomes thermodynamically possible. Thus, ferrite which is supersaturated with carbon forms by a displacive mechanism causing an IPS shape change (Ko and Cottrell, 1952). This excess carbon is found to partition after the completion of the displacive transformation event, giving rise to bainite (Hehemann, 1970; Hehemann *et al.*, 1972). The orientation relationship between the bainitic ferrite and the austenite is found to be close to either the Kurdjumov-Sachs or the Nishiyama-Wassermann orientation relationships.

At high temperatures upper bainite forms, when the excess carbon diffuses out of the bainite grain to enrich the austenite that surrounds it. Cementite (Fe_3C) subsequently precipitates from this enriched austenite. At lower temperatures, the phase known as lower bainite forms, when some cementite precipitates within the supersaturated bainitic ferrite due to the reduced diffusivity of carbon, and a smaller proportion of carbon partitions into the austenite to subsequently precipitate as in upper bainite (Figure 1.7). However, the precipitation of cementite is considered to be a secondary reaction which occurs after the displacive growth of the bainitic grain is completed. In some alloys containing high concentrations of silicon or aluminium, the kinetics of cementite precipitation from austenite are so slow that bainite forms without any cementite precipitation. The high strain energy ($\simeq 400$ J mole^{-1}) of the IPS shape change associated with bainitic growth causes extensive plastic deformation local

to the bainite-austenite interface because the yield strength of austenite is relatively low at these temperature. The high dislocation density that this creates is thought to prevent the continuous growth of the bainite grain, and thereby limit its maximum size. Growth must therefore proceed by the nucleation of new bainite sub-units, although nucleation is thought to be facilitated by the presence of suitable embryos in the dislocation debris. These bainite sheaves are made up of fine bainite sub-units separated by regions of austenite, martensite and cementite. These sheaves grow in quite a coarse parallel manner (Figure 1.6) to form a non-lamellar structure which is considered detrimental to toughness (Ishikawa and Takahashi, 1995).
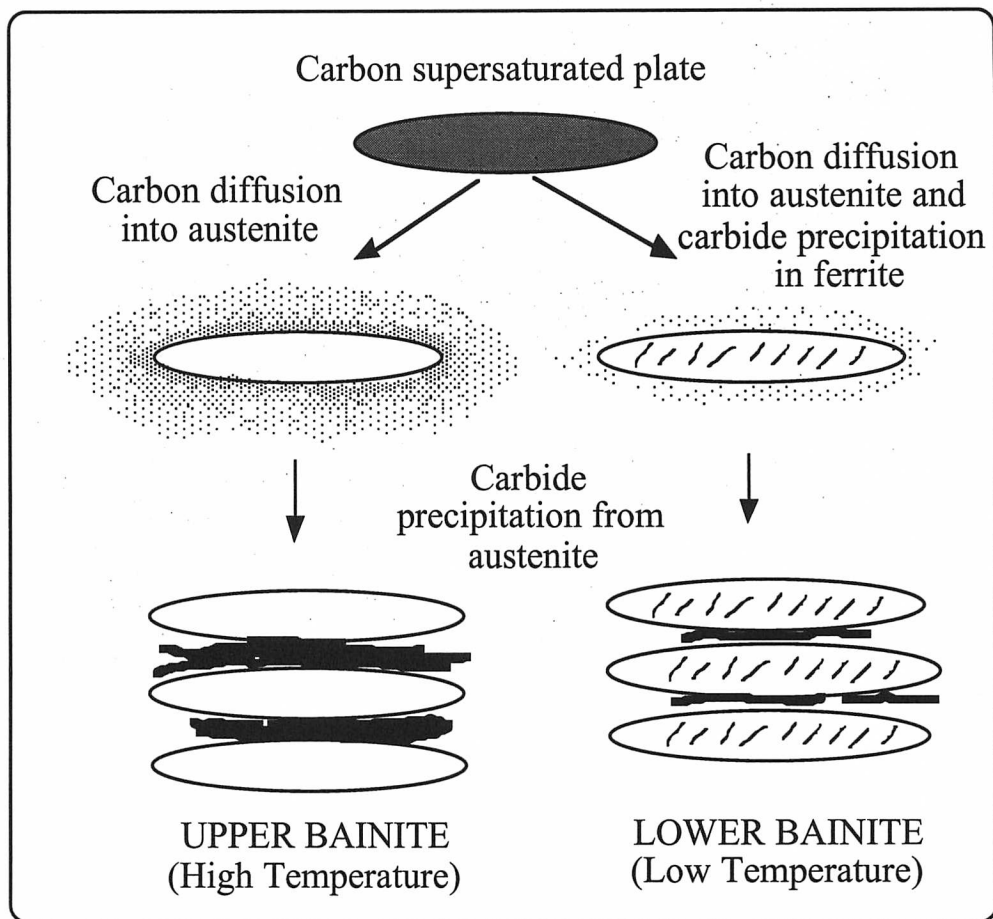
Figure 1.7 Illustration of upper and lower bainite formation (Bhadeshia, 1992).

Individual sub-units of bainite are found to lengthen at a rate much less than martensite plates whose velocity can be limited by the speed of sound in steel. However, the lengthening rate is many orders of magnitude greater than that expected due to carbon diffusion control (Bhadeshia, 1992). The growth rate of bainite sheaves is even slower because it is also a

function of the *delay time* needed to repeatedly nucleate new sub-units. Calculations by Ali and Bhadeshia (1989) suggest that the measured growth rates of bainite sheaves are approximately an order of magnitude greater than those expected by the carbon diffusion controlled growth of plates (Trivedi, 1970).

The bainite transformation is particularly interesting because it has an unusual character which may be rationalised (Bhadeshia and Edmonds, 1980) in terms of the two stage mechanism suggested by Hehemann (1970):

(1) There is a well defined bainite start temperature B_S above which bainite will not form because the thermodynamic driving force is insufficient to allow the initial displacive transformation event.

(2) Below the B_S temperature the bainite reaction has the character of a nucleation and growth process (*i.e.* both the rate and extent of transformation are temperature and time dependent). However, the bainite reaction is an 'incomplete reaction' because the maximum amount of bainite that forms is always much less than that given by the application of the lever rule to the paraequilibrium phase diagram. Bhadeshia and Edmonds (1979) suggested that this is a direct consequence of the two stages in the bainitic transformation. As the bainite reaction proceeds the partitioning of carbon from the supersaturated bainitic ferrite increases the carbon concentration of the residual austenite. The reaction always stops when the carbon concentration of the residual austenite reaches the T_o' curve (Figure 1.8), and not the Ae_3' boundary (the paraequilibrium Ae_3 phase boundary). The T_o' curve is the locus of all those points for which austenite and ferrite of the *same* composition have equal free energies, after allowing for 400 J mole^{-1} of stored strain energy in the ferrite. The bainite reaction stops at the T_o' curve because the thermodynamic driving force is no longer sufficient to allow further diffusionless transformation.

Recent research by Bhadeshia and co-workers (1992) has demonstrated that in many welds acicular ferrite is essentially an intragranularly nucleated form of bainite (section 6.2). If sufficient intragranular nucleation sites exist, then bainite will nucleate upon them, but because the growth of these sheaves is stifled by hard impingement, with sheaves independently nucleated at neighbouring sites, the microstructure appears very different to conventionally nucleated bainite. However, this does not preclude the possibility that Widmanstätten ferrite may nucleate intragranularly and be interpreted as coarse acicular ferrite.
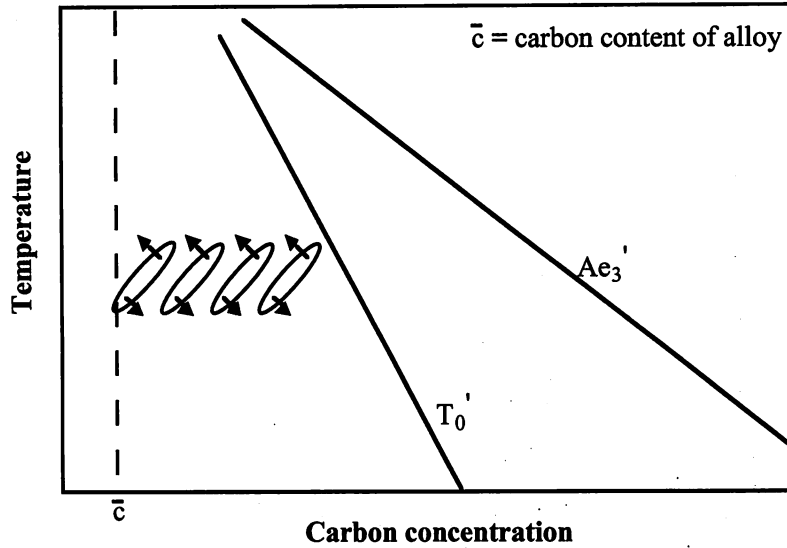
Figure 1.8 Schematic of the phase diagram which illustrates the 'incomplete' bainite transformation.

The acicular ferrite microstructure can best be described as a chaotic arrangement (Figure 1.6) of very fine interlocking ferrite laths ($\simeq$ 2-3 μm in length) that are separated by high angle grain boundaries. This microstructural product is considered invaluable to weld toughness because of the tortuous path it forces propagating cracks to take (Abson, 1987; Easterling, 1992). The fine grain size and high dislocation density associated with acicular ferrite mean that it is also a hard and strong microstructural product. Acicular ferrite then appears to offer that rare combination of high strength and toughness. Indeed commercial research in several countries is directed towards 'inoculating' wrought steels with non-metallic particles that nucleate acicular ferrite during controlled cooling. Nippon Steel had by 1987 succeeded in achieving this on an industrial scale (Chijiiwa *et al.*, 1987; Yamamoto *et al.*, 1987).

The fusion zone of a steel weld contains very large numbers (between 10^8 and 10^9 per mm^3) of randomly distributed non-metallic inclusions, which are usually less than 1 μm in diameter. These inclusions form as the weld is deoxidised at very high temperatures and provide the primary intragranular nucleation sites for acicular ferrite (Ito and Nakanishi, 1976; Abson *et al.*, 1978; Abson, 1987; Dowling *et al.*, 1986; Thewlis, 1986). Inclusions are by their nature relatively brittle and can act as initiation sites for brittle fracture processes at low temperatures. Above the ductile to brittle transformation temperature, inclusions nucleate voids leading to failure by ductile void coalescence. Thus, the optimisation of weld toughness requires that a balance be found between the need for sufficient inclusions capable of nucleating the relatively tough phase acicular ferrite, and the desire to minimise the number of inclusions which can promote fracture or ductile void coalescence. Maximum toughness is therefore

thought to be associated with a relatively low volume fraction of small, but potent inclusions. Unfortunately inclusions are very small and complex multiphase structures, not amenable to easy examination or analysis using electron microscopy, so this compromise might be aided through computer modelling.

1.3.4 Martensite and Retained Austenite

Martensite forms by a completely diffusionless shear transformation which occurs at very high undercoolings, when the thermodynamic driving force for transformation is very large. A consequence of this diffusionless shear transformation is the existence of a reproducible orientation relationship between the parent and product lattices. This orientation relationship consists of a parallelism between the close packed-packed planes in the austenite and those in the martensite, with a corresponding parallelism between the close-packed directions in both phases. However, the austenite lattice (f.c.c.) cannot transform to a martensite lattice (distorted b.c.c.) through the application of an IPS shape change alone. The transformation occurs via a combination of the Bain strain with a suitable rigid body rotation and a lattice invariant deformation that can be either twinning or slip (Christian, 1975). This produces a semi-coherent glissile interface between the austenite and the martensite. Transformation can then occur at very low temperatures, even below room temperature, because a glissile interface is able to move very rapidly.

In an unconstrained transformation the 'habit' plane between the martensite and the austenite is flat. However, in a constrained system, such as an austenite grain, the plate adopts a curved interface to minimise the strain energy per unit volume that is induced upon transformation. The degree to which the martensitic transformation occurs is virtually independent of time, but is instead found to be a function of the undercooling below the M_S (martensite start) temperature. Retained austenite is left over if the martensitic reaction does not go to completion during quenching.

Untempered martensite can be very hard but brittle. If a weld cools very quickly and/or is heavily alloyed, then some of the residual austenite may transform to lath or lenticular martensite, which forms independently of the grain boundaries (Easterling, 1992). This martensite often forms as a thin 'film' around existing displacive transformation products such as Widmanstätten ferrite, bainite and acicular ferrite. Martensite forms at relatively low temperatures in low-alloy steel welds and is therefore largely untempered and brittle. Consequently these welds are designed with the aim of minimising the fraction of martensite that forms.

As the weld cools and ferrite formation proceeds the carbon concentration in the residual austenite increases considerably. Therefore, it is not unusual for a small amount of austenite

to remain stable to ambient temperatures. Retained austenite exists as a thin 'film' around the various displacive transformation products.

CHAPTER TWO

Transformation Kinetics

This chapter summarises the various theoretical and empirical models that have been developed to describe the kinetics of solid state phase transformations. In the first part theoretical models which are based on the methods of Johnson, Mehl and Avrami are described. Models of the austenite to ferrite phase transformation in wrought and welded steels are outlined in the second part.

2.1 The Johnson–Mehl–Avrami Approach

2.1.1 Random Nucleation and Growth

In the present context the theory of transformation kinetics describes the relationship between the fraction of an assembly transformed and the time at the isothermal holding temperature. An exact treatment requires that the problem of hard impingement and interference between regions growing from different nuclei be considered. Johnson and Mehl (1939) and Avrami (1939, 1940 and 1941) were the first to develop a satisfactory theory for this geometrical problem. This theory is described in a comprehensive review by Christian (1975).

Consider the precipitation of β from the parent phase γ. A precipitate particle can be considered to become perceptible after an incubation period τ. Assuming isotropic growth at a constant rate G, the volume v_τ of such a spherical particle is given by:

$$v_\tau = (4\pi/3)G^3(t - \tau)^3 \qquad (t > \tau) \qquad (2.1)$$

$$v_\tau = 0 \qquad (t < \tau) \qquad (2.2)$$

where t is the time defined to be zero at the instant the sample reaches the isothermal transformation temperature.

Particles nucleated at different locations may eventually touch. This problem of hard impingement is neglected at first, by allowing particles to grow through each other and by permitting nucleation to occur even in regions which have already transformed. Avrami described the latter as phantom nuclei and the calculated volume of the particle of β phase as an *extended volume*. The change in the *extended* volume due to all those particles nucleated in a time interval τ to $\tau + d\tau$ is, therefore, given by:

$$dV_\beta^e = v_\tau I(V_\gamma + V_\beta)\, d\tau \qquad (2.3)$$

where I is defined as the nucleation rate per unit volume, V_γ is the volume of untransformed γ at any instant and V_β is the volume of the precipitating phase β at any instant. The total extended volume of β at the time t is obtained by integrating between $\tau = 0$ and $\tau = t$ to give:

$$V_\beta^e = (4\pi V/3) \int_{\tau=0}^{t} G^3 I(t - \tau)^3\, d\tau \qquad (2.4)$$

where $V = V_\gamma + V_\beta$ is the total sample volume. This extended volume V_β^e may be larger than the total volume V. Its importance is that it allows the separation of the kinetics of nucleation and growth from the geometrical problems of phantom nucleation and hard impingement.

Clearly only those parts of the change in the extended volume which lie in untransformed regions of the parent phase γ can contribute to the change in the real volume of β. If nucleation occurs completely randomly throughout the volume of the parent material then the probability that any change in the extended volume lies in the untransformed parent phase is proportional to the fraction of untransformed material at that instant. It follows that the real change in volume in the time interval t to $t + dt$ is:

$$dV_\beta = \left(1 - \frac{V_\beta}{V}\right) dV_\beta^e \qquad (2.5)$$

i.e.

$$V_\beta^e = -V \ln \left(1 - \frac{V_\beta}{V}\right) \qquad (2.6)$$

Therefore, eliminating V_β^e from equations 2.4 and 2.6 gives:

$$-\ln \left(1 - \frac{V_\beta}{V}\right) = (4\pi/3) G^3 \int_0^t I(t - \tau)^3 \, d\tau \qquad (2.7)$$

In making this conversion from extended to real volume, all information about individual particles is lost, so that the application of the Avrami model yields only the volume fraction transformed. Equation 2.7 can be integrated with specific assumptions about the nucleation rate – when the nucleation rate is constant:

$$\zeta_\beta = \frac{V_\beta}{V} = 1 - \exp \left(-\frac{\pi}{3} G^3 I t^4\right) \qquad (2.8)$$

where ζ_β is the volume fraction of β formed at the time t. This is the form of the classic Johnson–Mehl–Avrami equation for random nucleation and linear growth, which is often written in a simplified form as:

$$\zeta_\beta = 1 - \exp \left(-kt^n\right) \qquad (2.9)$$

where the constants k and n are obtained by fitting to experimental data. The theory can be adapted for a variety of nucleation and growth mechanisms, however, it is restricted to the precipitation of a single phase from the parent.

The growth rate need not be constant. In diffusion controlled growth, the particle dimension will vary with the square root of time, the constant of proportionality being the three-dimensional parabolic thickening rate constant (ξ). The value of ξ remains constant as long as the far field concentration in the matrix does not change. Therefore, equations 2.1 and 2.2 are rewritten as:

$$v_\tau = (4\pi/3)\xi^3 (t - \tau)^{3/2} \qquad (t > \tau) \qquad (2.10)$$

18

$$v_\tau = 0 \qquad\qquad (t < \tau) \qquad\qquad (2.11)$$

and equation 2.3 becomes:

$$dV_\beta^e = \frac{4}{3}\pi\xi^3(t-\tau)^{3/2}IV\,d\tau \qquad\qquad (2.12)$$

where ξ is the three-dimensional parabolic thickening rate constant of β.

However, in a diffusion controlled transformation ζ_β cannot be defined as the fraction of the whole assembly which has transformed. Instead, if ϕ is the equilibrium volume fraction of β as given by the application of the lever rule to the phase diagram, then equation 2.6 may be rewritten as:

$$V_\beta^e = -\phi V \ln\left(1 - \frac{V_\beta}{\phi V}\right) \qquad\qquad (2.13)$$

Therefore, ζ_β is redefined as $V_\beta/\phi V$, the fraction of the equilibrium volume fraction of β transformed at any time t, so that the integration yields:

$$\zeta_\beta = 1 - \exp\left(-\frac{8}{15\phi}\pi\xi^3 I t^{5/2}\right) \qquad\qquad (2.14)$$

It is emphasized that this analytical relationship is strictly valid only if the value of ξ does not change during transformation, i.e. at very small degrees of transformation.

2.1.2 Nucleation at a Grain Surface

The models for random nucleation and growth discussed above rely upon the assumption that nucleation is completely random in the volume of the assembly. However, in many real systems nucleation occurs preferentially on grain boundaries and dislocations (Christian, 1975). Fortunately the theory due to Johnson–Mehl–Avrami can be extended to allow for such 'clustered' nucleation. In this section the theory for preferential nucleation along the grain boundaries of the parent material, due to Cahn (1956), is presented.

The phase β grows with an isotropic and constant growth rate G and a constant nucleation rate I_B per unit area of grain boundary. Consider a planar boundary of area O_b. The radius of a spherical particle nucleated at τ at the time t is $G(t-\tau)$ when $t > \tau$, and zero when $t < \tau$. This particle intersects an arbitrary plane parallel to the boundary, but separated by a distance y from it, as a circle. The radius of this circle is $[G^2(t-\tau)^2 - y^2]^{1/2}$ for $G(t-\tau) > y$, and zero for $G(t-\tau) < y$. Therefore, the contribution to this extended area from those particles nucleated between the times τ and $\tau + d\tau$ is:

$$dO_\beta^e = \pi O_b I_B[G^2(t-\tau)^2 - y^2]\,d\tau \qquad G(t-\tau) > y \qquad (2.15)$$

$$dO_\beta^e = 0 \qquad\qquad G(t-\tau) < y \qquad (2.16)$$

19

Noting that only those particles nucleated such that $\tau < (t - y/G)$ can contribute to the extended area permits the total extended area of intersection at the time t to be evaluated as:

$$O_\beta^e = \int_{\tau=0}^{t} dO_\beta^e = \pi O_b \int_{\tau=0}^{t-y/G} [G^2(t-\tau)^2 - y^2] I_B \, d\tau \qquad (2.17)$$

This can be integrated to give:

$$O_\beta^e = (\pi/3) O_b I_B G^2 t^3 (1 - 3\theta^2 - 2\theta^3) \qquad (\theta < 1) \qquad (2.18)$$

$$O_\beta^e = 0 \qquad (\theta > 1) \qquad (2.19)$$

where $\theta = y/Gt$.

The relationship between the extended and real area is determined in a manner identical to that used to derive the relationship between an extended and a real volume (section 2.1.1), so that:

$$\frac{O_\beta^e}{O} = -\ln\left(1 - \frac{O_\beta}{O}\right) \qquad (2.20)$$

Assuming that there is no interference from other nucleating boundaries, the total volume V_β^b of material originating from this planar grain boundary is obtained by integrating for all y between negative and positive infinity (assuming that particles of β can grow into the parent grains on both sides of the nucleating boundary) to give:

$$V_\beta^b = 2\int_{y=0}^{\infty} O_\beta \, dy = 2\int_{\theta=0}^{1} O_b Gt \left[1 - \exp(-O_\beta^e/O_b)\right] \, d\theta \qquad (2.21)$$

Substituting O_β^e from equation 2.18 allows this to be written as:

$$V_\beta^b = 2O_b Gt \int_0^1 \left[1 - \exp\{(-\pi/3) I_B G^2 t^3 (1 - 3\theta^2 - 2\theta^3)\}\right] d\theta \qquad (2.22)$$

or

$$V_\beta^b = 2O_b Gt \, f(G, I_B, t) \qquad (2.23)$$

where

$$f(G, I_B, t) = \int_0^1 \left[1 - \exp\{(-\pi/3) I_B G^2 t^3 (1 - 3\theta^2 - 2\theta^3)\}\right] d\theta \qquad (2.24)$$

If the total grain boundary area in the assembly is $O_B = \sum O_b$, then by substituting O_B for O_b in the above equation the total extended volume V_β^e of material emanating from all of the grain boundaries is found. This is an *extended* volume because allowance was not made for impingement with discs originating from different grain boundaries. Thus:

$$V_\beta^e = 2O_B Gt \, f(G, I_B, t) \qquad (2.25)$$

If S_V is the grain surface area per unit volume this may be expressed as:

$$V_\beta^e = 2S_V V G t \, f(G, I_B, t) \qquad (2.26)$$

Equation 2.6 may used to calculate the real volume, if it is assumed that the nucleating grain boundaries are randomly distributed throughout the volume of the assembly. Therefore, the volume fraction of β at any time t is:

$$\zeta_\beta = \frac{V_\beta}{V} = 1 - \exp\left(-2S_V G t \, f(G, I_B, t)\right) \qquad (2.27)$$

If either G, I_B or t is large then site saturation occurs and the function $f(G, I_B, t)$ tends to unity. Thus, equation 2.27 reduces to an equation which describes the planar thickening of a phase with a constant growth rate:

$$\zeta_\beta = \frac{V_\beta}{V} = 1 - \exp\left(-2S_V G t\right) \qquad (2.28)$$

2.2 Modelling the Allotriomorphic Ferrite Transformation in Wrought Steels

2.2.1 Gokhale

Research by Gokhale (1986) modelled the isothermal kinetics of the allotriomorphic or proeutectoid ferrite transformation in hot-rolled microalloyed steels that were the subject of an extensive experimental study by Crook and Chilton (1984). Site saturation occurred in the early stages of transformation so that the austenite grain boundaries were almost completely covered by a thin layer of ferrite. Consequently the subsequent transformation to ferrite occurred via the growth of existing ferrite particles in a direction perpendicular to the nucleating austenite grain surface. This one-dimensional growth geometry was represented by assuming that the ferrite grains could be modelled as cylinders with a constant radius R_0 and a length $L = 2\vartheta(t - t_0)^{1/2}$, where ϑ is the one-dimensional parabolic thickening rate constant, t is the time at the isothermal holding temperature and t_0 is the *delay* time before a complete layer of ferrite forms. Assuming that growth occurs on both sides of the austenite grain surface the extended volume fraction of ferrite is $V_v^e = 2\pi R_0^2 N_v \vartheta (t - t_0)^{1/2}$, where N_v is the number of ferrite grains per unit volume.

The real volume fraction of ferrite was determined using an approach due to Hillert (1959) because the classical Johnson–Mehl–Avrami equation for nucleation and growth (section 2.1.1) is not applicable if the spatial distribution of nuclei is *not* random in the volume of the assembly but is 'clustered'. Hillert suggested the following phenomenological equation for such situations

$dV_v = (1 - V_v)^w \, dV_v^e$, where dV_v is the change in the real volume fraction of ferrite in a small time interval $t + dt$ and dV_v^e is the corresponding change in the extended volume fraction of ferrite. The exponent w is greater than unity for clustered nucleation processes. Gokhale assumed that $w = 2$ throughout the course of the transformations studied. Thus integration gives:

$$V_v = \frac{V_v^e}{1 + V_v^e} \qquad (2.29)$$

Using this approach and a similar model for the real surface area of the ferrite-austenite interface per unit volume, Gokhale fitted the parameters t_0, R_0 and N_v to a range of steels that were subjected to a variety of isothermal heat treatments. The correlation between the predicted and measured fraction of allotriomorphic ferrite as a function of time was very high. However, this approach is of limited use as a modelling tool because it requires the empirical fitting of parameters for each steel and heat treatment.

2.2.2 Bhadeshia et al.

Bhadeshia *et al.* (1987) and Reed and Bhadeshia (1992) modelled the isothermal transformation kinetics of allotriomorphic ferrite for a wide range of wrought steels following the method of Cahn (1956) which is described in section 2.1.2. Consequently only the essential differences are presented here.

The model assumes diffusion controlled growth in which the proportionality constant relating the thickness of the allotriomorph to time is ϑ, the one-dimensional parabolic thickening rate constant. Each allotriomorph prior to site saturation is modelled as a disc parallel to the austenite grain boundary plane on which it nucleated (Figure 2.1). The allotriomorph has a half-thickness $q = \vartheta(t - \tau)^{1/2}$ and radius ηq, where η is an aspect ratio taken to be equal to 3. The aspect ratio is considered to be constant because in reality, lengthening and thickening are coupled processes, at least prior to impingement along the austenite grain boundary plane.

The extended area O_β^e is defined as the sum of the areas of intersection of the discs of the phase β with an arbitrary plane at y. The change dO_β^e in O_β^e due to those discs nucleated in the interval τ to $\tau + d\tau$ is:

$$dO_\beta^e = \pi O_b I_B [(\eta\vartheta)^2 (t - \tau)] \, d\tau \qquad \vartheta(t - \tau)^{1/2} > y \qquad (2.30)$$

$$dO_\beta^e = 0 \qquad \vartheta(t - \tau)^{1/2} < y \qquad (2.31)$$

If the nucleation rate per unit area of austenite grain boundary I_B remains invariant during the course of the transformation and noting that only those particles nucleated such
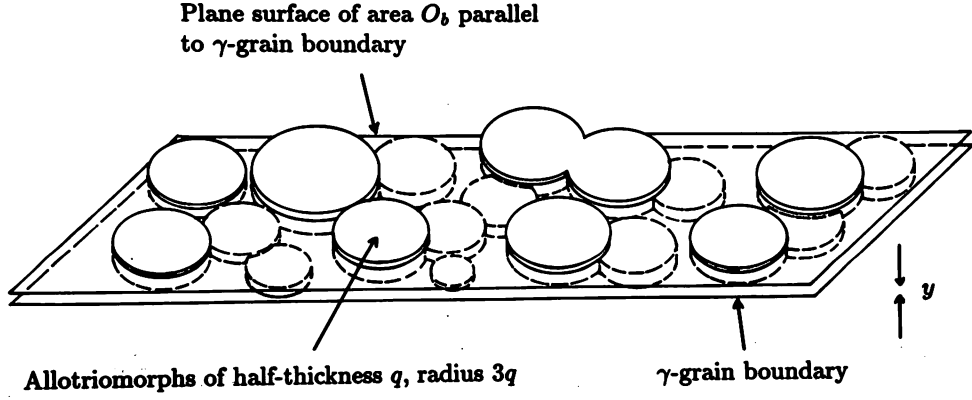
Figure 2.1 Model of allotriomorphic ferrite particles nucleating on a planar austenite grain boundary (Reed and Bhadeshia, 1992).

that $\tau < [t - (y/\vartheta)^2]$ can contribute to the extended area intersected with the plane at y, then the total extended area intersected at the time t is given by:

$$O_\beta^e = \int_{\tau=0}^{t-(y/\vartheta)^2} (\eta\vartheta)^2 \pi O_b I_B(t-\tau)\, d\tau \qquad (2.32)$$

Integration gives:

$$O_\beta^e = (1/2)\pi O_b I_B (\eta\vartheta)^2 t^2 [1 - \theta^4] \qquad (2.33)$$

where $\theta = y/(\vartheta t^{1/2})$. Assuming that there is no interference from other nucleating boundaries, the total volume V_β^b of material originating from this grain boundary is:

$$V_\beta^b = 2 \int_{\theta=0}^{1} O_b \vartheta t^{1/2} (1 - \exp\{-O_\alpha^e/O_b\})\, d\theta \qquad (2.34)$$

or

$$V_\beta^b = 2 O_b \vartheta t^{1/2} f(\eta, \vartheta, I_B, t) \qquad (2.35)$$

where:

$$f(\eta, \vartheta, I_B, t) = \int_0^1 [1 - \exp\{-(1/2)\pi I_B (\eta\vartheta)^2 t^2 (1 - \theta^4)\}]\, d\theta \qquad (2.36)$$

The total extended volume V_β^e of material emanating from all of the grain boundaries in an assembly is:

$$V_\beta^e = 2 S_V V \vartheta t^{1/2} f(\eta, \vartheta, I_B, t) \qquad (2.37)$$

If ϕ is the equilibrium volume fraction of β then the fraction of the equilibrium volume ϕV transformed at any time t is:

$$\zeta_\beta = \frac{V_\beta}{\phi V} = 1 - \exp[-2(S_V/\phi)\vartheta t^{1/2} f(\eta, \vartheta, I_B, t)] \qquad (2.38)$$

If either ϑ, I_B or t is large then the grain boundaries rapidly saturate so that the function $f(\eta, \vartheta, I_B, t)$ tends to unity. Therefore, equation 2.38 reduces to an equation which describes the planar thickening of a phase with parabolic growth characteristics:

$$\zeta_\beta = \frac{V_\beta}{V} = 1 - \exp[-2(S_V/\phi)\vartheta t^{1/2}] \qquad (2.39)$$

In this model nucleation at grain edges or corners is ignored, so that the analysis strictly only applies at high supersaturations when the grain boundary faces are the dominant nucleation sites. Nucleation on grain edges may be modelled by considering the concept of an extended line intercept on a straight nucleating edge. Therefore, the total length L_β due to particles nucleating from one straight edge of length L may be determined using the following equation (Cahn, 1956):

$$\frac{L_\beta^e}{L} = -\ln\left(1 - \frac{L_\beta}{L}\right) \qquad (2.40)$$

where L_β^e is the corresponding total extended length. If the edges are randomly distributed in the volume of the assembly then hard impingement with particles nucleated on other grain edges may be allowed for using equation 2.13. Nucleation on grain corners may be treated using the original Johnson–Mehl–Avrami theory for random nucleation and parabolic growth in the volume of the assembly (section 2.1.1).

Unfortunately, it is strictly not possible to combine these three analytical models to allow for the simultaneous nucleation of ferrite on grain faces, edges and corners, as is the case in real systems. Consequently, Reed and Bhadeshia used the model detailed above for grain face nucleation, but approximated the nucleation rate per unit area I_B as a sum of the nucleation rates determined for grain faces, edges and corners, so that:

$$I_B = I_B^f + I_B^e + I_B^c \qquad (2.41)$$

where I_B^f, I_B^e and I_B^c are the nucleation rates per unit area of grain boundary for grain faces, edges and corners respectively. These nucleation rates were calculated using classical nucleation theory. Grain faces have the highest activation energy barrier to nucleation and the highest site density per unit area of grain boundary, whilst grain corners have the lowest barrier to nucleation and the lowest site density per unit area. The situation for grain edges is intermediate between these extremes.

Reed and Bhadeshia used this approach to calculate reconstructive TTT curves for steel alloys documented in a published TTT atlas. In the first series of calculations an equilibrium mode of transformation was assumed, and the concept of local equilibrium (section 1.3.1) was

used to determine the one-dimensional parabolic thickening rate constant ϑ. In the second series of calculations a paraequilibrium mode of transformation was assumed for the calculation of ϑ. Comparison between the predicted and published TTT curves indicated that below the Ae'_3 temperature the paraequilibrium model described the measured transformation kinetics far better than the equilibrium model. Between the Ae'_3 and Ae_3 temperatures, where a paraequilibrium mode of transformation is thermodynamically impossible, the equilibrium model described the measured transformation kinetics reasonably well. The main limitation of this analytical method is that it does not take into account changes in the far field composition of the untransformed austenite as the transformation progresses, so that the nucleation rate I_B and the parabolic thickening parameter ϑ remain invariant. The assumption of a constant nucleation rate is considered to be reasonable because site saturation at the austenite grain boundaries will occur during the early stages of transformation. However, appreciable soft impingement will occur in the latter stages of transformation, changing the growth conditions, so that this analytical method is only suitable if the fraction transformed is less than or equal to 0.5.

2.2.3 Enomoto

Enomoto (1992) developed an alternative method for predicting the TTT diagram of allotriomorphic or proeutectoid ferrite in Fe–C and Fe–C–X wrought alloys, where X is a substitutional alloying element, using diffusion controlled growth theory. A computer implemented numerical procedure was adopted which allowed the effects of solute enrichment and depletion to be considered. The initiation time for transformation was taken to be the incubation time of an allotriomorphic ferrite nucleus. This was calculated using nucleation theory described by Aaronson and Lee (1975) which estimates the time required for an embryo to form. The solute concentration at the ferrite-austenite interface at any stage of the transformation was determined according to whether local equilibrium (PLE or NPLE) or paraequilibrium conditions were operative (section 1.3.1). For example, Enomoto suggested that when the carbon concentration of the untransformed austenite is sufficiently enriched a switch from NPLE to PLE might be expected to occur, even during isothermal holding. This is because the carbon concentration gradient becomes negligibly small, so that the flux of carbon becomes comparable to that of the alloying elements.

The influence of enrichment and depletion of solute atoms in the untransformed austenite matrix was modelled using a quasi-stationary approximation to determine the diffusion field in the austenite. Both planar and spherical growth geometries were modelled. Enomoto considered that the spherical growth model, in which the diameter of the sphere was assumed to

be equal to the austenite grain size, represented the enrichment and depletion of an austenite grain more realistically. The model was found to accurately predict the well known retardation in transformation kinetics with an increased austenite grain size. However, Enomoto noted that the model did not represent the transformation kinetics of Widmanstätten ferrite adequately because the build up of carbon in front of the plate tip is minimal, so that the plates lengthen linearly with respect to time. It was suggested that this would not lead to significant errors at high temperatures in samples with a small austenite grain size ($< 20~\mu$m) because the Widmanstätten ferrite start temperature in the untransformed austenite would be strongly depressed by solute enrichment. Significant errors were, however, anticipated at lower temperatures and larger austenite grain sizes.

2.3 Modelling Competitive Transformations in Wrought Steels

2.3.1 Saito and Shiga

A computerised model describing the sequential formation of allotriomorphic (proeutectoid) ferrite, pearlite and bainite in thermo-mechanically processed wrought steels was presented by Saito and Shiga (1992) and Saito (1993). This model used chemical thermodynamics, classical nucleation theory and kinetic theory due to Johnson, Mehl and Avrami to predict microstructural evolution during continuous cooling. All three transformations were assumed to occur sequentially (*i.e.* successively and independently). Modules which described carbonitride precipitation, austenite grain growth and recrystallisation were also incorporated into this model.

Saito and Shiga presented a generalised version of the Johnson–Mehl–Avrami equation as:

$$X(t) = 1 - \left[-\exp\left(\int_{t'=0}^{t} J(t')~V(t,t')~dt' \right) \right] \tag{2.42}$$

where $X(t)$ is the volume fraction transformed at the time t, $J(t')$ is the nucleation rate at the time t' and $V(t,t')$ is the extended volume at the time t of a stable nucleus formed at the time t'. The term $\int_{t'=0}^{t} J(t')~V(t,t')~dt'$ represents the total extended volume at the time t.

The total extended volume of allotriomorphic ferrite was determined using equation 2.42. The dimensions of each extended particle (spherical) of allotriomorphic ferrite were calculated by assuming diffusion controlled parabolic growth. The nucleation rate was found using a classical approach. Allotriomorphic ferrite formation ceased and pearlite formation started when the carbon concentration in the untransformed austenite reached the eutectoid carbon concentration. Site saturation was assumed in the simulation of the pearlite transformation, such that the total extended volume of pearlite at the time t is simply the product of the total

austenite-ferrite interfacial area and the thickness of the extended pearlite layer (Hillert, 1975). If the free energy change associated with the nucleation of a phase with the same composition as the untransformed austenite exceeded 400 J mole^{-1} then bainite was assumed to form instead of pearlite. The transformation kinetics of the complex bainite reaction were modelled in the same manner as the pearlite transformation kinetics. Paraequilibrium conditions were assumed for all three transformations.

To permit the evaluation of transformation kinetics during continuous cooling, the cooling curve was divided into a series of small isothermal time steps. The eutectoid carbon concentration and the thermodynamic driving force for transformation in the carbon enriched austenite were updated at the end of every time step, so as to determine which phase would form in the next time step. This simple approach was found to describe the transformation behaviour of low-alloy wrought steels reasonably well. At a slow cooling rate and/or a small austenite grain size, a microstructure consisting of allotriomorphic ferrite and pearlite was predicted. Increasing the cooling rate and/or the austenite grain size was found to reduce the volume fraction of allotriomorphic ferrite formed, so that the final microstructure was composed of allotriomorphic ferrite and bainite.

2.3.2 Anelli et al.

Anelli *et al.* (1991) developed a more complex model for sequential phase transformations to allotriomorphic and idiomorphic ferrite, Widmanstätten ferrite, pearlite, bainite and martensite in thermo-mechanically processed low-carbon steels. The effects of work-hardening on the austenite to ferrite transformation were considered by increasing the driving force for the austenite to ferrite transformation due to the strain energy associated with dislocations in the austenite, and by calculating an 'effective' austenite grain size as a function of the actual austenite grain size and the total strain in the assembly.

With the exception of allotriomorphic and idiomorphic ferrite the volume fraction of each phase at any instant in time is determined using methods based on those due to Johnson, Mehl and Avrami. If site saturation is not immediately perceptible then the volume fraction formed is found using the theory for random nucleation and linear growth. Equation 2.8 is differentiated with respect to time to give:

$$\dot{\zeta}_\beta = \frac{d\zeta_\beta}{dt} = 4(1 - \zeta_\beta) \left(\frac{\pi I \, G^3}{3} \right)^{1/4} \left[\log_e \left(\frac{1}{1 + \zeta_\beta} \right) \right]^{3/4} \tag{2.43}$$

A grain boundary nucleated transformation may be *approximately* represented as:

$$\dot{\zeta}_\beta = 4(1 - \zeta_\beta) \left(\frac{\pi I_B S_V \, G^3}{3} \right)^{1/4} \left[\log_e \left(\frac{1}{1 + \zeta_\beta} \right) \right]^{3/4} \tag{2.44}$$

where I_B is the nucleation rate per unit area of boundary and S_V is the grain boundary area per unit volume. Alternatively, if the transformation is nucleated at a grain boundary and site saturation occurs rapidly, then equation 2.28, which describes linear planar thickening, is differentiated with respect to time to obtain:

$$\dot{\zeta}_\beta = 2 S_V G (1 - \zeta_\beta) \tag{2.45}$$

These equations enable the total volume fraction of each phase at any instant to be calculated via a summation in a computer implemented iterative procedure, in which the cooling cycle or isothermal heat treatment is represented as a series of small isothermal time steps. The average carbon concentration in the untransformed austenite is updated at the end of each time step, with the assumption that all of the phases form under paraequilibrium conditions. Anelli *et al.* then developed the following methodology for modelling the expected series of sequential phase transformations.

The first phases to form are allotriomorphic and idiomorphic ferrite which are assumed to grow simultaneously. These grow in a parabolic manner at a rate determined by the diffusion of carbon in austenite. Classical theory is used to calculate the nucleation rates of allotriomorphic and idiomorphic ferrite. The nucleation rate $I_\alpha S'_V$ of allotriomorphic ferrite per unit volume tends rapidly towards zero as the transformation progresses because it is determined as the product of the untransformed austenite grain surface area S'_V per unit volume and I_α the nucleation rate per unit area. A probabalistic approach based on the work of Abbruzzese (1985) is used to establish the volume fractions of allotriomorphic and idiomorphic ferrite at any instant. This involves classifying the ferrite particles (assumed to be spherical) into groups of different sizes at any instant. As the transformation proceeds the growing grains may impinge. This hard impingement is modelled by considering a 'radius of influence' which is calculated as the average radius that all of the growing spherical particles must have to occupy the unit volume available. An advantage of this probabalistic method is that it provides an estimation of the real ferrite grain size distribution - this is not possible using the Johnson–Mehl–Avrami theory which considers *extended* particle dimensions.

Pearlite or Widmanstätten ferrite are the next phases to form. Pearlite nucleates if the carbon concentration in the untransformed austenite exceeds that given by the A_{cm} phase boundary. Anelli *et al.* supposed that the pearlite transformation proceeds in a process which immediately saturates the α-γ interface, the area $S_V^{\alpha\gamma}$ per unit volume of which is approximated as a function of the transformed volume fractions of allotriomorphic and Widmanstätten ferrite. The growth rate of pearlite G_p is obtained using a method due to Hillert (1982), so that the

28

volume fraction of pearlite is estimated from equation 2.45 as:

$$\dot{\zeta}_p = 2S_V^{\alpha\gamma}G_p(1 - \zeta_p)(1 - \zeta_f - \zeta_w) \tag{2.46}$$

where ζ_f is the total volume fraction of allotriomorphic and idiomorphic ferrite and ζ_w is the volume fraction of Widmanstätten ferrite. The thermodynamic criteria used for the displacive Widmanstätten ferrite transformation are those given by Bhadeshia (1981). However, the nucleation rate I_w of Widmanstätten ferrite per unit area is obtained classically in a similar fashion to that of allotriomorphic ferrite. The constant growth rate G_w of Widmanstätten ferrite was found using Trivedi's (1970) theory for the diffusion controlled growth of parabolic cylinders. So the volume fraction of Widmanstätten ferrite is approximated from equation 2.44 as:

$$\dot{\zeta}_w = 4(1 - \zeta_w)\left(\frac{\pi I_w S_V' G_w^3}{3}\right)^{1/4}\left[\log_e\left(\frac{1}{1 + \zeta_w}\right)\right]^{3/4}(1 - \zeta_f - \zeta_p) \tag{2.47}$$

Bainite forms if thermodynamic criteria established by Bhadeshia (1981) are met. The growth rate of bainite is found using Trivedi's (1970) theory, however, nucleation is assumed to occur homogeneously at rate I_b per unit volume found using classical theory. Thus the volume fraction of bainite is estimated from equation 2.43 as:

$$\dot{\zeta}_b = 4(1 - \zeta_b)\left(\frac{\pi I_b G_b^3}{3}\right)^{1/4}\left[\log_e\left(\frac{1}{1 + \zeta_b}\right)\right]^{3/4}(1 - \zeta_f - \zeta_p - \zeta_w) \tag{2.48}$$

Martensite is assumed to form when the M_S temperature is reached. The volume fraction of martensite is estimated as an empirical function of the undercooling below M_S and the extent of the preceding transformations to allotriomorphic and idiomorphic ferrite, Widmanstätten ferrite, pearlite and bainite.

The model was tested to ensure that it was consistent with metallurgical expectations. Decreasing the austenite grain size and the alloy carbon content were both found to cause an acceleration in the rate of isothermal transformation. During continuous cooling the transformation start temperature was appropriately sensitive to the cooling rate - the higher the cooling rate the lower the start temperature. Deformation caused an increase in the rate of transformation. The main limitations of this approach are the assumption of a completely random distribution of nuclei in the austenite and the adoption of a spherical particle geometry for all phases except martensite. Both of these assumptions are unrealistic.

2.3.3 Umemoto et al.

Perhaps the most comprehensive model for sequential microstructural evolution in wrought steels to date is due to Umemoto *et al.* (1992). This model considered the formation of

five phases; allotriomorphic ferrite, Widmanstätten ferrite, pearlite, bainite and martensite in work-hardened steels. The thermodynamics of the alloy were modelled under paraequilibrium conditions for a system containing up to ten elements (Fe, C, Si, Mn, Ni, Cr, Mo, V, W and Cu). Continuous cooling was represented as series of small isothermal heat treatments.

Allotriomorphic ferrite was assumed to nucleate at the austenite grain boundaries and grow in a parabolic fashion. Pearlite transformation is thermodynamically possible when the carbon concentration in the untransformed austenite reaches the A_{cm} phase boundary. However, Umemoto *et al.* introduced an additional criterion, that the allotriomorphic ferrite-austenite interface moves sufficiently slowly that cementite can nucleate on it (*i.e.* the incubation time for cementite nucleation must be shorter than the time taken for the interface to advance a distance greater than the radius of a critical cementite particle). The model used to calculate the nucleation rate of pearlite was not given. Hillert's (1970) model was used to calculate the pearlitic growth rate. The criteria used to determine the thermodynamic feasibility of Widmanstätten ferrite and bainite nucleation were based on a displacive model due Bhadeshia (1981), however, the nucleation rate was obtained via classical nucleation theory. The growth rates of Widmanstätten ferrite and bainite were described using theory for the diffusion controlled growth of parabolic cylinders (Trivedi, 1970).

A summary of the various nucleation sites and morphologies adopted by Umemoto *et al.* to model the transformation kinetics of the various phases is given in Table 2.1. Note that Umemoto *et al.* gives analytical solutions, based on the methods due to Cahn (1956), for unusual boundary nucleated morphologies; the isothermal and parabolic growth of ellipsoids (*e.g.* allotriomorphic ferrite), and the isothermal and linear growth of paraboloids (*e.g.* Widmanstätten ferrite and bainite).

Microstructural evolution was modelled sequentially using a numerical method. Iterative equations describing the extent of each 'independent' transformation during continuous cooling were developed from the equivalent analytical solutions for isothermal transformation. The actual volume fraction of each phase was obtained by reducing the 'independent' volume fraction according to the real volume fraction of austenite remaining untransformed at the start of each 'independent' transformation. For example, the bainite reaction is often preceded by transformations which result in the formation of allotriomorphic ferrite, Widmanstätten ferrite and pearlite. Consequently the actual volume fraction of bainite formed is approximately given by:

$$X_b = (1 - X_\alpha + X_w + X_p)X_b' \qquad (2.49)$$

where X_b' is the 'independent' volume fraction of bainite and X_α, X_w and X_p are the actual

Phase	Nucleation Site	Morphology
Allotriomorphic ferrite	Intragranular	Sphere
	Intergranular	Ellipsoid
Widmanstätten ferrite	Intragranular	Disc
	Intergranular	Paraboloid
Pearlite	Intragranular	Sphere
	Intergranular	Sphere
Bainite	Intragranular	Disc
	Intergranular	Paraboloid

Table 2.1   Summary of the various nucleation sites and morphologies adopted by Umemoto *et al.* (1992).

volume fractions of allotriomorphic ferrite, Widmanstätten ferrite and pearlite that had formed prior to the start of the bainite transformation. Transformation finished when the M_S temperature was reached. The volume fraction of martensite was obtained as an empirical function of the undercooling below M_S and the extent of the other transformations.

Work-hardening was considered to accelerate the austenite to ferrite transformation in a number of ways:

(1) The driving force for the austenite to ferrite transformation is increased due to the accumulated strain energy in the austenite.

(2) An increase in the austenite grain surface area per unit volume.

(3) The activation energy barrier to nucleation at the austenite grain surface is reduced.

(4) Deformation structures within the austenite grains (*e.g.* dislocation tangles and annealing twins) promote intragranular nucleation.

In such a system, a phase will nucleate at more than one type of site so that ferrite nucleates in a simultaneous inter- and intra-granular fashion. Allotriomorphic or idiomorphic ferrite, for example, will nucleate on the austenite grain surface, annealing twins and dislocations. Thus the total 'independent' volume of allotriomorphic or idiomorphic ferrite was estimated as:

$$X'_\alpha = 1 - \exp[-(X^e_g + X^e_t + X^e_d)] \qquad (2.50)$$

where X^e_g, X^e_t and X^e_d are the extended volumes of allotriomorphic or idiomorphic ferrite at the austenite grain surface, annealing twins and dislocations.

31

Using this approach Umemoto *et al.* found that the work-hardening of austenite noticeably accelerates the allotriomorphic ferrite and pearlite transformations. The effect on the bainite transformation was considerably less. Inoue *et al.* (1992) applied this model, in combination with a finite element method (FEM) model which described strain and temperature and a recrystallisation model, to predict the final microstructure as a function of position in hot-rolled steel plate. Comparison with experimental trials indicated that microstructural evolution was successfully predicted in plates that were subject to air cooling, however, accuracy was not maintained if the plate was water cooled. It is considered that the main limitations inherent in this approach due to Umemoto *et al.* are the assumption that each phase transformation occurs sequentially and independently, and the approximation shown in equation 2.50 which is used to represent the simultaneous inter- and intra-granular nucleation of ferrite.

2.4 Modelling Competitive Transformations in Steel Weld Deposits

Bhadeshia and co-workers (1993 and 1985) have over a number of years developed a computer model for predicting the as-deposited microstructure in low-alloy steel welds. Thermodynamic and kinetic equations are used to describe the transformation start temperatures and the growth rates of the various microstructural constituents. These equations take account of the heat input, welding speed, welding processes and weld metal composition. Thus, it is possible to estimate the volume fractions of the various microstructural constituents, that form competitively, to make up the final weld microstructure. From these microstructural predictions it is possible to estimate some elementary mechanical properties.

The first step is to model the cooling behaviour of the weld metal. If the thickness of the parent plate is sufficiently large with respect to the heat input then heat flow will occur in three-dimensions (Figure 2.2). The cooling rate is then approximately given as (Weisman, 1981):

$$\frac{dT}{dt} = \frac{2\pi k(T - T_i)^2}{Q\eta} \tag{2.51}$$

where k is the thermal conductivity of solid iron, Q is the electrical energy input per unit length of weld deposit, T is the temperature at any instant, T_i is the interpass temperature and η is arc energy transfer efficiency, taken to be 0.95 for submerged-arc welds (Easterling, 1992). Unfortunately experience has indicated that this equation does not adequately represent experimental cooling curves (Bhadeshia *et al.*, 1985). However, if equation 2.51 is rewritten as:

$$\frac{dT}{dt} = \frac{C_1(T - T_i)^{C_2}}{Q\eta} \tag{2.52}$$
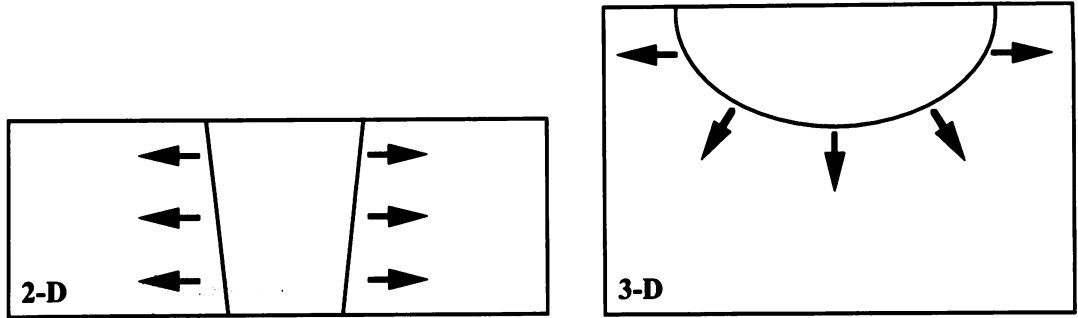
Figure 2.2 Schematic of two- and three-dimensional heat flow in the welding process.

where C_1 and C_2 are constants fitted to different welding systems then an accurate representation of the cooling rate is obtained over the temperature range 800 to 500 °C.

The growth of allotriomorphic ferrite involves the reconstructive thickening of the grain boundary layers. Work by Dallam and Olson (1989) has demonstrated that the thickness of the allotriomorphic layer does not vary with the austenite grain size, which implies that nucleation effects can frequently be neglected when calculating the volume fraction. Assuming paraequilibrium conditions, the half-thickness of the layer during isothermal growth is modelled as $q = \vartheta t^{1/2}$ where ϑ is the one-dimensional parabolic thickening constant and t is the time available for growth (Christian, 1975). The one-dimensional parabolic thickening rate constant is obtained by solving diffusion equations (section 4.3.2), which requires a knowledge of the chemical compositions of the phases at the interface. These are calculated using computed phase diagrams (Bhadeshia, 1982c). The model does not take account of soft impingement effects which may become significant with decreasing austenite grain size. Scheil's rule (Grong, 1994) is used to allow for the fact that the transformation is not in fact isothermal. This involves dividing the calculated cooling curve into an equivalent series of small isothermal time steps. If $\tau(T)$ is the incubation time prior to the start of detectable transformation at the temperature T, as given by the computed TTT curve (Bhadeshia, 1982b), then transformation is considered initiated at the temperature T_h when:

$$\int_{t=0}^{t} \frac{dt}{\tau(T)} = 1 \qquad (2.53)$$

where dt is the duration of the small isothermal step at the temperature T. Allotriomorphic ferrite growth is taken to finish when the reconstructive and displacive C-curves on the calculated TTT diagram intersect. This is the temperature T_l at which displacive transformations

become kinetically more advantageous (Bhadeshia *et al.*, 1985). Therefore, the half-thickness of the layer of allotriomorphic ferrite during continuous cooling is:

$$q = \int\limits_{t=0}^{t_l} \frac{\vartheta}{2} t^{-1/2} dt \qquad (2.54)$$

where $t = 0$ at T_h and $t = t_l$ at T_l. The volume fraction of allotriomorphic ferrite can then be estimated using the expression:

$$\nu_\alpha = \frac{2q \tan 30°(2a - 4q \tan 30°)}{a^2} \qquad (2.55)$$

where a is the cross sectional side length of the base of a hexagonal prism which is used to describe the austenite grain structure (a is related to the austenite grain size via stereological equations given by Bhadeshia and Svensson, 1993). This method works well after correction by a factor of approximately 2. The model allows for substitutional solute segregation due to non-equilibrium solidification, by calculating the temperature T_h at which allotriomorphic ferrite formation begins in the solute depleted regions which have the lowest hardenability. The composition of the solute depleted regions is estimated from partitioning coefficients for each element at the liquidus temperature. This approach relies upon the assumption that diffusion during cooling does not lead to significant homogenisation.

The growth rate V_2 of Widmanstätten ferrite is estimated (Bhadeshia, 1985) using theory due to Trivedi (1970) which is documented in section 4.4.3. This transformation is taken to begin at the allotriomorphic stop temperature T_l, and is usually completed in a fraction of a second because the growth rate is so large. This allows the transformation to be modelled isothermally. The volume fraction of Widmanstätten ferrite is given by:

$$\nu_w = \frac{C_4 V_2 t_2^2 (2a - 4q \tan 30°)}{4a^2} \qquad (2.56)$$

where C_4 is a constant independent of alloy composition, q is the half-thickness of allotriomorphic ferrite layer and t_2 is the time available for Widmanstätten ferrite growth. However, the growth of Widmanstätten ferrite is now considered to be in direct competition with intragranularly nucleated acicular ferrite for the residual austenite (Figure 2.3). Thus, hard impingement with acicular ferrite must be allowed for.

To model this competition a phenomenological approach is adopted, where t_c is the time between the nucleation of Widmanstätten ferrite and the nucleation of acicular ferrite. If the time $t_3 = (2a \sin 60° - 2q)/V_2$ required for a plate of Widmanstätten ferrite to grow across the austenite grain is less than t_c, then Widmanstätten ferrite can grow unhindered and $t_2 = t_3$.
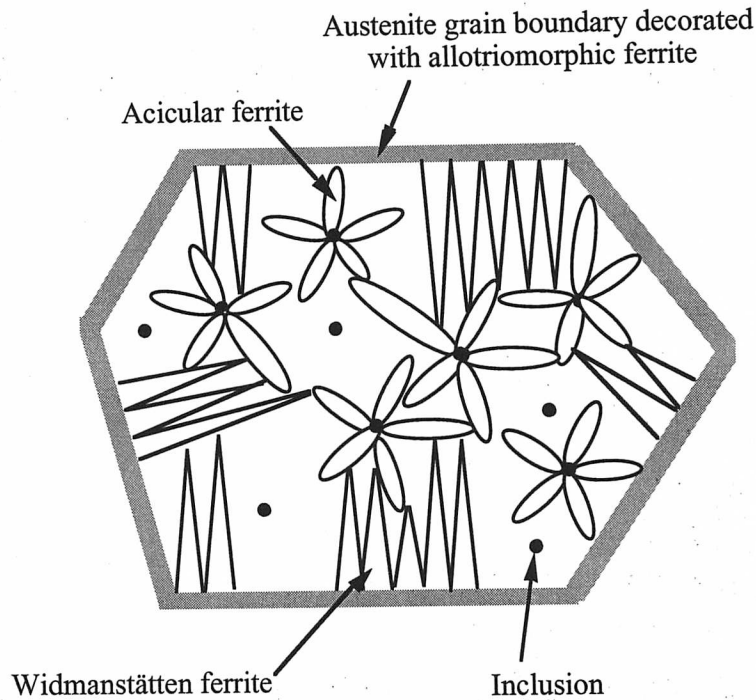
Figure 2.3 The competition between acicular and Widmanstätten ferrite for the residual austenite.

If not, then Widmanstätten ferrite growth is taken to finish when acicular ferrite begins to nucleate and $t_2 = t_c$. The critical time $t_c \simeq 0.21$ s is derived empirically and is invariant. Comparison with published data reveals good agreement for most welds. However, t_c is a function of various parameters such as alloy hardenability and the inclusion population (nucleation potency and number density) which are known to influence the temperature at which acicular ferrite starts to form. It is suggested here that to model such complex systems more effectively requires a fundamental approach which considers the simultaneous and competitive formation of a number of phases which nucleate at both the austenite boundaries and on non-metallic inclusions.

CHAPTER THREE

Inclusion Nucleation Potency

This chapter contains a literature survey which describes the formation, composition and morphology of non-metallic inclusions in steel weld metals. It documents the way in which they influence the austenite to ferrite transformation by acting as intragranular nucleation sites for the phase known as acicular ferrite. The nucleation potency of the inclusions is examined in the context of the various nucleation mechanisms which have been suggested.

3.1 Non-metallic Inclusions in Steel Welds

3.1.1 An Introduction

Weld inclusions form when solubility limits are exceeded as the liquid or solid metal cools. The resulting non-metallic compounds are typically 0.1 to 1 μm in diameter and are usually distributed randomly in the microstructure. Inclusion number densities can be very high in steel welds, $\simeq 10^8$ to 10^9 mm^{-3}, far greater than in most wrought steels (Court and Pollard, 1989; Kluken and Grong, 1989; Es-Souni and Beaven, 1990). The surface area presented by the inclusions can be comparable to the austenite grain boundaries in any given volume of material. Inclusions tend to be heterogeneous in nature with a central oxide-rich core surrounded by incomplete surface layers of a variety of phases. The actual composition can vary widely depending on the parent plate, flux and filler wire. Elements such as O, Al, Mn, Si, Ti, S, N and Cu occur in the form of various oxides, silicates, nitrides and sulphides; they may be crystalline or glassy.

Non-metallic inclusions influence the austenite to ferrite transformation in two ways. Firstly; they provide intragranular nucleation sites for acicular ferrite, and secondly; they might pin the austenite grain boundaries, thereby decreasing alloy hardenability. This research will focus on the former effect.

3.1.2 Inclusion Morphology

An extensive scanning electron microscope (SEM) based automated image analysis of non-metallic inclusions by Kluken *et al.* (1988), revealed that weld metal inclusions are approximately spherical in shape with a mean aspect ratio of 1.13. The most irregular inclusions (relatively few) have an aspect ratio of less than 1.55. Inclusions which are rich in the various titanium oxides tend to be faceted and more irregular (Kayali *et al.*, 1983; Dowling *et al.*, 1986).

Inclusion structure can vary from the core to the surface. Minerals which have higher melting points precipitate first to form the core, the surface layers forming later from the phases with lower melting points. Experimental analysis generally confirms this. Court *et al.* (1989) reported that large numbers of inclusions have surface cavities which may be formed by gas evolution or solidification contraction.

3.1.3 Inclusion Formation

The heterogeneity of inclusions is primarily due to the deoxidation sequence by which they are formed. For a slag protected weld the flux is the major oxygen source. Oxidation is considered to be completed quickly due to the high temperatures, large surface areas and

intense turbulence in the weld pool. During solidification the weld pool oxygen content has to adjust by reacting with deoxidants as its solubility decreases < 0.002 wt % in solid steel. The supersaturation of oxygen and large undercooling mean that oxide inclusions are able to nucleate homogeneously ($\simeq 10^8$ nuclei per mm^3). If the rejected oxygen is unable to find suitable elements with which to combine, it will form undesirable voids filled with carbon monoxide. The oxygen content of a weld deposit can be estimated (Figure 3.1) from the 'basicity index' B of the flux which is given as (Eagar, 1978):

$$B = \frac{\Sigma(\text{basic oxides wt \%})}{\Sigma(\text{non} - \text{basic oxides wt \%})} \tag{3.1}$$

or explicitly:

$$B = \frac{CaO + MgO + BaO + SrO + Na_2O + K_2O + Li_2O + (1/2)(MnO + FeO)}{SiO_2 + (1/2)(Al_2O_3 + TiO_2 + ZrO_2)} \tag{3.2}$$
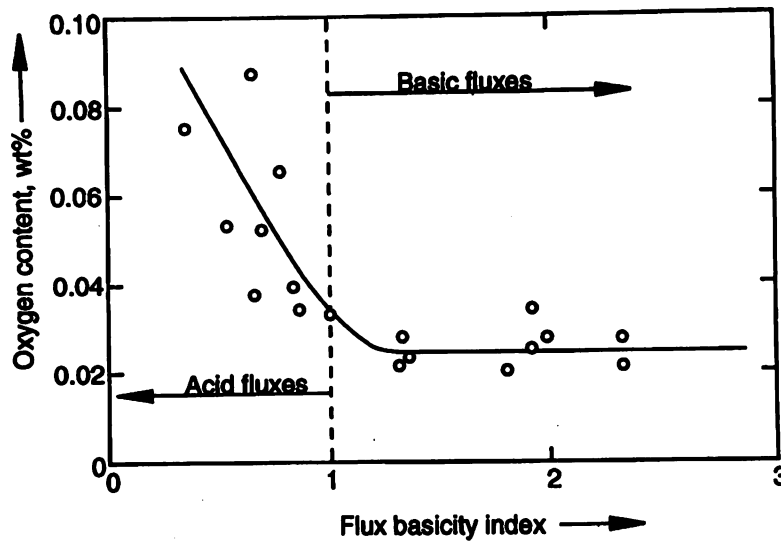
Figure 3.1 Weld metal oxygen content versus the flux 'basicity index' (Grong, 1994).

Weld pool compositions are designed with elements that react with oxygen to form inclusions. Grong *et al.* (1986) divided the weld pool into two zones. In the 'hot' zone, just below the arc, the deoxidation products are swept out of the weld pool by highly turbulent flows (primarily due to the intense electromagnetic forces induced by the welding arc), whilst in the 'cold' zone such products are entrapped as finely dispersed inclusions. The relative sizes of these two zones is thought to influence the final weld oxygen content. Kluken and Grong concluded in 1989 that the oxide cores are formed during the primary deoxidation stage which is thought to occur in the 'cold' zone. The exact deoxidation product depends on the relative

activities of Al, Ti, Si, Mn, and O. The composition of the inclusion core is strongly dependent upon the aluminium to oxygen ratio in the weld pool. Either $Al_2O_3.MnO$ or γ-Al_2O_3 form according to the exact aluminium to oxygen ratio. If the titanium concentration is increased at the expense of aluminium then titanium-rich oxides are found. In the absence of sufficient titanium or aluminium the glassy phase $MnO.SiO_2$ is commonly found. Court and Pollard (1989) considered that the globular shape of many inclusions is consistent with their forming as immiscible liquids in the weld pool. The surface coatings of sulphides (manganese or possibly copper sulphides) and Ti-rich compounds (Ti-oxides, TiN, or Ti(C,N)) precipitate during and possibly after weld solidification, in the solute rich interdendritic regions.

It is very difficult in the non-equilibrium welding process to identify the exact deoxidation sequence for a particular welding system. However, Kluken and Grong (1989) have demonstrated that it is possible to estimate average inclusion compositions in terms of their constituent phases, using a simple mass balance technique. This approach assumes that aluminium is the first element to react with oxygen, followed by titanium, silicon and manganese. A similar approach is used to estimate the amount of manganese and copper sulphide that forms. Recent theoretical work by Babu *et al.* (1995) has addressed the thermodynamics and kinetics of inclusion nucleation and growth. Figure 3.2 shows calculated TTT (time–temperature–transformation) curves for a variety of possible oxides in two weld metals that contain different concentrations of titanium. It is apparent that the actual deoxidation sequence varies with the concentration of the trace elements in the weld.

3.1.4 Inclusion Composition and Mineralogy

A review of the inclusion phases found in wrought steels was given by Pickering in 1979. Expected oxides include SiO_2, Al_2O_3, (Fe,Mn)O, TiO, TiO_2, Ti_2O_3, Ti_3O_5 and complex Cr-oxides. FeS, MnS, $Ti_{(1+x)}S$, CaS and ZrS are also anticipated. Other possible mineral phases are various nitrides and sulphides. Manganese silicates, together with complex silicates such as spinels, pyroxenes, olivines, garnets, feldspars, and cordierites might be expected. Calcium aluminates could also form. Fortunately real weld inclusions are not quite as varied and complex as this. An excellent and comprehensive description of the chemical and physical characteristics of such inclusion phases is given by Kiessling (1978).

3.1.5 Aluminium Minerals

Thermodynamic considerations indicate that aluminium is generally the strongest oxide former present in significant quantities in most steel weld metals. Consequently it is considered that aluminium oxides will form first from the melt. This has been confirmed by various studies
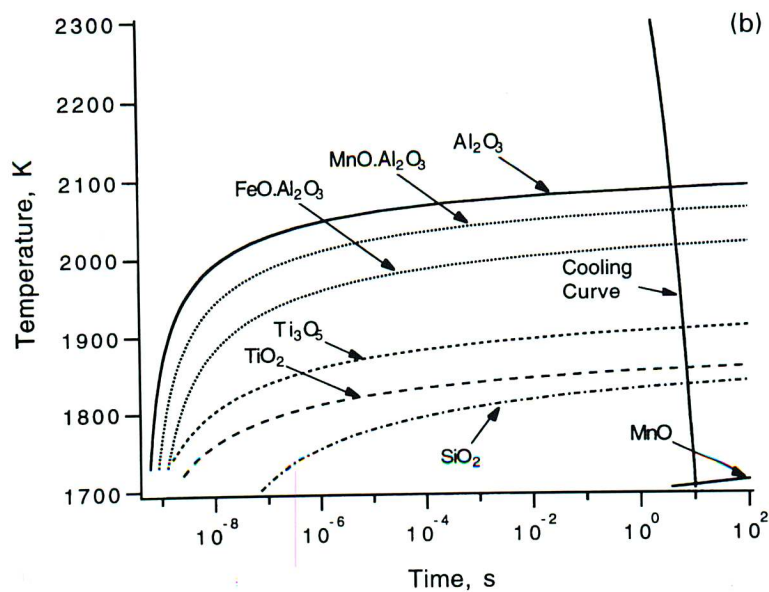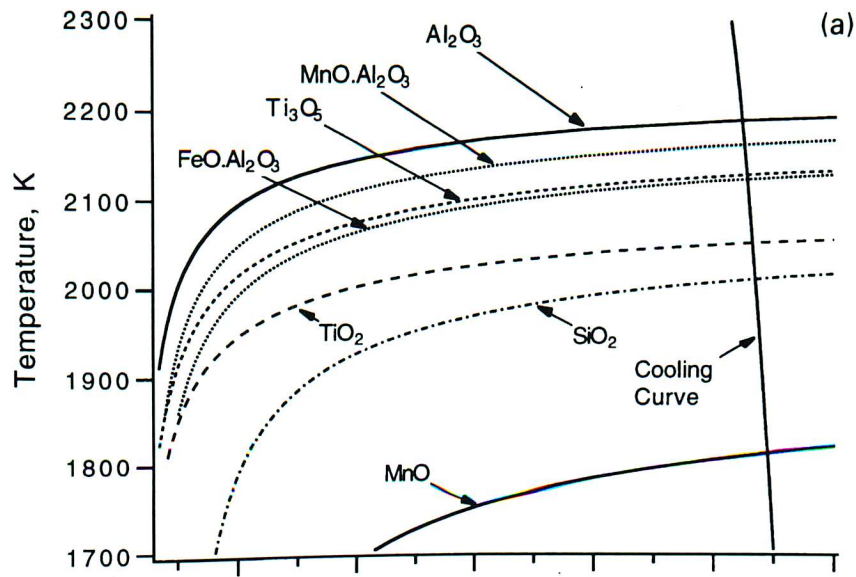
Figure 3.2   Calculated TTT curves for various oxide inclusions for two weld metals with different titanium contents; (a) a titanium and aluminium rich weld deposit (250 ppm wt Ti and 260 ppm wt Al), (b) an aluminium rich weld deposit (30 ppm wt Ti and 170 ppm wt Al). (Babu *et al.*, 1995).

which indicate that when sufficient aluminium is available, it will form a major part of the inclusion core. Dowling *et al.* (1986), Mills *et al.* (1986), Es-Souni and Beaven (1990) and Fox and Brothers (1995) have identified the spinel galaxite Al_2O_3.MnO with a lattice parameter

of 0.82 nm. Work by Thewlis (1989a and 1989b) demonstrated that if the aluminium content was increased whilst the oxygen and sulphur levels were maintained constant, the average inclusion composition changed from $MnO.SiO_2$ to the spinel galaxite $Al_2O_3.MnO$ and finally γ-Al_2O_3. Barritte and Edmonds (1981), Saggese *et al.* (1983) and Evans (1990b) found that the composition of an inclusion core generally lies in the ternary oxide system MnO–SiO_2–Al_2O_3 with an approximately constant MnO / SiO_2 ratio and a variable Al_2O_3 content which depends upon the Al content (Figure 3.3). Selected area diffraction patterns (Evans, 1990a) indicate that in welds containing negligible amounts of Al and Ti, the phase $MnO.SiO_2$ occurs in either its tetragonal, monoclinic or triclinic form. Work by Zhang and Farrar (1996) is consistent with these findings.
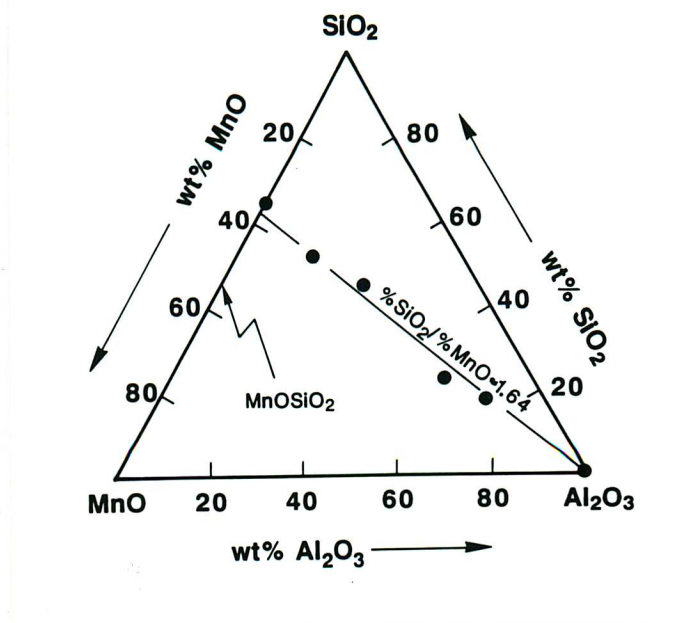
Figure 3.3   Phase diagram for the ternary oxide system MnO–SiO_2–Al_2O_3 with measured inclusion compositions (Evans, 1990b).

3.1.6   Titanium Minerals

In welds containing large concentrations of titanium (> 0.090 wt %) faceted inclusions form, consisting of Ti-oxide in combination with smaller amounts of Al, Mn and S (Kayali *et al.*,1983). Dowling *et al.* (1986) reported similar results. Court and Pollard (1989) observed that inclusions comprised primarily of Ti, would form even at low Ti levels, if the Al concentration was very low. Such inclusions had compositions in the MnO–SiO_2–TiO_2 system. Figure 3.4 shows that at very low titanium concentrations the inclusions consist primarily of $MnO.SiO_2$, but that SiO_2 is progressively replaced by TiO_2 as the weld metal Ti content is

increased. Indeed very recent research by Fox and Brothers (1995) using HVEM (high voltage electron microscopy) has unambiguously identified the hexagonal pyrophanite $MnO.TiO_2$. They further suggested that inclusions less rich in Ti might be $2MnO.TiO_2$.

Large titanium concentrations are not usually encountered in practice, the concentration 0.01 to 0.02 wt % being more typical. It is commonly found that face centred cubic (f.c.c.) titanium-rich phases with a lattice parameter of between 0.42 and 0.44 nm are present at the surface of the inclusions in such welds. The actual phase might be TiN, TiO, TiC or Ti(C,N) (for example see Dowling *et al.*, 1986). Ito and Nakanishi in their 1976 paper, considered this phase to be TiN claiming that free nitrogen levels dropped considerably in Ti containing welds. Evans (1991) found that this Ti-rich phase precipitated on $MnO.SiO_2$ inclusions in the welds they examined. The solidification temperature of $MnO.SiO_2$ (1270 °C) and published solubility products for TiN (Suzuki *et al.*, 1987) and TiC (Irvine *et al.*, 1967), suggest that TiN should be the first phase to nucleate, at approximately 980 °C. Evans calculated that TiC was also likely to precipitate at temperatures close to 830 °C and further suggested that TiC was likely to enter solution in TiN to give Ti(C,N). Thewlis (1986) pointed out that while it was not possible to distinguish between TiN and TiO by measuring lattice parameters, the presence of weak X-ray diffraction (XRD) lines indicated that TiN was present. Research by Kluken and Grong (1989) is consistent with this.
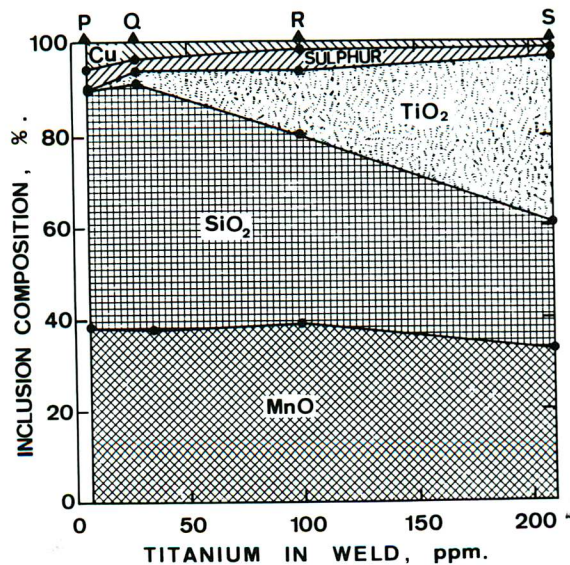
Figure 3.4 Average measured composition of non-metallic inclusions as a function of weld metal titanium content (Evans, 1991).

Mori *et al.* (1981) reported Ti-rich particles but believed them to be TiO, Ti_2O_3 and $FeO.TiO_2$ after XRD examination, whilst Zhang and Farrar (1996) believed that they were TiO and/or TiO_2 and TiN. TiO is thermodynamically more stable under standard conditions than TiN and would be expected to form first. However, the activities of the reactants and products together with kinetic effects may alter the sequence of transformation. St-Laurent and L'Espérance (1992) used a windowless energy-dispersive X-ray spectrometer which allowed the detection of the lighter elements carbon, boron, nitrogen and oxygen. They found a large oxygen peak in the inclusions studied, but were unable to detect either carbon or nitrogen and concluded that titanium was combined preferentially with oxygen. However, the weld studied contained less than 0.001 wt % Al and only 0.02 wt % Ti, whilst the oxygen and nitrogen contents were was 0.0231 and 0.0267 wt % respectively. According to the simple sequential deoxidation and mass balance model of inclusion formation suggested by Kluken and Grong (1989), all the titanium and aluminium in this weld metal would combine with oxygen - none would remain to react with either nitrogen or carbon. Thus, St-Laurent and L'Espérance work appears to demonstrate that TiN, TiC, and Ti(C,N) can only form if excess Ti remains available after the reaction with oxygen is completed.

Bhadeshia (1992) claimed that the presence of titanium oxide at the inclusion surface is unlikely given the strong deoxidising potential of titanium. He suggested an alternative explanation whereby the main inclusion body, consisting of manganese and silicon oxides, nucleates and grows on the titanium oxide, but the degree of wetting with the substrate is so small that the other oxides do not succeed in engulfing the titanium oxide.

Recent research has indicated that very small additions of Ti (≥ 0.0005 wt %) can coexist in oxides such as $MnO.SiO_2$ and may significantly affect their character and nucleation potency by enabling them to exist in crystalline rather than a glassy form (Horii *et al.*, 1995). Another interesting observation was made by Barbaro *et al.* (1988) who found TiN cuboids at inclusion cores and thought these may have acted as nucleation sites for inclusions.

3.1.7 Sulphides

Sulphur rich regions, often found at the inclusion surface, have been documented in many papers (Barritte *et al.*, 1981; Barbaro *et al.*, 1988). These are generally thought to be either manganese or copper sulphides. Dowling *et al.* (1986) and Evans (1990a) identified α-MnS with an f.c.c. structure and a lattice parameter of 0.52 nm. α-MnS was also found by Kluken *et al.* (1990). However, in another weld Kluken *et al.* detected β-MnS which also has an f.c.c. structure, but a lattice parameter of 0.56 nm. Both of these welds metals had similar Mn and S contents.

Dowling *et al.* (1986) observed regions rich in Cu and S with a cubic structure and a lattice parameter of 0.59 nm in a wide variety of welds. This could have been CuS_2 or Cu_xS where $1.8 \leq x \leq 2$. Es-Souni and Beaven (1990) have also identified regions rich in both Cu and S. They identified two phases, the cubic digenite phase $Cu_{1.8}S$ with a lattice parameter of 0.56 nm and cubic $Cu_{1.6}S$ with a lattice parameter of 0.54 nm. Work by Court and Pollard (1989) likewise established that Cu and S were often associated with discrete areas at the inclusion surface. These regions had a characteristic globular appearance and often contained high levels of Mn and small amounts Cu, which was considered to indicate the presence of a copper-manganese sulphide. Zhang and Farrar (1996) also detected sulphide coatings on oxide inclusions, which they found to be MnS and (Mn,Cu)S. These results are compatible with earlier studies by Salmon Cox and Charles (1965) who established that in wrought alloys small amounts of Cu can enter solid solution in MnS. Kayali *et al.* (1983) also reported the presence of a Mn, Cu and S rich envelope around many inclusions they examined, but concluded that most sulphur was present in the form of MnS. However, Evans (1990a) found that increasing the Cu content from 0.02 to 1.4 wt % whilst maintaining a constant Mn concentration ($\simeq 1.5$ wt %) had no measurable effect on the inclusion population. This finding is in agreement with the early work by Morrogh (1946) which found that Cu_2S would only form in cast irons if the Mn content was very low and the Cu and S contents very high. Kluken and Grong (1989) have recently argued that CuS is an unlikely reaction product in steel welding. WDS (wavelength dispersive spectrometer) data indicated that the peak Cu counts in the sulphur rich regions were not significantly greater than those found throughout the steel when mechanically polished specimens were examined. They considered that the Cu reported by other researchers might have been introduced as contamination which is inherent in the carbon extraction replica process used.

3.1.8 Other Phases

The following elements have also been detected in various weld metal inclusions: boron, vanadium, calcium, various rare earth metals and nitrogen. Thewlis (1994) introduced calcium into a series of welds and found that the inclusions were significantly larger, containing what were thought to be complex alumino-silicates or calcium silicates. Contrary to this Dowling *et al.* (1986) and Pargeter (1981) failed to detect calcium in any inclusions despite using calcium based fluxes. Dowling suggests that either calcium does not dissolve, or that large calcium inclusions form early and are removed with the slag. Dowling *et al.* (1986) observed the silica (SiO_2) phase β-cristobalite which has a spinel type structure and a lattice parameter of 0.71 nm in a small proportion of the inclusions they studied. Both Evans (1990b) and

Zhang and Farrar (1996) detected significant numbers of silica inclusions, but only in those welds which contained negligible concentrations of the strong deoxidisers Al and Ti. Various boron oxides, carbides and nitrides may also precipitate depending on the weld composition and thermal history.

3.2 Inclusion Nucleation Mechanisms

3.2.1 Acicular Ferrite Nucleation

Numerous authors (Barritte *et al.*, 1981; Kayali *et al.*, 1983; Dowling *et al.*, 1986; Abson *et al.*, 1978; Ferrante and Farrar, 1982; Barbaro, 1990) have concluded that acicular ferrite is nucleated on non-metallic inclusions. Several nucleation mechanisms have been proposed in an attempt to explain the nucleation potency of different inclusions. Unfortunately, despite considerable effort, no dominant mechanism has been conclusively identified. This is probably due to several factors which are summarised below:

(1) Inclusions are complex heterogeneous structures which vary considerably in size, shape and composition, even in the same weld deposit.

(2) It has not been possible to measure inclusion nucleation potency directly. Researchers have therefore tended to assume that a high volume fraction of acicular ferrite indicates that potent inclusions are present. However, all inclusions are potential nucleants if the undercooling below the Ae_3 temperature is sufficiently large.

(3) Acicular ferrite formation is influenced not only by inclusion type, but also by inclusion population density and size distribution, cooling rate, alloy hardenability, austenite grain size and soluble boron concentration.

(4) The Zener type pinning effect that inclusions might have on the austenite grain size.

(5) The possibility that no one mechanism controls inclusion nucleation potency (Abson, 1987).

The following mechanisms have been proposed to explain the preferential nucleation of acicular ferrite on certain types of non-metallic inclusion:

(1) Nucleation on an inert substrate. Inclusion nucleation potency is then controlled by the size, shape and interfacial energy of the nucleating austenite-inclusion surface.

(2) Chemical reaction and/or depletion of the austenite matrix local to the inclusion surface. This increases the thermodynamic driving force for the γ-α transformation.

(3) Lattice matching (epitaxy) between the ferrite and the inclusion surface. This reduces the ferrite-inclusion interfacial energy, that opposes nucleation.

(4) Localised stresses due to differential thermal contraction between the austenite matrix and the inclusion. This might increase the driving force for transformation, or favour the nucleation of certain crystallographic variants of ferrite, or promote nucleation on dislocations local to the inclusion surface.

3.2.2 Nucleation on an Inert Substrate

Several authors (Dowling *et al.*, 1986; Barbaro *et al.*, 1988; Zhang and Farrar, 1996) have put forward the view that because inclusions do not seem to have an epitaxial relationship with the acicular ferrite grains they appear to have nucleated, nor appear to chemically react with surrounding steel, nor appear to be affected by differential thermal contraction, they simply act as inert nucleating substrates. Nucleation will then be preferred at high energy interfaces between the inclusion, or some part of it, and the surrounding austenite. The size and shape of the nucleating substrate will also influence the nucleation potency. For example, a discontinuity or cavity upon the inclusion surface would significantly reduce the activation energy barrier to nucleation (Gutzow, 1980). A corollary to this is that decreasing the inclusion size increases the activation energy barrier to nucleation.

Dowling *et al.* considered that inclusions were inert substrates, primarily because they were unable to firmly establish the existence of an alternative mechanism during a systematic study conducted in 1986. They assumed that interfacial surface energies would be higher for those phases with higher melting points and proposed the following ranking - in descending order of potency, TiO, SiO_2, MnO, Al_2O_3.MnO, MnS, Mn-silicates and Cu-sulphides. However, as Es-Souni and Beaven pointed out in their 1990 paper, this cannot explain why titanium containing phases are considered to be much more potent than other phases, such as Al_2O_3 which has a very high interfacial energy with the surrounding austenite. Extensive research by Zhang and Farrar (1996) using *in situ* water quenched weld metals (these experiments involved quenching the welded piece into agitated water whilst the welding process continued), transmission electron microscopy (TEM), energy dispersive X-ray spectroscopy (EDX) and dilatometry, also failed to find any correlation between inclusion nucleation potency and inclusion chemistry. They came to the conclusion that the inclusions may nucleate acicular ferrite

by acting simply as a substrate which will reduce the activation energy barrier to nucleation according to classical heterogeneous nucleation theory. Small amounts of TiO and/or Al_2O_3 were thought to promote the nucleation of acicular ferrite by improving the size distribution of the inclusion population. They attributed this to the high melting points and low free energies of formation of TiO and Al_2O_3 compared with manganese silicate and sulphide inclusions. TiO and Al_2O_3 particles therefore form at high temperatures in the liquid weld metal. These particles then provide nucleation sites for other inclusions phases which form via precipitation and subsequent coalescence. Zhang and Farrar believed that this would result in the formation of larger inclusions which would offer a lower activation energy barrier to nucleation. They suggested that the most favourable inclusion sizes are within the range 0.3 to 0.9 μm.

Thermodynamic calculations by Ricks *et al.* in 1982 demonstrated how the classical heterogeneous activation energy barrier to nucleation decreases with increasing inclusion size (Figure 3.5). They predicted that inclusions would not become potent nucleation sites unless they were greater than 0.25 to 0.5 μm in radius. Their results indicate that grain boundaries are energetically more favourable inert nucleation sites than inclusions. Jang and Indacochea (1987) reported that inclusions of less than 0.6 μm in diameter were generally associated with the nucleation of acicular ferrite, whilst those greater than 1.0 μm tended to pin austenite grain boundaries and be associated with blocky allotriomorphic ferrite. They also found that very small inclusions of less than 0.3 μm diameter were ineffective nucleants and could only pin grain boundaries. More recent research (Barbaro, 1990) indicates that if the inclusion radius drops below 0.4 - 0.5 μm then acicular ferrite nucleation is almost entirely suppressed. Liao and Liu (1992) found the highest volume fraction of acicular ferrite in those welds with inclusions which were about 0.45 μm in diameter. This tendency to quote a minimum particle size below which nucleation does not occur, has been criticised recently by Bhadeshia (1992), who reminds us that the activation energy barrier to nucleation will depend on other factors which will vary according to the transformation conditions. Furthermore, Rees and Bhadeshia (1994) consider that if acicular ferrite is a displacive transformation product (a bainite) then classical nucleation theory is not really appropriate (section 3.2.3).

Inclusion size is also thought to influence the austenite grain size via Zener type pinning. A dense distribution of small inclusions will restrain grain growth most effectively, promoting a higher volume fraction of grain boundary nucleated phases such as allotriomorphic ferrite, thereby reducing the maximum volume fraction of acicular ferrite that can subsequently form. Consequently, for a given volume fraction of inclusions a higher volume fraction of acicular ferrite would be expected the larger the mean inclusion size. Hence, it is very difficult to
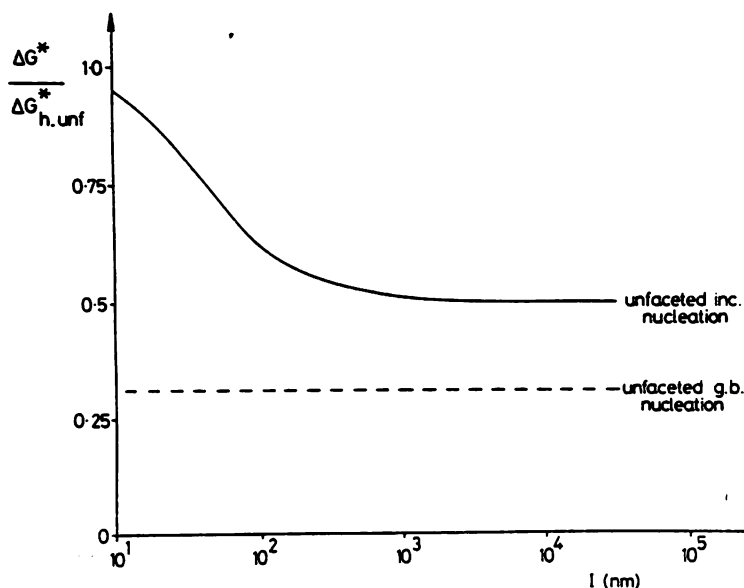
Figure 3.5 Plot of the normalised heterogeneous activation energy barriers to the nucleation of ferrite at a spherical inclusion and at a planar grain boundary. These are normalised with respect to the homogeneous activation energy barrier to nucleation (Ricks *et al.*, 1981).

separate the effects of inclusion size *per se* on nucleation potency. On balance then, the evidence available to date suggests that an inert surface mechanism on its own is unlikely to adequately explain the nucleation potency of inclusions.

3.2.3 Localised Stresses and Inclusion Nucleation Potency

Differential thermal contraction between an inclusion and the austenite matrix during cooling will induce high stresses and elastic / plastic strains local to the inclusion surface. However, if the cooling rate is sufficiently slow then the magnitude of these stresses and strains might be significantly reduced or even eliminated by dynamic recovery and recrystallisation processes that occur above the Ae_3 temperature. In spite of this possibility numerous authors have suggested a variety of mechanisms whereby differential thermal contraction might assist nucleation upon or local to an inclusion surface:

(1) Nucleation could occur upon the dislocations debris local to the inclusion surface, that forms during the plastic deformation associated with differential thermal contraction.

(2) The strain energy associated with these dislocations might assist nucleation at the inclusion surface by contributing towards the driving force for the γ-α transfor-

48

mation.

(3) The complex elastic and plastic strain fields that are generated around inclusions could promote the formation of specific variants of ferrite which are orientated in a crystallographically favourable manner.

(4) The dislocation debris could produce embryos for displacive transformation products such as bainite (acicular ferrite is thought to be a bainite).

The strain raising potential due to differential thermal contraction between an inclusion and the austenite matrix is of the general form (Brooksbank and Andrews, 1972):

$$\pm \left[\Phi(\delta_\gamma - \delta_I)\Delta T \right] \tag{3.3}$$

where Φ is a complex function of the mechanical properties of the inclusion and the austenite matrix, and of the inclusion shape, size and distribution. δ_γ and δ_I are the coefficients of thermal expansion of the austenite matrix and the inclusion respectively. ΔT is the temperature change (a decrease is negative). Table 3.1 gives mean values of δ_γ and δ_I. Note that all of the likely constituent phases have lower coefficients of thermal expansion than the austenite matrix.

It is thought that differential thermal contraction between inclusions and the austenite matrix during cooling leads to a high dislocation density local to the inclusion surface. Acicular ferrite might nucleate upon these dislocations. However, classical nucleation theory indicates that although heterogeneous nucleation on dislocations is much more favourable than homogeneous nucleation, it is considerably less likely than heterogeneous nucleation at the austenite grain boundaries or directly at the inclusion surface. Therefore, differential thermal contraction might be better considered to assist nucleation directly upon the inclusion surface, because the stored strain energy due to the dislocation debris would increase the driving force for the γ-α transformation.

Liu and Olson (1986) evaluated the effects of differential thermal contraction between an inclusion and the austenite matrix on weld metal transformations, by considering 'a ball in an elastic hole' model. During cooling the austenite will contract more than the inclusion. Assuming continuity at the interface and an incompressible inclusion, the total strain energy in the austenite can then be estimated by calculating work done on the hole. This is estimated to be $\simeq$ 0.5 J cm^{-3} which is several orders of magnitude lower than the γ-α free energy change during transformation $\simeq$ 100 J cm^{-3}. This indicates that the strain energy generated is relatively insignificant and that localised stresses might not explain the nucleation of acicular ferrite.

Phase	Expansivity ($\times 10^{-6}$ $^{\circ}$C^{-1})
$(Al_2O_3)_2.(MnO)_2.(SiO_2)_5$	2.0
β-SiO_2	3.0
BN	3.8
SiC	4.4
$(Al_2O_3)_3(SiO_2)_2$	5.0
NbC	6.2
$Al_2O_3.CaO$	6.5
TiC	7.4
Cr_2O_3	7.9
γ-Al_2O_3	8.0
$Al_2O_3.MnO$	8.0
$Al_2O_3.MgO$	8.4
$Al_2O_3.FeO$	8.6
TiN	9.4
$MnO.SiO_2$	9.5
Fe_3O_3	12.2
CaO	13.5
MgO	13.5
MnO	14.1
FeO	14.2
CaS	14.7
Fe_3O_4	15.3
TiO	16.0
MnS	18.1
Austenite	23.0

Table 3.1 Approximate mean coefficients of thermal expansivity for various phases and austenite (Brooksbank and Andrews, 1972; Kim *et al.*, 1990; Weatherly, 1968).

Yamamoto *et al.* (1987) considered that the thermal stresses due to differential contraction on cooling are compressive in the austenite around most inclusions. This would tend to oppose the austenite to ferrite transformation, which is accompanied by an expansion in volume. However, this simplification might not be justified. When the inclusion has a lower coefficient of thermal expansion than the austenite matrix (true for virtually all inclusions), the

principal circumferential stresses in the austenite are tensile, whilst the principal radial stress is compressive. Another possibility is revealed in experiments conducted by Babu (1991). These demonstrate that applying a compressive uniaxial elastic stress to a specimen of weld metal favours the development of specific crystallographic variants of the displacive transformation product acicular ferrite. This results in the destruction of the conventional chaotic acicular ferrite microstructure. Similarly the complex internal stresses generated around an inclusion by differential thermal contraction might favour specific crystallographic variants of acicular ferrite. However, it is suggested by the author that the complex stress fields around spherical inclusions in combination with the random nature of an inclusion population, would still ensure that a chaotic microstructure resulted.

Rees and Bhadeshia (1994) suggested that because acicular ferrite is a displacive transformation product (intragranularly nucleated bainite) the activation energy for nucleation varies linearly with the chemical driving force. This contrasts with classical nucleation theory, which predicts that the activation energy for nucleation is inversely proportional to the square of the chemical driving force. The linear dependence arises from a nucleation process controlled by the rate at which an embryo-austenite interface advances. A nucleation event occurs when one of these embryos becomes unstable *i.e.* rapid growth commences. This necessitates the existence of a glissile interface between the ferrite and the austenite. Rees and Bhadeshia suggested that dislocation debris in the austenite local to the inclusion surface could dissociate into such embryos. Differential thermal contraction between the austenite and the inclusion might cause extensive plastic deformation local to the inclusion surface which would drastically increase the amount of dislocation debris and thereby increase the rate of displacive nucleation.

Those minerals with thermal expansion coefficients significantly less than the austenite matrix (Table 3.1) might be expected to be the more potent nucleants of acicular ferrite. Therefore, minerals such as Mn-cordierite $(Al_2O_3)_2.(MnO)_2.(SiO_2)_5$ and β-SiO_2 could be very potent nucleants for acicular ferrite. However, Mn-cordierite has never been found in weld metal inclusions (see the review by Abson, 1987) and β-SiO_2 has only been detected occasionally (Dowling *et al.*, 1986 and Evans, 1990b). A recent paper by Gregg and Bhadeshia (1994a) failed to find any correlation between the coefficients of thermal expansion and the nucleation potency of various minerals. It is interesting to note that Yamamoto *et al.* (1987) found that Al_2O_3 and ZrO_2 have very different nucleation potencies, but similar thermal expansion coefficients. Zhang and Farrar (1996) found that inclusions such as MnS, which have some of the smallest strain fields, played an active role in the nucleation of acicular ferrite.

Barritte and Edmonds (1981) noted that often two adjacent inclusions appear to act as

the primary nucleation site. They suggested that if stresses are important in the nucleation of acicular ferrite, then stress concentrations due to overlapping stress fields in the matrix will create more favourable nucleation sites. Andrews and Brooksbank (1972) have calculated the magnitude of such tessellated stresses for inclusions in close proximity. These show that the close proximity of inclusions significantly increases the magnitude of the elastic stresses found in the matrix.

Barbaro *et al.* (1988) and numerous other authors have noted that many oxide inclusions are partially covered with a MnS shell. MnS has a similar coefficient of thermal expansion to austenite and thus the MnS shell might be expected to reduce the magnitude of the stresses exerted by the oxide core of the inclusion. Therefore, these stresses were considered unlikely to exert an influence upon inclusion potency. Calculations by Brooksbank and Andrews (1970) confirm that a thin MnS envelope around an oxide inclusion acts as a compensating 'cushion' during cooling, and therefore significantly reduces the magnitude of the elastic stresses that are generated. This would also be true for a shell of copper sulphide. Summarising, the evidence to date indicates that localised stresses alone are unlikely to explain adequately the nucleation potency of inclusions in welds.

3.2.4 Chemical Reaction with the Austenite Matrix

This involves an inclusion chemically reacting with the surrounding austenite and depleting it in key alloying elements such as manganese and/or carbon, thereby destabilising it and promoting the nucleation of ferrite local to the inclusion surface. However, much of the early work that attempted to investigate this mechanism failed to find any evidence of depletion in these key alloying elements around nucleating inclusions (Barritte *et al.*, 1981; Barbaro *et al.*, 1988). Es-Souni and Beaven (1990) reasoned that because manganese silicate inclusions are formed during or before solidification, enough diffusion should be possible at high temperatures to alleviate local compositional differences before the austenite to ferrite transformation begins. However, Svensson (1994) has suggested that higher spatial resolution work might reveal subtle differences. Even a small depleted zone ($\simeq$ 0.01 to 0.1 μm in thickness) would be sufficient to promote the nucleation of ferrite. Indeed the dissolution and re-precipitation of various phases such as MnS and Ti(C,N) during the weld thermal cycle could cause a depleted zone to form as the weld deposit cools through the Ae_3 temperature. The depleted zone might then be removed by diffusional homogenisation as the weld cools to room temperature, leaving no detectable evidence of it ever having existed.

Yamamoto *et al.* (1987 and 1996), Homma *et al.* (1987) and Chijiiwa *et al.* (1987) have suggested that during cooling the dissolution and re-precipitation of MnS on Ti_2O_3 and/or

TiN particles in inoculated wrought alloys leads to the formation of a Mn depleted zone local to the particle surface. This zone is thought to promote the nucleation of acicular ferrite. Yamamoto *et al.* found that reducing the S content prevented the nucleation of acicular ferrite (see below for further details). In an interesting experiment using hot-stage microscopy Tomita *et al.* (1994) noted that the intragranular nucleation of allotriomorphic ferrite (idiomorphic ferrite) in wrought alloys largely occurred on duplex MnS–TiN particles. It was considered that a Mn depleted zone of between 0.35 and 3.5 μm in thickness might form during the MnS precipitation process. This would significantly increase the thermodynamic driving force for the austenite to ferrite transformation. They suggested that epitaxy between ferrite and TiN local to the MnS might further increase nucleation potency, but considered Mn depletion to be primary nucleation mechanism.

Ishikawa *et al.* (1994) also studied the intragranular nucleation of allotriomorphic ferrite, but on duplex MnS–VN particles in wrought alloys. They established that increasing the V and N concentration simultaneously promoted a substantial increase in intragranular nucleation. However, their calculations revealed that the depletion of V below the nominal concentration of the alloy (0.13 wt %) did not significantly increase the thermodynamic driving force for ferrite nucleation. Instead Ishikawa *et al.* suggested that a Baker-Nutting type of epitaxial relationship existed between the allotriomorphic ferrite and the VN, and that this was more likely to account for the increased nucleation efficacy.

Carbon depletion of the austenite matrix may also reduce hardenability adjacent to inclusions, thereby promoting nucleation at the inclusion surface. Since carbon is an interstitial element and therefore able to diffuse more readily than either Mn or Si, significant carbon depletion of the austenite matrix might occur at lower temperatures just before the γ-α transformation begins. Unfortunately carbon depletion cannot be easily identified using EDX systems unless a windowless detector is employed. Es-Souni and Beaven (1990) have suggested that carbon depletion of the austenite matrix may be possible in the vicinity of the phase Ti(C,N) due to the relatively high solubility of carbon in TiN.

Recent studies by Gregg and Bhadeshia (1993, 1994a and 1994b), following on from initial work performed by Strangwood and Bhadeshia (1988), provide strong evidence in support of various types of chemical reaction mechanisms for certain phases which are known to be potent nucleants of acicular ferrite. They examined the efficacy of numerous chemically pure compounds in enhancing the nucleation rate of bainite at chemical-austenite interfaces, in a series of pressurised bonding experiments. Their reasoning was that this would give a strong indication of those compounds which promoted the intragranular nucleation of acicular ferrite.

Specific details of what compounds they found to be effective and ineffective are given in Table 3.2. They observed that TiO_2 was particularly potent in nucleating bainite, but noted that this did not emanate directly from the TiO_2 - steel interface. Instead the oxide had induced the formation of a thin zone of allotriomorphic ferrite which contained amorphous silica precipitates. The oxygen had diffused into the steel creating a 'reaction zone' which was likely to be decarburised. This had reduced the hardenability of the austenite local to the interface, promoting the nucleation of bainite. Work on structural and behavioural analogues of TiO_2, such as SnO_2, MnO_2 and PbO_2, produced similar findings. Gregg and Bhadeshia considered that the tendency of such minerals to form oxygen vacancy (anion) defects at high temperatures would cause oxygen to be released into the adjacent steel. In order to test this theory the nucleation potency of defect perovskites (ABO_3) was compared to the similarly structured normal perovskites (BO_3). Defect perovskites release far more oxygen than normal perovskites at high temperatures. As expected the nucleation potency of the defect perovskites was far greater than that of the normal perovskites. Gregg and Bhadeshia concluded that those minerals which are natural oxygen sources are effective nucleants; further work indicated that the Mn and Si concentrations were considerably reduced in the 'reaction zone'. This prompted additional experiments which demonstrated that such depletion was a direct result of the formation of the reaction zone. Silicon combined with oxygen to form silica and manganese was found to be rejected ahead of the allotriomorphic ferrite interface. Consequently fresh experiments were conducted using a low silicon steel. These suggested that the formation of a reaction zone and the associated depletion in substitutional alloying elements, was not necessary to stimulate bainite nucleation. It was concluded that the enhanced rate of nucleation was primarily due to the release of oxygen into the steel which caused decarburisation.

Gregg and Bhadeshia also examined the nucleation potency of TiO and Ti_2O_3. Both compounds were found to be very effective nucleants, but no 'reaction zone' could be found for either. Ti_2O_3 was found to induce a dramatic depletion in the manganese concentration in the steel local to the interface, which was thought to stimulate nucleation. Closer examination revealed a high manganese concentration in the Ti_2O_3. Consistent with the absence of silica particles no silicon depletion was noted in the steel. Ti_2O_3 was therefore considered to act as a sink for manganese cations, thereby stimulating nucleation. The mechanism by which TiO induced nucleation could not be established. Table 3.2 represents a summary of the work by Gregg and Bhadeshia.

Exciting new research by Yamamoto *et al.* (1996) suggests strongly that acicular ferrite nucleation is promoted on fine titanium oxide particles because of a combined chemical and

Nucleation Mechanism	Phases
Chemically Effective (O Source)	TiO_2, SnO_2, MnO_2, PbO_2, WO_3, MoO_3, KNO_3, V_2O_5
Chemically Effective (Mn Sink)	Ti_2O_3
Chemically Inert and Effective	TiO
Chemically Inert and Ineffective	TiN, α-Al_2O_3, γ-Al_2O_3, $CaTiO_3$, $SrTiO_3$, NbC, Al_2O_3.MnO, MnS

Table 3.2   Chemically effective and ineffective bainite nucleants (Gregg, 1993 and 1994a).

epitaxial reaction mechanism. Yamamoto *et al.* studied the acicular ferrite transformation in the heat-affected zone of low-alloy steel welds that had been inoculated with a fine dispersion of titanium oxide particles. Electron beam diffraction indicated that the stoichiometry of the titanium oxides was Ti_2O_3. Secondary ion mass spectroscopy (SIMS) was used to analyse the variations in concentration of B, Mn and Ti in the particles. Figure 3.6 shows a depth profile through a Ti_2O_3 particle, which was obtained by ion beam sputtering in the SIMS. It is apparent that the B concentration in the oxide is approximately 20 times greater than in the steel matrix, whilst the Mn concentration is approximately 3 times greater than that in the matrix (this is consistent with the experimental observation by Gregg and Bhadeshia that Ti_2O_3 acts as Mn sink). These results indicate the existence of a B and Mn depleted zone around the particle.

The diffusion of manganese and boron into the particle requires the existence of cation vacancies in the Ti_2O_3 lattice. This was confirmed using argon sputtering in an Auger electron spectroscope (AES). The measured atomic ratio of O to Ti near the oxide surface is higher than the stoichiometric value of 1.5 for Ti_2O_3. The titanium oxide particles were found to be $Ti_{(2-x)}O_3$, where $x \simeq 0.052$. These cation vacancies contributed to the precipitation of MnS and TiN at the surface of Ti_2O_3 because both the interfacial energy and the internal energy of Ti_2O_3 particles decreases with the diffusion of Mn and Ti atoms into the Ti_2O_3. Yamamoto *et al.* suggested that the nucleation rate of acicular ferrite on these complex Ti_2O_3–MnS–TiN precipitates might therefore be enhanced because of some or all of the following factors:

(1)   An increase in the chemical driving force for transformation due Mn depletion caused by partitioning into the Ti_2O_3 and/or the precipitation of MnS at the oxide surface. Figure 3.7 shows the calculated distribution of the Mn concentration in the austenite (bulk concentration $\simeq 1.5$ wt % Mn) around a MnS precipitate after slow cooling. It is apparent that the concentration in the austenite decreases by
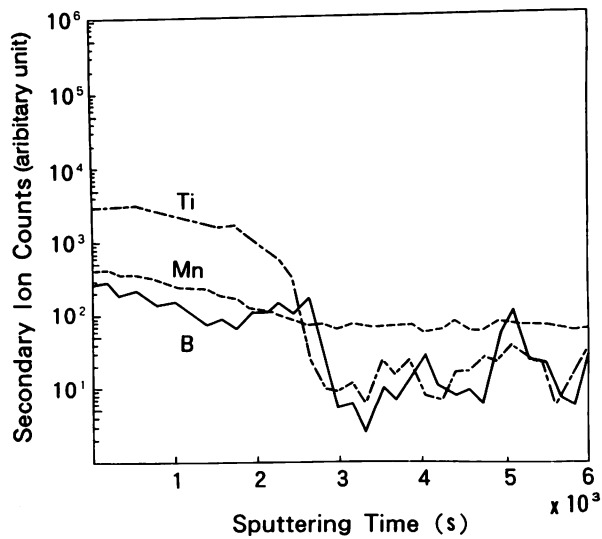
Figure 3.6 Depth profile obtained by SIMS for elements in a Ti_2O_3 particle. The Ti_2O_3 particle disappeared after 3×10^3 s (Yamamoto *et al.*, 1996).

$\simeq 0.15$ wt %. The size of this depleted zone (0.1 to 0.2 μm) prevented additional experimental confirmation of its existence. Yamamoto *et al.* suggested that this depletion destabilised the austenite, and thereby increased the Ar_3 temperature, at which austenite begins to transform to ferrite during cooling, by approximately 8 °C.

(2) Boron atoms have a low solubility and high diffusivity in austenite. They readily segregate to the Ti_2O_3 particles and the austenite grain boundaries. The segregation to the austenite grain boundaries suppresses the nucleation of allotriomorphic and Widmanstätten ferrite (section 3.4). However, the B atoms which segregate to the oxide particles are absorbed as B^{3+} ions in cation vacancies in Ti_2O_3 and do not suppress the intragranular formation of ferrite. This favours intragranular nucleation over intergranular nucleation. Fission track methods were used to test this hypothesis. Continuous B segregation was observed at the austenite grain boundaries, whereas spots of B were observed inside the grains which is consistent with the presence of B inside the Ti_2O_3 particles.

(3) Epitaxy between the ferrite and TiN was also thought to promote ferrite nucleation, the lattice disregistry between ferrite and TiN being small.

Recent experiments by Fox and Brothers (1995) support an oxidation type of chemical reaction mechanism similar to that identified for TiO_2 by Gregg and Bhadeshia. They detected
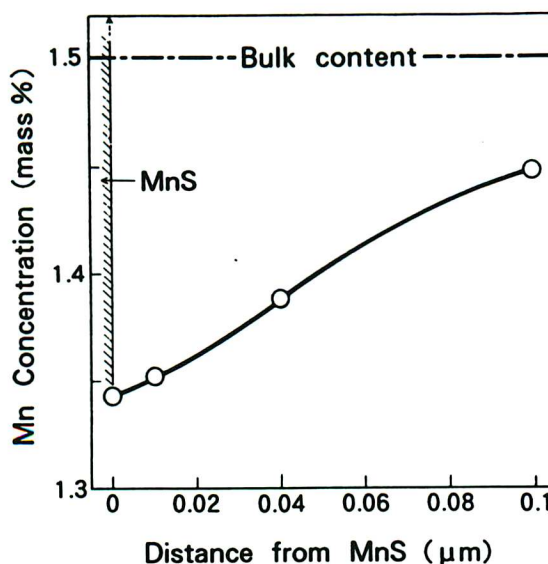
Figure 3.7 Calculated distribution of the Mn in the austenite matrix at 800 °C after MnS precipitation during cooling at 10 °C s^{-1} from 1400 °C (Yamamoto *et al.*, 1996).

the pyrophanite $MnO.TiO_2$ in those inclusions which appeared to nucleate acicular ferrite. Fox and Brothers argued that in the $MnO–TiO_2–Al_2O_3–SiO_2$ quaternary phase system the first inclusions to solidify in the still molten weld metal are $Al_2O_3.MnO$ at approximately 1800 °C. The remaining liquid becomes enriched with MnO and TiO_2. Eventually after the weld metal has solidified the pyrophanite $MnO.TiO_2$ nucleates upon the $Al_2O_3.MnO$ inclusion surface at about 1360 °C. The pyrophanite $MnO.TiO_2$ oxidises the adjacent austenite, thereby reducing the amount of C in solution and stimulating the nucleation of acicular ferrite.

3.2.5 Lattice Matching (Epitaxy)

Nucleation may be promoted due to the formation of a low-energy interface between the ferrite nucleus and the inclusion substrate. This is a popular hypothesis, but with relatively little experimental verification. The interfacial energy of a system depends on the chemistry, topography and crystallography of the interface. However, experiments by Turnbull and Vonnegut (1952), Bramfitt (1970) and Nuri *et al.* (1982) have found a strong correlation between the effectiveness of a substrate in promoting the heterogeneous nucleation of a solid from a supercooled liquid, and the crystallographic disregistry (misfit) between the nucleated solid and the nucleating substrate.

Turnbull and Vonnegut (1952) used a simple measure of linear disregistry which correlated well with the degree of supercooling needed to induce solidification. Bramfitt (1970) developed

a more sophisticated model which allows lattice matching to be described in terms of a mean planar lattice disregistry between parallel planes:

$$\Pi_{(hkl)_n}^{(hkl)_s} = \sum_{i=1}^{3} \frac{1}{3} \left[\frac{d_{[uvw]_s^i} \cos \chi - d_{[uvw]_n^i}}{d_{[uvw]_n^i}} \right] \times 100 \qquad (3.4)$$

This assumes a substrate (inclusion) faceted on a low-index plane $(hkl)_s$, and a nucleus (ferrite) that forms epitaxially with its low-index plane $(hkl)_n$ parallel to $(hkl)_s$ where:

$[uvw]_s^i$ = a low-index direction in $(hkl)_s$.

$[uvw]_n^i$ = a low-index direction in $(hkl)_n$.

$d[uvw]_s^i$ = the interatomic spacing along $[uvw]_s^i$.

$d[uvw]_n^i$ = the interatomic spacing along $[uvw]_n^i$.

χ = the angle between $[uvw]_s^i$ and $[uvw]_n^i$ (often zero).

Bramfitt suggested that the nucleus and substrate would be orientated such that the planar parallelism generated offered the minimum mean planar disregistry Π_m. Nuri *et al.* (1982) found that Bramfitt's mean planar disregistry model largely determined the efficacy of various rare earth metal oxides and sulphides in stimulating solidification during the continuous casting of steel.

Mills *et al.* (1987) assumed that planar disregistry can be used to explain the nucleation potency of inclusions in stimulating the solid-state austenite to ferrite phase transformation. They considered numerous planes and directions of low crystallographic indices. Table 3.3 indicates the minimum mean planar disregistry values they obtained.

Phase	Parallelisms	Π_m (%)
$Al_2O_3.MnO$	$\{100\}_\alpha \parallel \{100\}_s < 100 >_\alpha \parallel < 110 >_s$	1.8
$Cu_{1.8}S$	$\{111\}_\alpha \parallel \{111\}_s < 110 >_\alpha \parallel < 110 >_s$	2.8
TiO	$\{100\}_\alpha \parallel \{100\}_s < 100 >_\alpha \parallel < 110 >_s$	3.0
γ-Al_2O_3	$\{100\}_\alpha \parallel \{100\}_s < 100 >_\alpha \parallel < 110 >_s$	3.2
TiN	$\{100\}_\alpha \parallel \{100\}_s < 100 >_\alpha \parallel < 110 >_s$	4.6
BN	$\{111\}_\alpha \parallel \{110\}_s < 110 >_\alpha \parallel < 100 >_s$	6.5
α-MnS	$\{111\}_\alpha \parallel \{111\}_s < 110 >_\alpha \parallel < 110 >_s$	8.8

Table 3.3   Calculated minimum mean planar disregistry Π_m between various phases *s* and ferrite α (Mills *et al.*, 1987).

Early investigations such as those conducted by Dowling *et al.* (1986) and Es-Souni and Beaven (1990) failed to detect any direct and unambiguous evidence for such epitaxial orien-

tation relationships between acicular ferrite and the nucleating inclusion. Bhadeshia (1992) explained that inclusions which form in liquid steel are randomly oriented in space, whilst the orientation relationship of acicular ferrite with the parent austenite is always found to be of the Kurdjumov-Sachs or similar type. This, it can be argued, precludes the development of an orientation relationship (*i.e.* epitaxy) between a ferrite nucleus and an inclusion. Cochrane and Kirkwood (1978) suggested an alternative hypothesis. They proposed that δ-ferrite grains sometimes nucleate on inclusions in the melt and this implies the possibility of an orientation relationship between the inclusions and the austenite, and thereby between the austenite and the α-ferrite. However, Bramfitt type planar disregistry calculations carried out by Kluken *et al.* (1991) imply that no such epitaxial relationship exists between δ-ferrite and inclusions, such that the only possible effect of inclusions during solidification is to act as inert substrates for the nucleation of δ-ferrite ahead of the advancing interface. Furthermore, it is generally considered that weld pool solidification occurs heterogeneously at the liquid-solid interface and not upon inclusions. This suggests that only a small fraction of the inclusions in a weld metal would be able to form epitaxial relationships with ferrite. However, the number of randomly oriented inclusions with a suitable relationship with ferrite might still be sufficient to account for the profuse nucleation of acicular ferrite observed in weld metals. Mills *et al.* (1987) suggest that the occurrence of a number of discrete Ti-rich patches at the inclusion surface would further increase the number of possible epitaxial nucleation sites. Following this reasoning Grong *et al.* (1995) calculated that about 12 % of inclusions will contain a phase which is suitably orientated to allow the epitaxial nucleation of ferrite.

Indeed recent research by Grong *et al.* (1995) has found experimental evidence for such orientation relationships between various phases (γ-Al$_2$O$_3$, Al$_2$O$_3$.MnO and TiN) and acicular ferrite. These epitaxial relationships appear to minimise the activation energy barrier to nucleation (Table 3.4). Ishikawa *et al.* (1994) observed a Baker-Nutting epitaxial relationship *i.e.* $(100)_{VN} \parallel (001)_{\alpha}$ $[100]_{VN} \parallel [\bar{1}10]_{\alpha}$ between ferrite idiomorphs and VN in medium-carbon steels. This epitaxial relationship offers a very high degree of interfacial coherency (disregistry $\simeq 2$ %). Therefore, in the light of recent evidence it is impossible to discount the lattice matching mechanism.

3.3 The Nucleation Potency of Various Inclusion Phases

3.3.1 The Nucleation Potency of Aluminium Minerals

Conflicting evidence exists as to the efficacy of various aluminium minerals in promoting the nucleation of acicular ferrite. Increasing the weld metal aluminium content and thus

Phase	Orientation Relationship
γ-Al_2O_3	$(100)_s \sim \parallel (011)_\alpha$ $[01\bar{1}]_s \sim \parallel [5\bar{3}3]_\alpha$
$Al_2O_3 \cdot MnO$	$(200)_s \sim \parallel (110)_\alpha$ and $(011)_s \parallel (010)_\alpha$ $[0\bar{1}1]_s \parallel [001]_\alpha$
TiN	$(\bar{1}10)_s \parallel (100)_\alpha$ $(112)_s \parallel (011)_\alpha$ $[11\bar{1}]_s \parallel [0\bar{1}1]_\alpha$ and $(10\bar{1})_s \parallel (\bar{1}03)_\alpha$ $(320)_s \parallel (112)_\alpha$ $[2\bar{3}2]_s \parallel [3\bar{5}1]_\alpha$ and $(\bar{1}01)_s \parallel (\bar{1}33)_\alpha$ $(221)_s \parallel (200)_\alpha$

Table 3.4   Experimentally observed orientation relationships between acicular ferrite α and different inclusion constituent phases s (Grong *et al.*, 1995).

changing the dominant inclusion type, has a somewhat confusing effect upon weld metal microstructure (Figure 3.8). It is apparent that the volume fraction of acicular ferrite goes through a maximum when the Al concentration is $\simeq$ 200 ppm wt (parts per million by weight) and the oxygen content is $\simeq$ 430 ppm wt. Various interpretations of this behaviour have been suggested:

(1)   Saggese *et al.* (1983) considered that γ-Al_2O_3 might be a particularly potent nucleant for acicular ferrite. Therefore, the maximum amount of acicular ferrite should form when the aluminium to oxygen ratio is equal to the stoichiometric value required for Al_2O_3 formation. Pargeter (1981) also noted an apparent association between Al-rich inclusions and a high volume fraction of acicular ferrite.

(2)   Kluken (1990) considered that the galaxite spinel $Al_2O_3 \cdot MnO$ is a particularly effective nucleant of acicular ferrite. Thus, the volume fraction of acicular ferrite found would decrease when the aluminium to oxygen ratio reaches and exceeds the stoichiometric value, leading to the formation of ineffective Al_2O_3. The galaxite

spinel $Al_2O_3.MnO$ was frequently found by Dowling *et al.* (1986) in those welds in which acicular ferrite dominated the microstructure.

(3) Svensson (1994) suggests that the decrease in acicular ferrite content, associated with an increasing the aluminium to oxygen ratio, could instead be due to the absence of sufficient nucleating Ti-oxides upon the surface of Al_2O_3 inclusions. All of the available oxygen forms aluminium oxides effectively preventing the formation of titanium oxides.

(4) Kluken *et al.* (1989) note that the very high surface energy of Al_2O_3 inclusions appears to increase the rate at which the inclusions coarsen and coagulate in the molten weld pool. This effect has been reported by Terashima and Hart (1983) and by Grong and Matlock (1986). If the inclusions coarsen and their spacing increases as the aluminium content is raised, as noted by Thewlis (1994), then the austenite grain size might increase as the Zener pinning effect diminishes. This would indirectly promote the development of acicular ferrite.

(5) Thewlis (1994) and Zhang and Farrar (1996) have suggested that an excess of soluble aluminium encourages extensive ferrite side plate formation (Widmanstätten ferrite and bainite) from the austenite grain boundaries. This indirectly depresses the volume fraction of intragranularly nucleated acicular ferrite. Work by Mabuchi and Nakao (1981) is consistent with this possibility.

Work by Gregg and Bhadeshia (1993) has thrown new light upon the role of aluminium containing minerals in promoting the nucleation of bainite and acicular ferrite (section 3.2.4). They determined that α-Al_2O_3, a mixture of α-Al_2O_3 and γ-Al_2O_3, and $Al_2O_3.MnO$ are all relatively ineffective nucleants.

It is difficult to draw any firm conclusions regarding the efficacy of the various aluminium phases. In conclusion, it seems that whilst certain aluminium phases are capable of nucleating acicular ferrite, if the undercooling below the Ae_3 temperature is sufficiently great, they are probably not as potent as some of the titanium minerals described in section 3.3.2.

3.3.2 The Nucleation Potency of Titanium Minerals

Titanium rich minerals are widely considered to be very potent nucleants for acicular ferrite (Figure 3.9), but considerable confusion still exists as to exactly which titanium rich phases are effective and as to what nucleation mechanism is operative for each phase (Ito and Nakanishi, 1976; Terashima and Hart, 1983; Es-Souni and Beaven, 1990; Evans, 1991; Thewlis, 1994; Saggese *et al.*, 1983; Pargeter, 1981; Kayali *et al.*, 1983; Homma *et al.*, 1986; Bailey,
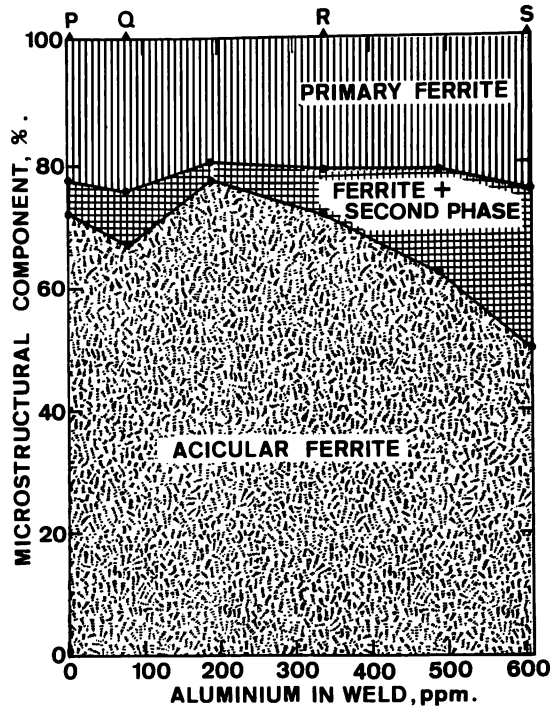
Figure 3.8 The effect of aluminium on the as-deposited microstructure of weld metal (Evans, 1990b). The following terminology is used; primary ferrite refers to allotriomorphic and idiomorphic ferrite, ferrite + second phase refers to Widmanstätten ferrite and conventional bainite.

1983; Liao and Liu, 1992; Yamamoto *et al.*, 1996). Ito and Nakanishi in their classic 1976 paper reported that small titanium additions to the weld metal promoted the formation of inclusions that were extremely effective as nucleants of acicular ferrite. They found that Ti additions greater than 0.03 wt % promoted a very fine acicular ferrite type of microstructure. They attributed this to the presence of very fine Ti-rich precipitates which they considered to be TiN. Saggese *et al.* (1983) and Terashima and Hart (1983) suggested that the introduction of Ti above a critical amount allowed high volume fractions of acicular ferrite to be consistently obtained. St-Laurent and L'Espérance (1992) studied welds which contained very small concentrations of Al (< 0.001 wt %). They found that when the weld Ti content was 0.002 wt % the volume fraction of acicular ferrite was only 0.08. Increasing the Ti content to 0.005 wt % raised the volume volume fraction of acicular ferrite to 0.48, whilst the maximum volume fraction of acicular ferrite was 0.84 when the weld Ti content was 0.008 wt %. St-Laurent and L'Espérance noted that additions of the much stronger deoxidiser aluminium would certainly change the minimum amount of titanium required to form these potent Ti-rich phases (which they considered to be an oxide). Studies conducted by Thewlis in 1986 and

1994 have also established that the presence of TiO and/or TiN greatly increases nucleation potency. Contradictory evidence was presented by Barbaro *et al.* in 1988. They found that those inclusions responsible for the nucleation of acicular ferrite often contained no TiO.
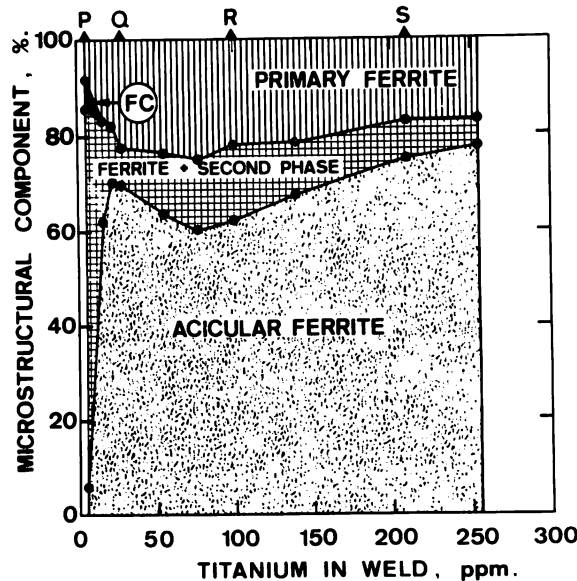
Figure 3.9 The effect of titanium on the as-deposited microstructure of weld metal (Evans, 1991). The following terminology is used; primary ferrite refers to allotriomorphic and idiomorphic ferrite, ferrite + second phase refers to Widmanstätten ferrite and conventional bainite, FC refers to ferrite carbide aggregates such as pearlite.

There is, however, a limit to the amount of titanium which can be added to weld metals with the aim of obtaining a high volume fraction of acicular ferrite. Studies conducted by Kayali *et al.* (1983) and Dowling *et al.* (1986) have both established that if the concentration of titanium present in the weld metal exceeds approximately 0.1 to 0.2 wt %, then the inclusions found were rich in titanium and tended to be angular. These weld deposits were found to be fully bainitic, indicating that these titanium rich inclusions were ineffective nucleants. Extensive research conducted by Evans (1991) is consistent with these findings. An alternative explanation is provided by Widgery (1976) and Oh *et al.* (1989). These authors suggested that the high concentration of soluble Ti stabilises the austenite to lower temperatures and thereby encourages the formation of bainitic ferrite. It is suggested here that this explanation might be flawed. Acicular ferrite is now thought to be an intragranularly nucleated form of bainite, which is fundamentally the same as conventional bainite which nucleates along the austenite grain boundaries (Bhadeshia, 1992). Therefore, the presence of excessive titanium in solution should not promote conventional bainite instead of acicular ferrite. Furthermore, titanium

additions are known to close the austenite phase field, which increases the Ae_3 temperature (Tofaute and Büttinghaus, 1938), and thereby promote reconstructive transformation products such as allotriomorphic ferrite and not displacive products such as bainite as suggested by Widgery and Oh *et al.*

Gregg and Bhadeshia (1994b) recently conducted an interesting range of pressure bonding experiments using wrought steels. These were designed to test the efficacy of pure titanium phases in inducing the nucleation of bainite (section 3.2.4). They concluded that the titanium oxides, TiO, TiO_2 and Ti_2O_3 were very effective nucleants for bainite, whilst surprisingly TiN was not. More recent experiments, using wrought steels which where inoculated with a fine dispersion of chemically pure minerals, gave similar results except that bainite nucleated intragranularly to form acicular ferrite (Gregg, 1994). Recent research by Yamamoto *et al.* (1996) supports these findings (section 3.2.4).

Numerous studies (section 3.4) have concluded that in order to achieve a consistently high volume fraction of acicular ferrite, titanium additions are particularly effective if they are used in conjunction with trace additions of boron. Soluble boron considerably reduces the nucleation potency of the austenite grain boundaries, and thus increases the volume fraction of residual austenite that is free to transform into intragranularly nucleated acicular ferrite (Thewlis, 1994; Mori *et al.*, 1981; Watanabe and Kojima, 1980a and 1980b; Shinada *et al.* 1992). In conclusion, it seems likely that if other factors such as alloy hardenability and the weld cooling cycle are favourable then certain titanium phases are very effective nucleants for acicular ferrite. However, it is not apparent which titanium-rich phases are effective nucleants.

3.3.3 The Nucleation Potency of Sulphides

Sulphur rich phases which form as patches on the inclusion surface have been suspected of playing a role in the nucleation of acicular ferrite by several researchers. Court and Pollard (1985 and 1989) associated many acicular ferrite nucleation events with the patches of copper and manganese sulphides they found on inclusions. Yamamoto *et al.* (1988 and 1996) also claim that MnS, which nucleates on titanium oxides, is responsible for the nucleation of acicular ferrite. They found that reducing the sulphur content below 0.001 wt % decreased the volume fraction of acicular ferrite obtained. Zhang and Farrar (1996) also claim that MnS particles frequently act as nucleation sites for acicular ferrite.

Contradictory evidence was presented by Kayali *et al.* (1983) who found incomplete shells rich in copper and sulphur, around nucleating and non-nucleating inclusions. St-Laurent and L'Espérance (1992) noted an increase in the amount of acicular ferrite when the sulphur content was raised. However, they did not directly relate this to the nucleation potency of the

sulphur rich phases *per se*. Instead they attributed it to an increase in the volume fraction and hence the number density and size of the inclusion population, which caused a significant variation in the austenite grain size. Es-Souni and Beaven (1990) indicated that nucleation events were generally associated with titanium rich phases at the inclusion surface and not copper sulphides. They considered that since carbon was not soluble in Cu_2S the surrounding austenite could not be destabilised by carbon depletion. Other studies by Horii *et al.* (1995), Evans (1986 and 1990a), Chijiiwa *et al.* (1988), Devillers *et al.* (1983) and Abson *et al.* (1978) appear to confirm the lack of efficacy of sulphur in promoting the nucleation of acicular ferrite. On balance then the evidence to date suggests that sulphides are relatively ineffective nucleants, and may even retard the nucleation of acicular ferrite by partially covering the inclusion surface.

3.3.4 The Nucleation Potency of Other Phases

Evans (1990b) noted that in welds containing less than 5 ppm wt Al the nucleating inclusions were typically $MnO.SiO_2$, although some copper and manganese sulphides and titanium rich phases were found at the inclusion surface. Thewlis (1994) found a significant increase in the mean inclusion size and spacing with increasing calcium additions. These larger inclusions were expected to offer a lower free energy barrier to ferrite nucleation, so as to encourage the nucleation of acicular ferrite. However, a decrease in the volume fraction of acicular ferrite was measured. This suggests that the activation energy barrier to nucleation on calcium rich inclusions might be relatively high. Experiments using $CaTiO_3$ are consistent with this (Gregg, 1994). Ochi *et al.* (1988) precipitated vanadium carbide and vanadium nitride on manganese sulphide particles. They believed that the vanadium carbide stimulated the intragranular nucleation of ferrite-pearlite structures in hot-forged steel products. Pressurised bonding experiments conducted by Gregg (1994) indicate that niobium carbide is an ineffective nucleant for acicular ferrite. Boron nitride and boron oxide are also suspected of nucleating acicular ferrite. The evidence for this is addressed in the following section.

3.4 The Role of Boron in Promoting Acicular Ferrite Nucleation

Trace additions of boron greatly increase the volume fraction of acicular ferrite found in a weld metal and thus improve toughness. Four mechanisms by which boron may influence the α-γ transformation have been suggested; however, only the first is generally accepted:

(1) Misfitting boron atoms segregate to the austenite grain boundaries and stabilise them by reducing the grain boundary surface energy. This is thought to be due to a decrease in the lattice strain energy at the interface, although this has not been

experimentally verified (see the reviews by Llewellyn, 1993; Morral and Cameron, 1981). However, if too much boron reaches the grain boundary boron oxides, carbides or nitrides may precipitate and these might enhance ferrite nucleation (Bhadeshia and Svensson, 1993).

(2) Boron with its high chemical affinity for oxygen, carbon and nitrogen is known to readily precipitate various oxides, carbides and nitrides. These may provide intragranular nucleation sites for ferrite (Ueda *et al.*, 1981; Thewlis, 1986; Funakoshi *et al.*, 1977).

(3) Free boron atoms may segregate to inclusions and reduce their nucleation potency, if the boron atoms remain at the austenite-inclusion interface (Jones *et al.*, 1993).

(4) The presence of fine boron nitrides might reduce the austenite grain size due Zener type pinning (Svensson, 1994; Thewlis, 1986)

Boron segregation is well known to retard the formation of allotriomorphic ferrite at the austenite grain boundaries in wrought steels. The dramatic effect of boron on the TTT diagram is illustrated in Figure 3.10. In steel welds this indirectly promotes the formation of acicular ferrite because a higher volume fraction of austenite remains untransformed at lower temperatures (Lin and Cheng, 1990; Oh *et al.*, 1989; Watanabe and Kojima, 1980b; Yamamoto *et al.*, 1996; Thewlis, 1986). It is important to appreciate that the boron atoms must remain free in solution if they are to segregate (section 5.8.2) to the austenite grain boundaries and increase alloy hardenability. Boron has a high affinity for oxygen and nitrogen, and combines readily with these elements in steel. Thus, weld metal compositions need to be carefully designed so that the concentrations of the nitride formers Ti, Al, V, and Nb are adequate to getter all of the nitrogen, leaving sufficient boron free in solution (section 5.8.3) to effectively saturate the austenite grain boundaries. Work by Thewlis (1994) indicates that the amount of soluble boron required to saturate the austenite grain boundaries increases with decreasing austenite grain size. This is because the boron atoms have to saturate a larger surface area per unit volume.

Oh *et al.* (1989) considered the influence of boron and titanium additions, both separately and simultaneously, upon weld microstructure. The weld metals used were designed to contain very low concentrations of Al, V and Nb to maximise the free nitrogen concentration. They concluded that the influence of separate additions of boron and titanium were relatively minor, compared to the synergistic effect of combining boron additions with sufficient titanium to protect the boron from nitrogen and provide potent nucleating inclusions. The volume fraction of acicular ferrite was maximised by maintaining 40 to 45 ppm wt boron and 400 to 500 ppm wt
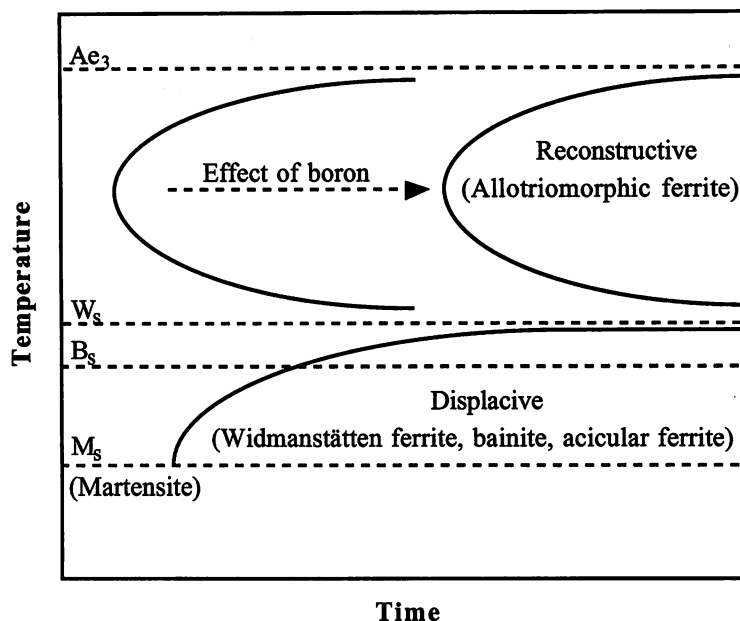
Figure 3.10 Illustration of the retarding effect of boron on the TTT diagram.

titanium in the weld metal. Work by Thewlis (1994), Shinada *et al.* (1990), Evans (1991) and Watanabe and Kojima (1980a and 1980b) reveals similar trends. An interesting experiment was performed by Oh *et al.* (1991) which compared microstructures produced by titanium and boron additions to those produced with zirconium and boron additions. The nucleation potency of titanium rich phases has been well documented, so that a higher yield of acicular ferrite was anticipated in these welds. Nevertheless, a higher yield was found in the zirconium containing welds. They noted that thermodynamic considerations indicate that zirconium getters nitrogen more effectively than titanium leaving a greater concentration of free boron to saturate the austenite grain boundaries.

More problematical is whether intragranular boron compounds have a direct role in stimulating acicular ferrite nucleation. Ito *et al.* (1982) , Funakoshi *et al.* (1977) and Ueda *et al.* (1981) have noted that various boron oxides and boron nitride may be potent nucleation sites for ferrite. Thewlis (1986) was able to discern very small particles ($\simeq$ 20 nm in diameter) of f.c.c. BN which were not associated with the larger inclusion population, but were arranged as a cellular network. Mori *et al.* (1981) also claimed to have found fine particles of BN. Thewlis proposed that BN particles could promote acicular ferrite nucleation due to their low misfit with acicular ferrite, in a manner similar to that proposed for TiN or TiO. Ueda *et al.* in an excellent paper published in 1981 found that boron nitrides and iron-borocarbides were responsible for accelerating the γ-α transformation by stimulating the intragranular nucleation of idiomorphic ferrite. It should be noted that the heat input in these welds was very high,

resulting in a particularly slow cooling rate (210 s to cool from 800 to 500 °C), so that acicular ferrite would not be expected to form. Nevertheless, it is debatable whether the presence of boron nitrides would promote the displacive acicular ferrite transformation in a similar manner. Contradictory results were published by Pakrasi *et al.* (1981). They postulated that in boron free steels, aluminium nitride particles act as nucleation sites for ferrite. However, boron additions promote boron nitride formation at the expense of aluminium nitride. They found that these BN particles did not act as ferrite nucleation sites because they were too small and incorrectly distributed.

It has been speculated that free boron may also segregate to the austenite-inclusion interface and decrease the interfacial energy, thereby reducing the nucleation potency of the inclusion (Jones *et al.*, 1993). However, research conducted by Yamamoto *et al.* (1996) has revealed that whilst free boron does segregate to Ti_2O_3 particles, it does not remain at the interface, but it is absorbed into cation vacancies in the Ti_2O_3 (section 3.2.4). The nucleation potency of the particle is therefore unaffected. However, the nucleation potency of the boron covered austenite grain boundaries is reduced, so that the volume fraction of acicular ferrite increases.

A recent paper by Bhadeshia and Svensson (1993) has revealed that the amount of Widmanstätten ferrite is also considerably reduced by small additions of boron. Data published by Thewlis (1994) reveals similar trends. This further increases the potential for acicular ferrite formation. Indeed, Widmanstätten ferrite is almost completely absent in those welds containing over 50 ppm wt boron. Bhadeshia and Svensson explained that this was indirectly due to boron's role in retarding the heterogeneous nucleation of allotriomorphic ferrite along the austenite grain boundaries. Widmanstätten ferrite is often found to nucleate on allotriomorphic ferrite grains. Each allotriomorphic ferrite grain may only have an orientation relationship with one of the adjacent austenite grains. Therefore, because of its displacive mechanism of transformation a Widmanstätten ferrite plate can only nucleate on one side of an allotriomorph. Boron additions are known to reduce the number of allotriomorphs considerably, so that the few which nucleate tend to grow along the grain boundaries. This effectively suppresses the nucleation rate of Widmanstätten ferrite. In conclusion, it seems that boron's role in promoting the nucleation of acicular ferrite is indirect and concerned with retarding the nucleation of allotriomorphic and Widmanstätten ferrite along the austenite grain boundaries. Boron's direct influence upon the intra-granular transformation to acicular ferrite remains uncertain.

3.5 Other Inclusion Effects

3.5.1 Oxygen Content and the Inclusion Population

Inclusions are formed due to the dramatic decrease in the solubility of oxygen in steel with decreasing temperature. Clearly then, the weld metal oxygen content will have a considerable influence on inclusion characteristics, and thus the γ-α transformation. Indeed much of the early research on the relationship between inclusion characteristics, the volume fraction of acicular ferrite and weld metal toughness focused upon the oxygen content of the weld metal. Ito and Nakanishi's classic 1976 paper first revealed how the weld metal oxygen content effects the γ-α phase transformation. At very low oxygen levels a predominantly bainitic microstructure is obtained. Increasing the oxygen concentration above this promotes the formation of acicular ferrite. However, too large an increase leads to a dramatic reduction in the measured volume fraction of acicular ferrite, which is replaced by grain boundary nucleated allotriomorphic and Widmanstätten ferrite (Abson and Dolby, 1978; Barritte and Edmonds, 1981; Ito *et al.*, 1982; Ferrante and Farrar, 1982; Harrison and Farrar, 1981; Liu and Olson, 1986).

This behaviour may be rationalised by considering the two main effects of inclusions upon the austenite to ferrite transformation; the intragranular nucleation of acicular ferrite and the pinning of the austenite grain boundaries (Barritte and Edmonds, 1981). If the oxygen content is very low (≤ 150 ppm wt) both the volume fraction and the number density of inclusions are reduced to such an extent that the potential for the intragranular nucleation of acicular ferrite is extremely limited. Therefore, conventional bainite is the dominant microstructural product. The volume fraction and number density of inclusions rises as the oxygen content is increased. The number of suitable intragranular nucleation sites therefore multiplies, stimulating the nucleation of a larger volume fraction of acicular ferrite. 200 to 300 ppm wt of oxygen is associated with a microstructure predominantly consisting of acicular ferrite. Increasing the oxygen content beyond this promotes the formation of larger volume fractions of boundary nucleated allotriomorphic and Widmanstätten ferrite, at the expense of acicular ferrite. In these high oxygen welds the austenite grain size is much finer, because the high density and volume fraction of inclusions restricts austenitic grain growth. This decreases the potential for intragranular acicular ferrite nucleation. Several recent studies (St-Laurent and L'Espérance, 1992; Lee, 1994) have attempted to address this problem by separating inter- and intra-granular nucleation in a quantitative manner. Both approaches have serious limitations (they ignore alloy hardenability, cooling rate and boron segregation), but they do demonstrate certain important phenomena and are therefore to be recommended.

Cochrane and Kirkwood (1978) have suggested that in high oxygen weld metals, more inclusions are located at the austenite grain boundaries, where they increase the rate of allotriomorphic ferrite nucleation. Lee (1994) found that the proportion of inclusions located at the austenite grain boundaries increased from 15 to 35 % when the observed grain size decreased from 180 to 80 μm. Other authors have noted that some inclusions are located at the austenite grain boundaries (Liu and Olson, 1986 and Fleck *et al.*, 1986). Calculations by Harrison (1983) reveal that inclusions are particularly potent when they lie in the grain boundary plane.

3.5.2 Primary and Secondary Nucleation of Acicular ferrite

Barritte *et al.* (1981) claim that secondary laths of acicular ferrite nucleate on inclusion nucleated primary laths (Figure 3.11). Work by Barbaro (1990) and Zhang and Farrar (1996) supports this hypothesis. Zhang and Farrar noted that secondary nucleation only occurred in those regions of *in situ* water quenched welds (section 3.2.2) which were subjected to the largest undercooling before quenching. These secondary laths were normally smaller than the primary laths and appeared to fill the space between the primary laths in the austenite matrix. The net result was the fine interlocking structure that is known as acicular ferrite. A single inclusion can, however, nucleate more than one acicular ferrite lath to form a 'rosette' or 'starlike' structure (Dowling *et al.*, 1986; Zhang and Farrar, 1996).
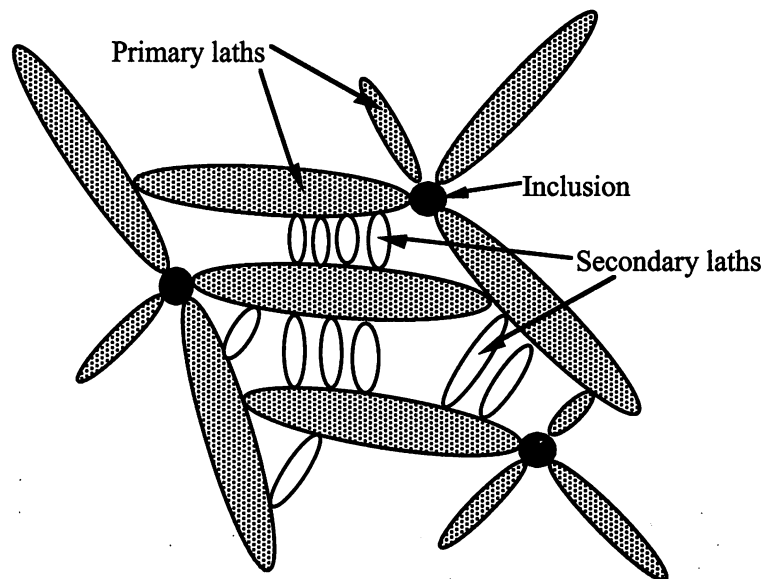

Figure 3.11 Illustration of the primary and secondary nucleation of laths of acicular ferrite.

3.5.3 Inclusion Size and Volume Fraction

Increasing the weld metal oxygen content dramatically increases the measured volume fraction of inclusions (Ito *et al.*, 1982; Jang and Indacochea, 1987). Liu and Olson (1986)

found that both the number density and the volume fraction of inclusions increased with increasing oxygen and sulphur concentrations. Work by Kluken and Grong (1989) noted that the measured volume fraction of inclusions in low alloy welds generally falls within the range 0.0017 to 0.0027. The following equation was found to describe the volume fraction of inclusions in the Si-Mn deoxidised welds they studied:

$$f_i = [5.0(\text{wt \% Oxygen}) + 5.4(\text{wt\% Sulphur} - 0.003)] \times 10^{-2} \qquad (3.5)$$

The influence of the oxygen content upon inclusion size is not so well understood. It can be argued that increasing the concentration of oxygen cause a greater supersaturation upon cooling and consequently a higher nucleation rate. Thus, a decrease in the mean inclusion size might occur as the oxygen content is increased. Were this to be the case, it would give an exceptionally dense distribution of fine inclusions that should be particularly effective at pinning the austenite grain boundaries. A number of studies have, however, concluded that with an increasing oxygen content, the mean inclusion size increases (Pargeter, 1981; Cochrane et al., 1983; Ferrante and Farrar, 1982). Other studies have shown the opposite or no variation (Liu and Olson, 1986). These discrepancies might be due to the resolution achieved in the different studies (Liu and Olson, 1986). On balance it seems reasonable to assume that inclusion size does not vary significantly with increasing weld oxygen content. However, a larger volume fraction of inclusions will form and greater austenite grain boundary pinning might result.

Pargeter (1981) noted that the effect of the oxygen content on inclusion size was most apparent in high heat input ($\simeq 6$ kJ mm^{-1}) welds. He postulated that the slower cooling rates experienced in these welds, would reduce the inclusion nucleation rate and increase the time available for diffusional growth, coalescence and Ostwald ripening. Kluken and Grong (1989) observed that the mean three-dimensional inclusion size increased from 0.33 to 0.70 μm, as the heat input was increased from 1 to 8 kJ mm^{-1}. They found that the following equation described the mean three-dimensional inclusion diameter:

$$\overline{d}_i \text{ (mm)} \approx 0.35(\eta E)^{1/3} \qquad (3.6)$$

where E is the electrical energy input per unit length (kJ mm^{-1}) and η is the arc transfer efficiency. Svensson (1994) argues that the very small diffusion distances and high diffusivity in the 'cold' zone, described by Grong et al. (1986), allows diffusional growth to be completed in a fraction of a second. Growth via the coalescence of colliding inclusions is limited in the relatively stagnant 'cold' zone. This indicates that Ostwald ripening (diffusional coarsening driven by the α-γ interfacial energy) is probably the dominant growth mechanism.

Increasing the weld metal aluminium concentration might also be expected to influence the size and volume fraction of inclusions. However, Kluken and Grong (1989) found that, whilst a higher fraction of coarse inclusions (> 1 μm) was associated with an increased aluminium content, the mean three-dimensional inclusion size and inclusion volume fraction did not vary significantly. This behaviour may be rationalised as follows. The higher volume fraction of coarse inclusions could be due to the high interfacial energy of inclusions primarily composed of Al_2O_3. This is thought to increase the rate at which they coarsen and/or coagulate during cooling. However, the weld pool will be deoxidised by the strongest oxide former available, so if insufficient aluminium is available other elements such as titanium will form oxides, and the volume fraction of inclusions should remain approximately constant.

3.5.4 Zener Pinning of the Austenite Grain Boundaries by Inclusions

Inclusions are thought by some authors to restrict the growth of the austenite grain boundaries during the welding thermal cycle (Harrison and Farrar, 1981; Liu and Olson, 1986; Fleck *et al.*, 1986). Barritte and Edmonds (1981) concluded that the inclusion population and austenite grain size are inter-related and can control weld microstructure. They found that increasing the weld oxygen content from 0.025 to 0.068 wt % reduced the austenite grain size from 150 to 60 μm. This increases the volume fraction of grain boundary nucleated phases such as allotriomorphic and Widmanstätten ferrite and reduces the volume fraction of acicular ferrite, irrespective of inclusion nucleation potency (Farrar *et al.*, 1993).

However, experiments performed by Bhadeshia *et al.* (1986b) revealed very different results. They found that the austenite grain size in as-deposited submerged-arc welds remained invariant when the oxygen content was increased from 0.012 to 0.042 wt %. They suggested that the Zener grain growth theory deals solely with the hindrance of the grain boundary motion. The application of this theory to as-deposited weld metals is not justified because the austenite grains form from δ-ferrite during continuous cooling. The driving force for the δ-ferrite to austenite transformation, which increases as the undercooling increases, would be sufficient to overcome any such boundary pinning effects. However, Bhadeshia *et al.* considered that pinning effects during grain coarsening might be important after the δ-ferrite to austenite transformation is completed, if the initial austenite grain size is extremely fine. They suggest that experiments to the contrary refer to the reheated weld metal, where the austenite grain size is related to a Zener type coarsening reaction driven by the austenite grain boundary interfacial energy.

CHAPTER FOUR

Modelling Simultaneous Transformation Kinetics

This chapter outlines an adaptation of the classic Johnson–Mehl–Avrami theory for overall transformation kinetics which allows simultaneous transformations to be rigorously described. These methods are used to model the competitive formation of intergranularly nucleated allotriomorphic ferrite and intragranularly nucleated idiomorphic ferrite. A model which describes the simultaneous decomposition of austenite into intergranularly nucleated allotriomorphic ferrite, Widmanstätten ferrite and pearlite is also discussed. These models are demonstrated to reproduce known metallurgical trends, and are shown to be of use in the design of steels. Note that the research presented in section 4.1.1 was conducted in collaboration with J. Robson and Dr. H.K.D.H. Bhadeshia.

4.1 Simultaneous Reactions – Randomly Nucleated

4.1.1 Analytical Illustration

The classic Johnson–Mehl–Avrami theory for overall transformation kinetics is described in section 2.1. This theory is, however, restricted to the precipitation of a single phase from the parent. In this section the theory is modified to treat the occurrence of two or more simultaneous reactions. Consider first a case in which α and β precipitate at the same time from the parent phase which is designated γ. It is assumed that the nucleation and growth rates do not change with time and that the particles grow isotropically. The increase in the extended volume due to particles nucleated in a time interval τ to $\tau + d\tau$ is, therefore, given by:

$$dV_\alpha^e = \frac{4}{3}\pi G_\alpha^3 (t-\tau)^3 I_\alpha V \, d\tau \qquad \text{and,} \qquad dV_\beta^e = \frac{4}{3}\pi G_\beta^3 (t-\tau)^3 I_\beta V \, d\tau \qquad (4.1)$$

where G_α, G_β, I_α and I_β are the growth and nucleation rates of α and β respectively, all of which are assumed here to be independent of time. $V = V_\gamma + V_\alpha + V_\beta$ is the total volume of the system. For each phase, the increase in extended volume will consist of three separate parts. Thus, for α:

(1) α which forms in untransformed γ.

(2) α which forms in existing α.

(3) α which forms in existing β.

Only α formed in untransformed γ will contribute to the real volume of α. On average a fraction $[1 - (V_\alpha + V_\beta)/V)]$ of the extended volume will be in previously untransformed material. It follows that the increase in the real volume of α in the time interval t to $t + dt$ is given by:

$$dV_\alpha = \left(1 - \frac{V_\alpha + V_\beta}{V}\right) dV_\alpha^e \qquad \text{and similarly for } \beta, \qquad dV_\beta = \left(1 - \frac{V_\alpha + V_\beta}{V}\right) dV_\beta^e \qquad (4.2)$$

In general, V_α will be some complex function of V_β and it is not possible to integrate these expressions to find the relationship between the real and extended volumes. However, in certain simple cases it is possible to relate V_α to V_β by multiplication with a suitable constant K, in which case $V_\beta = KV_\alpha$. The equations relating the increment in the real volume to that of the extended volume can therefore be written as:

$$dV_\alpha = \left(1 - \frac{V_\alpha + KV_\alpha}{V}\right) dV_\alpha^e \qquad \text{and,} \qquad dV_\beta = \left(1 - \frac{V_\beta + KV_\beta}{KV}\right) dV_\beta^e \qquad (4.3)$$

These may then be integrated to find an analytical solution relating the extended and real volumes analogous to that for single phase precipitation:

$$\frac{V_\alpha^e}{V} = \frac{-1}{1+K} \ln\left[1 - \frac{V_\alpha}{V}(1+K)\right] \quad \text{and,} \quad \frac{V_\beta^e}{V} = \frac{-K}{1+K} \ln\left[1 - \frac{V_\beta}{V}\left(\frac{1+K}{K}\right)\right] \quad (4.4)$$

The total extended volume of each phase at the time t is found by integrating equations 4.1 with respect to τ between $\tau = 0$ and $\tau = t$. Eliminating V_α^e and V_β^e gives:

$$\zeta_\alpha = \left(\frac{1}{1+K}\right)\left(1 - \exp\left[-\frac{\pi}{3}(1+K)G_\alpha^3 I_\alpha t^4\right]\right) \quad (4.5)$$

$$\zeta_\beta = \left(\frac{K}{1+K}\right)\left(1 - \exp\left[-\frac{\pi}{3}\left(\frac{1+K}{K}\right)G_\beta^3 I_\beta t^4\right]\right) \quad (4.6)$$

These equations resemble the well known Avrami equation 2.8 for single phase precipitation, with additional factors to account for the second precipitate phase. When the fractions of both precipitating phases are small, the equations approximate to the expressions for each phase precipitating alone. This is because nearly all of the extended volume then lies in previously untransformed material and contributes to the real volume. It is possible for constant nucleation and growth rates to calculate explicitly the value of K, which is given by:

$$K = \frac{V_\beta}{V_\alpha} = \frac{I_\beta G_\beta^3}{I_\alpha G_\alpha^3} \quad (4.7)$$

Some example calculations for the case of constant growth rate are presented in Figure 4.1. When the nucleation and growth rates of α and β are set to be identical, their transformation curves superimpose and each phase eventually achieves a maximum fraction of 0.5 (Figure 4.1a). When the nucleation rate of β is set to be twice that of α, then for identical growth rates, the terminal fraction of β is twice that of α (Figure 4.1b). The case where the growth rate of β is set to be twice that of α (with identical nucleation rates) is illustrated in Figure 4.1c. The final volume fraction of the β phase is then eight times that of the α phase because volume fraction is a function of the growth rate cubed.
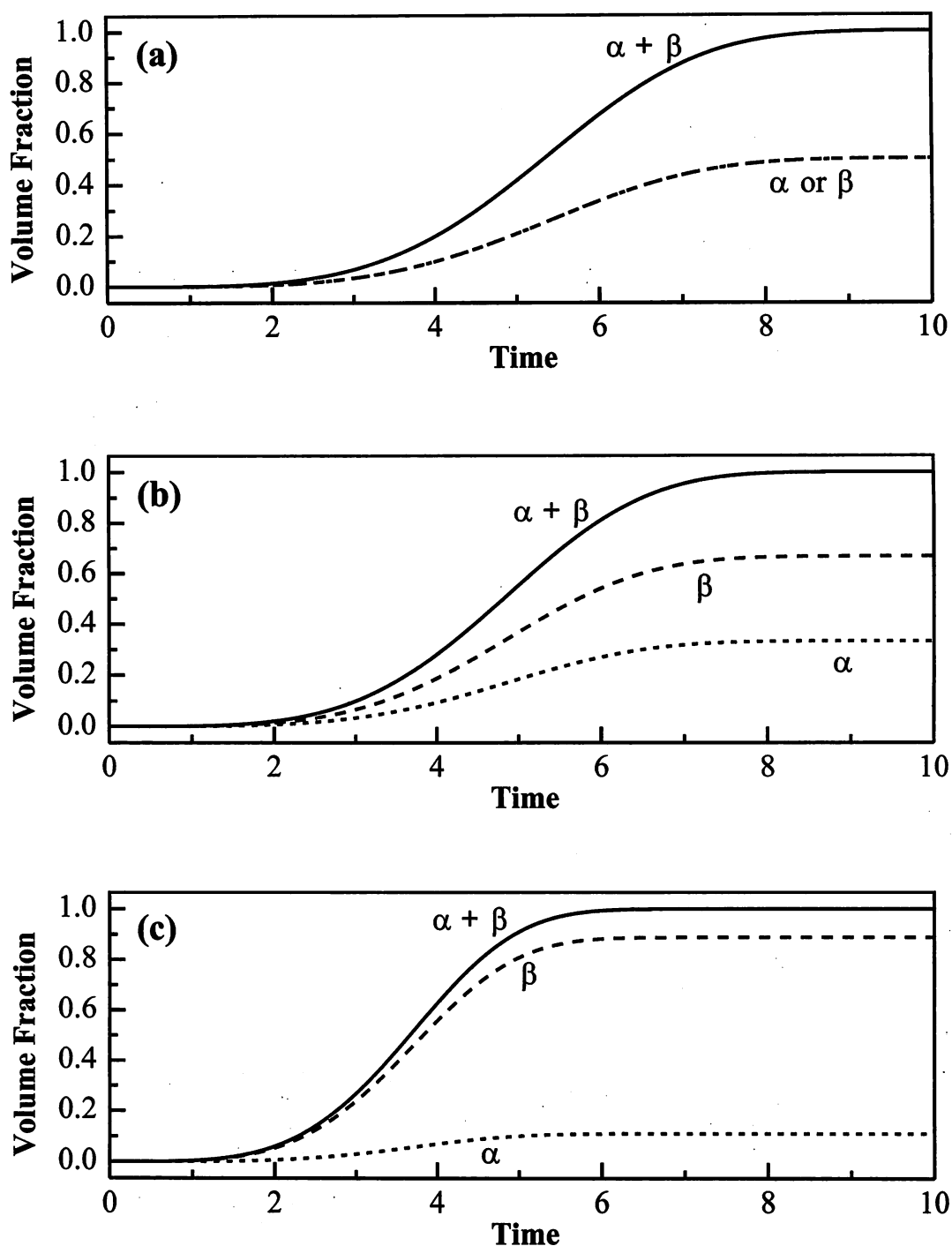
Figure 4.1   An illustration of the kinetics of two reactions occurring simultaneously, both of which nucleate randomly and grow in a linear manner. (a) Both phases have identical nucleation and growth rates; (b) Identical growth rates but with β nucleating at twice the rate of α; (c) Identical nucleation rates but with β growing at twice the rate of α.

4.1.2 Numerical Solution

Whilst the analytical method is more transparent, a numerical procedure is appropriate when the boundary conditions for nucleation and growth change during transformation. Consider a system with n precipitating phases which nucleate randomly and grow via their individual mechanisms. The change in the real volume of the phase j in the time interval t to $t + \Delta t$ is:

$$\Delta V_j = \left(1 - \frac{\Sigma_{i=1}^n V_i}{V}\right)\Delta V_j^e \tag{4.8}$$

where ΔV_j^e is the corresponding change in the extended volume of the phase j in the same time interval, V_i is the real volume of the i'th phase at the time t and V is the total volume of the assembly. ΔV_j^e may have a contribution from all particles nucleated since the start of transformation to $t = m\Delta t$, where m is an integer such that $m\Delta t$ is the current time t, so that:

$$\Delta V_j^e = \sum_{k=0}^{m}(VI_{j,k}\Delta\tau)(v_{j,k}\Delta t) \tag{4.9}$$

where $v_{j,k}$ is the rate of change of extended volume of a particle of the phase j which nucleated between $k\Delta\tau$ and $(k+1)\Delta\tau$, during the current time interval $m\Delta t$ to $(m+1)\Delta t$. $I_{j,k}$ is the nucleation rate per unit volume of the phase j during the time interval $k\Delta\tau$ to $(k+1)\Delta\tau$. $VI_{j,k}\Delta\tau$ is the number of extended particles of j nucleated in this time interval. Δt and $\Delta\tau$ are taken to be numerically identical.

The instantaneous value of ΔV_j, together with the corresponding changes in the real volumes of the other $n-1$ phases, is used to update the total real volume of each phase at the time $t + \Delta t$ in a computer implemented numerical procedure by writing:

$$V_{j,t+\Delta t} = V_{j,t} + \Delta V_j \qquad \text{for} \qquad j = 1\ldots n \tag{4.10}$$

so that a plot of the real volume of each phase can be obtained as a function of time. The growth and nucleation rates can also be updated during this step, should they have changed because of solute enrichment in the untransformed parent material or because there is a change in temperature during continuous cooling transformation.[1]

---

[1] The theory shown assumes, for clarity, that the time step (*i.e.* Δt and $\Delta\tau$) remains invariant throughout the course of the transformation. However, to model transformations in real systems necessitates the use of a variable time step to minimise the computational effort. For example, a small time interval is appropriate at the start of transformation but a longer time interval is required as the transformation nears completion.

4.2 Simultaneous Reactions – Boundary Nucleated

The analysis for boundary nucleated simultaneous reactions presented below is a numerical adaptation of the general method due to Cahn (1956), in which there are two applications of extended space, the first applying to the gradual elimination of free grain boundary area and the second to the gradual elimination of the volume of untransformed material (section 2.1.2). Consider a planar boundary of area O_B (which is equal to the total grain boundary area per unit volume in the assembly) in a system with n precipitating phases, where $O_{i,y}$ is the total real area intersected by the i'th phase on a plane parallel to the boundary but at a distance y normal to that boundary at the time t, then for the j'th phase:

$$\Delta O_{j,y} = \left(1 - \frac{\Sigma_{i=1}^{n} O_{i,y}}{O_B}\right) \Delta O_{j,y}^e \qquad (4.11)$$

where $\Delta O_{j,y}$ is the change in the real area intersected with the plane at y by the phase j, during the small time interval t to $t + \Delta t$. $\Delta O_{j,y}^e$ is similarly, the change in the *extended* area of intersection with the same plane at y. This may have a contribution from all particles nucleated since the start of transformation to $t = m\Delta t$, where m is an integer such that $m\Delta t$ is the current time t, so that:

$$\Delta O_{j,y}^e = \sum_{k=0}^{m} (O_B I_{j,k} \Delta\tau)(A_{j,k,y} \Delta t) \qquad (4.12)$$

where $A_{j,k,y}$ is the rate of change of the extended area of intersection on plane y of a particle of the phase j which nucleated between $k\Delta\tau$ and $(k+1)\Delta\tau$, during the current time interval $m\Delta t$ to $(m+1)\Delta t$. $I_{j,k}$ is the nucleation rate per unit area of the phase j during the time interval $k\Delta\tau$ to $(k+1)\Delta\tau$. $O_B I_{j,k} \Delta\tau$ is the number of extended particles nucleated in this time interval. Note that Δt and $\Delta\tau$ are taken to be numerically identical. $\Delta O_{j,y}$ is then used to update the total real area of intersection of the phase j with the same plane at y at the time $t + \Delta t$ by writing:

$$O_{j,y,t+\Delta t} = O_{j,y,t} + \Delta O_{j,y} \qquad \text{for} \qquad j = 1 \ldots n \qquad (4.13)$$

To obtain a change in the extended volume of the phase j on one side of the boundary, it is necessary to integrate as follows:

$$dV_j^e = \int_{y=0}^{q_j^{max}} dO_{j,y}\, dy \qquad (4.14)$$

where the integrand $dO_{j,y}$ is equivalent to $\Delta O_{j,y}$ and q_j^{max} is the maximum extended size of a particle of phase j in a direction normal to the grain boundary plane. Thus, the change in the

extended volume of the phase j on one side of the boundary in the time interval t to $t + \Delta t$ may be numerically evaluated as:

$$\Delta V_j^e = \Delta y \sum_{y=0}^{q_j^{max}} \Delta O_{j,y} \qquad (4.15)$$

where Δy is a small interval in y. Therefore, the corresponding change in the real volume after allowing for impingement with particles originating from other boundaries is:

$$\Delta V_j = \left(1 - \frac{\Sigma_{i=1}^n V_i}{V}\right)\Delta V_j^e \qquad (4.16)$$

where V_i is the real volume of the i'th phase at the time t. The instantaneous value of ΔV_j, together with the corresponding changes in the volumes of the other $n - 1$ phases, can be used to calculate the total real volume of each phase at the time $t + \Delta t$ in a computer implemented numerical procedure by writing:

$$V_{j,t+\Delta t} = V_{j,t} + \Delta V_j \qquad \text{for} \qquad j = 1 \ldots n \qquad (4.17)$$

so that a plot of the fraction of each phase can be obtained as a function of time. The growth and nucleation rates can also be updated during this step, should they have changed because of solute enrichment in the untransformed parent material or because there is a change in temperature during continuous cooling transformation.[1]

4.3 Simultaneous Formation of Allotriomorphic and Idiomorphic Ferrite

4.3.1 Introduction

It is well established that a refinement of the steel microstructure leads to an improvement in both the strength and toughness. Since ferrite generally nucleates at the austenite grain surfaces, the steel microstructure can be made finer by reducing the size of the austenite grains, thus providing a greater number density of nucleation sites. An alternative (or complementary) approach is to introduce additional heterogeneous nucleation sites in the form of finely dispersed and carefully chosen non-metallic particles. These act as sites for the intragranular nucleation of ferrite (Ito and Nakanishi, 1976; Imagumbai *et al.*, 1985; Ochi *et al.*, 1988; Ishikawa *et al.*, 1994; Ishikawa; Takahashi *et al.*, 1995; Linaza *et al.*, 1993).

A microstructure in which the ferrite is nucleated at both the austenite grain surfaces and at intragranular sites also tends to be more random. It presents many more crystallographic orientations of ferrite per unit volume of sample, so that propagating cleavage cracks are

frequently deflected. This leads to an improvement of toughness beyond that expected from grain refinement alone.

Much of the work in the development of steels which rely on intragranularly nucleated ferrite has been done empirically. In other contexts, attempts at modelling continuous cooling transformations involving simultaneous reactions have assumed that the different reactions occur successively (sections 2.3 and 2.4). The aim here was to develop an overall transformation kinetics model (Appendix One) capable of treating the simultaneous formation of ferrite from a variety of different nucleation sites, by adapting the classical Johnson–Mehl–Avrami theory. Modelling the simultaneous formation of both intra- and inter-granularly nucleated ferrite (*i.e.* allotriomorphic and idiomorphic ferrite) is then straightforward using equations very similar to those discussed earlier (sections 4.1.2 and 4.2). In this case only one phase is forming, however, it is nucleating at two different types of site. Therefore, in this section the subscript $j = 1$ is used to distinguish allotriomorphic ferrite nucleated at the austenite grain boundaries from intragranularly nucleated idiomorphic ferrite which is given the subscript $j = 2$.

The boundary model is modified slightly, because only allotriomorphic ferrite nucleates along the austenite grain boundaries. Therefore, removing the summation term from equation 4.11 yields:

$$\Delta O_{1,y} = \left(1 - \frac{O_{1,y}}{O_B}\right)\Delta O^e_{1,y} \tag{4.18}$$

The competition between allotriomorphic and idiomorphic ferrite particles for the untransformed volume of austenite is modelled by using equation 4.16 (where j has been redefined as above) to determine how the real volumes of allotriomorphic and idiomorphic ferrite change during each time interval. Thus for allotriomorphic and idiomorphic ferrite respectively:

$$\Delta V_1 = \left(1 - \frac{V_1 + V_2}{V}\right)\Delta V^e_1 \quad \text{and,} \quad \Delta V_2 = \left(1 - \frac{V_1 + V_2}{V}\right)\Delta V^e_2 \tag{4.19}$$

4.3.2 Allotriomorphic Ferrite

The nucleation and growth of allotriomorphic ferrite has been described by modelling the allotriomorphs as discs (Figure 4.2) having their faces parallel to the nucleating grain boundary plane (Bhadeshia *et al.*, 1987; Reed and Bhadeshia, 1992). The discs are assumed to grow on both sides of the parent boundary under paraequilibrium conditions, so that the half-thickness q_1 of each disc during isothermal growth is given by:

$$q_1 = \vartheta(t - \tau)^{1/2} \tag{4.20}$$

where ϑ is the one-dimensional parabolic thickening rate constant. The growth rate slows down as the concentration gradient ahead of the moving interface decreases to accommodate the

carbon that is partitioned into the austenite. The growth rate parallel to the grain boundary plane is taken to be three times that normal to it, giving a constant aspect ratio η_1 of 3.0 (Bradley and Aaronson, 1977), so that the disc radius is $\eta_1 q_1$.
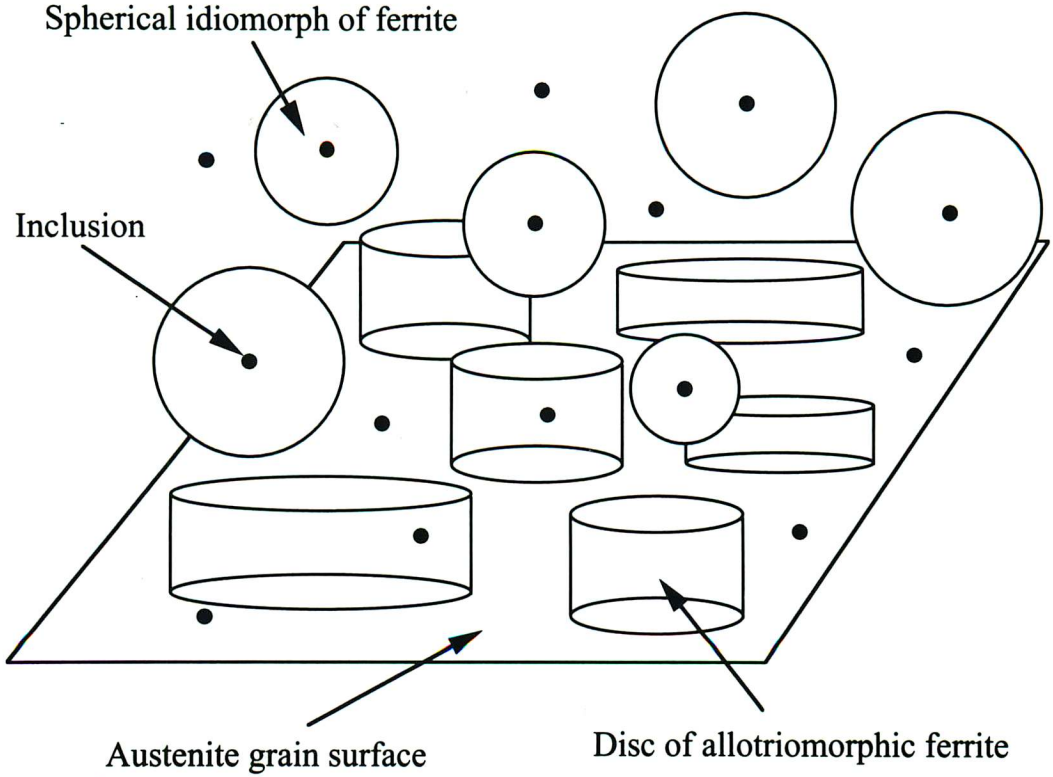
Figure 4.2   Illustration of the morphologies used to model the simultaneous formation of allotriomorphic and idiomorphic ferrite.

For non-isothermal growth the change in thickness during a time interval dt is given by differentiating equation 4.20 to give:

$$dq_1 = \frac{1}{2}\vartheta(t - \tau)^{-\frac{1}{2}} dt \tag{4.21}$$

Therefore, for a particle nucleated at $k\Delta\tau$ the half-thickness at the time $(m+1)\Delta t$ is evaluated numerically as:

$$q_{1,(m+1)\Delta t} = q_{1,m\Delta t} + \frac{1}{2}\vartheta(m\Delta t - k\Delta\tau)^{-\frac{1}{2}}\Delta t \tag{4.22}$$

The rate of change of area of intersection on a plane y of a disc of allotriomorphic ferrite nucleated at $k\Delta\tau$, at the time $m\Delta t$, is taken as:

$$A_{1,k,y} = \pi\eta_1^2\vartheta^2 \qquad\qquad (q_{1,(m+1)\Delta t} > y) \tag{4.23}$$

$$A_{1,k,y} = \left(\pi \eta_1^2 q_{1,(m+1)\Delta t}^2 \right) / \Delta t \qquad (q_{1,(m+1)\Delta t} = y) \qquad (4.24)$$

$$A_{1,k,y} = 0 \qquad (q_{1,(m+1)\Delta t} < y) \qquad (4.25)$$

Since the ferrite allotriomorphs can grow into both of the adjacent austenite grains, if follows from equation 4.15 that:

$$\Delta V_1^e = 2\Delta y \sum_{y=0}^{q_1^{max}} \Delta O_{1,y} \qquad (4.26)$$

To validate this numerical method precipitation was restricted to a single phase β which could only nucleate on grain surfaces. Figure 4.3 shows two plots of the volume fraction of β at any instant in time; one curve was calculated using an analytical equation 2.38 due to Bhadeshia *et al.* (1987) which describes the microstructural evolution of a single phase with a parabolic growth mechanism which nucleates at a grain surface; the second curve was determined numerically using the method outlined above. To allow direct comparison between these predictions the equilibrium volume fraction of β in the analytical equation was assumed to be unity, whilst in the numerical procedure both the one-dimensional parabolic thickening constant and the nucleation rate remained invariant during transformation. It is apparent that the numerical method is equivalent to the analytical approach.
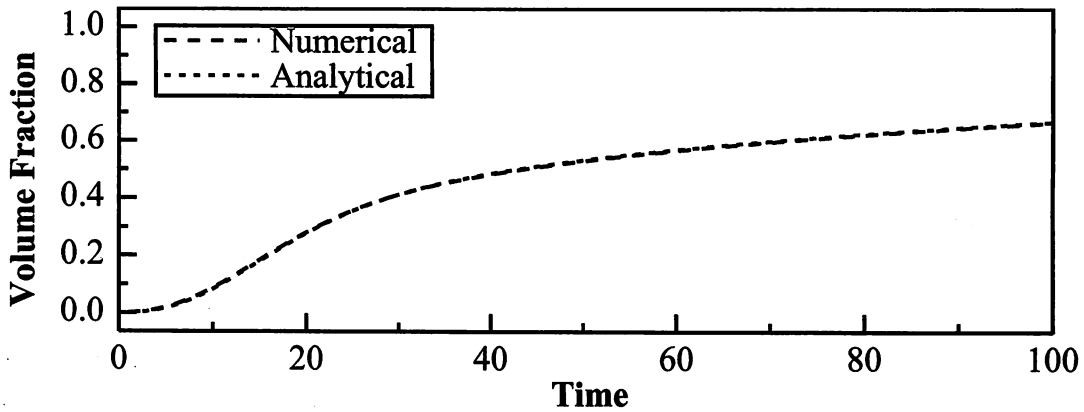
Figure 4.3 The evolution of a single phase β with parabolic growth characteristics which is nucleated along the grain surface of the parent phase. Two curves are presented; one was determined using an analytical approach (equation 2.38) due to Bhadeshia *et al.* (1987) and the other using a numerical technique (section 4.3.2).

The one-dimensional parabolic thickening constant ϑ is obtained by solving (Christian, 1975):

$$2\left(\frac{D}{\pi}\right)^{\frac{1}{2}} \Omega = \vartheta \exp\left(\frac{\vartheta^2}{4D}\right) \mathrm{erfc}\left(\frac{\vartheta}{2D^{\frac{1}{2}}}\right) \qquad (4.27)$$

where the supersaturation Ω is:

$$\text{with} \qquad \Omega = \frac{x^{\gamma\alpha} - \overline{x}}{x^{\gamma\alpha} - x^{\alpha\gamma}} \tag{4.28}$$

where $x^{\gamma\alpha}$ and $x^{\alpha\gamma}$ are the paraequilibrium carbon concentrations in austenite and ferrite respectively at the interface, obtained using a calculated multicomponent phase diagram (Bhadeshia, 1982c), $\overline{x}$ is the average carbon concentration of the austenite and $\underline{D}$ is a weighted average diffusivity (Trivedi and Pound, 1967) of carbon in austenite, given by:

$$\underline{D} = \int\limits_{x^{\gamma\alpha}}^{\overline{x}} \frac{D\{x\}\, dx}{\overline{x} - x^{\gamma\alpha}} \tag{4.29}$$

where $D\{x\}$ is the diffusivity of carbon in austenite at a particular concentration of carbon (Bhadeshia, 1981a).

Classical nucleation theory (Christian, 1975) is used to model the nucleation rate of allotriomorphic ferrite on the austenite grain boundaries, with the nucleation rate per unit area of boundary given by:

$$I_1 = C_a \frac{kT}{h} \exp\left(-\frac{G_1^* + Q}{RT}\right) \exp\left(-\frac{\tau^*}{t}\right) \tag{4.30}$$

where h is the Planck constant, k is the Boltzmann constant, T is the absolute temperature, $C_a = 4.86 \times 10^{10}\,\text{m}^{-2}$ is a fitted constant, R is the universal gas constant and $Q = 200\,\text{kJ}\,\text{mol}^{-1}$ is a constant activation energy representing the barrier to the transfer of atoms across the interface. The activation energy for nucleation, $G_1^* = C_b\sigma^3/\Delta G_m^2$, where $\sigma = 0.024\,\text{J}\,\text{m}^{-2}$ represents the austenite-ferrite interfacial energy per unit area. C_b is another fitted constant (4.19 for an austenite boundary free of soluble boron and 5.53 for a boundary saturated with soluble boron) and ΔG_m is the maximum chemical free energy change per unit volume available for nucleation (Bhadeshia, 1982c). The second exponential term relates to the achievement of a steady-state nucleation rate; $\tau^* = n_c^2 h(4a_c kT)^{-1}\exp(Q/RT)$, where n_c is the number of atoms in the critical nucleus and a_c is the number of atoms in the critical nucleus which are at the interface.

4.3.3 Idiomorphic Ferrite

The random nucleation and growth of idiomorphic ferrite on non-metallic particles has been described by modelling the idiomorphs as spheres (Figure 4.2) which grow parabolically under paraequilibrium conditions. For non-isothermal growth the rate of change of the extended volume of a particle of idiomorphic ferrite which nucleated at $k\Delta\tau$ at the time $m\Delta t$ is:

$$v_{2,k} = 2\pi\xi^3(m\Delta t - k\Delta\tau)^{1/2} \qquad (m\Delta t > k\Delta\tau) \tag{4.31}$$

$$v_{2,k} = \frac{4}{3}\pi\xi^3\Delta t^{1/2} \qquad (m\Delta t = k\Delta\tau) \qquad (4.32)$$

where ξ is the three-dimensional parabolic thickening parameter which is given by Christian (1975) as:

$$\xi = \left[\frac{2\underline{D}(\overline{x} - x^{\gamma\alpha})}{x^{\alpha\gamma} - \overline{x}}\right]^{1/2} \qquad (4.33)$$

To examine the validity of this numerical technique a single phase β was permitted to nucleate intragranularly (*i.e.* randomly). Figure 4.4 illustrates two plots of the volume fraction of β versus time; one curve was predicted using an analytical approach due to Johnson, Mehl and Avrami (equation 2.14) which describes the microstructural evolution of a single phase with parabolic growth characteristics which nucleates randomly in the volume of an assembly; the other curve was found numerically using the method detailed above. To facilitate direct comparison between these calculations the equilibrium volume fraction of β in the analytical equation was taken to be unity, whilst in the numerical method both the three-dimensional parabolic thickening parameter and the nucleation rate were invariant. The numerical method is thus demonstrated to be equivalent to the analytical procedure.
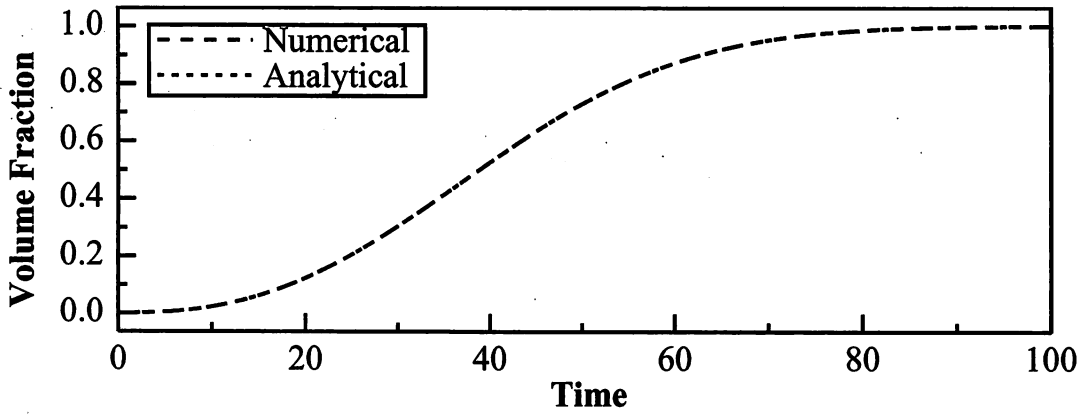
Figure 4.4 The evolution of a single phase β with parabolic growth characteristics which nucleates randomly in the volume of an assembly. Two curves are shown; one was determined using an analytical approach due to Johnson, Mehl and Avrami (equation 2.14) and the second using an equivalent numerical procedure (section 4.3.3).

The nucleation rate I_2 of idiomorphic ferrite on non-metallic particles per unit volume is obtained in a similar fashion to the nucleation rate of allotriomorphic ferrite (section 4.3.2):

$$I_2 = C_c N_V \frac{kT}{h}\exp\left(-\frac{G_2^* + Q}{RT}\right)\exp\left(-\frac{\tau^*}{t}\right) \qquad (4.34)$$

where $C_c = 0.088$ is a fitted constant and N_V is the number of non-metallic particles per unit volume (m^{-3}). $G_2^* = C_d\sigma^3/\Delta G_m^2$, where $C_d = 7.54$ is another fitted constant. Note that the

parameter C_d is larger than C_b, which is consistent with the widely accepted view that inert inclusions are less potent sites for nucleation than the austenite grain boundaries.

4.3.4 Results and Discussion

The model described above was validated in two ways, first by a comparison against published experimental data, and secondly by examining the predicted trends to ensure consistency with metallurgical expectations.

There is one quantitative study on the balance between idiomorphic and allotriomorphic ferrite, due to Ueda *et al.* (1980) and Funakoshi *et al.* (1976), who studied transformation in the three steels listed in Table 4.1. Using their designations, steel *b* is a mild steel which is free of boron, steels *c* and *d* both contain deliberate additions of boron but the latter has an exceptionally low nitrogen concentration. Transformation in all of the alloys occurs to varying degrees, by heterogeneous nucleation at the austenite grain surfaces or intragranularly at non-metallic particles. Ueda *et al.* thought that these particles were boron-nitrides, although, iron-borocarbides were also suspected of inducing a small number of nucleation events. The key features of this series of steels are illustrated in Figure 4.5, and can be summarised as follows:

(1) The boron-free steel *b* can be regarded as the reference material with transformation originating mostly from the austenite grain surfaces.

(2) Transformation in the boron-containing high-nitrogen steel *c* is dominated by intragranular nucleation at boron nitride particles. A relatively small amount of soluble boron segregates to the austenite grain surfaces making them slightly less effective as heterogeneous nucleation sites.

(3) The boron-containing low-nitrogen steel *d* contains a high concentration of soluble boron which segregates to the austenite grain surfaces making them significantly less effective as heterogeneous nucleation sites. A small increase in the number density of intragranular nucleation sites occurs because some boron nitride precipitation is inevitable.

Alloy	C	Si	Mn	B	N	Comment
b	0.12	0.25	1.47	–	0.0045	Boron-free steel
c	0.12	0.23	1.44	0.0029	0.0074	High-nitrogen, boron steel
d	0.13	0.23	1.45	0.0030	0.0014	Low-nitrogen, boron steel

Table 4.1 The chemical compositions (wt %) of the steels studied by Ueda *et al.* (1980)

The model requires values for certain parameters which are steel dependent. These are listed in Table 4.2. The austenite grain sizes are from Funakoshi *et al.* (1976); they influence the number density of grain boundary nucleation sites. The term C_b occurs in the activation energy for nucleation, with $G_1^* = C_b \sigma^3 / \Delta G_m^2$. The value of the austenite-ferrite interfacial energy per unit area σ was taken to be $0.025 \, \mathrm{J \, m^{-2}}$. However, boron modifies the interfacial energy of the $\gamma - \gamma$ surface and thus increases the activation energy barrier to nucleation; this modification is taken into account by adjusting empirically the value of C_b in a way consistent with the increasing quantities of soluble boron in steels *b*, *c* and *d* respectively. In the boron-containing steels *c* and *d* the volume fraction of nucleating particles V_I was estimated as the equilibrium volume fraction of boron nitride. This was calculated (section 5.8.1) using the solubility product of BN in austenite due to Maitrepierre *et al.* (1980), for the transformation temperature of 720 °C. The boron nitride particle size is unknown but was taken as 0.02 μm (Thewlis, 1989a). In the boron-free steel *b* the volume fraction of nucleating particles was assumed to be an order of magnitude less than the calculated volume fraction of BN in steel *c*. The particle size was assumed to be the same as that in steels *c* and *d*.

Steel	d_γ (μm)	C_b	V_I	d_I (μm)	C_d
b	195	4.19	2.3×10^{-5}	0.02	7.54
c	195	4.86	2.3×10^{-4}	0.02	7.54
d	177	5.53	7.8×10^{-5}	0.02	7.54
Model Steel *e*	45	4.19	0	–	–
Model Steel *f*	45	4.19	2.0×10^{-3}	0.5	7.54

Table 4.2 Parameters necessary to compare experimental data (Ueda *et al.*, 1980) against theory, together with those used to predict the reconstructive (allotriomorphic and idiomorphic ferrite) TTT curves in two model steels. d_γ is the austenite grain size (mean lineal intercept), V_I the volume fraction of nucleating particles and d_I the particle diameter.

Figure 4.6 shows the transformation curves estimated for steels *b*, *c* and *d*; these can be compared against the experimental curves given in Figure 4.5. It should, however, be borne in mind that Figures 4.5b,c are plots of the number densities of intragranular or boundary particles, rather than the volume fractions plotted in Figures 4.6b,c.

Isothermal transformation at 720 °C can only continue until the equilibrium volume fraction is reached, leaving some austenite untransformed. To allow a comparison against the experimental data, which are in effect normalised with respect to the equilibrium fraction, Figure 4.6a has been normalised with respect to the calculated paraequilibrium volume fraction. It is clear that all of the trends evident in the experimental transformation curves

are reproduced faithfully. Examination of Figures 4.6b,c shows that consistent with the experimental data (Figures 4.5b,c) grain boundary transformation dominates in the boron-free steel *b*. The reverse is true for the boron-rich high-nitrogen steel *c*, where the boron nitride particles stimulate intragranular transformation and soluble boron retards grain boundary allotriomorph nucleation. As expected, the suppression of allotriomorphic ferrite is largest for the low-nitrogen boron steel *d*.

These results are encouraging given that the only parameter which has been adjusted to distinguish the steels is the value of C_b, which alters the potency of the austenite grain boundaries to account for the differing levels of soluble boron. The model was further tested to ensure that it was consistent with metallurgical expectations.

A reduction in the austenite grain size should lead to a change in the balance between allotriomorphic and idiomorphic ferrite. This is illustrated in Figure 4.7 for steel *c* where data are presented for austenite grain sizes of 150, 50 and 25 μm. The reduction in the austenite grain size d_γ leads to a change from an idiomorphic to an allotriomorphic ferrite dominated transformation. Such an effect is well established from a qualitative point of view (Bhadeshia and Svensson, 1993); large austenite grain sizes favour intragranularly nucleated transformation products for two reasons. Firstly, the number density of grain boundary nucleation sites decreases relative to intragranular sites as d_γ is increased. Secondly, the grain boundary nucleation sites are more potent than the inclusions so transformation commences first at the boundaries.
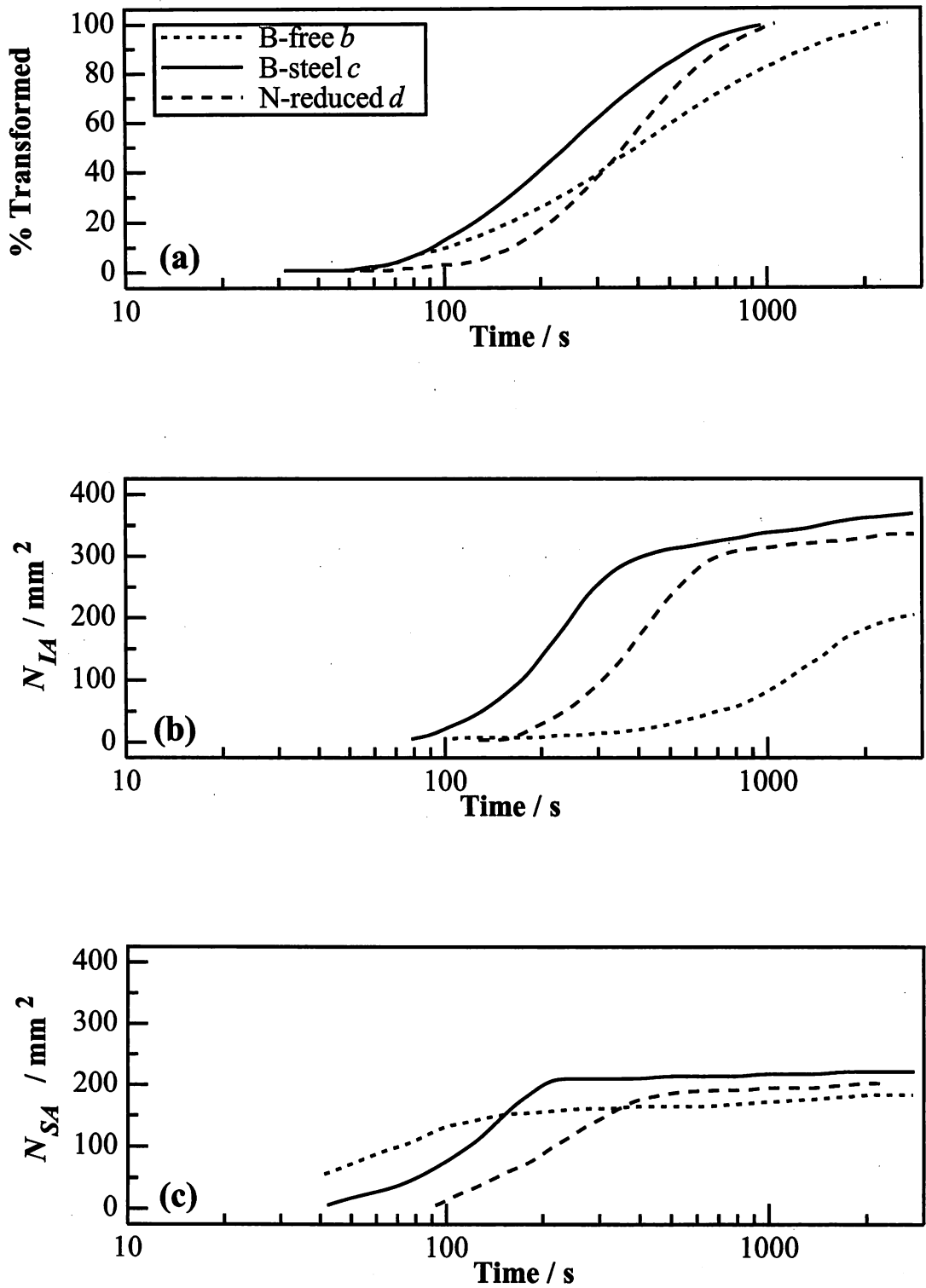
Figure 4.5 Experimental data reported by Ueda *et al.* (1980) for the alloys listed in Table 4.1. (a) Total normalised fraction of transformation as a function of time at 720 °C, following austenitisation at 1350 °C for ten seconds; (b) number density N_{IA} of ferrite grains observed to grow from intragranular nucleation sites; (c) number density N_{SA} of ferrite grains observed to grow from austenite grain surfaces.
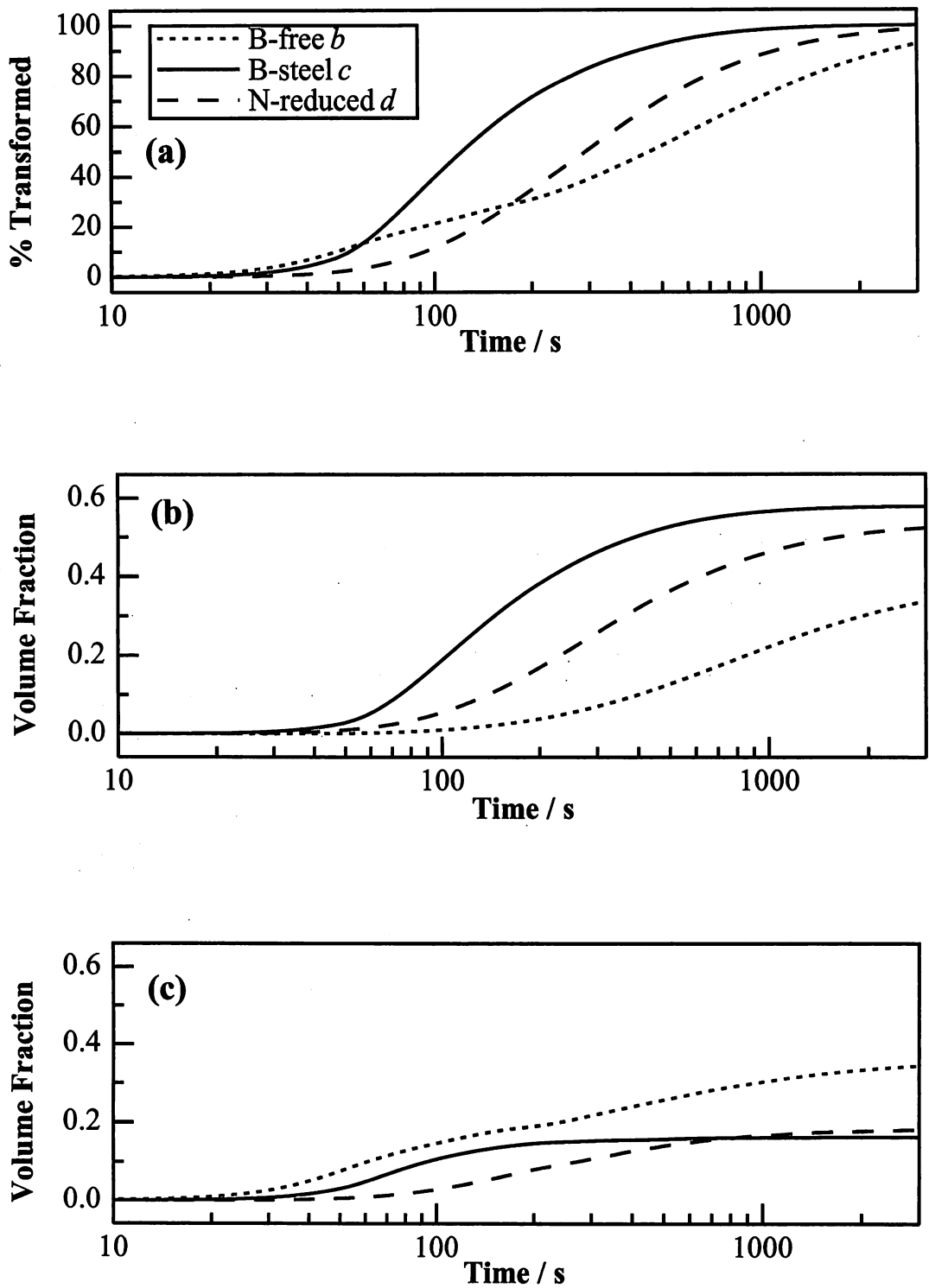
Figure 4.6   Calculated data for the steels listed in Table 4.1. (a) Total normalised fraction of transformation as a function of time at 720 °C; (b) absolute volume fraction of intragranularly nucleated idiomorphic ferrite; (c) absolute volume fraction of grain boundary nucleated allotriomorphic ferrite.
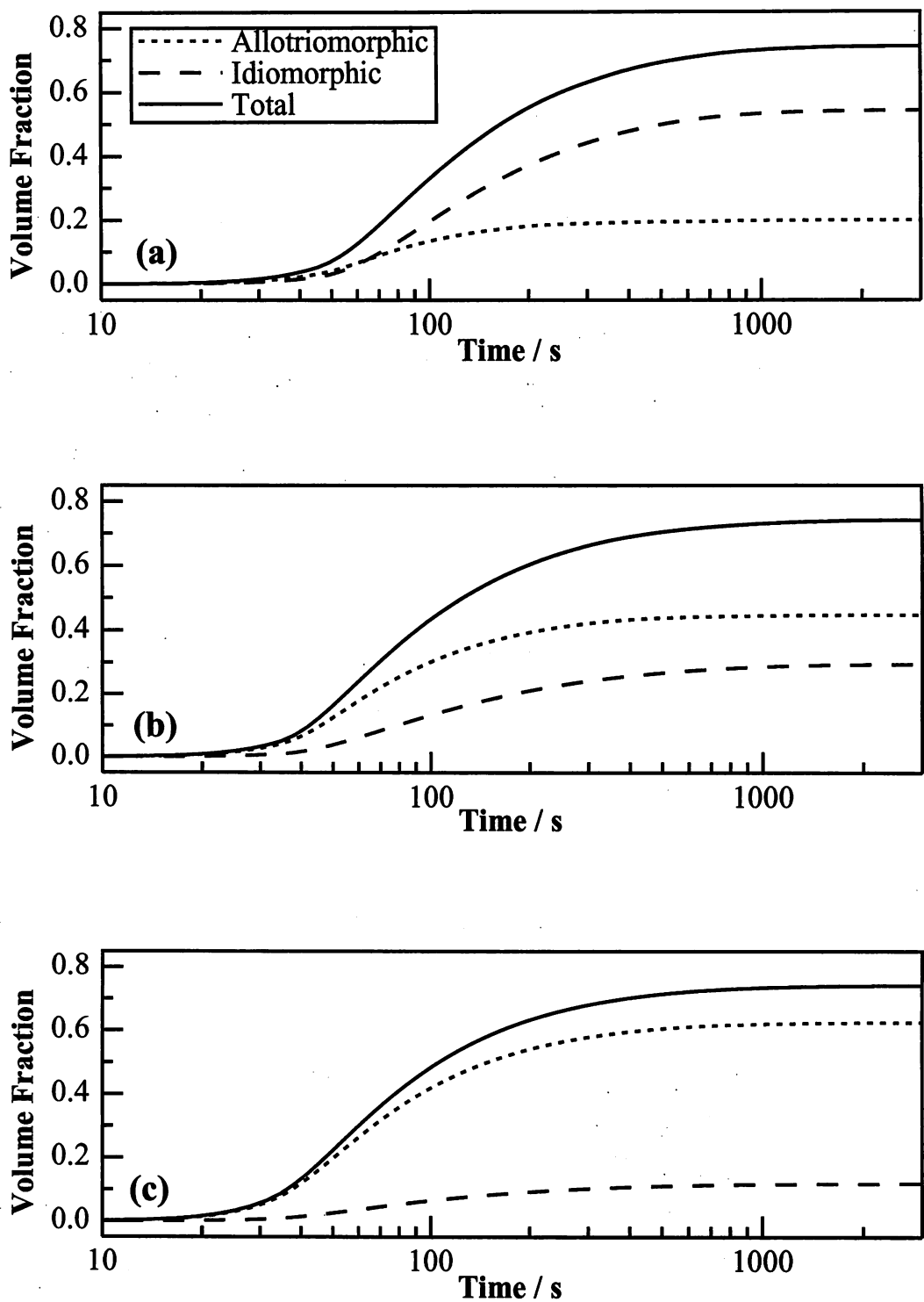
Figure 4.7 The influence of the austenite grain size d_γ on transformations in steel c. (a) An austenite grain size of 150 μm; (b) an austenite grain size of 50 μm; (c) an austenite grain size of 25 μm.

Numerical methods are particularly suited to the modelling of phase transformations in complex systems where the boundary conditions for nucleation and growth vary throughout the course of the transformation. This is demonstrated in Figure 4.8 which corresponds to transformation in steel c with an austenite grain size of 50 μm (Figure 4.7b). Figure 4.8a shows that nucleation rates increase rapidly during the initial stages of transformation until a steady-state is achieved after approximately 20 s. This is followed by a dramatic decrease in the rates of nucleation because of the progressive stabilisation of the untransformed austenite as it becomes enriched in carbon. Carbon enrichment also influences the rate of particle growth as the parabolic thickening parameters tend asymptotically towards zero as the far field carbon concentration rises (Figure 4.8b).

It has been emphasised that the activation energy for nucleation at inclusions (G_2^*) is larger than for nucleation at the austenite grain surfaces (G_1^*). However, the significance of this difference decreases as the magnitude of the chemical driving force ΔG_m increases. This is because the net activation energy for nucleation is a sum of two terms, G^* and Q. The former is inversely proportional to the square of the chemical driving force and decreases rapidly as the chemical driving force increases. The latter, on the other hand, is constant since it represents an activation energy for diffusion across the transformation interface. Therefore, a decrease in the chemical driving force will have a larger effect on inclusion nucleated transformations than grain surface nucleated reactions, but for the reasons explained above, the effects will be most pronounced when the driving force is small. A corollary is that anything which reduces ΔG_m will exaggerate the difference between inclusion and grain surface nucleation rates. This is illustrated in Figure 4.9, which should be compared against Figure 4.7b. For transformation at 720 °C, an increase in either the carbon or the manganese concentration leads to a drastic suppression of idiomorphic ferrite (Figures 4.9a,b). Both of these elements stabilise austenite and hence reduce the magnitude of ΔG_m; this is evident also in the net retardation of transformation. On the other hand, idiomorphic ferrite is promoted if the magnitude of ΔG_m is increased by reducing the transformation temperature to 700 °C (Figure 4.9c, which should be compared with Figure 4.7b).
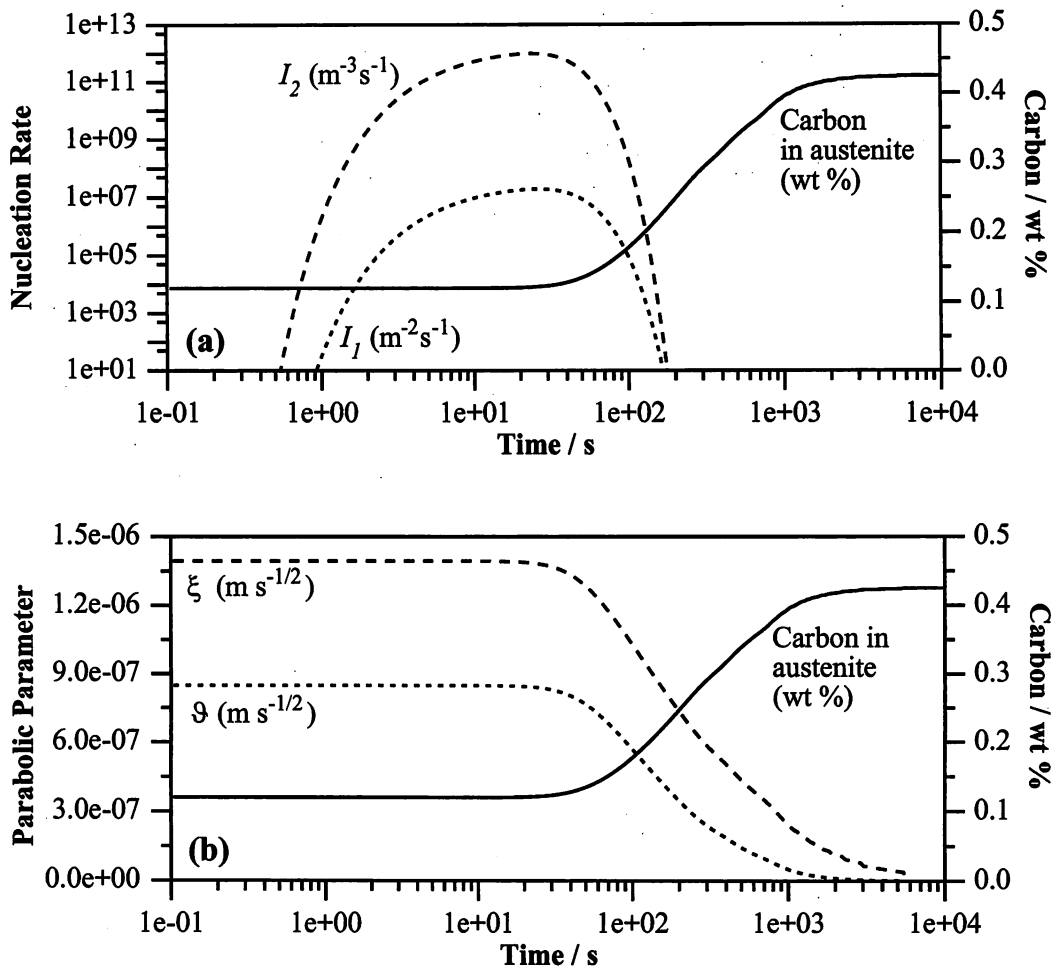
Figure 4.9 The predicted variation in nucleation and growth characteristics as a function of time at 720 °C in alloy c with an austenite grain size of 50 μm; (a) the nucleation rates of allotriomorphic (I_1) and idiomorphic ferrite (I_2). Note that to allow direct comparison between I_1 and I_2 then I_1 must be multiplied by 40000 m^{-1} (the austenite grain boundary area per unit volume); (b) the one-dimensional (ϑ) and three-dimensional (ξ) parabolic thickening parameters. The average carbon concentration in the untransformed austenite is also plotted.

Figure 4.9 Transformations in steel c with $d_\gamma = 50$ μm. (a) An increase in the carbon concentration from 0.12 to 0.18 wt %; (b) an increase in the manganese concentration from 1.5 to 1.7 wt %; (c) a decrease in the transformation temperature from 720 to 700 °C. These graphs should be compared with Figure 4.7b.

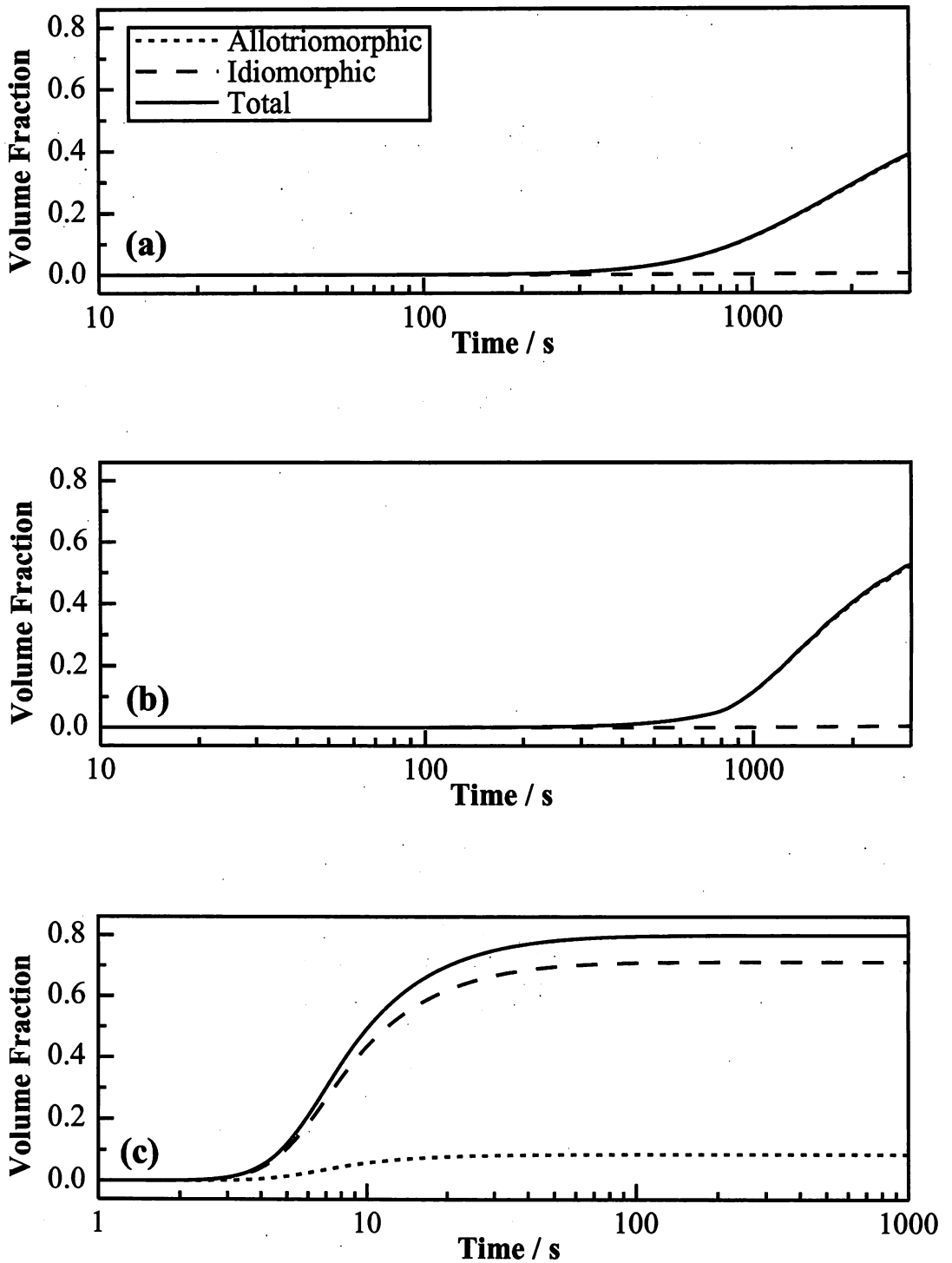The formation of allotriomorphic ferrite occurs during two different stages. Discrete particles first nucleate along the grain boundaries and eventually impinge to form a continuous layer which decorates the boundaries. Consequently, if nucleation is *limited* to the boundaries, then the overall rate of transformation is greatly reduced when these discrete particles impinge to form a continuous layer. This occurs due to two reasons. Firstly, this continuous layer saturates the austenite grain boundary and thereby prevents further nucleation. Only those extended particles which were nucleated prior to site saturation can contribute to the real volume fraction. Secondly, for discrete particles, the carbon diffuses in all directions but after impingement the problem is reduced to slower one-dimensional diffusion normal to the layer.

This is illustrated in the calculated time–temperature–transformation (TTT) curve for reconstructive transformation (allotriomorphic and idiomorphic ferrite) in two model steels (Fe–0.1C–0.4Si–1.0Mn wt %), as illustrated in Figure 4.10a. Steel *e* contains no inclusions, whilst steel *f* contains a dense population of non-metallic inclusions. The parameters used to calculate these TTT curves are given in Table 4.2. In steel *e* the time interval to achieve 10 % allotriomorphic ferrite is much smaller than that to achieve 30 % transformation (bearing in mind the logarithmic time scale). This is because transformation slows down once the austenite grain boundaries are completely decorated with allotriomorphic ferrite. The situation changes dramatically when intragranular nucleation sites in the form of non-metallic inclusions (steel *f*) are added (Figure 4.10b). The intragranular nucleation of idiomorphic ferrite continues over the full course of the transformation because the non-metallic inclusions are randomly distributed throughout the volume of the assembly. Therefore, all of the extended particles of idiomorphic ferrite that are nucleated during the course of the transformation can contribute to the real volume. Furthermore, these intragranularly nucleated ferrite particles grow more rapidly due to the three-dimensional diffusion of carbon in the austenite around them. Consequently, whilst the overall transformation rate is increased in a manner consistent with the greater density of nucleation sites, the later stages of transformation are greatly accelerated by contributions from intragranularly nucleated idiomorphic ferrite.
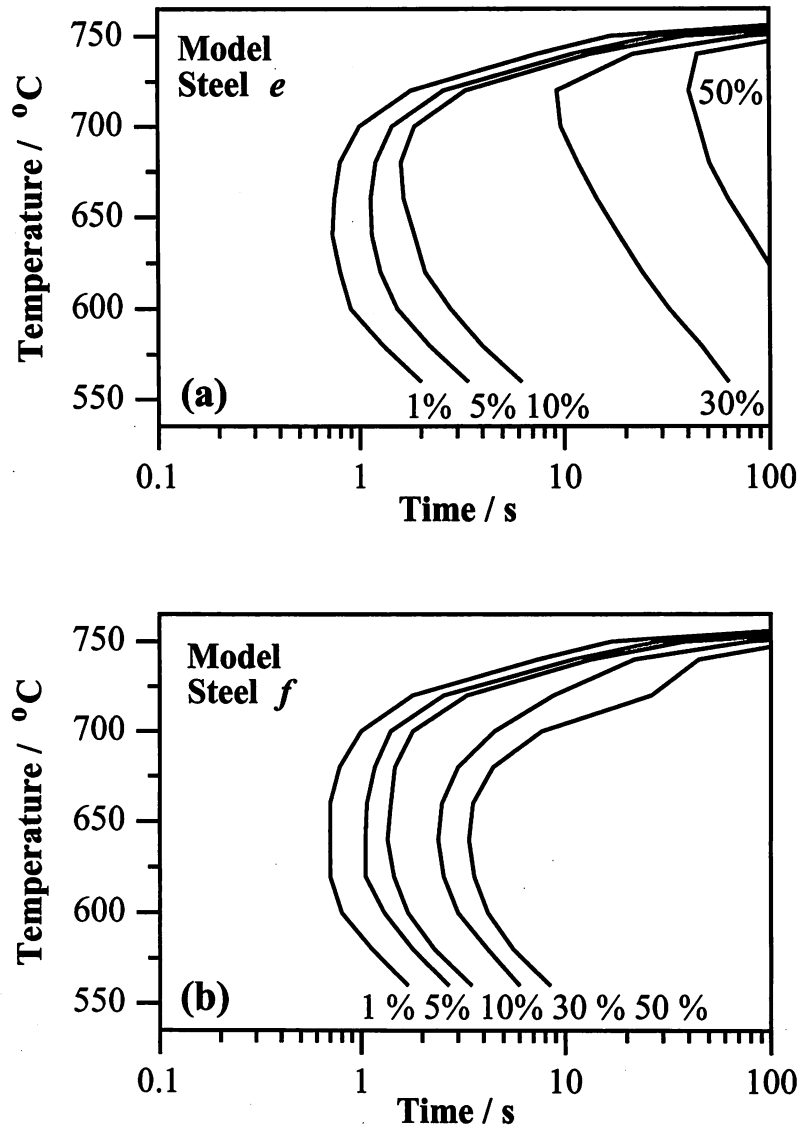
Figure 4.10 Transformation to reconstructive ferrite in two model steels (Fe–0.1C–0.4Si–1.0Mn wt %). (a) steel *e* - grain surface nucleation sites only, giving just allotriomorphic ferrite; (b) steel *f* - grain surface and intragranular nucleation sites, giving both allotriomorphic and idiomorphic ferrite.

4.3.5 Summary

An overall transformation kinetics model has been produced for dealing with the simultaneous and competitive formation of allotriomorphic and idiomorphic ferrite. It has been possible to reproduce experimentally observed trends in published data and the analysis gives insight into the competing effects of inter- and intra-granular nucleation sites. These methods could be used in the design of new steels. Furthermore, this approach can readily be extended to allow for the simultaneous inter- and intra-granular nucleation of a variety of phases, such as allotriomorphic ferrite, Widmanstätten ferrite, bainite and pearlite (section 4.4).

95

4.4 Simultaneous Formation of Multiple Phases

4.4.1 Introduction

Almost all commercial steels are produced using heat treatments in which the austenite cools continuously through the transformation temperature range. This usually leads to a final microstructure which is a mixture of many transformation products, because the austenite can decompose into a large variety of ferritic transformation products, each of which can form by a different mechanism. These reactions may overlap and interact with each other, either by 'hard'–impingement in which adjacent particles touch, or by 'soft'–impingement where their diffusion or thermal fields overlap (Christian, 1975). These interactions are known to be important in determining the final microstructure.

It follows that in order to model the development of microstructure, it is necessary to develop theory capable of handling *simultaneous*, interacting precipitation reactions. In particular, structural steels frequently have a microstructure consisting of allotriomorphic ferrite, Widmanstätten ferrite and pearlite. Although a great deal is known about allotriomorphic ferrite and pearlite, kinetic theory for Widmanstätten ferrite is rather limited. An understanding of Widmanstätten ferrite is important because it is a phase which greatly influences the mechanical properties of steels. There are many investigations which indicate that Widmanstätten ferrite can be detrimental to toughness (*e.g.* Bodnar and Hansen, 1994b). It tends to grow in packets of parallel plates across which cracks may propagate without much deviation.

Widmanstätten ferrite forms in a displacive transformation in which carbon partitions continuously into the austenite (section 1.3.2). The transformation is therefore a paraequilibrium displacive transformation with the growth rate controlled by the diffusion of carbon in the austenite ahead of the plate tip, after an appropriate allowance is made for the strain energy due to the IPS shape change (Bhadeshia, 1985). The nucleation mechanism of Widmanstätten ferrite is understood to the extent that it is possible to calculate the transformation start temperature (W_S) and the rate as a function of the undercooling below W_S (Bhadeshia, 1981; Rees and Bhadeshia, 1994). It should therefore be possible to estimate the overall transformation kinetics as a function of the steel composition and heat treatment. It is emphasised that Widmanstätten ferrite rarely occurs in isolation. It is usually preceded by the formation of allotriomorphic ferrite at the austenite grain surfaces and there may be other transformations such as pearlite which compete for the untransformed austenite (Bodnar and Hansen, 1994a). Consequently the nucleation and growth rates of allotriomorphic ferrite, Widmanstätten ferrite and pearlite may change with the progress of the transformation as the composition of

the austenite and/or the temperature changes. This complexity necessitates the use of numerical methods (section 2.3) which are amenable to changes in the boundary conditions during transformation (Saito and Shiga, 1992; Anelli *et al.*, 1991; Umemoto *et al.*, 1992).

This section outlines work (Appendix One) which uses the theory described in section 4.2 to model multiple reactions during the continuous cooling of low-alloy wrought steels, so that a plot of the fraction of each phase can be obtained as a function of time. The phases allotriomorphic ferrite, Widmanstätten ferrite and pearlite are identified by setting the phase index as $j = 1, 2$, or 3 respectively; these subscripts are also used in identifying the nucleation and growth rates of the phases concerned.

4.4.2 Allotriomorphic Ferrite

Classical nucleation theory is again used to model the nucleation of allotriomorphic ferrite, with the grain boundary nucleation rate I_1 per unit area given by equation 4.30. However, the fitted constants used in this section are $C_a = 1.21 \times 10^{12}\,\mathrm{m}^{-2}$ and $C_b = 5.58$. The nucleation and growth of allotriomorphic ferrite has been described by modelling the allotriomorphs as discs (Figure 4.11) having their faces parallel to the nucleating grain boundary plane, so that equations 4.20 through to 4.29 apply.
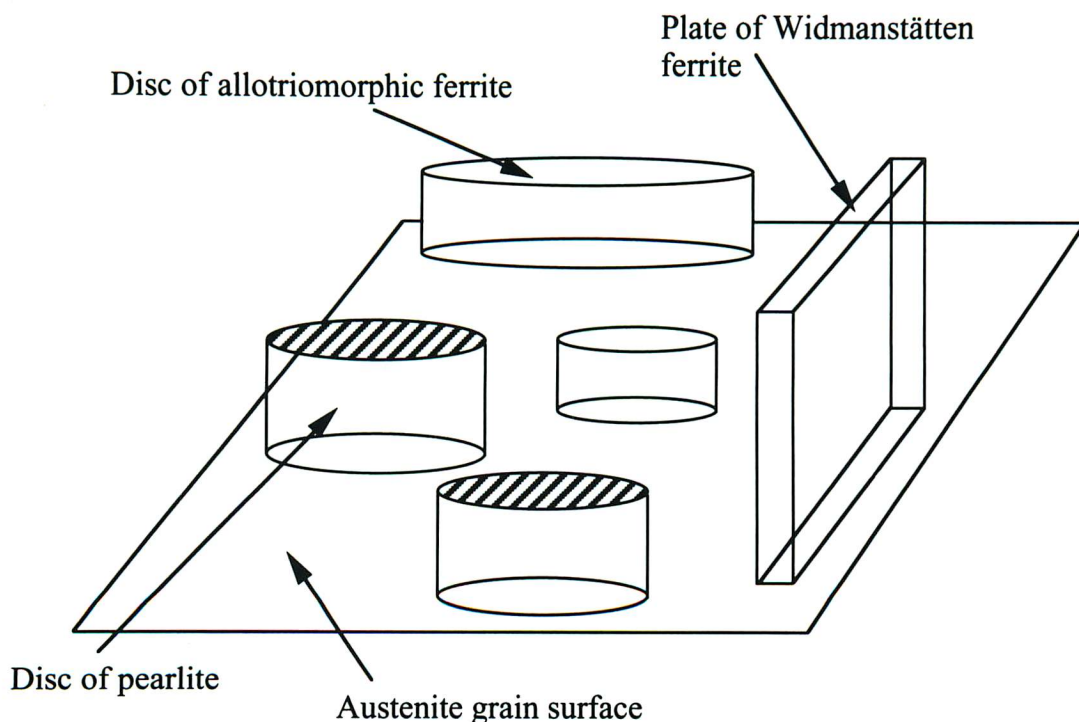
Figure 4.11 Illustration of the morphologies used to model the various boundary nucleated phases that form in low-alloy wrought steels.

4.4.3 Widmanstätten Ferrite

There is fine detail in *TTT* diagrams, but they consist essentially of two C-curves (Figure 4.12). One of these represents reconstructive transformations at elevated temperatures where atoms are mobile within the time scale of the usual experiments on steels. The lower temperature C-curve represents displacive transformations such as Widmanstätten ferrite and bainite.
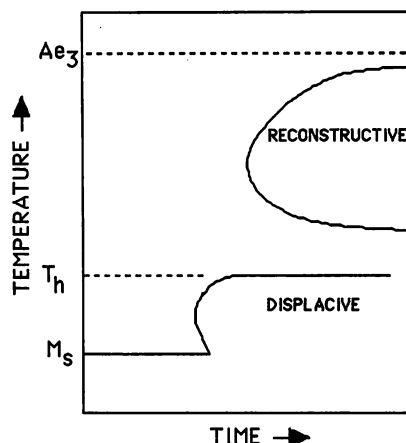
Figure 4.12 Schematic TTT diagram illustrating the two C-curves and the T_h temperature.

The lower C-curve has a flat top; the temperature corresponding to this flat top is identified as T_h, the highest temperature at which displacive transformation occurs during isothermal heat treatment. T_h is either the Widmanstätten ferrite start (W_S) or bainite start (B_S) temperature depending on the thermodynamic driving force available at T_h for the steel concerned.

Figure 4.13 shows two plots; the first is a calculation of the driving force for the paraequilibrium nucleation of ferrite at T_h, allowing carbon to partition between the austenite and ferrite. The second is the case where there is no partitioning at all during the nucleation of ferrite. It is evident that the nucleation of Widmanstätten ferrite or bainite cannot in general occur without the partitioning of carbon. The second interesting point is that the curve illustrated in Figure 4.13a is linear. This straight line, which represents all steels, is henceforth called the *universal G_N function* and is given by:

$$G_N = 3.637(T - 273.18) - 2540 \qquad (\mathrm{J\,mol^{-1}}) \qquad (4.35)$$

with G_N giving the minimum free energy change necessary to nucleate Widmanstätten ferrite or bainite in any steel (Bhadeshia, 1981).

As discussed elsewhere (Bhadeshia, 1981), a linear relation such as this cannot be explained by nucleation based on heterophase fluctuations. Consider a classical nucleation rate
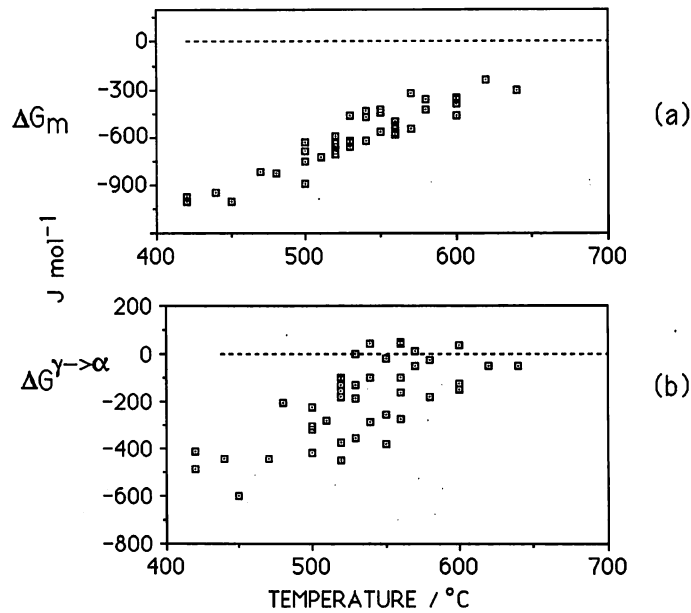
Figure 4.13 Curves representing the free energy change necessary in order to obtain a detectable degree of transformation to Widmanstätten ferrite or bainite (Bhadeshia, 1981). Note that each point represents a different steel. (a) The free energy change assuming paraequilibrium nucleation. (b) The free energy change assuming partitionless nucleation.

I equation:

$$I \propto \nu \exp\left(-G^*/kT\right) \qquad (4.36)$$

where ν is an attempt frequency and all the other terms have their usual meanings. When this is rearranged, the following equation is obtained:

$$-G^* \propto \beta T \qquad (4.37)$$

where $\beta = k \ln\{I/\nu\}$. Consequently, the G_N versus T relation can only be linear if $G^* \propto G_N$ and not the inverse square relationship implied by classical nucleation theory. This is entirely consistent with the theory for martensitic nucleation (Olson and Cohen, 1970).

What then are the conditions which determine whether at T_h, it is Widmanstätten ferrite that forms first or bainite? In order for a phase to form, it must nucleate and grow. Nucleation will occur at T_h when the maximum possible driving force for nucleation becomes less than G_N (*i.e* $\Delta G_m \leq G_N$). The nucleated phase can develop into Widmanstätten ferrite if a further condition is satisfied, that the driving force for paraequilibrium growth exceeds the stored energy of Widmanstätten ferrite, which amounts to about 50 J mol^{-1} (Bhadeshia, 1981). Note, if the driving force for diffusionless growth exceeds 400 J mol^{-1} then bainite forms in place of Widmanstätten ferrite.

For the theory presented here, the nucleation rate per unit area of boundary for Widmanstätten ferrite (phase 2) is given by:

$$I_2 = \frac{1}{2A_a} \exp\left[-\frac{A_b}{RT} - \frac{A_b \Delta G_m}{A_c RT}\right] \tag{4.38}$$

where $A_a = 6.78 \times 10^{-10}\,\mathrm{m^2 s}$, $A_b = 2.065 \times 10^4\,\mathrm{J\,mol^{-1}}$ and $A_c = 2540\,\mathrm{J\,mol^{-1}}$, all of which are constants determined by fitting to experimental data (Rees and Bhadeshia, 1994). This equation applies below the Widmanstätten ferrite start temperature.

Trivedi (1970) has given a solution for the problem of the diffusion controlled growth of plates. The shape of the plates is taken to be that of a parabolic cylinder and is assumed to remain constant throughout growth. The steady-state plate lengthening rate V_2 at a temperature T is obtained by solving:

$$\Omega = (\pi p)^{1/2} \exp\{p\}\mathrm{erfc}\{p^{1/2}\}[1 + (r_c/r)\Omega S_2\{p\}] \tag{4.39}$$

where the Péclet number p, which is a dimensionless velocity, is given by $p = V_2 r/2\underline{D}$, the weighted-average diffusion coefficient for carbon in austenite is used as before (equation 4.28), but with the integral evaluated over the range $\bar{x}$ to x_r, where x_r is the carbon concentration in the austenite at the plate tip. x_r may significantly differ from the equilibrium carbon concentration $x^{\gamma\alpha}$ because of the Gibbs-Thomson capillarity effect (Christian, 1975) which allows for the change in equilibrium concentration as a function of interface curvature; x_r decreases as interface curvature increases, and growth ceases at a critical plate tip radius r_c when $x_r = \bar{x}$. For a finite plate tip radius r:

$$x_r = x^{\gamma\alpha}[1 + (\Gamma/r)] \tag{4.40}$$

where Γ is the capillarity constant (Christian, 1975) given by:

$$\Gamma = \frac{\sigma V_m}{RT} \frac{(1 - x^{\gamma\alpha})/(x^{\alpha\gamma} - x^{\gamma\alpha})}{1 + [d(\ln \Gamma_C)/d(\ln x^{\gamma\alpha})]} \tag{4.41}$$

where σ is the interface energy per unit area, taken to be $0.2\,\mathrm{J\,m^{-2}}$, Γ_C is the activity coefficient of carbon in austenite, and V_m is the molar volume of ferrite. Note that for Widmanstätten ferrite, the paraequilibrium concentrations (*e.g.* $x^{\gamma\alpha}$) are calculated after allowing for the $50\,\mathrm{J\,mol^{-1}}$ of stored energy (Bhadeshia, 1981).

This approach assumes that the ferrite composition is unaffected by capillarity, since $x^{\alpha\gamma}$ is always very small. r_c can be obtained by setting $x_r = \bar{x}$. The function $S_2\{p\}$ depends on the Péclet number; it corrects for variation in composition due to changing curvature along the

interface and has been numerically evaluated by Trivedi (1970). Consistent with experimental data the Zener hypothesis has been assumed, whereby the plate tip adopts a radius which is consistent with the maximum possible rate of growth (Christian, 1975).

For the purposes of modelling the transformation kinetics, the plates of Widmanstätten ferrite were represented as tetragonal prisms (Figure 4.11), the longest dimension of which is given by $q_2 = V_2(t - \tau)$ during unhindered isothermal growth. For non-isothermal transformation:

$$q_{2,(m+1)\Delta t} = q_{2,m\Delta t} + V_2 \Delta t \tag{4.42}$$

The rate of change of area of intersection on a test plane at a distance y from the austenite grain boundary is therefore:

$$A_{2,k,y} = 2\eta_2 V_2^2 (m\Delta t - k\Delta \tau) \qquad (q_{2,(m+1)\Delta t} > y) \tag{4.43}$$

$$A_{2,k,y} = \left(\eta_2 q_{2,(m+1)\Delta t}^2\right) / \Delta t \qquad (q_{2,(m+1)\Delta t} = y) \tag{4.44}$$

$$A_{2,k,y} = 0 \qquad (q_{2,(m+1)\Delta t} < y) \tag{4.45}$$

where η_2 is the ratio of the length to the thickness of the Widmanstätten ferrite plate, taken to be 0.02. Since the plates grow by displacive transformation, they can only grow into one of the adjacent austenite grains, so that the change in the extended volume (ΔV_2^e) is given directly by equation 4.15.[2]

4.4.4 Pearlite

Pearlitic transformation was assumed to begin when the carbon concentration in the untransformed austenite reached the A_{cm} phase boundary. The nucleation of pearlite is treated as for allotriomorphic ferrite but with a nucleation rate which is two orders of magnitude smaller. This is achieved by reducing the number density of nucleation sites. The growth of pearlite was approximated to occur by a paraequilibrium mechanism, although it never in practice grows in this way. It is also assumed that the majority of diffusion occurs in the austenite just ahead of the transformation front. In these circumstances, the growth rate is given by (Hillert, 1957):

$$V_3 = \frac{D}{g} \frac{s^2}{s_\alpha s_\theta} \frac{x^{\gamma\alpha} - x^{\gamma\theta}}{x^{\theta\gamma} - x^{\alpha\gamma}} \frac{1}{s} \left(1 - \frac{s_C}{s}\right) \tag{4.46}$$

where θ represents cementite, α the ferrite within the pearlite and γ the austenite. g is a geometric factor equal to 0.72 in plain carbon steels, s is the interlamellar spacing, whose critical value at which growth stops is s_C and s_α, s_θ are the respective thickness of ferrite and

cementite lamellae. The values of s and s_C are estimated empirically (Takahashi, 1992) and it is assumed that s adopts a value consistent with the maximum possible rate of growth.

Like allotriomorphic ferrite, pearlite growth occurs by a reconstructive mechanism and is not restricted by the presence of a grain boundary. The shape of a pearlite colony (Figure 4.11) is taken to be that of a disc (aspect ratio $\eta_3 = 1$) of half-thickness:

$$q_3 = V_3(t - \tau) \qquad \text{so that,} \qquad q_{3,(m+1)\Delta t} = q_{3,m\Delta t} + V_3\Delta t \qquad (4.47)$$

The rate of change of area of intersection on a test plane located at a distance y is given by:

$$A_{3,k,y} = 2\pi\eta_3^2 V_3^2(m\Delta t - k\Delta\tau) \qquad (q_{3,(m+1)\Delta t} > y) \qquad (4.48)$$

$$A_{3,k,y} = \left(\pi\eta_3^2 q_{3,(m+1)\Delta t}^2\right)/\Delta t \qquad (q_{3,(m+1)\Delta t} = y) \qquad (4.49)$$

$$A_{3,k,y} = 0 \qquad (q_{3,(m+1)\Delta t} < y) \qquad (4.50)$$

Since pearlite nodules may grow into either of the adjacent austenite grains, ΔV_3^e is obtained from equation 4.26.[2]

4.4.5 Results and Discussion

There have been many studies about the occurrence of Widmanstätten ferrite in steels as a function of the chemical composition, austenite grain size and the cooling rate during continuous cooling transformation (Mehl *et al.*, 1933; Bodnar and Hansen, 1994a; Aaronson *et al.*, 1989; Krahe *et al.*, 1972). It is consequently well established that Widmanstätten ferrite is favoured in austenite with a large grain structure. This is probably because Widmanstätten ferrite is rarely found in isolation but often forms as secondary plates growing from allotriomorphic ferrite layers. The prior formation of allotriomorphic ferrite, which is favoured by a *small* grain size, enriches the untransformed residual austenite with carbon and reduces the volume fraction of residual austenite which can subsequently transform into Widmanstätten ferrite, so it is not surprising that a small austenite grain size suppresses Widmanstätten ferrite. For the same reasons, an increase in the cooling rate will tend to favour the formation of Widmanstätten ferrite.

These and other concepts are implicitly built into the model presented here. This is because allotriomorphic ferrite, Widmanstätten ferrite and pearlite are allowed to grow together assuming that thermodynamic and kinetic conditions are satisfied. Their interactions are all

---

[2] The numerical models used to describe the transformation kinetics of Widmanstätten ferrite and pearlite were successfully tested using equivalent analytical theories for isothermal transformation which are documented in Appendix Six.

taken into account during the course of transformation. It follows that it should be possible to reproduce the excellent quantitative data recently published by Bodnar and Hansen (1994a). The present analysis is restricted to Fe–Si–Mn–C steel rather than the microalloyed steels also studied by Bodnar and Hansen. The chemical composition of the steel is given in Table 4.3. They used heat treatments which led to three different austenite grain sizes of 30, 55 and 100 μm. In addition, samples were cooled at five different rates; 11, 16, 30, 59 and 100 $^\circ$C min^{-1}.

Widmanstätten ferrite can nucleate directly from the austenite grain surfaces or indirectly from allotriomorphic ferrite-austenite interfaces. The present model includes both of these scenarios because of an approximation made in the formulation of extended area in equation 4.11. It is strictly not possible to separate out the contributions ΔO_j^e from each phase (for all values of y) when the phases grow at different rates. The result of this approximation is therefore to allow Widmanstätten ferrite to form even if the entire austenite grain surface is decorated with allotriomorphic ferrite. This is approximately equivalent to the secondary nucleation of Widmanstätten ferrite and pearlite on allotriomorphic ferrite.[3]

C	Si	Mn	Cu	V
0.18	0.18	1.15	0.09	< 0.003
P	S	Nb	Al	N
0.015	0.030	< 0.005	0.026	0.0073

Table 4.3 Chemical composition (wt %) of the Fe–Si–Mn–C steel used by Bodnar and Hansen (1994a).

The reasonable overall level of agreement between experiment and theory is illustrated in Figure 4.14, for all of the data from Bodnar and Hansen (1994a). In all cases where the allotriomorphic ferrite content is under estimated, the Widmanstätten ferrite content is over estimated. This is expected both because the composition of the austenite changes when allotriomorphic ferrite forms and because its formation changes the amount of austenite that

---

[3] This approximation is reasonable if the growth rates of those phases which nucleate in a secondary fashion are relatively high compared to phases which nucleated directly on the grain surface during the early stages of transformation. However, it is possible to introduce a further approximation to deal with such cases. This involves determining the mean *extended* thickness h of an imaginary layer containing the total extended volume of all the phases which have formed by the time t. This thickness h is added to the extended length q_j of particles which are nucleated during the next time interval t to $t + dt$. Particle dimensions parallel to the nucleating plane are unaffected.
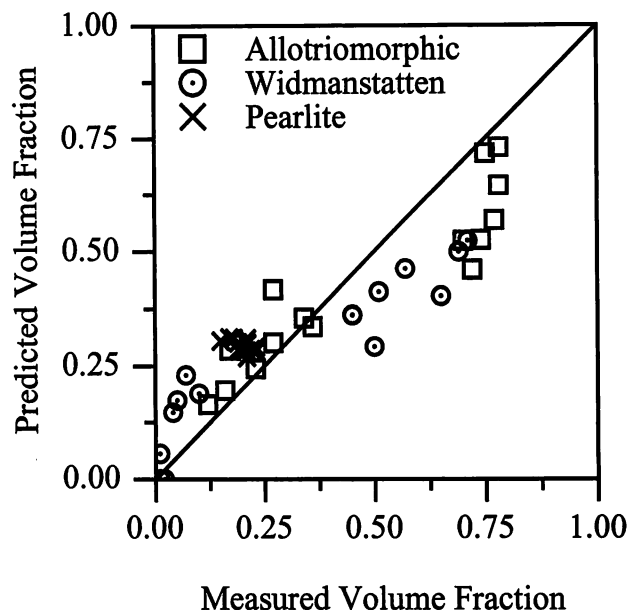
Figure 4.14 A comparison of the calculated volume fraction versus experimental data reported by Bodnar and Hansen (1994a).

is free to transform to Widmanstätten ferrite.

4.4.6 Microstructure Maps

Figure 4.15 shows calculations which illustrate how the model can be used to study the evolution of microstructure as the sample cools. The calculations are for the steel composition stated in Table 4.3. All of the generally recognised metallurgical trends are reproduced. The amount of Widmanstätten ferrite clearly increases with the austenite grain size, and with the cooling rate within the range considered. Bodnar and Hansen (1994a) suggested that the effect of cooling rate on the amount of Widmanstätten ferrite formed was smaller than that of the austenite grain size (for the values considered). This is also evident in Figure 4.15.

The model also correctly predicts the influence of alloying elements such as carbon or manganese. At large cooling rates, Figure 4.16 shows that an increase in the carbon concentration reduces the amount of Widmanstätten ferrite; this is because of the reduction in the temperature at which the Widmanstätten ferrite first nucleates and also by suppressing its growth rate.[4] The suppression of transformation temperatures also reduces the concentration of carbon in the residual austenite at which the formation of pearlite begins, since the $\gamma/\gamma + \theta$ phase boundary has a positive slope on a plot of temperature versus carbon concentration.

---

[4] For an austenite grain size of 30 μm and a cooling rate of 101 °C min^{-1}, Widmanstätten ferrite formation is suppressed from 725 to 693 °C with the increase in carbon concentration. Similarly, the growth rate of Widmanstätten ferrite at 675 °C is reduced approximately by a factor of four with the increase in carbon concentration.

The fraction of pearlite is therefore increased in the microstructure.

The effect of carbon at the slower cooling rate is mainly to suppress the formation of allotriomorphic ferrite and hence to increase the proportion of pearlite (Figure 4.16). At the austenite grain size of 30 μm and a cooling rate of 11 °C min^{-1}, Widmanstätten ferrite is essentially absent at both the carbon concentrations studied. An increase in the concentration of manganese to 2 wt % (Figure 4.16) has a different effect because the effect on the pearlite transformation is less pronounced than carbon. Thus, the suppression of allotriomorphic ferrite permits a greater degree of transformation to Widmanstätten ferrite.
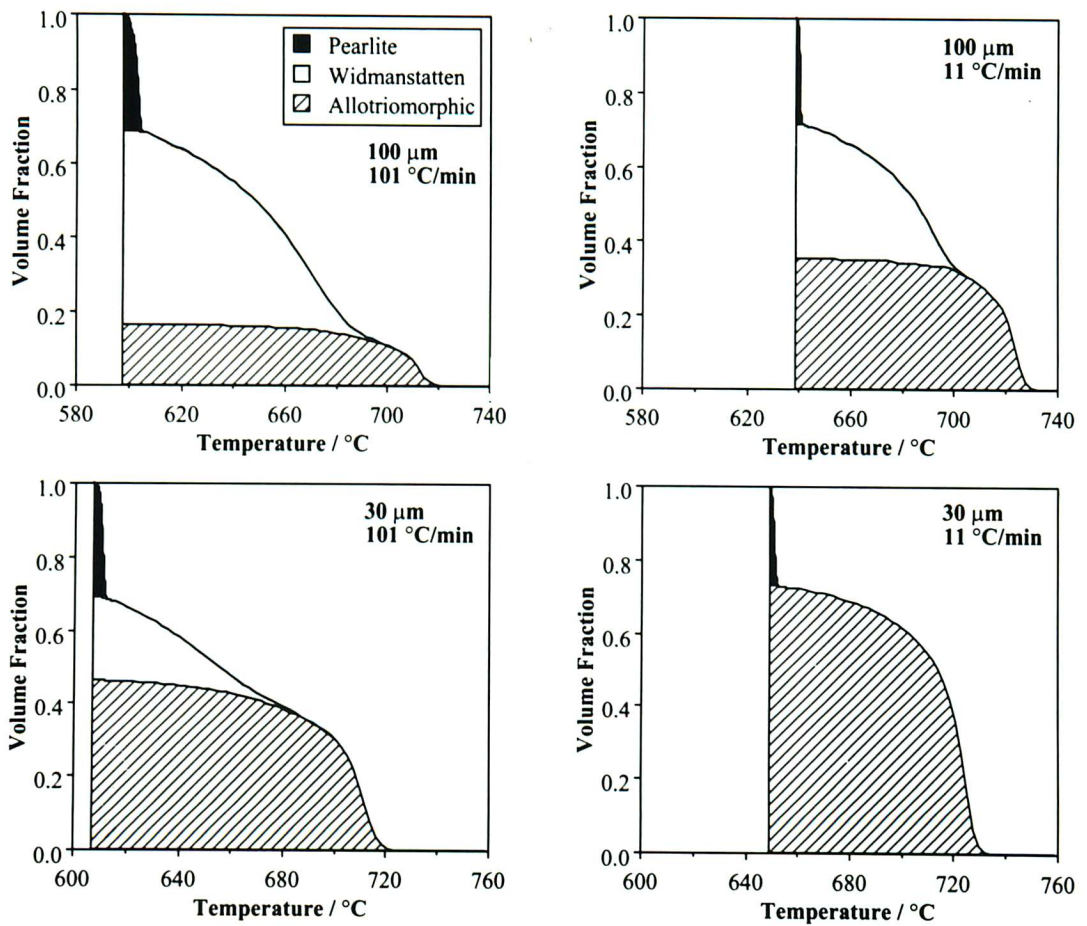
Figure 4.15   Calculated evolution of microstructure as a function of the austenite grain size and the cooling rate.

4.4.7 Summary

The Johnson–Mehl–Avrami theory for overall transformation kinetics has been success-
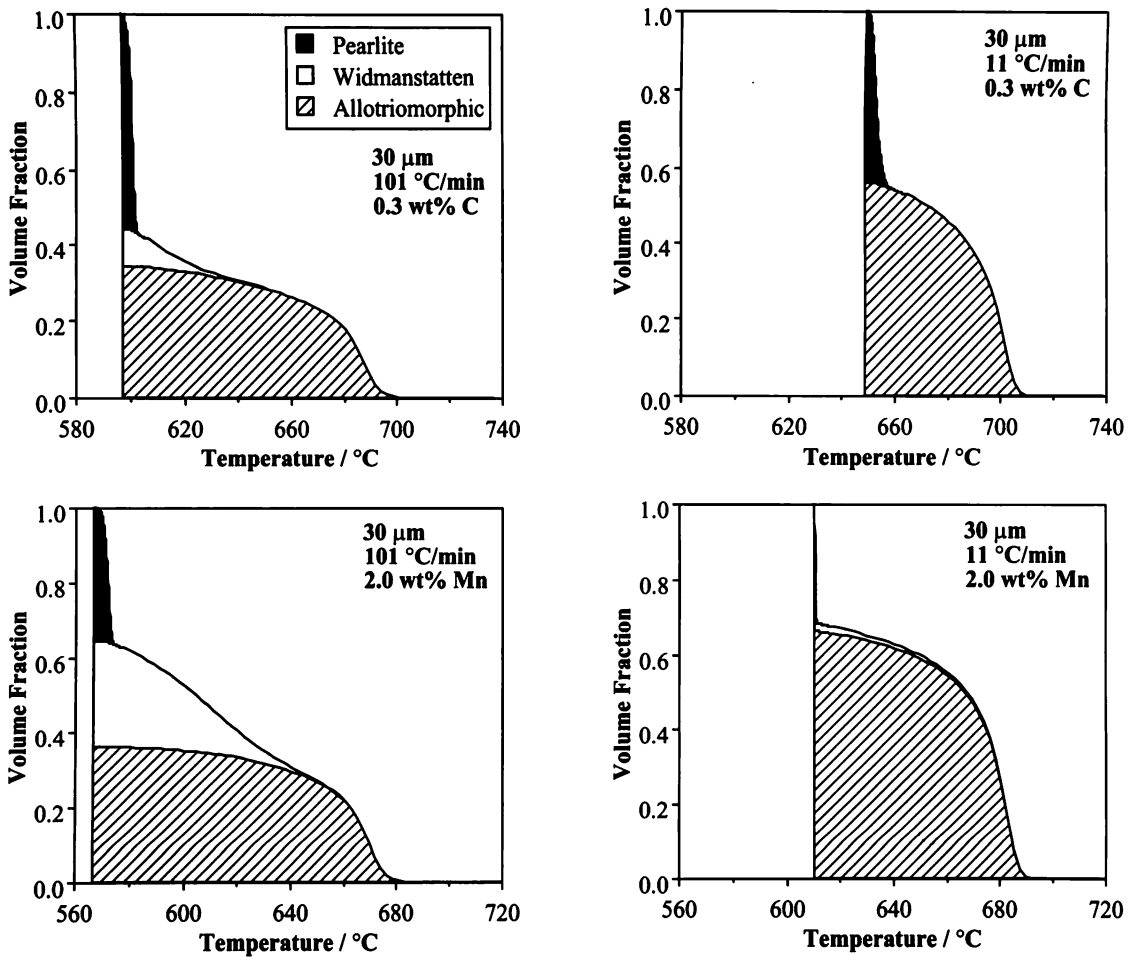
Figure 4.16   Calculated evolution of microstructure as a function of the austenite grain size and the cooling rate. The steel composition is as given in Table 4.3, but with the carbon or manganese concentrations increased as indicated.

fully adapted to deal with the simultaneous intergranular nucleation of allotriomorphic ferrite, Widmanstätten ferrite and pearlite. A comparison with published experimental data has shown that the model developed is reasonable both quantitatively and with respect to well established metallurgical trends. The model can now be used to study theoretically, the evolution of microstructure as a function of the alloy composition, the austenite grain size and the cooling conditions. Further work is need to include other phases such as bainite and martensite, and to allow nucleation at intragranular sites such as inclusions (section 4.3) or dislocations. In this way it should be possible to develop a 'complete' model to describe microstructural evolution in complex systems such as steel weld metals and thermomechanically processed steels.

CHAPTER FIVE

Modelling Inclusion Nucleation Potency

The ability of inclusions to act as heterogeneous nucleation sites for ferrite is investigated using models based upon classical nucleation theory. The effects of inclusion size, differential thermal contraction, chemical depletion of the austenite, lattice matching and boron segregation are assessed using a range of theoretical and semi-empirical methods. The results are then used to develop a simple model for calculating the TTT (time–temperature–transformation) curve of a weld metal from the known TTT curve of a reference wrought steel with a similar chemical composition.

5.1 Introduction

An astounding amount of research has been published on the ability of non-metallic inclusions to act as heterogeneous nucleation sites for ferrite (Chapter Three), primarily for weld metals but also for wrought steels. A number of qualitative correlations have emerged from this work indicating the role of crystallographic coincidence between the inclusion and matrix; incompatibilities in thermal properties between inclusions and steel; chemical reactions at the inclusion / matrix interface (section 3.2).

In spite of considerable advances in the understanding of inclusion effects, alloy design in practice remains extremely difficult. This is because of the large number of variables involved which introduce considerable non-linearities in conceptual models. The aim of this work was to express these models quantitatively into a framework capable of simultaneously accounting for the many interactions between inclusions and steel.

5.2 The Activation Energy Barrier to Nucleation on an Inclusion

Barritte (1982) developed a model for the heterogeneous activation energy of nucleation on a spherical inclusion, using classical theory. The essential details of this work are given in a paper by Ricks *et al.* (1981). Figure 5.1 reveals the geometry of the model which assumes that the interfacial tensions at the austenite–ferrite–inclusion triple point balance, so that the 'wetting' angle μ is 90°. A new model based on this original approach is therefore developed in which μ is determined by the relative magnitudes of the interfacial tensions at the austenite–ferrite–inclusion triple point.

This new model (Appendix Two) assumes that the inclusion is spherical with a radius I. The critical radius of curvature R of the ferrite nucleus is determined using classical nucleation theory (ignoring strain energy terms) as:

$$R = \frac{2\sigma_{\alpha\gamma}}{-\Delta G} \tag{5.1}$$

where $\sigma_{\alpha\gamma}$ is the interfacial energy of the incoherent ferrite-austenite surface per unit area and ΔG is the free energy change per unit volume driving the austenite to ferrite transformation (Christian, 1975).

Figure 5.2 illustrates the essential details of the model. The ferrite nucleus has a low-energy facet that is partially coherent with the austenite in order to reduce the energy barrier to nucleation. $\sigma_{\gamma I}$ is the energy of the austenite-inclusion interface per unit area, $\sigma_{\alpha I}$ is the energy of the ferrite-inclusion interface per unit area and $\varphi_{\alpha\gamma}$ is the interfacial energy of the ferrite-austenite facet per unit area. To determine the activation energy barrier to nucleation
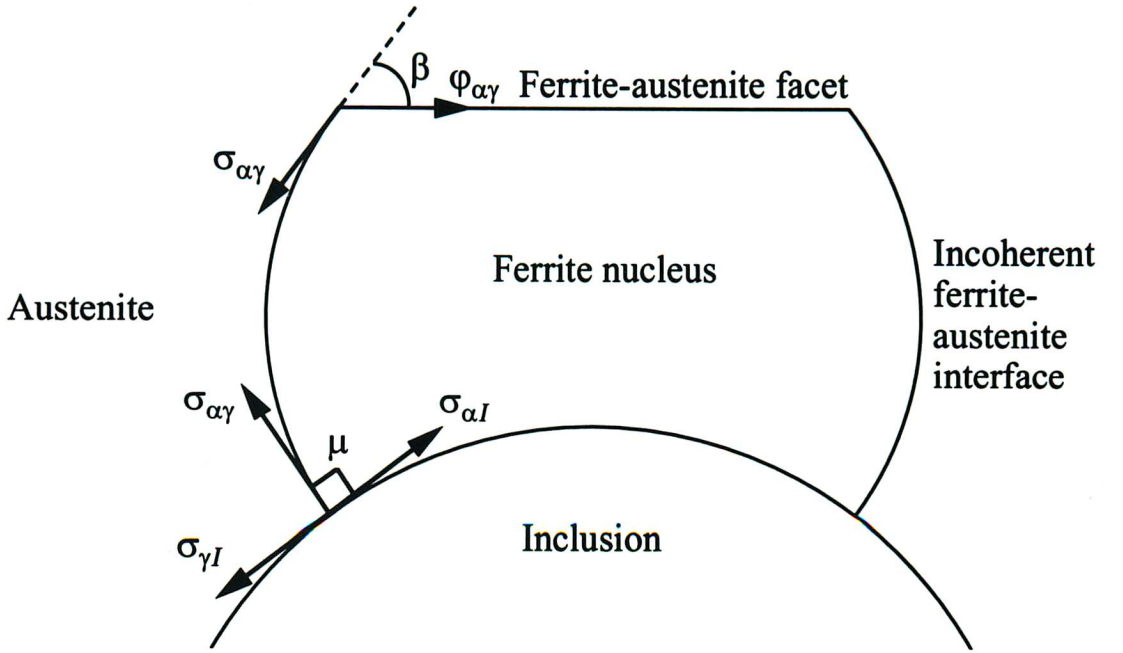
Figure 5.1 The nucleus geometry used by Barritte (1982) to model the heterogeneous activation energy barrier to nucleation on a spherical inclusion. $\sigma_{\gamma I}$ is the energy of the austenite-inclusion interface per unit area, $\sigma_{\alpha I}$ is the energy of the ferrite-inclusion interface per unit area, $\sigma_{\alpha\gamma}$ is the interfacial energy of the incoherent ferrite-austenite surface per unit area and $\varphi_{\alpha\gamma}$ is the interfacial energy of the ferrite-austenite facet per unit area.

requires a description of the nucleus geometry (Figure 5.3). The angle μ is calculated from the balance of the interfacial energies along the tangent to the inclusion surface at the austenite–ferrite–inclusion triple point:

$$\mu = \cos^{-1}\left(\frac{\sigma_{\gamma I} - \sigma_{\alpha I}}{\sigma_{\alpha\gamma}}\right) \tag{5.2}$$

The angle β between the low-energy facet and the tangent to the ferrite nucleus at the edge between the faceted and unfaceted ferrite-austenite interfaces is obtained by considering the Wulff construction which defines the shape of the critical nucleus in relation to the ratio of these interfacial energies (Johnson *et al.*, 1975):

$$\beta = \cos^{-1}\left(\frac{\varphi_{\alpha\gamma}}{\sigma_{\alpha\gamma}}\right) \tag{5.3}$$

The separation (Figure 5.3) between the centre of the inclusion and the centre of the ferrite nucleus (real or imaginary) is $z = \sqrt{R^2 + I^2 - 2RI\cos\mu}$.

The angles δ and θ (Figure 5.3) are also required. These are obtained using the following

conditional procedure:

$$\text{If } R \leq I, \qquad \delta = \sin^{-1}\left(\frac{R\sin\mu}{z}\right) \qquad \text{and,} \qquad \theta = 180° - \mu - \delta \qquad (5.4)$$

$$\text{If } R > I, \qquad \theta = \sin^{-1}\left(\frac{I\sin\mu}{z}\right) \qquad \text{and,} \qquad \delta = 180° - \mu - \theta \qquad (5.5)$$

Note that the nucleus model is only geometrically valid if the ferrite-austenite facet does not intersect the inclusion surface (Figure 5.3). Intersection occurs if $x \leq y$:

$$x = R(1 + \cos\theta) - I(1 - \cos\delta) \qquad \text{and,} \qquad y = R(1 - \cos\beta) \qquad (5.6)$$
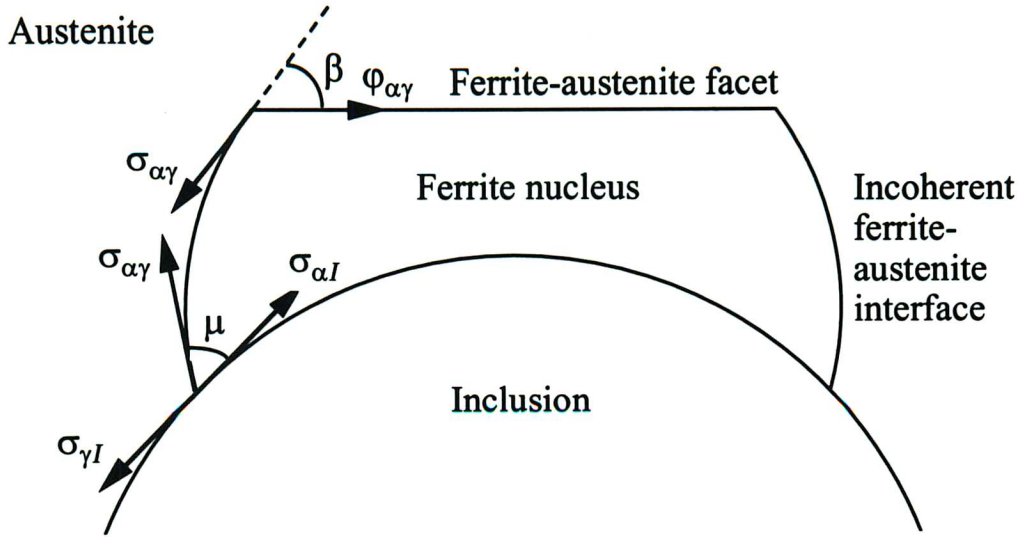
Figure 5.2   The nucleus geometry and interfacial energy terms used to calculate the heterogeneous activation energy barrier to nucleation of ferrite on a spherical inclusion.

It is necessary to define various volumes and surface areas as:

V_s = volume of a spherical nucleus of radius R.

V_{c1} = volume lost due to the sectioning of the nucleus by the inclusion.

V_{c2} = volume lost due to intrusion into the nucleus by the inclusion.

V_{c3} = volume lost due to the formation of a low-energy facet.

A_s = surface area of a spherical nucleus of radius R.

A_{c1} = surface lost due to sectioning of the nucleus by the inclusion.

A_{c2} = inclusion surface area covered by nucleus.

A_{c4} = curved surface lost due to the formation of a low-energy facet.

A_f = planar surface area of the low-energy facet.
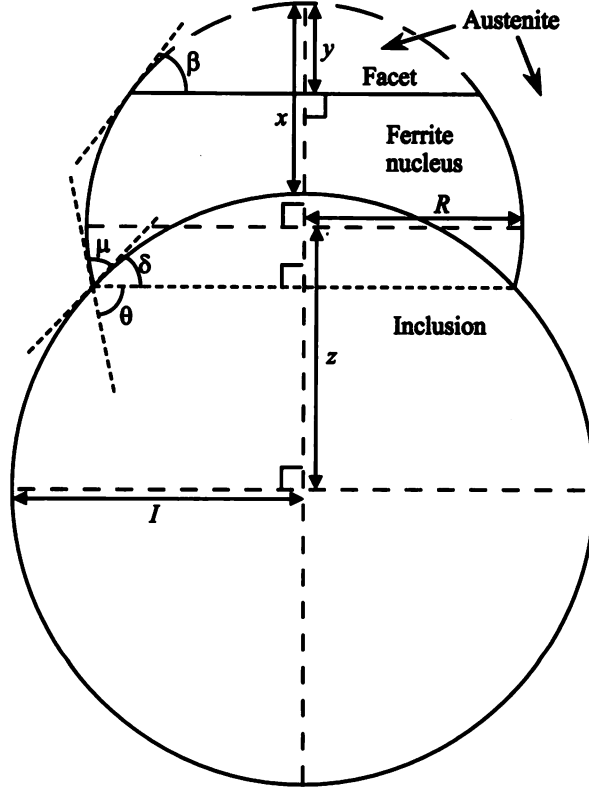
Figure 5.3 The geometry used to determine the heterogeneous activation energy barrier to nucleation of ferrite on a spherical inclusion.

These are obtained via:

$$V_s = \frac{4}{3}\pi R^3 \tag{5.7}$$

$$V_{c1} = \frac{1}{3}\pi R^3 f(\theta) \tag{5.8}$$

$$V_{c2} = \frac{1}{3}\pi I^3 f(\delta) \tag{5.9}$$

$$V_{c3} = \frac{1}{3}\pi R^3 f(\beta) \tag{5.10}$$

$$A_s = 4\pi R^2 \tag{5.11}$$

$$A_{c1} = 2\pi R^2 (1 - \cos\theta) \tag{5.12}$$

$$A_{c2} = 2\pi I^2 (1 - \cos\delta) \tag{5.13}$$

$$A_{c4} = 2\pi R^2 (1 - \cos\beta) \tag{5.14}$$

$$A_f = \pi R^2 (1 - \cos^2\beta) \tag{5.15}$$

where the functions $f(\theta)$, $f(\delta)$ and $f(\beta)$ are:

$$f(\theta) = 2 - 3\cos\theta + \cos^3\theta \qquad (5.16)$$

$$f(\delta) = 2 - 3\cos\delta + \cos^3\delta \qquad (5.17)$$

$$f(\beta) = 2 - 3\cos\beta + \cos^3\beta \qquad (5.18)$$

The activation energy barrier to nucleation at the inclusion is then:

$$G_i^* = \Delta G(V_s - V_{c1} - V_{c2} - V_{c3}) + \sigma_{\alpha\gamma}(A_s - A_{c1} - A_{c4}) + (\sigma_{\alpha I} - \sigma_{\gamma I})A_{c2} + \varphi_{\alpha\gamma}A_f \qquad (5.19)$$

Those terms relating to ΔG and $\sigma_{\gamma I}$ promote nucleation, whilst those terms relating to $\sigma_{\alpha\gamma}$, $\varphi_{\alpha\gamma}$ and $\sigma_{\alpha I}$ oppose nucleation. However, the interfacial energies also influence the nucleus-inclusion geometry and thus the activation energy barrier to nucleation. It is worth noting that this new model reduces to that suggested by Barritte (1982) if μ is 90°. Furthermore, if the inclusion radius I is very large relative to the nucleus radius R then the activation energy barrier predicted is identical to that for nucleation on a planar substrate.

5.3 Nucleation Mechanisms

Over the years various mechanisms have been suggested to explain the nucleation potency of non-metallic inclusions in steel weld deposits (section 3.2):

(1) *Inert Substrate* – the model described in section 5.2 is sensitive to the inclusion radius and the energy of the austenite-inclusion interface.

(2) *Localised Stresses* – the plastic strain due to differential thermal contraction introduces a stored energy which is added to the driving force for transformation.

(3) *Chemical Depletion* – the inclusion may change the composition of the surrounding austenite in a way which makes it more amenable to transformation.

(4) *Lattice Matching* – good epitaxy between the inclusion and ferrite may assist nucleation.

(5) *Boron Segregation* – the austenite-inclusion interfacial energy may be changed by the segregation of boron to the inclusion surface.

In the following discussion inclusion nucleation potency is numerically defined as $P = (1 - G_i^*/G_h^*)$, where G_h^* is the activation energy barrier for homogeneous nucleation and G_i^* is the corresponding term for heterogeneous nucleation on the inclusion. P tends to unity as the inclusion potency increases and serves as a normalised parameter for comparison purposes.

5.4 Inert Substrate

The carbon concentration of the ferrite nucleus was selected to give the maximum possible free energy change ΔG_m per unit volume on nucleation (*i.e.* $\Delta G = \Delta G_m$). This was performed using the parallel tangent construction (Bhadeshia, 1982b) for an alloy of composition 0.045C-1.47Mn-0.4Si (wt %). $\sigma_{\alpha\gamma}$, $\sigma_{\alpha I}$ and $\sigma_{\gamma I}$ were taken as 0.05, 0.06 and 0.07 J m^{-2} respectively, which is consistent with increased chemical interactions at both the ferrite-inclusion interface and the austenite-inclusion interface.

Figure 5.4 illustrates how inclusion potency P varies with inclusion radius and the undercooling below the Ae'_3 temperature (the highest temperature at which ferrite precipitates from austenite under paraequilibrium conditions). The Ae'_3 temperature in this alloy was estimated as 815 °C (Bhadeshia, 1982c). It is apparent that P is very sensitive to the inclusion radius at high temperatures when the undercooling is small. This variation is due to intrusion by the spherical inclusion into the ferrite nucleus. Consider a typical weld metal inclusion about 0.2 μm in radius. At 800 °C (*i.e.* a small undercooling below the Ae'_3 temperature) ΔG_m is small and the radius of curvature R of the ferrite nucleus is large (equation 5.1) relative to the inclusion radius I. The nucleus surface area to volume ratio is then forced to be large thus decreasing the potency P. By contrast at lower temperatures where the driving force for transformation is higher and $I >> R$ the potency P approaches that of a planar substrate.

To summarise, nucleation is most difficult at low ΔG_m. Consequently, the largest inclusions are the most effective nucleation sites, because they are associated with the smallest nucleus surface area to volume ratio. As the magnitude of ΔG_m increases, the sensitivity of the activation energy for nucleation to inclusion size decreases sharply. It follows that at temperatures close to B_S (the bainite start temperature), acicular ferrite will tend to nucleate on the larger inclusions.

5.5 Localised Stresses

It has been postulated that plastic deformation due to differential thermal contraction between an inclusion and the austenite may increase the driving force for the austenite to ferrite transformation. A portion of the plastic work done on the austenite near the inclusion surface will introduce dislocations, the remainder being dissipated as heat. The stored energy due to dislocations is assumed to assist nucleation.

There are many models of the elastic and plastic stresses and strains around misfitting spherical particles (Lee *et al.*, 1980; Earmme *et al.*, 1981; Brooksbank and Andrews, 1969; Dunand and Mortensen, 1991; Weatherly, 1968; Mott and Nabarro, 1940). Perhaps the most
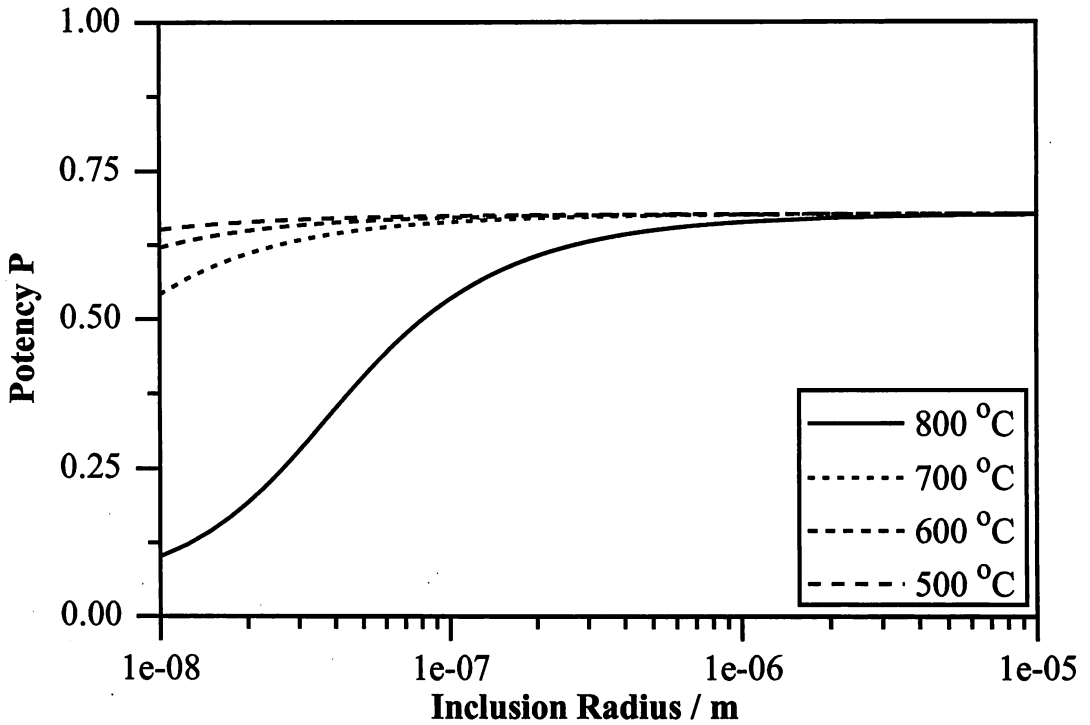
Figure 5.4 Calculated inclusion potency P as a function of inclusion radius I at four temperatures in a low-alloy steel.

complete model specifically concerned with misfit due to differential thermal contraction is by to Kim *et al.* (1990), who provided solutions for the principal circumferential and radial stresses and strains in both the inclusion and the matrix. Expressions describing the elastic and plastic components of the total strains in the plastic zone were also provided. Elasticity and continuum plasticity theories were used to model the elastic-plastic deformation in both the inclusion and the matrix, with the following assumptions:

(1) The inclusions are assumed to be spherical and uniformly distributed in the matrix.

(2) The inclusions are assumed to be homogeneous (in reality they are multiphase).

(3) It is assumed that work hardening is absent.

(4) Both the inclusion and the austenite are assumed to have isotropic elastic and thermal properties.

(5) The inclusion and matrix are assumed to be unstressed at an upper reference temperature which is taken as 1000 °C.

The plastic work done per unit volume for an element located at a distance r from the inclusion centre is given by:

$$w^p(r) = \frac{2(1 - 2\nu_m)\sigma_y^2}{E_m} \left[\left(\frac{r_p}{r} \right)^3 - 1 \right] \tag{5.20}$$

where:

ν_m= Poisson's ratio of the matrix.

σ_y= yield stress of the matrix.

E_m= Young's modulus of the matrix.

r_p= radius of the plastic zone.

r_p was obtained by solving the following equation iteratively using a root finding algorithm developed by Van Wijngaarden *et al.* (Press *et al.*, 1986):

$$2\sigma_y \log_e \left(\frac{r_p}{I}\right) - \frac{(\delta_m - \delta_i)\Delta T + \frac{1-\nu_m}{E_m}\left(\frac{r_p}{I}\right)^3}{\frac{1-2\nu_m}{E_m} - \frac{1-2\nu_i}{E_i}} = -\sigma_y \left[\frac{1+\nu_m}{3(1-2\nu_m)}\left(\frac{r_p}{\varpi}\right)^3 + \frac{2}{3}\right] \qquad (5.21)$$

where:

I= inclusion radius.

δ_m= coefficient of thermal expansion of the matrix.

δ_i= coefficient of thermal expansion of the inclusion.

ΔT= change in temperature (a decrease is negative).

ϖ= half of the inter-inclusion spacing (centre to centre).

ν_i= Poisson's ratio of the inclusion.

E_i= Young's modulus of the inclusion.

ϖ is obtained by numerically solving (Bansal and Ardell, 1972):

$$\varpi = I \left[1 + \frac{\exp(8f_i)}{6f_i^{1/3}} \int_{x=8f_i}^{\infty} \frac{dx}{x^{2/3}\exp(x)}\right] \qquad (5.22)$$

where f_i is the inclusion volume fraction, $x = f_i(R/r)^3$ and ϖ' represents any inter-inclusion spacing. Equation 5.22 is considered to be accurate for $f_i < 0.1$ (Kim *et al.*, 1990).

Thermal and mechanical property data necessary for the analysis were largely obtained from a paper by Brooksbank and Andrews (1972). In the present work, the elastic properties substituted for the inclusions were those for ambient temperatures. The austenite yield strength was taken at the mean temperature between 1000 °C and the temperature considered (henceforth termed the lower reference temperature).

The geometry of the ferrite nucleus model is complicated (Figure 5.5) so the nucleus is assumed to be contained within the plastic zone defined by r_p. The total plastic work done in the austenite that forms the potential ferrite nucleus is:

$$U_T = U_1 - U_2 \qquad (5.23)$$

where U_1 is the plastic work done in a volume defined by the ferrite-inclusion interface, the incoherent austenite-ferrite interface and the curved surface defined by the radius L which just contains all of the ferrite nucleus (Figure 5.5). It is apparent that U_1 over estimates U_T by an amount U_2 which represents the plastic work done in the volume defined by the coherent facet and the curved surface defined by L.
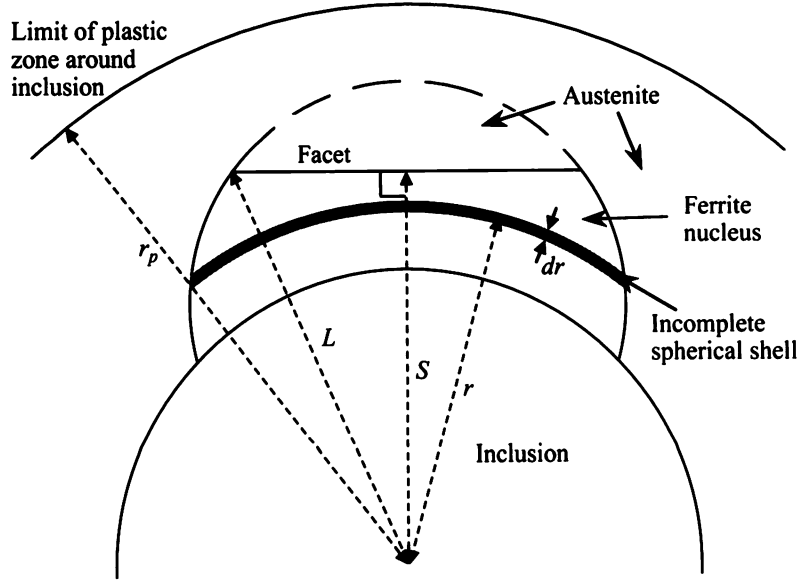
Figure 5.5 The ferrite nucleus in relation to the zone of plastic deformation in the austenite matrix due to differential thermal contraction between the inclusion and the matrix.

Imagine an incomplete elemental shell of thickness dr at the radius r (Figure 5.5). The plastic work done in the shell is $w^p(r) \, c(r) \, dr$ where $c(r)$ is the curved surface area of the shell. Adopting this approach U_1 may be obtained by integration using the function $c(r) = 2\pi r[2r - (r^2 + 2rz + z^2 - R^2)/2z]$:

$$U_1 = \int_{r=I}^{L} \left[4\pi r \frac{(1 - 2\nu_m)\sigma_y^2}{E_m} \left\{ 2r - \frac{r^2 + 2rz + z^2 - R^2}{2z} \right\} \left\{ \left(\frac{r_p}{r}\right)^3 - 1 \right\} \right] dr \qquad (5.24)$$

where the limiting radius (Figure 5.5) is $L = \sqrt{R^2 + z^2 + 2Rz\cos\beta}$. Integration yields:

$$U_1 = 4\pi \frac{(1 - 2\nu_m)\sigma_y^2}{E_m}$$

$$\times \left[\frac{r_p^3}{2} \left(2z \log_e |r| - r + \frac{z^2 - R^2}{r} \right) + \frac{r^2}{24}(3r^2 + 6z^2 - 8rz - 6R^2) \right]_I^L \qquad (5.25)$$

U_2 is calculated via a similar integration with the function $c(r) = 2\pi r[r - S]$ where $S =$

$z + R \cos \beta$ is the smallest radius that intersects the nucleus facet (Figure 5.5):

$$U_2 = \int_{r=S}^{L} \left[4\pi r(r - S) \frac{(1 - 2\nu_m)\sigma_y^2}{E_m} \left\{ \left(\frac{r_p}{r} \right)^3 - 1 \right\} \right] dr \qquad (5.26)$$

Integration yields:

$$U_2 = 4\pi \frac{(1 - 2\nu_m)\sigma_y^2}{E_m} \left[r_p^3 \left(\log_e |r| + \frac{S}{r} \right) + \frac{r^2}{6}(3S - 2r) \right]_S^L \qquad (5.27)$$

Therefore, the total plastic work done when the nucleus is entirely contained within the plastic zone defined by r_p is given by equation 5.23 as:

$$U_T = 4\pi \frac{(1 - 2\nu_m)\sigma_y^2}{E_m}$$
$$\times \left(\left[\frac{r_p^3}{2} \left(2z \log_e |r| - r + \frac{z^2 - R^2}{r} \right) + \frac{r^2}{24}(3r^2 + 6z^2 - 8rz - 6R^2) \right]_I^L \right.$$
$$\left. - \left[r_p^3 \left(\log_e |r| + \frac{S}{r} \right) + \frac{r^2}{6}(3S - 2r) \right]_S^L \right) \qquad (5.28)$$

It is now appropriate to remove the initial assumption that the ferrite nucleus lies completely within the plastic zone around the inclusion. Four possibilities exist which can be dealt with by modifying the limits due to integration that are present in equation 5.28 to produce:

$$U_T = 4\pi \frac{(1 - 2\nu_m)\sigma_y^2}{E_m}$$
$$\times \left(\left[\frac{r_p^3}{2} \left(2z \log_e |r| - r + \frac{z^2 - R^2}{r} \right) + \frac{r^2}{24}(3r^2 + 6z^2 - 8rz - 6R^2) \right]_I^A \right.$$
$$\left. - \left[r_p^3 \left(\log_e |r| + \frac{S}{r} \right) + \frac{r^2}{6}(3S - 2r) \right]_S^B \right) \qquad (5.29)$$

where the limits A and B are determined using the following conditional procedure:

(1) If $r_p = I$ then no integration is required because U_T is zero.

(2) If $r_p > I$ but $r_p \leq S$ then the surface defined by the plastic-elastic boundary lies below the nucleus facet and $A = r_p$ and $B = S$ (*i.e.* $U_2 = 0$).

(3) If $r_p > I$ and $r_p > S$ but $r_p < L$ then the surface defined by the plastic-elastic boundary intersects the nucleus facet so that $A = r_p$ and $B = r_p$.

(4) If $r_p > I$ and $r_p \geq L$ then the entire nucleus is contained within the plastic zone such that $A = L$ and $B = L$.

Only a small proportion of this total plastic work done will be stored in the austenite as lattice defects such as dislocations. A review by Titchener and Bever (1958) suggests that on

average approximately 15 % (± 10 %) of the mechanical energy expended during the plastic deformation (cold working) of ferritic steels is stored in the steel. The remainder is converted into heat energy. Assuming that recovery and recrystallisation during cooling do not alter this then the stored defect energy is $U_S \simeq 0.15 U_T$. This should increase the driving force for transformation such that the activation energy barrier to nucleation on the inclusion is found by rewriting equation 5.19 as:

$$G_i^* = \Delta G(V_s - V_{c1} - V_{c2} - V_{c3}) - U_S$$
$$+ \sigma_{\alpha\gamma}(A_s - A_{c1} - A_{c4}) + (\sigma_{\alpha I} - \sigma_{\gamma I})A_{c2} + \varphi_{\alpha\gamma}A_f \tag{5.30}$$

Since U_S influences the driving force for transformation, the critical radius of curvature of the nucleus depends on the extent of differential thermal contraction and is estimated as:

$$R = \frac{2\sigma_{\alpha\gamma}}{-\Delta G + U_S/(V_s - V_{c1} - V_{c2} - V_{c3})} \tag{5.31}$$

Consequently the activation energy barrier to nucleation is determined using a simple iterative procedure until convergence is attained.

Figure 5.6 shows the results for the phases listed in Table 5.1 as a function of temperature for an inclusion radius of 0.25 μm. The yield strength of austenite σ_y at a temperature $\widetilde{T}$ (K) midway between the upper and lower reference temperatures was estimated using an equation $\sigma_y = 10^6 \times [955.0 - 0.95(\widetilde{T} - 273.15)]$ (MPa) fitted to experimental data (between 1023 and 1223 K) given by Weiss *et al.* (1981). The thermal expansivity of austenite δ_m was measured to be 21.4 $\times 10^{-6}$ °C^{-1} for the alloy studied. At high temperatures the Poisson's ratio ν_m and the Young's modulus E_m of austenite were assumed to be 0.34 and 155 GPa respectively. Figure 5.6 suggests that even at very high temperatures differential thermal contraction has only a minor effect on inclusion nucleation potency. At lower temperatures the effect is negligible.[1]

Further calculations were carried out for γ-Al$_2$O$_3$ inclusions, 0.25 μm in radius, in a steel where $f_i = 0.003$. Figure 5.7 demonstrates the strong influence that both the thermal expansivity of the inclusion and the change in temperature during cooling have on the plastic work done in the austenite. A plastic zone exists even when there is a relatively minor mismatch in expansivity. The radius of the plastic zone is large compared to a ferrite nucleus (Figure 5.8). As Figure 5.9 illustrates, the plastic zone size increases with inclusion size, though its contribution to the already high nucleation potency P of large inclusions ($I = 2.0$ μm) was found to be insignificant.

---

[1] This result does not preclude the generation of arrays of dislocations which promote displacive nucleation in the close proximity of the inclusion (Rees and Bhadeshia, 1994).

Phase	δ_i $(\times 10^{-6}\ {}^\circ\mathrm{C}^{-1})$	E_i (GPa)	ν_i
$Al_2O_3.MnO$	8.0	271.0	0.26
$\gamma\text{-}Al_2O_3$	8.0	388.8	0.25
BN	3.8	150.0	0.19
$Cu_{1.8}S$	18.1	103.4	0.30
MnO	14.1	177.9	0.31
$\alpha\text{-}MnS$	18.1	103.4	0.30
TiN	9.4	317.2	0.19
TiO	16.0	177.9	0.31
$\beta\text{-}SiO_2$	3.0	75.8	0.16

Table 5.1   Thermal and mechanical property data for various inclusion phases; δ_i is the coefficient of thermal expansivity, E_i the Young's modulus and ν_i the Poisson's ratio. (Brooksbank and Andrews, 1972; Callister, 1991; Samsonov 1973). The properties of $Cu_{1.8}S$ were assumed to be identical to those of α-MnS and the mechanical properties of TiO were taken to be the same as those of MnO.
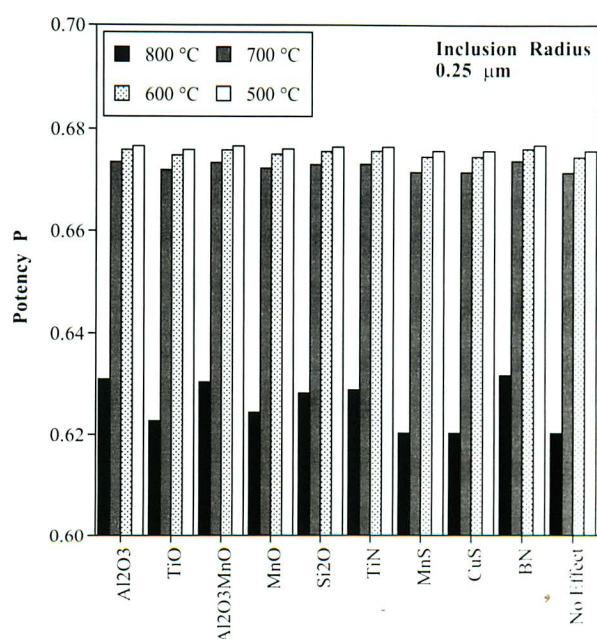
Figure 5.6   Calculated inclusion potency P as influenced by differential thermal contraction between various inclusion phases (Table 5.1) and the austenite matrix. The inclusions are 0.25 μm in radius.
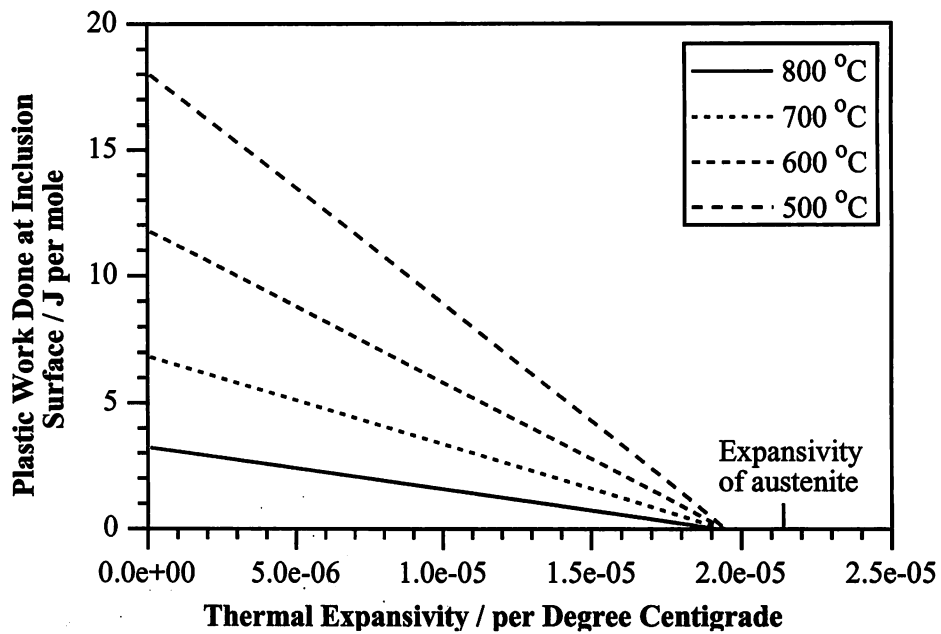
Figure 5.7   The effect of the thermal expansivity δ_i of the inclusion phase on the plastic work done per mole of austenite local to the inclusion surface. The graph illustrates data at four lower reference temperatures. The inclusions are 0.25 μm in radius with the mechanical properties of γ-Al$_2$O$_3$.
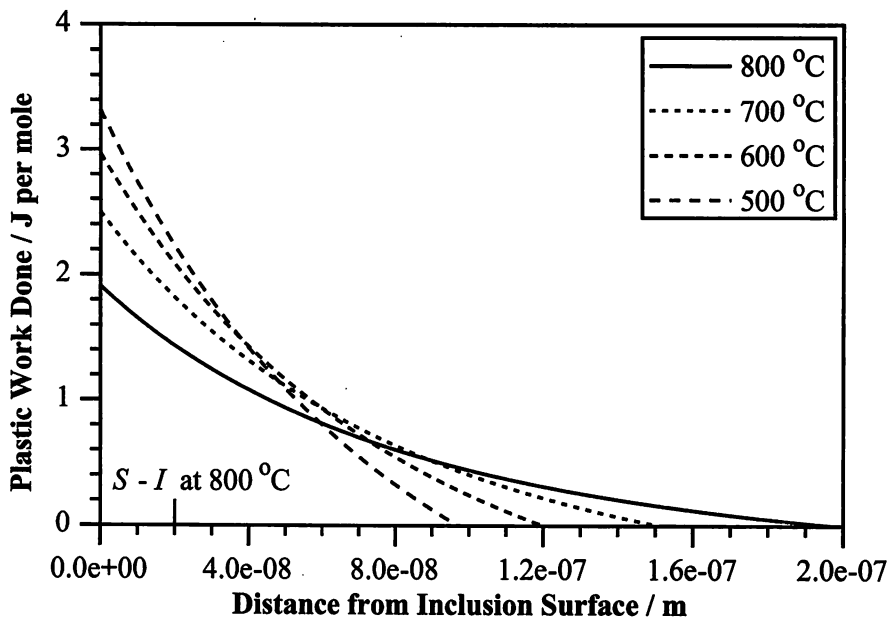
Figure 5.8   The variation of the plastic work done per mole of austenite as a function of the distance $(r - I)$ from a γ-Al$_2$O$_3$ inclusion $(I = 0.25 \ \mu$m$)$ surface. Data are illustrated at four lower reference temperatures. The curves overlap because σ_y is a function of the lower reference temperature. For comparison the size of the ferrite nucleus relative to the inclusion surface $(S - I)$ varies between 2×10^{-8} and 4×10^{-10} m at 800 and 500 °C respectively.
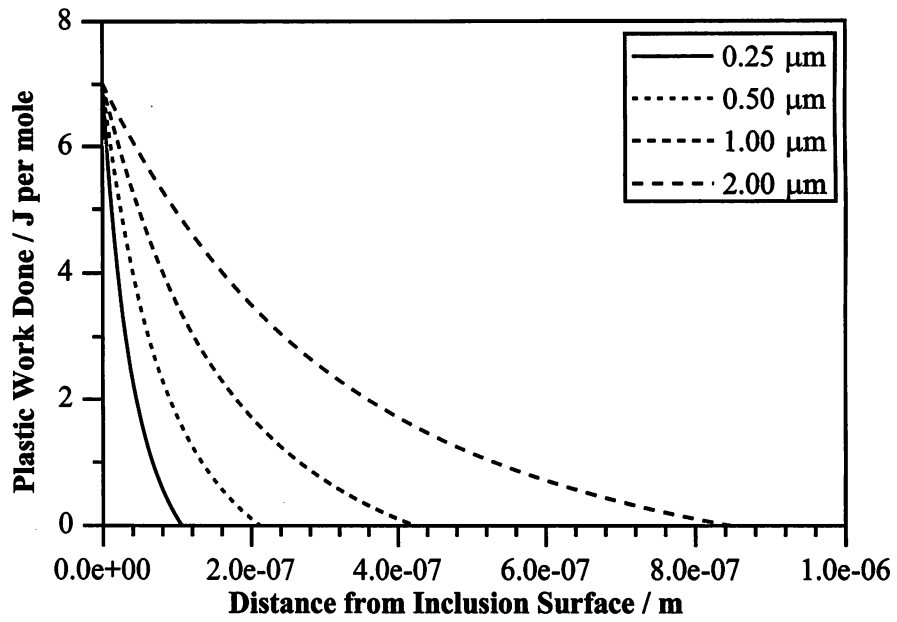
Figure 5.9 The variation of the plastic work done per mole of austenite as a function of the distance $(r - I)$ from a γ-Al_2O_3 inclusion ($I = 0.25$ μm) surface. Data are illustrated for four inclusion sizes (I). The lower reference temperature is 600 °C.

5.6 Chemical Depletion

Chemical changes in the austenite adjacent to an inclusion can change the driving force ΔG_m for nucleation; this change can be estimated (Bhadeshia, 1982c) using computed thermodynamics. The average composition of the alloy was again assumed to be 0.045C-1.47Mn-0.4Si (wt %) with an inclusion radius of 0.25 μm.

Figure 5.10 demonstrates the pronounced influence of carbon depletion (from 0.045 to 0.035 wt %) on P at low undercooling. The corresponding effect at greater undercoolings is far smaller because the driving force for nucleation in the undepleted alloy remote from the nucleating inclusions is also large. The effect of manganese depletion is shown in Figure 5.11. A reduction from 1.47 to 1.10 wt % raises the potency P from 0.62 to 0.94 at 800 °C. This strong effect reflects the influence of manganese upon alloy hardenability.

Calculations by Yamamoto *et al.* (1993) suggest that the precipitation of MnS reduces the Mn concentration of the austenite close to the precipitate surface by about a tenth (Figure 3.7). Figure 5.11 indicates that even this relatively modest degree of Mn depletion would significantly increase the inclusion nucleation potency P. Research by Gregg and Bhadeshia (1994b) indicates that various titanium oxides may deplete the Mn and C concentration in the local austenite. However, it is as yet not possible to calculate the level of this depletion.
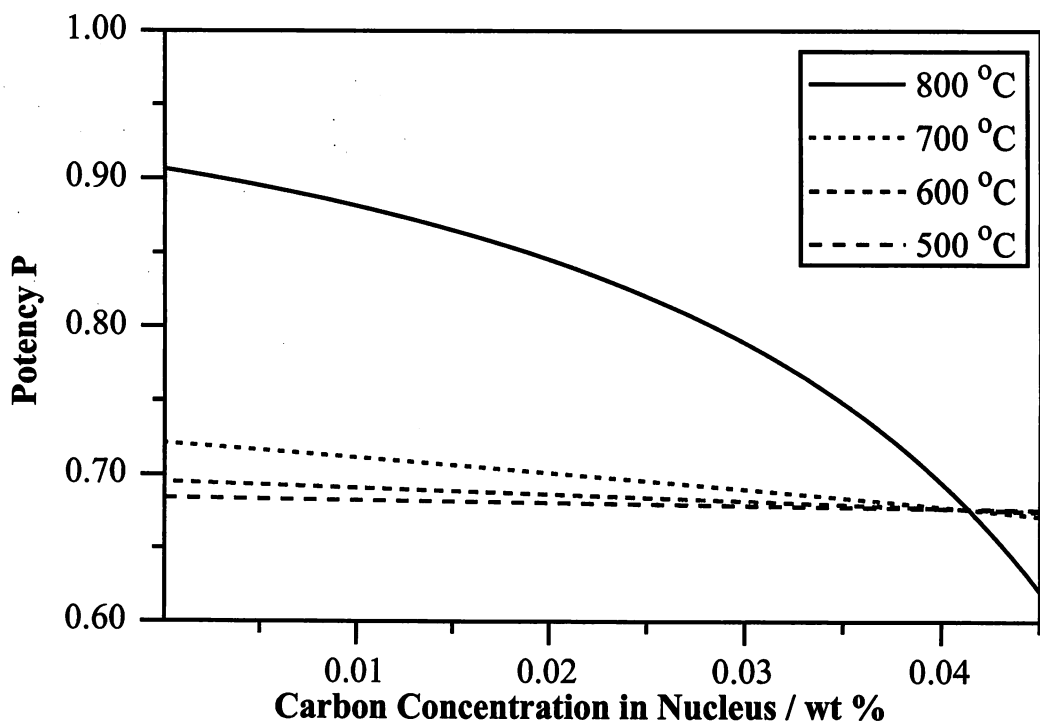
Figure 5.10   The variation of inclusion potency P with carbon depletion of the austenite local to the inclusion surface in an alloy with the bulk composition 0.045C-1.47Mn-0.4Si (wt %).
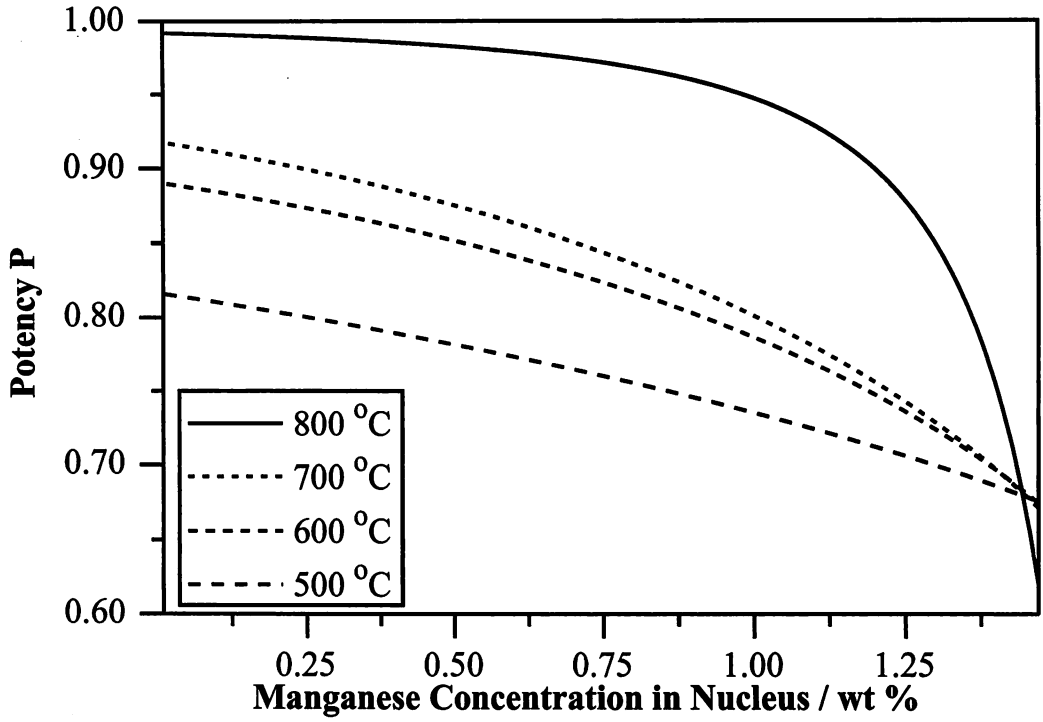
Figure 5.11 The variation of inclusion potency P with manganese depletion of the austenite local to the inclusion surface in an alloy with the bulk composition 0.045C-1.47Mn-0.4Si (wt %).

5.7 Lattice Matching

Epitaxy between the ferrite and inclusion reduces their interfacial energy and thus enhances nucleation efficacy. The effect on the activation energy of nucleation can be estimated by finding the optimum lattice match as a function of the inclusion phase. Bramfitt (1970) developed a model which allows lattice matching to be described in terms of a mean planar lattice disregistry between parallel planes:

$$\Pi_{(hkl)_n}^{(hkl)_s} = \sum_{i=1}^{3} \frac{1}{3} \left[\frac{d_{[uvw]_s^i} \cos \chi - d_{[uvw]_n^i}}{d_{[uvw]_n^i}} \right] \times 100 \ \% \tag{5.32}$$

This assumes a substrate (inclusion) faceted on a low-index plane $(hkl)_s$, and a nucleus (ferrite) that forms epitaxially with its low-index plane $(hkl)_n$ parallel to $(hkl)_s$ where:

$[uvw]_s^i = $ a low-index direction in $(hkl)_s$.

$[uvw]_n^i = $ a low-index direction in $(hkl)_n$.

$d[uvw]_s^i = $ the interatomic spacing along $[uvw]_s^i$.

$d[uvw]_n^i = $ the interatomic spacing along $[uvw]_n^i$.

$\chi = $ the angle between $[uvw]_s^i$ and $[uvw]_n^i$ (often zero).

Bramfitt suggested that the nucleus and substrate would be orientated to minimise the planar disregistry. Mills *et al.* (1987) used this approach to describe the solid-state austenite to ferrite

123

transformation in steel welds (Table 3.3). Their work is here extended over a wider range of orientations and inclusion phases.

A computer model was constructed to determine the optimum Π_m mean planar disregistries for various mineral phases. All possible planar parallelisms that can be generated using combinations of $\{100\}$, $\{110\}$ and $\{111\}$ planes, and $\langle 100 \rangle$, $\langle 110 \rangle$, $\langle 111 \rangle$ and $\langle 211 \rangle$ directions were considered. The model was first tested against the results of Mills *et al.* (1986). With the exception of BN, the results obtained were identical to those obtained by Mills *et al.* (Table 3.3). The planar disregistry of 7.5 % determined for BN agrees with that obtained by Mills *et al.* for the same planar parallelism *i.e.* $\{110\}_\alpha \parallel \{111\}_s < 100 >_\alpha \parallel < 110 >_s$. However, for $\{111\}_\alpha \parallel \{110\}_s < 110 >_\alpha \parallel < 100 >_s$ the disregistry calculated was 42.75 %, and not 6.5 % as found by Mills *et al.* A comprehensive set of results is presented in Table 5.2. It is apparent that many phases offer a very low planar disregistry with ferrite. It seems unlikely then that lattice matching can explain adequately the wide variations in inclusion potency found in practice.

The interfacial energy $\sigma_{\alpha I}$ was expressed as a simple function of Π_m to give $\sigma_{\alpha I} = m\Pi_m + c$ (J m^{-2}), where $m = 1.4 \times 10^{-3}$ is a constant which describes the variation in interfacial energy due to lattice disregistry and $c = 0.04$ describes those contributions due to chemical and topographical interactions. These chemical and topographical interactions are assumed here to be independent of the inclusion phase - an approximation which is unlikely to be realistic in practice.

5.8 Soluble Boron

Segregation of boron to the austenite grain boundaries reduces their interfacial energy and thus nucleation potency (section 3.4). The concentration of boron required to saturate the austenite grain surface depends on the grain size (Thewlis, 1994). Boron may also segregate to the austenite-inclusion interface thereby reducing the intragranular nucleation potency (Jones *et al.*, 1993). However, Yamamoto *et al.* (1993) found that boron is absorbed into cation vacancies in Ti_2O_3, and is therefore unlikely to affect the inclusion nucleation potency.

5.8.1 Soluble Boron Concentration

Bhadeshia and Svensson (1993) described a model to predict the amount of soluble boron present in a weld deposit from the total concentration. However, recent investigations have revealed that this iterative procedure does not work under all circumstances and is not required. A new analytical method (Appendix Four) is now described:

Table 5.2 Calculated minimum mean planar disregistries (II_m) between various phases (s) and ferrite (α). C (NaCl) indicates a face centred cubic (f.c.c.) lattice of the rock salt type, C (Spinel) indicates a f.c.c. lattice of the spinel type ($*$ is an idealised lattice) and C (ZnS) indicates a f.c.c. lattice of the zinc blende or sphalerite type. a_s is the lattice parameter of the phase s at ambient temperature. The data are due to Bramfitt (1969), Donnay (1963), Dowling et al. (1986), Mills et al. (1987) and Samsonov (1973).

Phase	Crystal System	a_s (nm)	Parallelisms	II_m (%)
CaS	C (NaCl)	0.5683	$\{111\}_\alpha \parallel \{111\}_s < 110 >_\alpha \parallel < 110 >_s$	0.87
VN	C (NaCl)	0.4090	$\{100\}_\alpha \parallel \{100\}_s < 100 >_\alpha \parallel < 110 >_s$	0.89
VO	C (NaCl)	0.4093	$\{100\}_\alpha \parallel \{100\}_s < 100 >_\alpha \parallel < 110 >_s$	0.97
$Al_2O_3.MnO$	C (Spinel)	0.8271	$\{100\}_\alpha \parallel \{100\}_s < 100 >_\alpha \parallel < 110 >_s$	2.01
TiO	C (NaCl)	0.4162	$\{100\}_\alpha \parallel \{100\}_s < 100 >_\alpha \parallel < 110 >_s$	2.67
$Cu_{1.8}S$	C (NaCl)	0.5570	$\{111\}_\alpha \parallel \{111\}_s < 110 >_\alpha \parallel < 110 >_s$	2.84
γ-Al_2O_3	C (Spinel*)	0.7850	$\{100\}_\alpha \parallel \{100\}_s < 100 >_\alpha \parallel < 110 >_s$	3.18
MgO	C (NaCl)	0.4200	$\{100\}_\alpha \parallel \{100\}_s < 100 >_\alpha \parallel < 110 >_s$	3.61
TiN	C (NaCl)	0.4240	$\{100\}_\alpha \parallel \{100\}_s < 100 >_\alpha \parallel < 110 >_s$	4.59
VC	C (NaCl)	0.4310	$\{100\}_\alpha \parallel \{100\}_s < 100 >_\alpha \parallel < 110 >_s$	6.32
$Fe_{(1-x)}O$	C (NaCl)	0.4312	$\{100\}_\alpha \parallel \{100\}_s < 100 >_\alpha \parallel < 110 >_s$	6.38
β-SiO_2	C (Spinel)	0.7032	$\{110\}_\alpha \parallel \{111\}_s < 100 >_\alpha \parallel < 110 >_s$	6.59
TiC	C (NaCl)	0.4328	$\{100\}_\alpha \parallel \{100\}_s < 100 >_\alpha \parallel < 110 >_s$	6.75
BN	C (ZnS)	0.3616	$\{110\}_\alpha \parallel \{111\}_s < 100 >_\alpha \parallel < 110 >_s$	7.54
SiC	C (ZnS)	0.4360	$\{100\}_\alpha \parallel \{100\}_s < 100 >_\alpha \parallel < 110 >_s$	7.54
NbC	C (NaCl)	0.4410	$\{100\}_\alpha \parallel \{100\}_s < 100 >_\alpha \parallel < 110 >_s$	8.79
α-MnS	C (NaCl)	0.5226	$\{111\}_\alpha \parallel \{111\}_s < 110 >_\alpha \parallel < 110 >_s$	8.84
MgS	C (NaCl)	0.5191	$\{111\}_\alpha \parallel \{111\}_s < 101 >_\alpha \parallel < 101 >_s$	9.45
MnO	C (NaCl)	0.4444	$\{100\}_\alpha \parallel \{100\}_s < 100 >_\alpha \parallel < 110 >_s$	9.62
ZrN	C (NaCl)	0.4560	$\{100\}_\alpha \parallel \{100\}_s < 100 >_\alpha \parallel < 110 >_s$	12.49
ZrC	C (NaCl)	0.4696	$\{100\}_\alpha \parallel \{100\}_s < 100 >_\alpha \parallel < 110 >_s$	15.84
CaO	C (NaCl)	0.4807	$\{111\}_\alpha \parallel \{111\}_s < 110 >_\alpha \parallel < 101 >_s$	16.14

(1) The residual N concentration after TiN formation is calculated using a model based on the methods of Kluken and Grong (1989).

(2) In the absence of B all of the residual N is assumed to enter solution and vice versa.

(3) When B and residual N are both present, then it is necessary to test whether or

not BN precipitates. The maximum possible soluble concentration of B if all of the residual N is dissolved is calculated using a solubility product; if the actual concentration of B is less than this value then all of the B is assumed to be in solution.

(4) The case where BN precipitates is determined using mass balance, stoichiometry and the solubility product as demonstrated below.

Mass balance requires that $B_T = B_S + B_{BN}$ and $N_T = N_S + N_{BN}$, where X_T is the total number of moles of species X per unit mass of steel, of which X_S is soluble and X_{BN} is precipitated. Stoichiometry dictates that $B_{BN} = N_{BN}$, so that:

$$B_T - B_S = N_T - N_S \tag{5.33}$$

The general form of a solubility product may be written as:

$$\log_{10}\left[(k_B B_S)(k_N N_S)\right] = C + \frac{D}{T} \tag{5.34}$$

where k_X is the constant used to convert the units of the species X from moles per unit mass of steel to wt %, C and D are the solubility parameters and T is the absolute temperature. Eliminating N_S from equations 5.33 and 5.34 reveals the soluble boron concentration:

$$B_S = \frac{(B_T - N_T) \pm \sqrt{(B_T - N_T)^2 + 4\frac{10^{C+(D/T)}}{k_N k_N}}}{2} \tag{5.35}$$

Figure 5.12 shows some calculated data for alloys containing 0.005 wt % N. Initially all of the B and N can be retained in solution. However, if the B concentration exceeds approximately 10^{-5} moles kg^{-1} then BN precipitation occurs and the amount of N in solution is reduced.

Unfortunately there is considerable variation in the published solubility products for BN in austenite. Table 5.3 gives the parameters C and D for various published solubility products. The solubility product is evaluated at 940 °C just above the Ae_3 temperature of pure iron.

Source	C	D
Fountain and Chipman (1962) - measured	5.24	-13970
Maitrepierre *et al.* (1979) - measured	0.20	-6700
Turkdogan (1989) - calculated	4.00	-11690

Table 5.3   Published solubility parameters (equation 5.34) for the solubility product of BN in austenite.
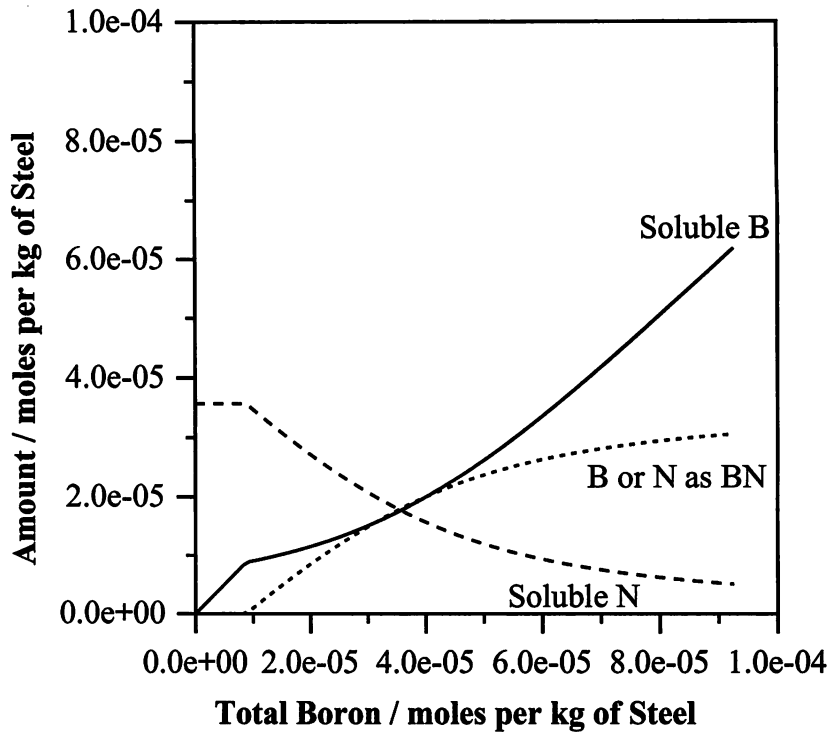
Figure 5.12 BN precipitation in alloys containing 0.005 wt % N ($\simeq 3.6 \times 10^{-5}$ moles of N per kg of steel), according to the solubility product of Maitrepierre *et al.* (1979) given in Table 5.3

Measured soluble boron concentrations were given by Thewlis (1994) for a series of Al-Ti deoxidised weld deposits, and by Mori *et al.* (1980) for Ti deoxidised weld deposits. The aluminium content was not stated by Mori *et al.* and was assumed to be zero. Their data were found to compare reasonably well with the theory described (Figure 5.13), the best results were obtained using the solubility product due to Maitrepierre *et al.*

5.8.2 Non-equilibrium Boron Segregation

During the welding thermal cycle boron nitrides and borocarbides in the steel will rapidly dissolve in the austenite matrix, dramatically raising the soluble boron concentration. These boron atoms will tend to associate with lattice vacancies to form boron-vacancy complexes. The equilibrium vacancy concentration decreases during cooling by the elimination of excess vacancies at 'sinks' in the austenite. This adjustment results in a net flow of the associated boron atoms to the austenite grain surface, inclusion surface and impurity atoms because the diffusivity of boron-vacancy complexes is significantly greater than that of the isolated boron atoms and vacancies at all temperatures. However, this 'non-equilibrium' segregation (Westbrook and Aust, 1963) will only be maintained if the isolated boron atoms cannot diffuse quickly enough to eliminate it (Williams *et al.*, 1976). Consequently the degree of boron segregation is greatest at intermediate cooling rates ($\simeq 10\ ^{\circ}\text{C s}^{-1}$) which maximises the extent
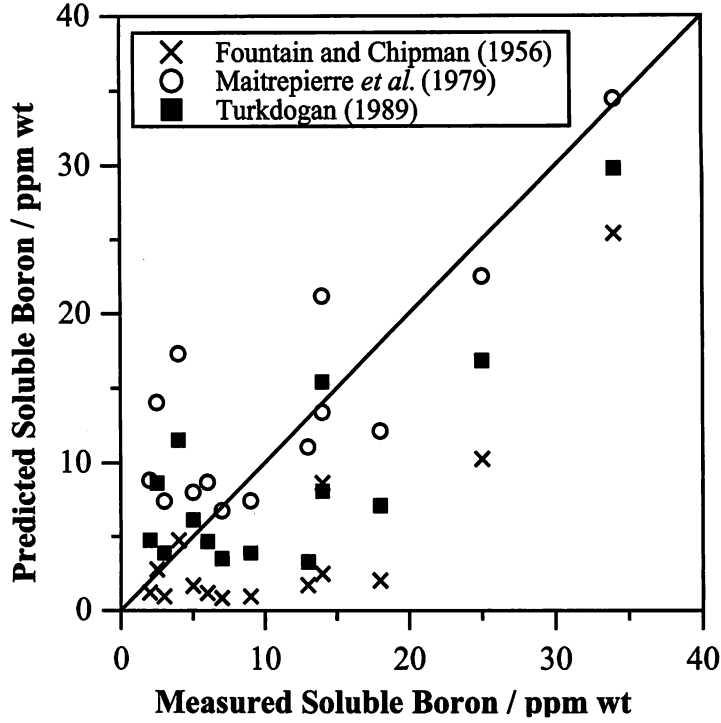
Figure 5.13 Predicted soluble boron concentration (using the three solubility products for BN given in Table 5.3) versus measured soluble boron concentration.

of the 'non-equilibrium' segregation boron-vacancy complexes to the grain boundaries, but minimises the 'equilibrium' segregation of isolated boron atoms (in excess of the equilibrium boundary concentration) away from the boundary region (Karlsson et al., 1988).

Grong (1994) used the work of Williams et al. to estimate the concentration of boron-vacancy complexes as:

$$B_v = B_s \left[m \exp \left(\frac{-E_f + E_b}{RT} \right) \right] = B_s \left[48 \exp \left(\frac{-86850 \ (\text{J mole}^{-1})}{RT} \right) \right] \qquad (5.36)$$

where B_s is the total soluble boron concentration (ppm wt), m contains various geometrical and entropy terms, E_f is the vacancy formation energy, E_b is the vacancy-boron binding energy, R is the universal gas constant (J mole^{-1}) and T is the absolute temperature. Assuming that the cooling rate is not so rapid ($\leq$ 50 °C s^{-1}) as to prevent significant boron-vacancy complex diffusion, the amount of boron B_g which should segregate during cooling, from the temperature T_p of austenite formation to the temperature T_a just above the Ae_3 temperature of pure iron, is obtained as:

$$B_g = [B_v]_{T_p} - [B_v]_{T_a} \simeq B_s \left[48 \exp \left(\frac{-86850 \ (\text{J mole}^{-1})}{RT_a} \right) \right] \qquad (5.37)$$

If T_p and T_a are assumed to be 1390 and 940 °C respectively then equation 5.37 suggests that approximately 8 % of the total soluble boron concentration should segregate to interfaces in the steel during cooling.

5.8.3 Saturation of the Austenite Grain and Inclusion Surfaces with Boron

A sharp reduction in the interfacial energy of an austenite grain boundary occurs when boron is first added to steel (Figure 5.14), but the effect then saturates when the coverage is equivalent to about 0.6 of a monolayer (Mortimer, 1973 and 1974). The surface area available for segregation depends on the austenite grain size, the inclusion volume fraction and the mean inclusion size. The amount of boron B^* (expressed in ppm wt with reference to the bulk alloy composition) required to segregate to the austenite grain and inclusion surfaces so as to achieve a coverage equivalent to 0.6 of a monolayer is:

$$B^*(\text{ppm wt}) \simeq \frac{1.2 \times 10^6 \, m_B (S_V + S_I)}{a_\gamma^2 \rho_{\text{Fe}}} \simeq 2.23 \times 10^{-5}(S_V + S_I) \qquad (5.38)$$

where m_B is the mass of a boron atom (kg), S_V the austenite grain surface area per unit volume (m^{-1}), S_I the inclusion surface area per unit volume (m^{-1}), a_γ the lattice parameter of austenite (m) and ρ_{Fe} the density of steel (kg m^{-3}). For $S_V + S_I$ between 30000 and 60000 m^{-1}, the concentration of segregated boron required to saturate the austenite grain and inclusion surfaces is estimated as 0.7 to 1.4 ppm wt. This approach can be validated using the results (Table 5.4) of Thewlis (1994).
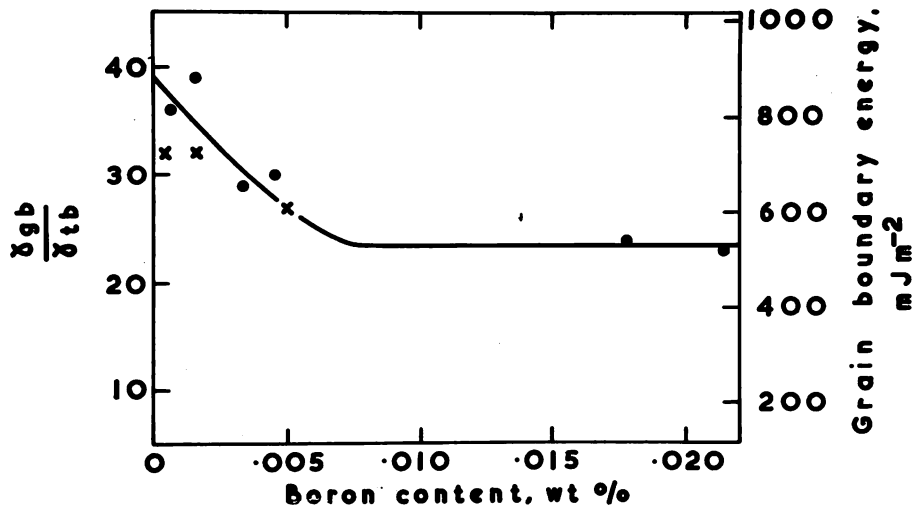
Figure 5.14 Grain boundary energies in iron-boron alloys at 1050 °C (Mortimer, 1974).

The welds studied by Thewlis contained an inclusion volume fraction f_i of approximately 0.003 and the mean inclusion diameter d_i was 0.45×10^{-6} m. The lattice parameter of austenite was taken as 0.357×10^{-9} m and the density of austenite as 7800 kg m^{-3}. Reheated weld metals were used which have an equiaxed grain structure, so $S_V(\text{m}^{-1}) \simeq 2/\bar{L}_{tn}(\text{m})$, where

Austenite Grain Size $\overline{L}_{tn}$ (μm)	30	120	170
Measured Total Soluble B (ppm wt)	22	16	14
Measured Acicular Ferrite (volume fraction)	0.90	0.90	0.86
Calculated Segregated B (ppm wt)	1.76	1.28	1.12

Table 5.4 The measured total concentration of soluble boron required to saturate the austenite grain surface (Thewlis, 1994). The percentage of the total measured concentration of soluble boron which segregated to the austenite boundaries and inclusions was estimated as 8 % using equation 5.37 and assuming that T_p and T_a are 1390 and 940 °C respectively

$\overline{L}_{tn}$ is the mean lineal intercept measurement of the austenite grain size. S_I was estimated as $S_I(\text{m}^{-1}) \simeq 6f_i/\pi d_i(\text{m})$. Using these data the concentration B^* of segregated boron required to saturate the austenite grain and inclusion surfaces was determined. Figure 5.15 shows the reasonable correlation between the predicted concentration and that suggested by the data due to Thewlis.
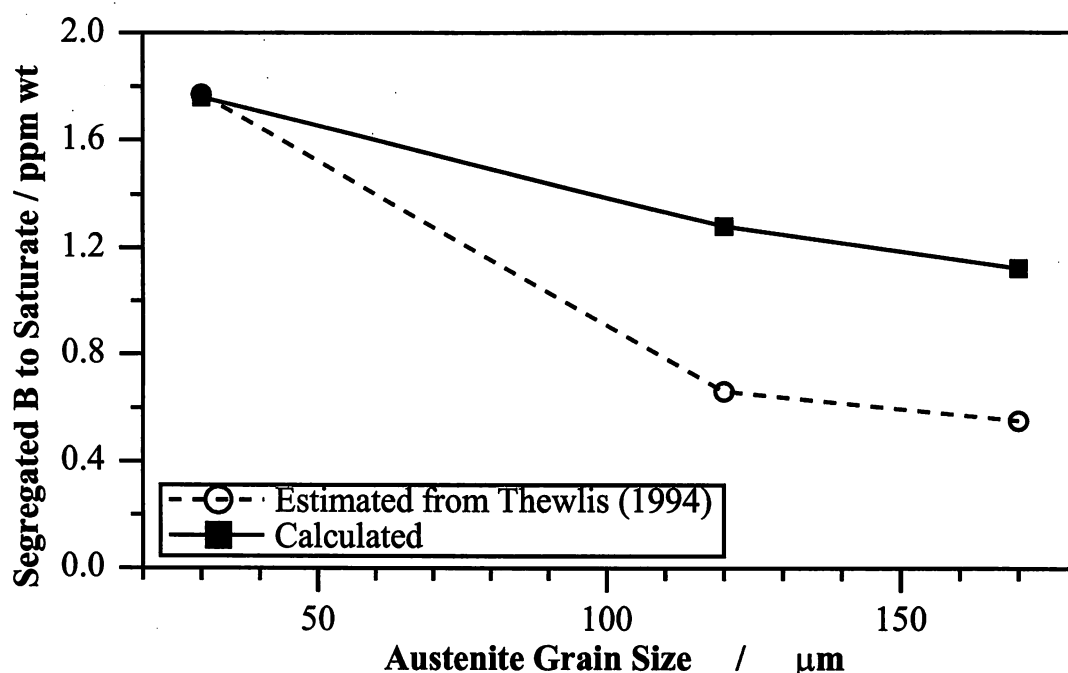
Figure 5.15 Measured and predicted concentrations B^* of segregated boron required to saturate the austenite grain boundary and inclusion surfaces as a function of austenite grain size ($\overline{L}_{tn}$).

To model the effect of boron on interfacial energy it can be assumed (Mortimer and Nicholas, 1976) that for a saturated surface the interfacial energy is reduced by at least 12 %, with proportional reductions for intermediate cases. Figure 5.16 illustrates the inclusion potency P as a function of the segregated boron concentration at the austenite-inclusion interface.
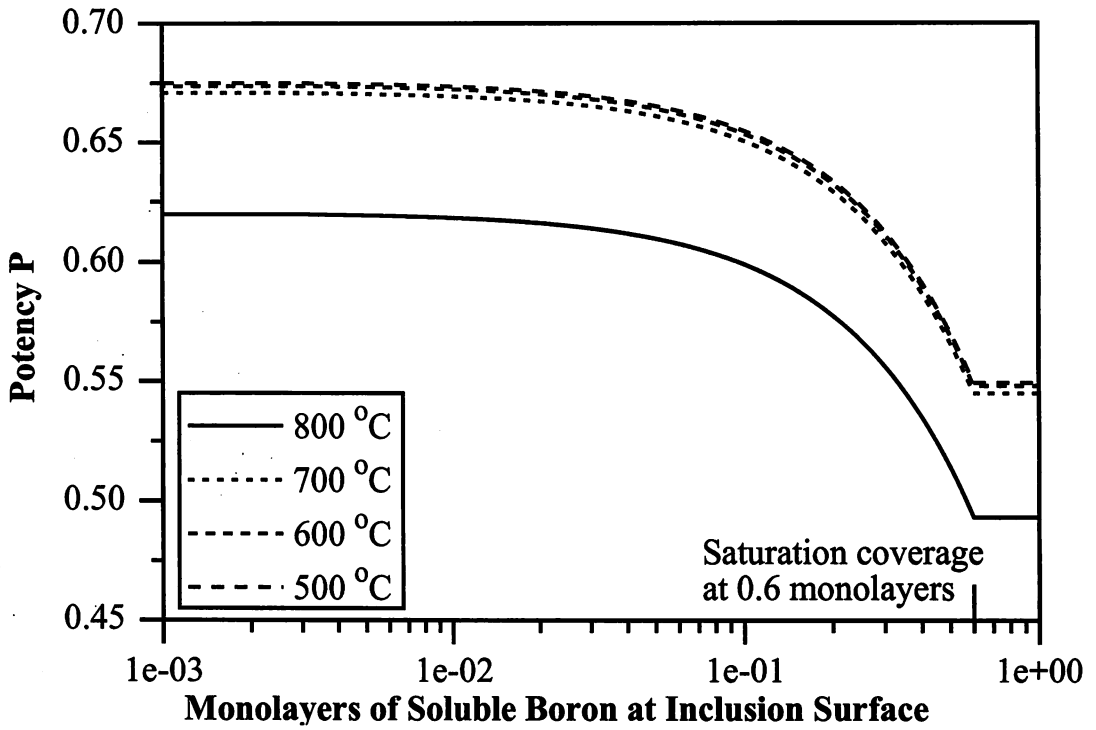
Figure 5.16 The calculated variation of inclusion potency P versus the boron concentration at the inclusion surface.

P drops sharply as saturation is approached.

5.9 Predicting Isothermal Transformation Start Kinetics in Welds

Many models have been developed which allow the prediction of TTT curves from alloy chemistry (Enomoto, 1992). A semi-empirical model developed by Bhadeshia (1982b) is adapted here to allow for the influence of inclusions and variations in the austenite grain size and boron concentration.

Johnson–Mehl–Avrami equations (section 2.1) for random nucleation and linear growth for two alloys; α and β with similar bulk compositions but different populations of nucleation sites are as follows:

$$\zeta_\alpha = \frac{V_\alpha}{V} = 1 - \exp\left(-\frac{\pi}{3}G_\alpha^3 I_\alpha t_\alpha^4\right) \qquad \text{and,} \qquad \zeta_\beta = \frac{V_\beta}{V} = 1 - \exp\left(-\frac{\pi}{3}G_\beta^3 I_\beta t_\beta^4\right) \qquad (5.39)$$

where G_α, G_β, I_α and I_β are the growth and nucleation rates of α and β respectively. ζ_α is the volume fraction of α transformed during the time t_α which is defined since the start of isothermal transformation. ζ_β and t_β are similarly defined with respect to β. For a specified fraction of transformation, such that $\zeta_\alpha = \zeta_\beta$, the following equation may be derived:

$$\frac{t_\beta^4 G_\beta^3}{t_\alpha^4 G_\alpha^3} = \frac{I_\alpha}{I_\beta} \qquad (5.40)$$

131

If the extent of transformation is small then $G_\alpha \simeq G_\beta$ so that:

$$\frac{t_\beta}{t_\alpha} \simeq \left(\frac{I_\alpha}{I_\beta}\right)^{1/4} \tag{5.41}$$

Therefore, the ratio between the times required to achieve a small degree of transformation depends upon the relative nucleation rates in the two alloys. If t_α is known, t_β can be estimated given the nucleation rates. If α is a wrought steel then t_α can be calculated using the TTT model due to Bhadeshia.

Equation 5.41 may be generalised to allow for multiple nucleation sites. If the alloy β is a weld metal then:

$$\frac{t_\beta}{t_\alpha} \simeq \left(\frac{I_{\alpha,1}}{\sum_{i=1}^2 I_{\beta,i}}\right)^{1/4} \tag{5.42}$$

where $I_{\alpha,1}$ and $I_{\beta,1}$ are the nucleation rates per unit unit volume at the austenite grain boundaries in the alloys α and β respectively and $I_{\beta,2}$ is the nucleation rate on inclusions per unit volume in the alloy β. Similarly, for the case where growth is parabolic (section 2.1):

$$\frac{t_\beta}{t_\alpha} \simeq \left(\frac{I_{\alpha,1}}{\sum_{i=1}^2 I_{\beta,i}}\right)^{2/5} \tag{5.43}$$

The steady-state nucleation rate at the austenite grain surface per unit volume was determined using classical nucleation theory (Christian, 1975) as:

$$I_{\alpha,1} = F_a S_V^\alpha \frac{kT}{h} \exp\left(-\frac{G_{\alpha,1}^* + Q}{RT}\right) \quad \text{and,} \quad I_{\beta,1} = F_a S_V^\beta \frac{kT}{h} \exp\left(-\frac{G_{\beta,1}^* + Q}{RT}\right) \tag{5.44}$$

where $F_a = 1.6 \times 10^{10}$ m^{-2} is a fitted constant, h is the Planck constant, k is the Boltzmann constant, T is the absolute temperature, R is the universal gas constant and $Q = 350$ kJ mole^{-1} is a constant activation energy representing the barrier to the transfer of atoms across the ferrite-austenite interface. The activation energy barriers to nucleation $G_{\alpha,1}^*$ and $G_{\beta,1}^*$ at the austenite grain surfaces in α and β respectively were calculated according to the method described in Appendix Three, with the energy of an incoherent austenite-austenite interface being determined according to the extent of boron segregation (section 5.8). In the absence of boron segregation the interfacial energy $\sigma_{\gamma\gamma}$ of the austenite grain boundary per unit area was assumed to be 0.07 J m^{-2}. The austenite grain surface area per unit volume for each alloy were evaluated as S_V^α(m^{-1})$\simeq 2/\overline{L}_{tn}^\alpha$(m) and S_V^β(m^{-1})$\simeq 2/\overline{L}_{tn}^\beta$(m), where $\overline{L}_{tn}^\alpha$ and $\overline{L}_{tn}^\beta$ are the mean lineal intercept measurements of the austenite grain sizes in α and β respectively.

Nucleation on inclusions was modelled as a summation of the various nucleation rates on nine possible inclusion types (Al$_2$O$_3$.MnO, γ-Al$_2$O$_3$, BN, Cu$_{1.8}$S, MnO, α-MnS, TiN, TiO

and β-SiO$_2$ were assumed to form homogeneous and spherical inclusions for the purposes of modelling). So that $I_{\beta,2} = \sum_{j=1}^{9} I_{\beta,2,j}$, where $I_{\beta,2,j}$ is the steady-state nucleation rate on an inclusion of type j which is:

$$I_{\beta,2,j} = F_c N_V^{\beta,j} \frac{kT}{h} \exp\left(-\frac{G^*_{\beta,2,j} + Q}{RT}\right) \qquad (5.45)$$

where $F_c = 2.0$ is a fitted constant, $N_V^{\beta,j}$ is the number of j type inclusions per unit volume (m^{-3}) and $G^*_{\beta,2,j}$ is the activation energy barrier to nucleation on an inclusion of type j, calculated according to the theoretical inclusion potency models discussed above. $N_V^{\beta,j}$ (m^{-3}) = $6f_j/[\pi \overline{d}_j^3(\text{m})]$, where f_j is the volume fraction of inclusions of type j and $\overline{d}_j$ is the mean diameter (m) of the inclusions of type j.

This approach was used to predict the TTT diagrams of two low-alloy steel weld metals the compositions of which are given in Table 6.1. This requires the calculation (Bhadeshia, 1982b) of the reconstructive and displacive TTT curves of a reference wrought alloy α which has the same bulk composition as the weld metal β. This reference alloy had an austenite grain size of 50 μm and contained no inclusions or boron. The second stage involves adjusting these calculated displacive and reconstructive TTT curves according to the ratios given by equations 5.42 and 5.43 respectively. The volume fractions f_j of the inclusion phases in each weld metal were found using a simple mass balance technique (section 3.1.3) due to Kluken and Grong (1989). The inclusions were assumed to have a mean diameter of 0.25 μm. The austenite grain size in both weld metals was about 34 μm. Thus, TTT curves were obtained for the two weld metals W279 and W280, these curves were then converted into CCT (continuous–cooling–transformation) curves by the successive application of Scheil's additive reaction rule (Grong, 1994) over a range of cooling rates (Appendix Five) to allow comparison with measured CCT curves (section 7.2).

Figure 5.17 and 5.18 show that this approach accurately describes the dramatic retardation of the start of reconstructive transformation according to the effect of boron segregation on the activation energy barrier to nucleation. At high temperatures the energy barrier to the transfer of atoms across the ferrite-austenite interface is relatively insignificant and the activation energy barrier for nucleation largely determines the nucleation rate. The effect of the greater volume fraction of the more potent TiO inclusions in W280 is to slightly accelerate the start of transformation at lower temperatures. However, as suggested in section 4.3.4 the most important effect of inclusions is during the latter stages of transformation where they greatly increase the rate of reaction when the austenite grain boundaries are saturated.
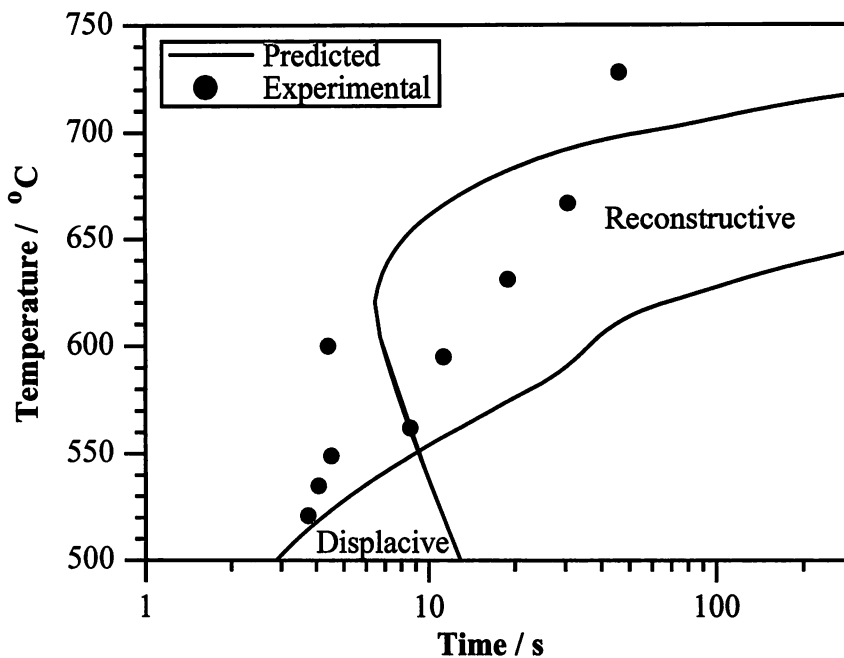
Figure 5.17 Calculated and measured CCT curves in the alloy W279 (5 ppm wt B and 20 ppm wt Ti).
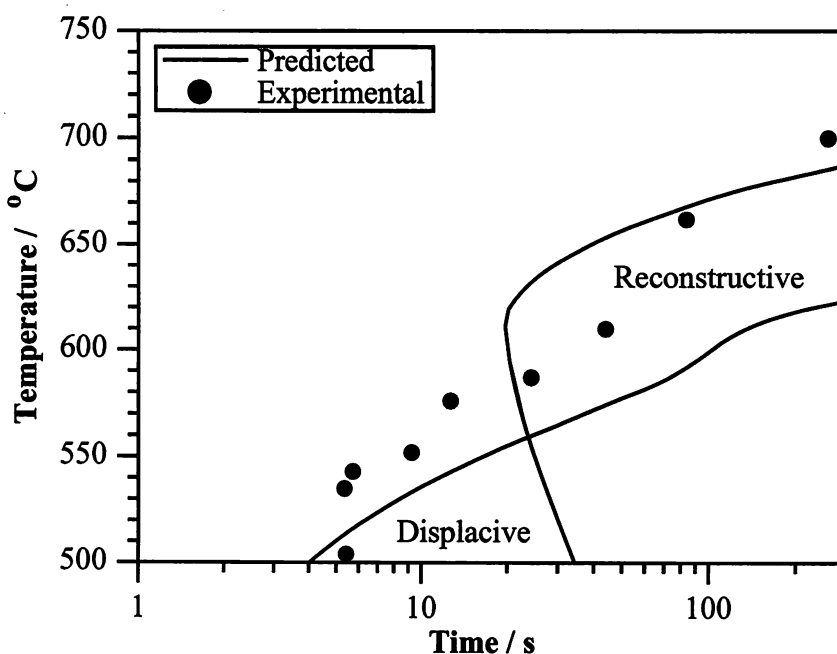
Figure 5.18 Calculated and measured CCT curves in the alloy W280 (40 ppm wt B and 150 ppm wt Ti).

5.10 Summary

The many ways in which non-metallic inclusions influence the nucleation of ferrite have for the first time been incorporated quantitatively into a framework model which permits the importance of different mechanisms to be assessed, and their interactions monitored. It has been possible to demonstrate that frequent claims about 'critical inclusion size', or other claims about particular mechanisms, cannot be sustained in general since inclusion effects depend on many factors acting simultaneously. However, this work suggests that the dominant inclusion nucleation mechanisms probably include chemical reaction with the austenite matrix and lattice matching between the inclusion and the ferrite nucleus.

CHAPTER SIX

Acicular Ferrite

This chapter documents experiments which indicate that consistent with earlier work the acicular ferrite which forms in low-alloy line-pipe welds is probably intragranularly nucleated bainite. Transformation to acicular ferrite only occurred below the thermodynamically calculated bainite start temperature and obeyed the 'incomplete' reaction phenomenon in which the reaction stops when the composition of the austenite is such that diffusionless growth cannot be sustained. The major experimental techniques used in reaching these conclusions are also described.

6.1 Experimental Techniques

6.1.1 Steel Welds

Two submerged-arc welds were made with the help of British Steel plc, Swinden Laboratories. The welds were designed to resemble current low-alloy line-pipe welds. Weld W279 contained trace concentrations of boron (≤ 5 ppm wt), whereas boron was introduced deliberately to weld W280 (40 ppm wt). Both weld metals contained a high density of potent non-metallic inclusions capable of nucleating acicular ferrite. A major experimental problem was the rapid rate with which both alloys transformed to ferrite during cooling.

The exact compositions of the two welds are given in Table 6.1. The alloys were made by welding together two 1 m long steel plates, parallel to the rolling direction, using a three wire submerged-arc process. The 19 mm thick plates of accelerated cooled commercial plate '3H10C' British Steel grade steel (Table 6.1) were machined to a 'double angle V with root faces' geometry (Figure 6.1). One pass was made on each side of the weld (Figure 1.1 shows weld W280). The interpass temperature was $\simeq 20$ °C. The welding speed was 26 mm s^{-1} and the total heat input was 3.72 kJ mm^{-1}. The arc efficiency of this process is considered to lie in the range from 0.9 to 0.99 (Easterling, 1992). The experimental Oerlikon Welding Industries flux used was 'OP122V4' which was applied to a depth of 50 mm. 'OP122V4' is a high Al_2O_3 variant of the commercial flux 'OP122' which is composed by weight of 20 % SiO_2+TiO_2, 30 % $CaO+MgO$, 25 % Al_2O_3+MnO, 20 % CaF_2 and 5 % of various other elements. W279, the low boron alloy, was welded using solid 'SD3' plain C-Mn welding wire and the high boron alloy W280 with flux-cored '12R92N'. Both of these consumables, whose average compositions are given in Table 6.1, were also manufactured by Oerlikon Welding Industries. The welding wires were 4 mm in diameter with a stick out length of 40 mm.

Code	C	Mn	Si	Ni	Mo	Cr	V	Al	Ti	S	O	N	B	Cu	P	Nb
3H10C	0.050	1.30	0.26	0.014	0.011	0.02	0.052	0.042	0.002	0.002	–	0.0038	0.0005	0.01	0.009	0.040
SD3	0.090	1.66	0.30	–	–	–	–	0.002	–	0.006	–	0.0060	–	–	0.009	–
12R92N	0.026	1.53	0.62	–	–	–	–	0.006	0.016	0.007	–	0.0047	0.0058	–	0.019	–
W279	0.062	1.47	0.32	0.010	0.009	0.03	0.030	0.026	0.002	0.005	0.0300	0.0049	0.0005	0.07	0.015	0.025
W280	0.045	1.47	0.41	0.090	0.009	0.03	0.031	0.026	0.015	0.005	0.0295	0.0050	0.0040	0.03	0.014	0.025

Table 6.1 The composition (wt %) of the parent plate, the welding consumables and the two weld metals used in this study.

6.1.2 Heat Treatment

Rod shaped specimens were machined out of the centre of the as-deposited weld, the rod axis being parallel to the welding direction. Cylindrical samples 8 mm in diameter and 12 mm
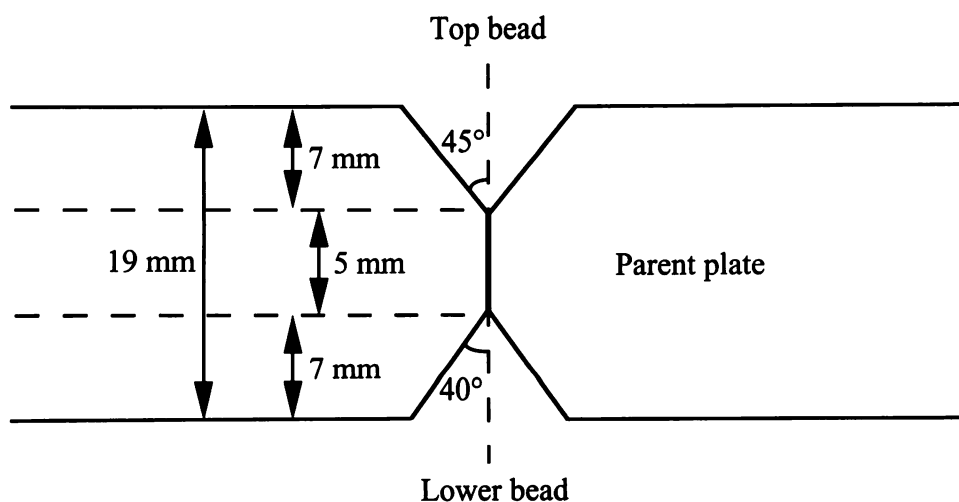
Figure 6.1 The geometry used to prepare the welds W279 and W280.

in length were machined from the rod. In order to facilitate high quench rates, some of the specimens were bored out to produce tubes with a wall thickness of 2 mm. All heat treatments were performed using a 'ThermecMastor' thermo-mechanical simulator manufactured by Fuji Electronic Industrial Co. Ltd. This was used in two ways. Dilatometry studies were used to monitor phase transformations *in situ*, whilst heat treatments were also designed to provide microstructures for subsequent examination under a microscope. A schematic of the 'ThermecMastor' is illustrated in Figure 6.2.

Using this device thermo-mechanical treatments can be programmed and data collected on a computer. The chamber is evacuated and 'flushed' with inert argon gas prior to pumping down to a vacuum of 10^{-4} Torr. The specimen is heated using a high-frequency induction coil (allowing homogeneous heating to within ± 5 °C), and cooled by quenching with either inert gas (helium or nitrogen) or water. Temperature was monitored using a Pt / Pt-13%Rh thermocouple which is spot welded to the surface of the specimen. Radial strain during transformation was measured using a laser system to within ± 1 μm.

6.1.3 Specimen Preparation, Optical Microscopy and Microhardness Testing

Samples were sectioned perpendicular to the welding direction before being mounted in conductive acrylic resin. To remove surface distortion they were ground using a Struers Abramin automated grinding and polishing machine with 180, 220, 320, 500, 800, 1200, 2400 and 4000 grit SiC paper, and polished with cloths coated with 6 μm and 1 μm diamond pastes and colloidal silica (0.04 μm). The specimens were then etched in 20 % Nital (concentrated

Force

High vacuum

Ceramic die

Combined induction heating
and gas cooling coils

Scanned
laser beam

Thermocouple

Test specimen

Force
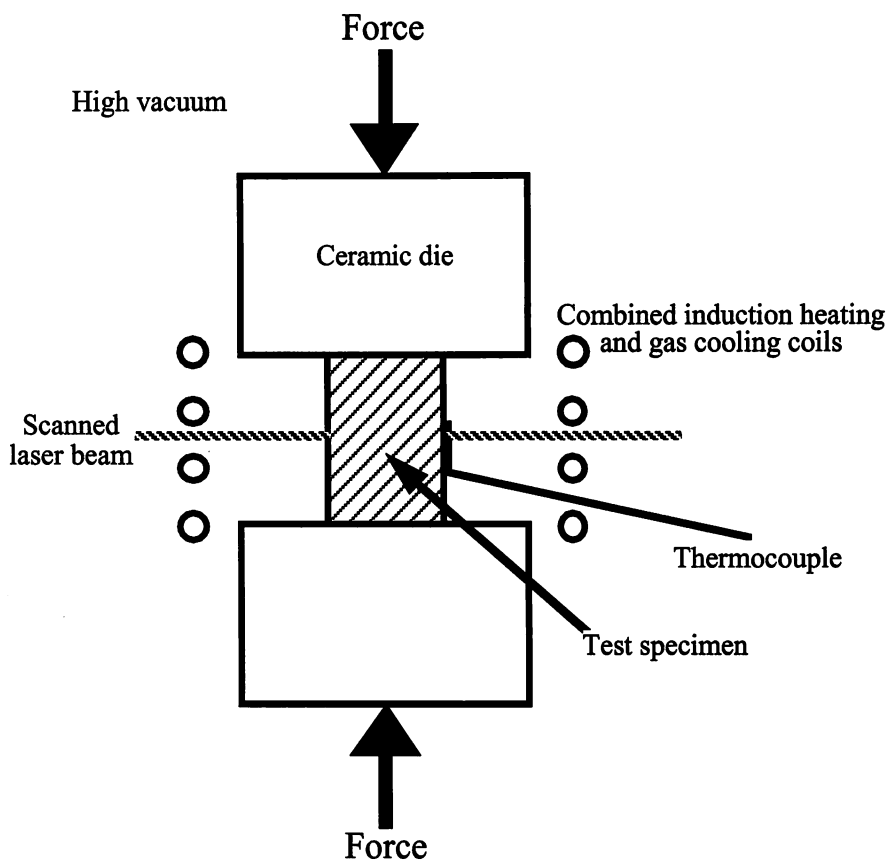
Figure 6.2 Schematic of the 'ThermecMastor' thermo-mechanical simulator.

nitric acid in methanol). Optical microscopy was performed using a Zeiss Axiotech microscope fitted with a Kyocera camera with automatic exposure control. Photomicrographs were taken using Ilford FP4+ ISO 125 film. Vickers microhardness measurements were obtained from a Leitz Miniload 2 machine using a load of 0.981 N, a loading time of 15 s and a dwell time of 15 s.

6.2 Acicular Ferrite – An Intragranularly Nucleated Bainite

Bhadeshia *et al.* (1989 and 1992) demonstrated that acicular ferrite is an intragranularly nucleated bainite (section 1.3.3) in a series of welds. The evidence for this is summarised below:

(1) The displacive shape change accompanying the transformation is characterised as an invariant-plane strain, similar to that found in conventional bainite. The plastic deformation which accompanies it produces a high dislocation density ($\simeq 10^{14}$ m^{-2}).

(2) Measurements indicate that the stored strain energy of acicular ferrite is about 400 J mole^{-1}, which is the same as for conventional bainite, whereas that for Widmanstätten ferrite is approximately 50 J mole^{-1}.

139

(3) Microanalysis indicates that there is no bulk partitioning of the substitutional solute elements during the transformation, which is expected during a reconstructive transformation.

(4) Plates of acicular ferrite have never been observed to cross austenite grain boundaries. The orientation relationship between the acicular ferrite and the parent austenite is always found to be such that close packed planes in each phase are within a few degrees of each other.

(5) The acicular ferrite transformation is an 'incomplete reaction' (section 1.3.3).

This study is concerned with modelling the nucleation of acicular ferrite in submerged-arc welds used to produce line-pipe. Therefore, it was decided to investigate whether the acicular ferrite formed in typical line-pipe welds under continuous cooling conditions was indeed intragranularly nucleated bainite. Two approaches were used to test this hypothesis:

(1) An attempt was made to see whether acicular ferrite could be nucleated above the calculated bainite start temperature B_S.

(2) Experiments were conducted to see whether acicular ferrite only forms under conditions where diffusionless transformation is thermodynamically feasible.

6.3 Bainite Start Temperature

6.3.1 Calculated Bainite Start Temperature

The bainite start temperature B_S is reduced by many alloying elements, but carbon has the largest effect (Honeycombe and Bhadeshia, 1995). Steven and Haynes (1956) developed a widely used empirical equation expressing the bainite start temperature as a function of alloy composition:

$$B_S(^\circ C) = 830 - 270w_C - 90w_{Mn} - 37w_{Ni} - 70w_{Cr} - 83w_{Mo} \qquad (6.1)$$

where w_X is the concentration of the species X in wt %. This equation is derived for the range of composition (wt %) given below:

$$
\begin{array}{lll}
\text{C} \;\; 0.1 - 0.55 & \text{Mn} \;\; 0.2 - 1.70 & \text{Ni} \;\; 0.0 - 5.00 \\
\text{Cr} \;\; 0.0 - 3.50 & \text{Mo} \;\; 0.0 - 1.00 & \text{Si} \;\; 0.1 - 0.35
\end{array}
$$

Bodnar *et al.* (1989) found, in a study of the bainite transformation during continuous cooling, that the upper temperature at which bainite formed was relatively insensitive to the rate

of cooling.[1] They developed the following empirical equation 6.2 for the bainite start temperature. As pointed out by Bhadeshia (1992) this equation does not describe the true B_S temperature, but the temperatures B'_S at which bainite first forms during continuous cooling conditions.

$$B'_S(°C) = 844 - 597w_C - 63w_{Mn} - 16w_{Ni} - 78w_{Cr} \qquad (6.2)$$

This equation is derived for the following range of composition (wt %):

C $0.15 - 0.29$	Mn $0.02 - 0.77$	Ni $0.21 - 3.61$
Cr $1.13 - 2.33$	Mo $0.44 - 1.37$	Si $0.01 - 0.23$

Bhadeshia (1981 and 1992) developed a more fundamental methodology for predicting both the bainite start B_S temperature and the Widmanstätten ferrite start W_S temperature according to alloy composition. The details of this approach with respect to the Widmanstätten ferrite start temperature are given in section 4.4.3. However, whilst Widmanstätten and bainitic ferrite, nucleate by the same mechanism, their growth mechanisms are different (sections 1.3.2 and 1.3.3). Bainite grows without diffusion with a large stored strain energy of 400 J mole^{-1}, so that the criteria for the detectable nucleation and growth of bainitic ferrite may be written as:

$$\Delta G^{\gamma \to \alpha} < -G_{SB} \qquad \text{and,} \qquad \Delta G_m < G_N \qquad (6.3)$$

where $\Delta G^{\gamma \to \alpha}$ is the thermodynamic driving force for diffusionless transformation from austenite to ferrite, G_{SB} is the stored strain energy of bainite, ΔG_m is the maximum possible driving force for nucleation and G_N is the *universal* nucleation function defined by Bhadeshia (1981). Using this approach and calculated free energy diagrams (1982c), it is possible to estimate the bainite start temperature for any low alloy steel. The bainite start temperatures of the two weld metals W279 and W280 calculated according these methods are shown in Table 6.2.

Model	W279	W280
Steven and Haynes (1956)	674*	679*
Bodnar *et al.* (1989)	710*	720*
Bhadeshia (1981)	586	591

Table 6.2   Calculated bainite start temperatures (°C). * Indicates that this calculation is not strictly valid because the alloy composition is outside the specified range.

---

[1]   This is because the bainite C-curve on TTT diagrams has a flat top.

The first point to note is that the empirical calculations are not strictly valid for such low-alloy welds. However, the wide disparity between the results is clear. The results attributed to Bodnar *et al.* should be ignored because the composition is well beyond the permitted range. If the carbon concentrations of W279 and W280 are artificially increased by approximately two times to 0.1 wt %, so as to fall in the range specified by Steven and Haynes, then the bainite start temperature for both alloys is recalculated as 664 °C.

6.3.2 Measured Acicular Ferrite Start Temperature

In order to determine the approximate acicular ferrite start temperature for the alloy W279, a series of isothermal heat treatments were performed in the 'ThermecMastor'. Samples were heated to an austenitising temperature of 1300 °C. After holding for 150 s at this temperature the specimens were cooled using helium gas at 50 °C s^{-1} to the isothermal treatment temperature (675, 630, 610, 590, and 550 °C), and held there until long after transformation ceased. Microstructural examination revealed that the specimens held at 610 °C and above (Figure 6.3) had transformed to allotriomorphic and idiomorphic ferrite, whereas that held at 550 °C (Figure 6.4) had transformed to acicular ferrite. Transformation at 590 °C (Figure 6.5) resulted in a mixed microstructure comprising allotriomorphic and idiomorphic ferrite together with acicular ferrite. This suggests that the acicular ferrite start temperature for alloy W279 is approximately 590 °C.

The detectable acicular ferrite start temperature found during continuous cooling experiments, is expected to be somewhat lower than the 'true' thermodynamic start temperature, due to kinetic effects. Continuous cooling experiments described in section 7.2 reveal interesting results. The microstructure found with cooling rates of between 10 and 50 °C s^{-1} is predominantly composed of acicular ferrite (> 75 %). Analysis of the dilatometric data (Figure 7.2) for a cooling rate of 10 °C s^{-1} shows that detectable transformation to ferrite does not start until below approximately 630 °C for alloy W279, and 590 °C for alloy W280. This is expected since boron retards the formation of allotriomorphic ferrite in alloy W280 when compared with the low boron alloy W279 (section 3.4). Both alloys are expected to transform relatively quickly upon cooling below the bainite start temperature, because boron does not significantly alter the start temperature or kinetics of the transformation to acicular ferrite. Note the increase in the slope of the dilatation curve for the low boron alloy W279 at approximately 570 °C, the same temperature at which the transformation starts in earnest in alloy W280 (Figure 7.2). This hypothesis is supported by the fact that the transformation finish temperatures for both alloys are nearly the same. Similar results were found as the cooling rate was increased to 20 °C s^{-1} (Figure 7.3), although the temperature at which acicular ferrite started to form
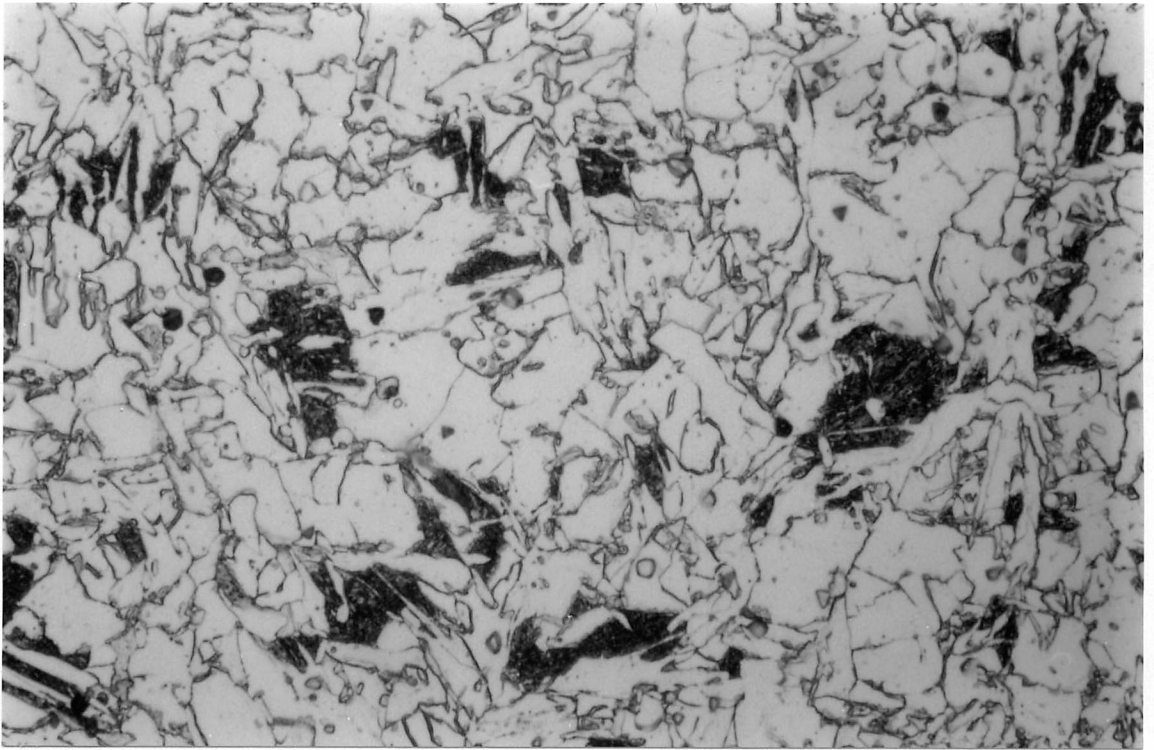
Figure 6.3 Optical micrograph of alloy W279 after isothermal transformation at 610 °C for 15 minutes.
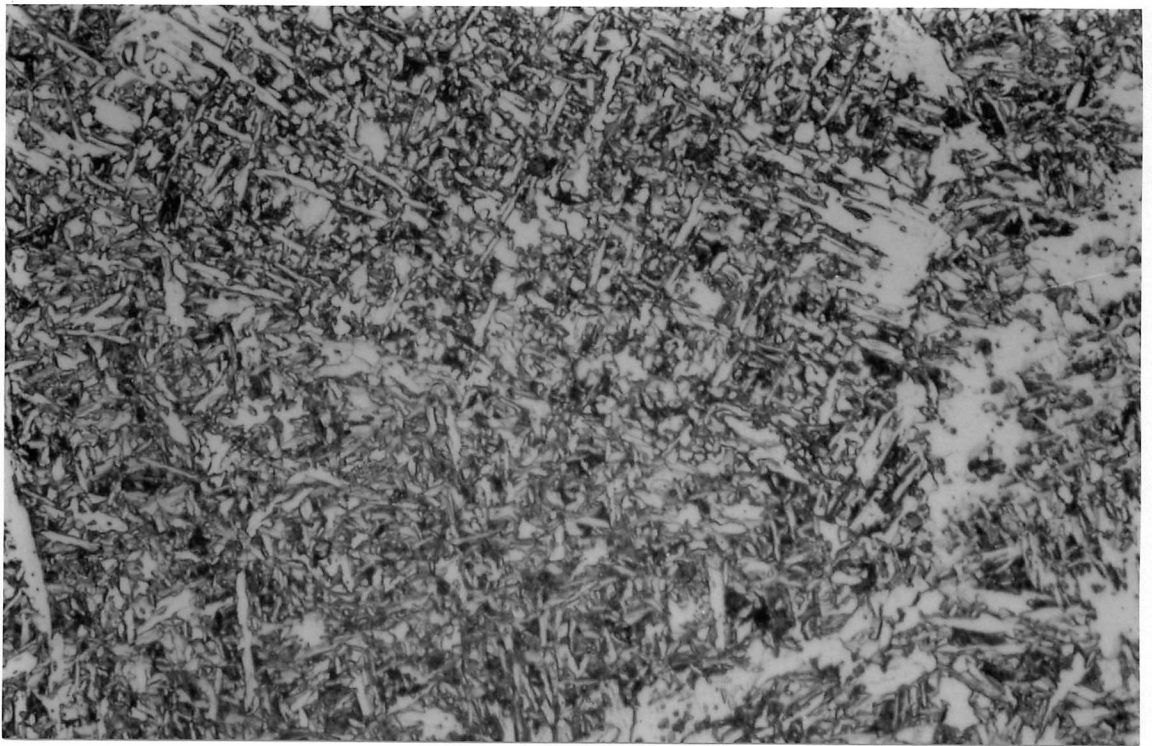
Figure 6.4 Optical micrograph of alloy W279 after isothermal transformation at 550 °C for 15 minutes.
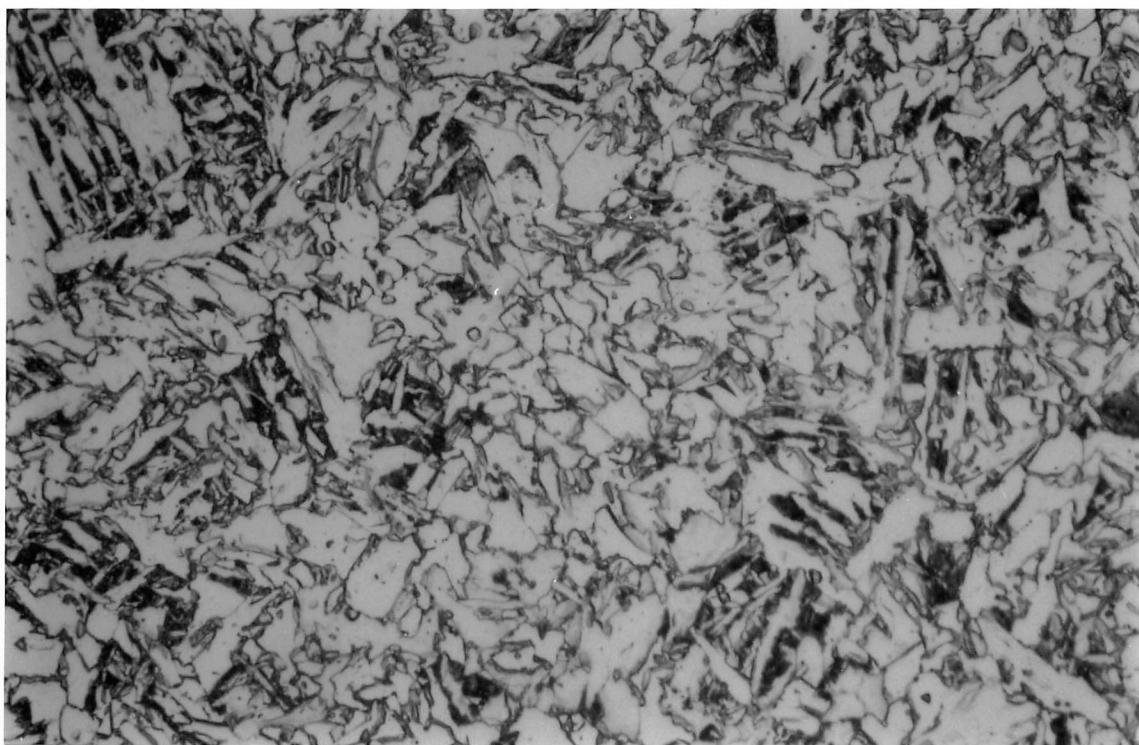
Figure 6.5 Optical micrograph of alloy W279 after isothermal transformation at 590 °C for 15 minutes.

decreased to approximately 560 °C. Increasing the cooling rate to 30 and 50 °C s^{-1} (Figures 7.4 and 7.5) suppresses almost completely any transformation to allotriomorphic ferrite. The transformation to acicular ferrite begins at approximately 565 °C in the low boron alloy W279, and 550 °C in the high boron alloy W279.

Further experiments were conducted to establish the temperature at which acicular ferrite formation begins during the conditions typical of commercial practice. Hollow cylindrical specimens of the low boron alloy W279 were austenitised in the 'ThermecMastor' at 1300 °C for 120 s before they were cooled at 9 °C s^{-1}. The cooling cycle was interrupted by a water quench at 630, 600, 570 and 540 °C in four separate experiments. The quench rate achieved was sufficient to cause the residual or untransformed austenite to transform to martensite. Microstructural examination revealed that allotriomorphic, Widmanstätten ferrite and acicular ferrite formed prior to the water quenches at 570 °C (Figure 6.6) and 540 °C. Only allotriomorphic and Widmanstätten ferrite formed above 600 °C, so that the residual austenite in the central region of the prior-austenite grains transformed to lath martensite during the water quench (Figure 6.7). Microhardness measurements taken at the centre of the prior-austenite grains, confirm that the transformation to acicular ferrite begins between 600 and 570 °C. Figure 6.8 shows the variation of the microhardness with the water quench temperature. Ten

144

microhardness measurements were taken from each specimen, the ± error bars representing one standard deviation from the mean. For comparison the mean microhardnesses of lath martensite, acicular and allotriomorphic ferrite are listed in Table 6.3.[2]

Figure 6.6   Optical micrograph of alloy W279 after cooling at 9 °C s^{-1} was interrupted by a water quench at 570 °C.

Phase	Vickers Microhardness
Allotriomorphic Ferrite	223 (± 7)
Acicular Ferrite	269 (±12)
Lath Martensite	383 (±13)

Table 6.3   Vickers (HV) microhardness of the various phases found in alloy W279. The quoted ± errors represent one standard deviation from the mean.

6.3.3 Discussion

Microstructural examination, after isothermal transformation, reveals that the acicular

---

[2] The microhardness of martensite was measured using a specimen of the alloy W279 placed in a quartz tube which was flushed with argon and evacuated using a vacuum pump. This specimen was austenitised in a furnace at 1300 °C for 120 s before quenching by immersion in water. Samples of acicular and allotriomorphic ferrite were obtained by isothermal heat treatment at 550 and 675 °C respectively, as described in section 6.3.2.

Figure 6.7   Optical micrograph of alloy W279 after cooling at 9 °C s^{-1} was interrupted by a water quench at 600 °C.
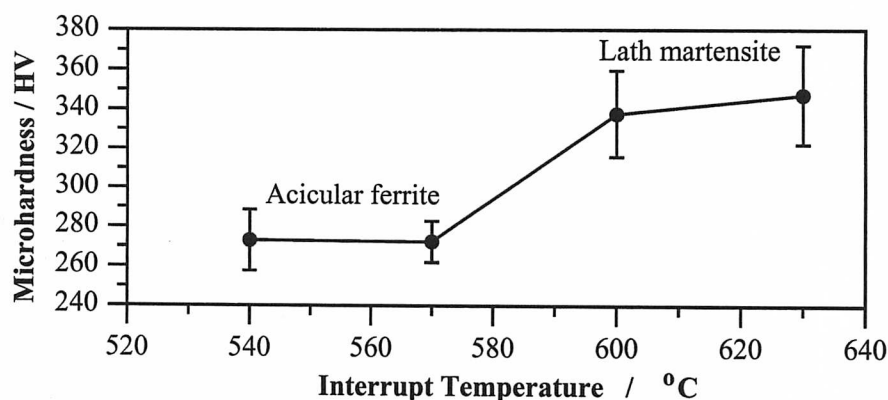
Figure 6.8 Vickers (HV) microhardness versus water quench temperature for the specimens of alloy W279 used in the interrupted cooling experiments. The ± errors bars represent one standard deviation from the mean.

start temperature of the low boron alloy W279 during isothermal transformation is approximately 590 °C. Dilatometric and microstructural data for slow (<10 °C s^{-1}) continuous cooling, indicate that the detectable acicular ferrite nucleation starts above 570 °C. Dilatometric data indicate that the acicular ferrite start temperature, for the high boron alloy W280, is also above 570 °C, although a little lower than that of the low boron alloy W279. It is apparent therefore, that acicular ferrite starts to form in both alloys at temperatures close to and below the bainite start temperature predicted by using the model due to Bhadeshia (1981), indicating

146

that it could be intragranularly nucleated bainite.

6.4 Acicular Ferrite - An Incomplete Reaction

A representative isothermal transformation heat treatment and the associated dilatation curve, is illustrated in Figure 6.9. The specimen is quenched rapidly from an austenitising heat treatment to an isothermal temperature below the calculated B_S temperature. At this point the specimen is assumed not to have begun transforming from austenite to bainitic ferrite. The specimen thus transforms to ferrite which has a lower density than austenite so the dilatation increases with time.
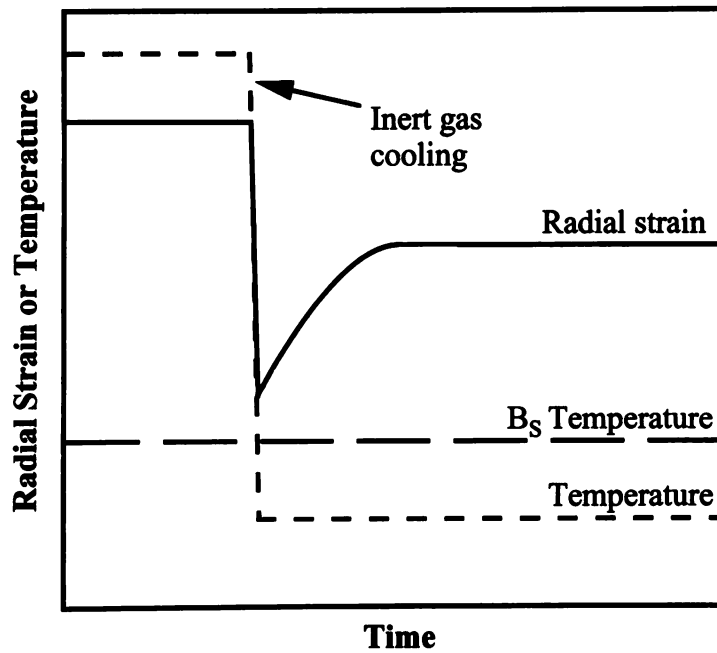
Figure 6.9 Typical isothermal transformation heat treatment.

To convert the dilatation to the volume fraction transformed, and hence obtain the carbon concentration of the residual austenite at any instant in time, it is necessary to know the lattice parameters of the phases involved, at the isothermal transformation temperature.

6.4.1 Lattice Parameter of Ferrite

Bhadeshia *et al.* (1991) developed the following equation which describes the lattice

parameter a'_α of alloyed iron in nm at 25 °C:[3]

$$a'_\alpha = a_{\alpha-\text{Fe}} + \frac{1}{3a_{\alpha-\text{Fe}}^2}\left[(a_{\alpha-\text{Fe}} - 0.0279c_C^\alpha)^2(a_{\alpha-\text{Fe}} + 0.2496c_C^\alpha) - a_{\alpha-\text{Fe}}^3\right]$$
$$-0.003c_{\text{Si}}^\alpha + 0.006c_{\text{Mn}}^\alpha + 0.007c_{\text{Ni}}^\alpha + 0.031c_{\text{Mo}}^\alpha + 0.005c_{\text{Cr}}^\alpha + 0.0096c_V^\alpha \tag{6.4}$$

where $a_{\alpha-\text{Fe}}$ is the lattice parameter of pure α-iron at 25 °C taken as 0.28664 nm and c_X^α is the mole fraction of the element X in the α-ferrite phase.

6.4.2 Lattice Parameter of Austenite

The lattice parameter of austenite a'_γ in nm at 25 °C can be estimated using the following equation due to Dyson and Holmes (1970):[4]

$$a'_\gamma = a_{\gamma-\text{Fe}} + 0.3300w_C^\gamma + 0.0095w_{\text{Mn}}^\gamma + 0.0020w_{\text{Ni}}^\gamma$$
$$+0.0060w_{\text{Cr}}^\gamma + 0.0310w_{\text{Mo}}^\gamma + 0.0180w_V^\gamma \tag{6.5}$$

where $a_{\gamma-\text{Fe}}$ is the lattice parameter of pure γ-iron at 25 °C and w_X^γ represents the weight fraction of the element X in the γ-austenite phase.

6.4.3 Linear Expansion Coefficients

Linear expansion coefficients are used to extrapolate the calculated room temperature lattice parameters of each phase to the isothermal transformation temperature. The lattice parameters of untransformed α and γ, at the absolute transformation temperature T, can be found using the following equations:

$$a_\alpha = a'_\alpha\left[1 + e_\alpha(T - 298.15)\right] \quad \text{and,} \quad a_\gamma = a'_\gamma\left[1 + e_\gamma(T - 298.15)\right] \tag{6.6}$$

where e_α and e_γ are the linear expansion coefficients of ferrite and austenite respectively.

6.4.4 Transformation and Carbon Enrichment of Austenite

Bhadeshia (1982a) and Bhadeshia *et al.* (1991) developed a method which enables the volume fraction v_α of bainitic ferrite and the carbon concentration $\tilde{w}_C^\gamma$ of the residual or untransformed austenite to be estimated at any stage of an isothermal transformation, assuming that the only phases present are bainitic ferrite and residual austenite.

Consider x_0 moles of austenite transforming into x_α moles of ferrite leaving x_γ moles of residual austenite. The total volume before transformation V_0 will increase to a new volume V_T after transformation. These volumes are given as:

$$V_0 = x_0 N_A\left(\frac{a_\gamma^3}{4}\right) \quad \text{and,} \quad V_T = N_A\left[x_\alpha\left(\frac{a_\alpha^3}{2}\right) + (x_0 - x_\alpha)\left(\frac{\tilde{a}_\gamma^3}{4}\right)\right] \tag{6.7}$$

[3] This equation was deduced from published data for iron to which separate additions (up to 6 atomic weight %) of various alloying elements were made.

[4] This equation was determined using austenitic Cr-Ni steels to which separate additions (up to 8 wt %) of various alloying elements were made.

where N_A is Avogadro's number. a_α is the lattice parameter of ferrite, a_γ is the lattice parameter of the austenite prior to transformation and $\tilde{a}_\gamma$ is the lattice parameter of the residual austenite enriched in carbon. These lattice parameters at the transformation temperature are determined using equations 6.4, 6.5 and 6.6.

Substitutional elements do not diffuse in the bainitic transformation, therefore only the carbon concentration of the residual austenite changes during the transformation. Thus, if the final microstructure consists only of bainite and residual austenite, then by considering mass balance and accounting for the different densities of ferrite and austenite, the carbon concentration of the residual austenite $\tilde{w}_C^\gamma$ in wt % is given approximately by:

$$\tilde{w}_C^\gamma = \overline{w}_C \left[1 + \frac{v_\alpha \tilde{a}_\gamma^3 (\overline{w}_C - w_C^\alpha)}{2 a_\alpha^3 (1 - v_\alpha)} \right] \tag{6.8}$$

where v_α is the volume fraction of bainitic ferrite and $\overline{w}_C$ is the mean carbon concentration of the alloy in wt % and w_C^α is the carbon concentration of the bainitic ferrite, assumed to be 0.03 wt % (Honeycombe and Bhadeshia, 1995). Note that because $\tilde{a}_\gamma$ is a function of $\tilde{w}_C^\gamma$ an iterative solution is required.

Now the relative volume change is approximately given by:

$$\frac{\Delta V}{V} = \frac{V_T - V_0}{V_T} = 1 - \frac{a_\gamma^3}{(x_\alpha/x_0)(2a_\alpha^3 - \tilde{a}_\gamma^3) + a_\gamma^3} \tag{6.9}$$

Furthermore, by considering mass balance and allowing for the different densities of ferrite and austenite the ratio (x_α/x_0) is approximately:

$$\frac{x_\alpha}{x_0} = \frac{1}{1 + [2(1 - v_\alpha)a_\alpha^3]/(v_\alpha \tilde{a}_\gamma^3)} \tag{6.10}$$

The experimental measurements correspond to dimensional changes ΔL, not volume changes ΔV. Assuming isotropic strain these changes are related by the equation:

$$\frac{\Delta V}{V} \simeq 3\frac{\Delta L}{L} \tag{6.11}$$

Using experimental dilatation $(\Delta L/L)$ data equations 6.8 to 6.11 may be solved using an iterative procedure to give the volume fraction of bainitic ferrite v_α, together with the carbon concentration of the residual austenite $\tilde{w}_C^\gamma$, at any time after the start of isothermal transformation.

6.4.5 Results

The high boron alloy W280 was chosen to minimise the extent of possible grain boundary nucleated transformation to allotriomorphic and Widmanstätten ferrite during quenching. The

linear expansion coefficients of ferrite (e_α) and austenite (e_γ) were determined using linear regression for the experimental alloy using the 'ThermecMastor'. The coefficient for ferrite was determined during heating over the temperature range 25 to 600 °C and that for austenite over the temperature range 900 to 1200 °C. This experiment was repeated with five heating rates between 0.5 and 5 °C s^{-1}. The expansion coefficients did not vary significantly with temperature or heating rate. The results are summarised in Table 6.4 where the error terms represent one standard deviation from the mean coefficients determined for the five heating rates.

Measurement	Ferrite (α)	Austenite (γ)
Coefficient (K^{-1})	15.3×10^{-6}	21.4×10^{-6}
Error (K^{-1})	0.47×10^{-6}	0.17×10^{-6}

Table 6.4   Measured linear expansion coefficients for ferrite and austenite in alloy W280.

The room temperature lattice parameter of bainitic ferrite was estimated as 0.28672 nm, using the method described in section 6.4.1. This is only slightly larger than 0.2866 nm, the lattice parameter of pure b.c.c. iron at room temperature. The room temperature lattice parameter of untransformed austenite was calculated as 0.35750 nm, using the method outlined in section 6.4.2. This is only slightly larger than 0.3573 nm, the lattice parameter of pure f.c.c. iron at room temperature (Dyson and Holmes, 1970). Specimens of the high boron alloy W280 were subjected to isothermal transformations at the following temperatures; 590, 580, 560, 540, 520, 500 and 480 °C. This temperature range was chosen because the calculated bainite start (section 6.2) and martensite start (Bhadeshia, 1981b and c) temperatures for the alloy W280 are 591 and 475 °C respectively. The experimental procedure (Figure 6.9), involved heating the specimens to an austenitising temperature of 1300 °C in the 'ThermecMastor'. After 2 minutes at this temperature solid cylindrical specimens were cooled, at a rate of 60 °C s^{-1}, with helium gas to the isothermal transformation temperature, which was maintained for 15 minutes. All of the transformations stopped during this time. However, technical difficulties prevented the electronic recording of data during the isothermal transformation at 580 °C. The specimens were then gas quenched to room temperature. Figure 6.10 shows the measured radial strain against time for all of the isothermal transformation temperatures. Using the procedure described in section 6.4.4, the strain data were processed, to give the volume fraction v_α of austenite transformed to acicular ferrite, illustrated in Figure 6.11. The carbon concentration $\widetilde{w}_C^\gamma$ of the residual austenite during the transformation was also determined. Figure 6.12 shows a typical plot, at 480 °C, of $\widetilde{w}_C^\gamma$ (expressed in mole fraction) as a function of v_α. The

carbon concentration of the residual austenite, at the end of each isothermal transformation was plotted on a computed (Bhadeshia,1982b) phase diagram (Figure 6.13).
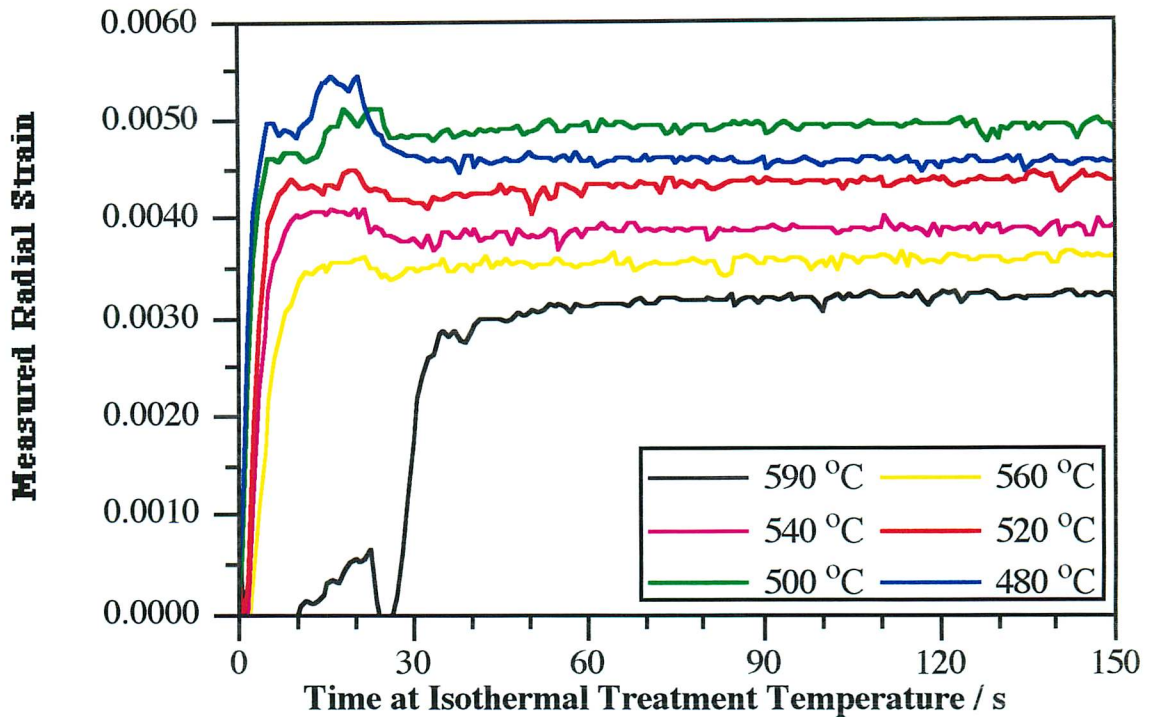
Figure 6.10   Measured radial strain versus time during the isothermal transformation of alloy W280 at various temperatures.

6.4.6 Discussion

The strain and volume fraction data, shown in Figures 6.10 and 6.11, reveal several interesting features. Firstly, the transformation to acicular ferrite proceeds rapidly, finishing in under 9 s at all temperatures less than or equal to 560 °C. The transformation at 590 °C is, on the other hand much slower, because the transformation product is not acicular ferrite but predominantly allotriomorphic ferrite mixed with some acicular ferrite (Figure 6.4). Secondly, the extent of transformation increases with undercooling, although the difference is not very pronounced. The volume fraction of acicular ferrite increases from 0.43 at 560 °C, to 0.66 at 500 °C. The unusual variations in the measured strain and the calculated volume fraction after about 20 s are experimental artifacts due to transient temperature instabilities (Figure 6.9 and 6.10). The high cooling rate 60 °C s^{-1} to the isothermal treatment makes these instabilities unavoidable in the 'ThermecMastor'. The carbon concentration of the residual austenite increases by approximately 66 % during the transformation to acicular ferrite (Figure 6.11). Plotting this information on the calculated phase diagram (Figure 6.12) indicates
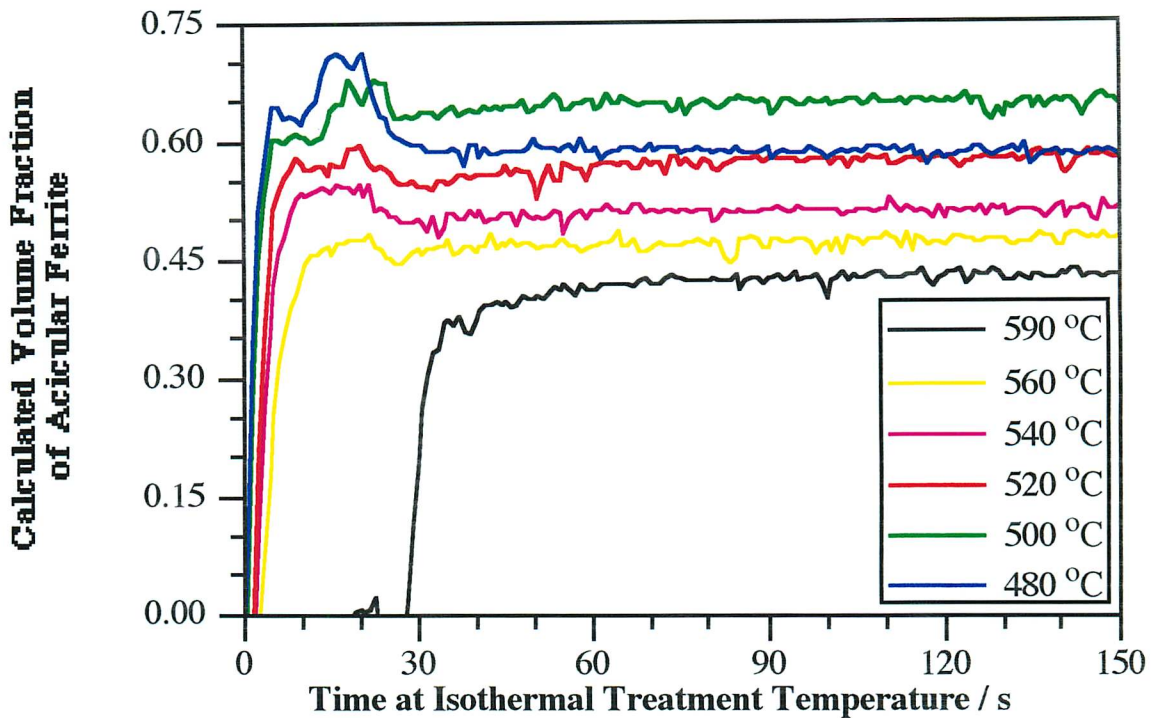
Figure 6.11   Calculated volume fraction of acicular ferrite versus time during the isothermal transformation of alloy W280 at various temperatures.

that the transformation to acicular ferrite is an 'incomplete' reaction. The ultimate carbon concentration is far less than the Ae_3'' phase boundary [5] calculated for the displacive transformation to Widmanstätten ferrite indicating that the acicular ferrite in this weld is probably an intragranularly nucleated bainite. However, the carbon concentration is also less than the T_0' line [6] predicted for the displacive transformation to bainitic ferrite. This inconsistency is thought to have occurred because the cooling rate of 50 °C s^{-1} was not sufficiently rapid to avoid partial transformation to acicular ferrite before the lower isothermal transformation temperatures were reached. This might explain why both the rate and extent of transformation, together with the carbon concentration of the residual austenite, did not increase dramatically with greater undercooling below the B_S temperature. A further series of experiments, in which hollow specimens were used to allow higher cooling rates ($\simeq$ 80 °C s^{-1}), proved unsuccessful because the cooling rate was so rapid that the transient temperature instabilities during isothermal transformation became too large.

---

[5] The Ae_3'' phase boundary is similar to the paraequilibrium Ae_3 boundary but allows for 50 J mole^{-1} of stored strain energy in the Widmanstätten ferrite.

[6] The T_0' line is the locus of all those points on the phase diagram where austenite and ferrite which have identical compositions have exactly the same free energy after allowing for 400 J mole^{-1} of stored strain energy in the bainitic ferrite.
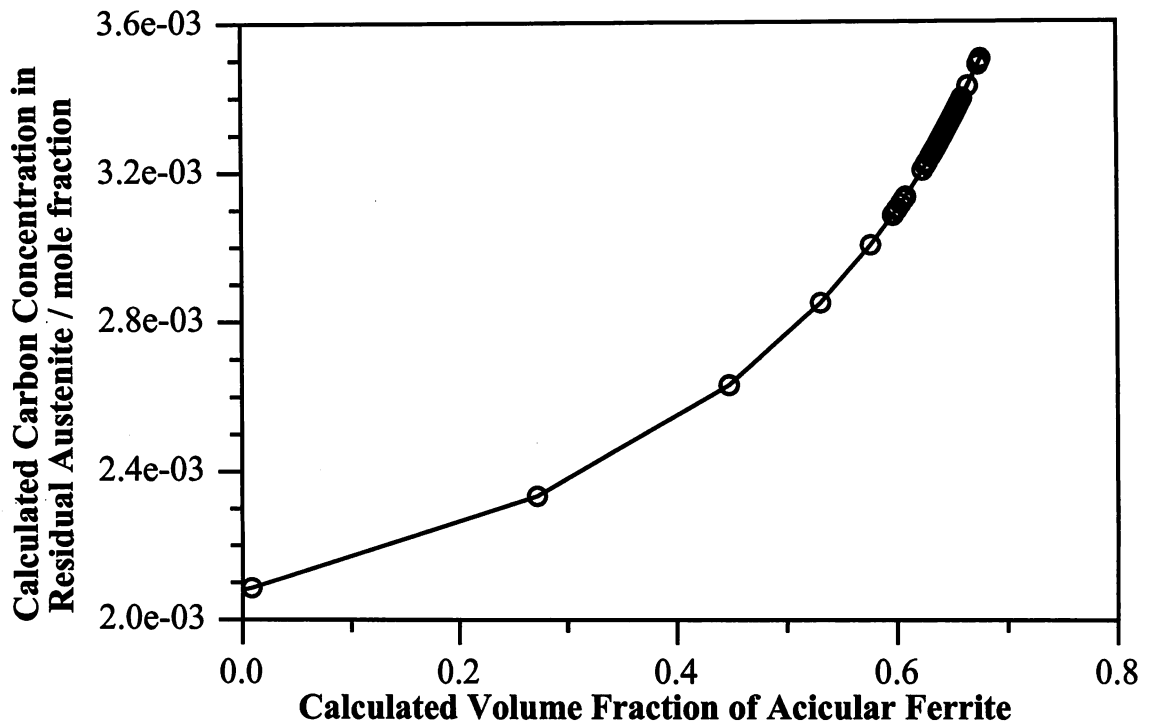
Figure 6.12   Calculated carbon concentration in the residual austenite as a function of the calculated volume fraction of acicular ferrite during the isothermal transformation of alloy W280 at 500 °C.

6.5   Summary

The indications are that the acicular ferrite found in the line-pipe weld considered here is intragranularly nucleated bainite. It has been determined experimentally that the transformation to acicular ferrite begins below the thermodynamically calculated bainite start temperature. The reaction is found to stop before a paraequilibrium volume fraction of acicular ferrite is obtained, consistent with the 'incomplete reaction' phenomenon reported for bainite. However, there have been experimental difficulties which have prevented a complete proof.
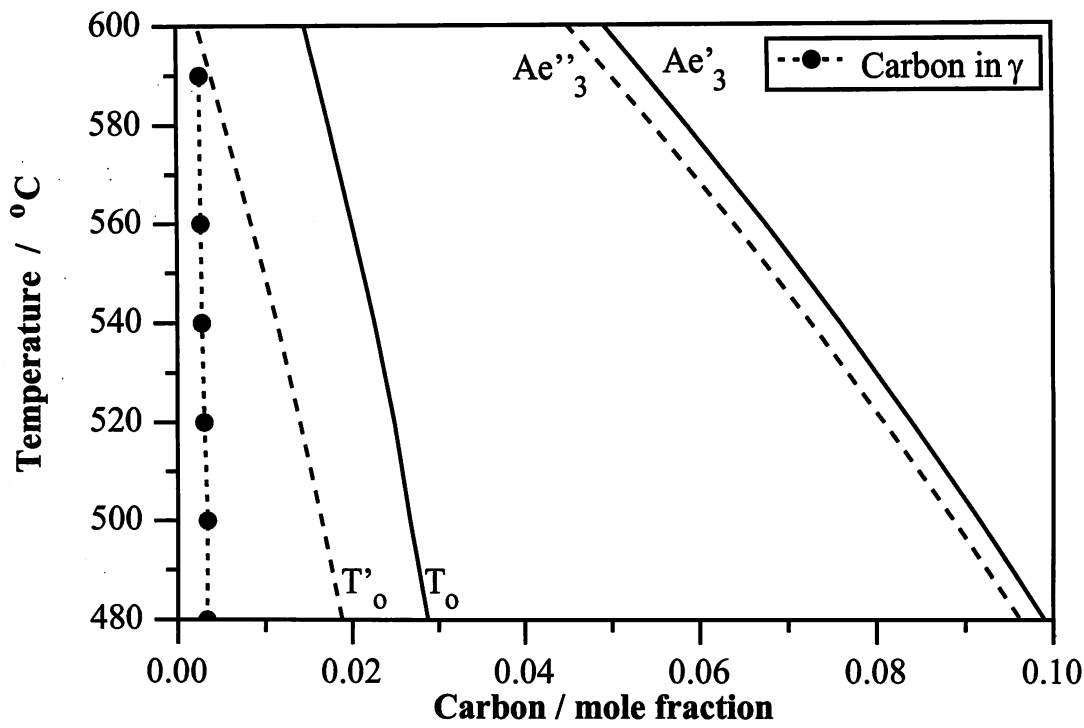
Figure 6.13 The calculated carbon concentration in the residual austenite at the end of the acicular ferrite transformation plotted on a computed (Bhadeshia,1982b) phase diagram for the alloy W280.

CHAPTER SEVEN

Boron - Effects In Steel Welds

Experimental work on the influence of trace quantities of boron on the transformation kinetics of low-alloy steel weld metals is presented in this chapter. Presented first is the relatively small retarding influence of boron on the forward transformation of austenite to acicular ferrite. The second section describes work which indicates that boron strongly retards the start of the reverse transformation of acicular ferrite to austenite. In the last part a new phenomenon is revealed whereby less than 5 ppm wt of boron causes the transformation behaviour to vary systematically as a function of the number of successive austenitising treatments performed.

7.1 Introduction

In section 3.4 the strong retarding influence of trace additions of boron on the austenite to allotriomorphic ferrite transformation was discussed. In this chapter new experimental work is described as follows:

(1) Experiments designed to test whether boron retards the displacive transformation to acicular ferrite.

(2) Work which examines the effect of boron on the reverse transformation of acicular ferrite to austenite.

(3) Experiments which examine how the transformation behaviour of boron containing alloys varies systematically as a function of the number of successive austenitising treatments performed.

7.2 The Austenite to Ferrite Transformation

7.2.1 Introduction

Boron is well known to retard the reconstructive transformation to allotriomorphic ferrite, however, the direct influence it has on the displacive transformation to acicular ferrite is not so well understood. It has been postulated that misfitting boron atoms may segregate to inclusions, either reducing or enhancing their nucleation potency. Consequently, a series of experiments have been designed to establish continuous cooling transformation (CCT) curves for both the low boron alloy W279 and the high boron alloy W280 described in section 6.1.1. These involved austenitising the specimens at 1200 °C for 300 s before subjecting them to controlled helium gas quenches. The cooling rates used were 80, 70, 60, 55, 50, 30, 20, 10, 5, 2, and 0.5 °C s^{-1}. The transformation to ferrite was considered to have started when the measured dilatation curve began to deviate appreciably from the dilatation due to linear thermal contraction. The incubation period before the start of transformation was taken as the time between the calculated Ae'_3 temperature (Bhadeshia, 1982c) and the detectable transformation start temperature. Continuous cooling transformation curves were plotted using this data by assuming that the volume fraction transformed at any instant is approximately given by the deviation of the radial strain from that expected due to linear thermal contraction alone.

7.2.2 Results

The Ae'_3 temperature of alloy W279 was calculated as 821 °C and that of W280 as 829 °C.

Microstructural examination [1] revealed that the prior-austenite grain size was similar in each alloy; the mean linear intercept was 33 μm in W279 and 34 μm in W280. Typical dilatation plots are illustrated in Figures 7.1 to 7.5. These were used to construct continuous cooling transformation curves which are shown in Figures 7.6 to 7.8. Inspection revealed that constant cooling rates were maintained to the transformation start temperature in all of the experiments. However, very high constant cooling rates could not be sustained during the course of the transformation to ferrite. Consequently the 50 and 100 % continuous cooling transformation curves do not contain data for cooling rates greater than 50 °C s^{-1}.
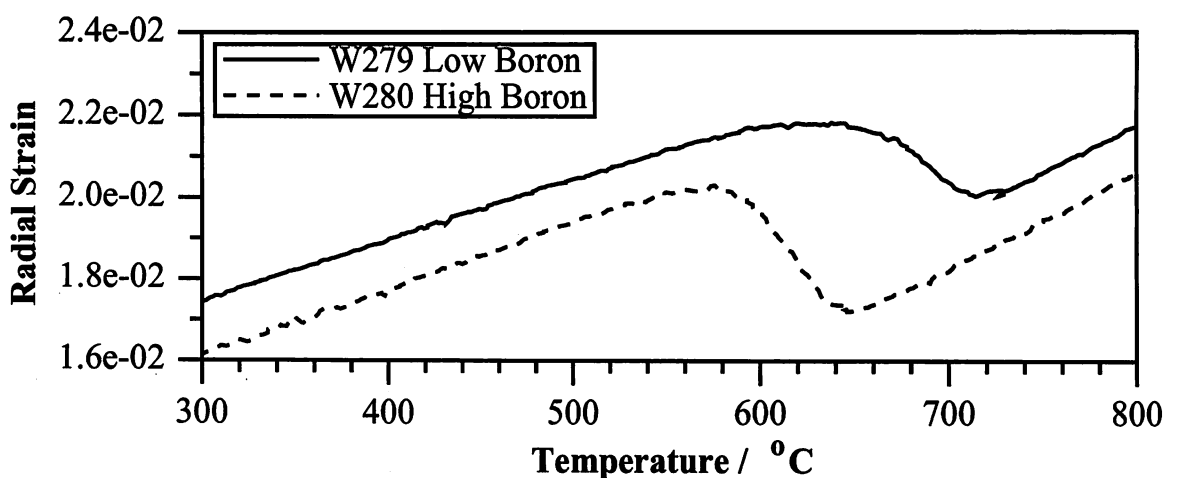
Figure 7.1 Dilatation curves for alloys W279 and W280 – continuous cooling 2 °C s^{-1}.
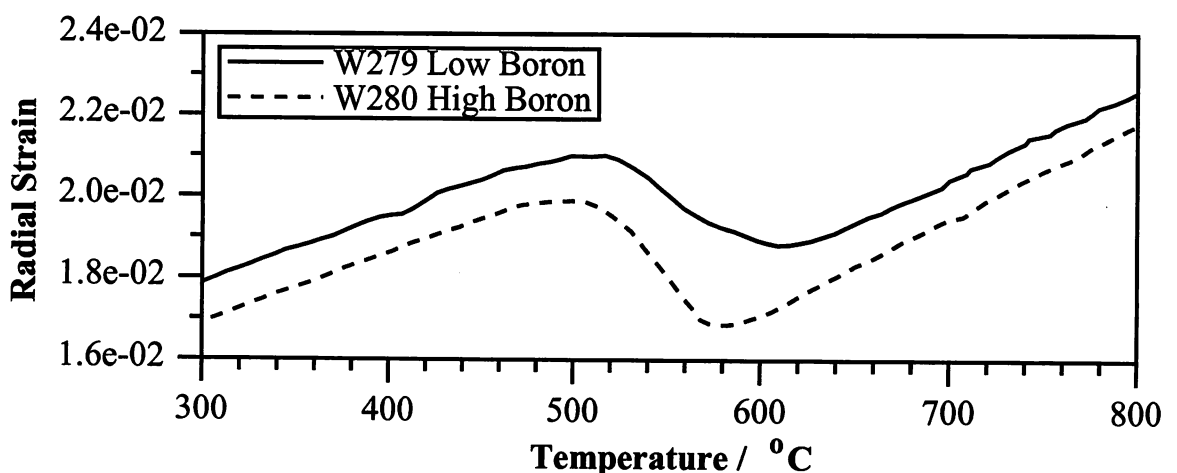
Figure 7.2 Dilatation curves for alloys W279 and W280 – continuous cooling 10 °C s^{-1}.

[1] Grain boundary etching was conducted using a picric acid based solution (40 g picric acid and 990 ml distilled water) at about 50 °C.
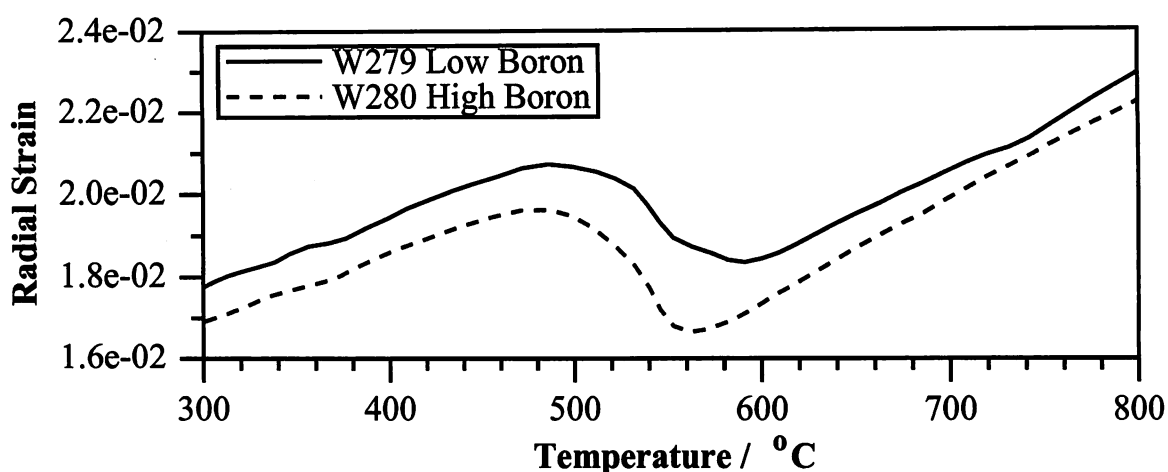
Figure 7.3 Dilatation curves for alloys W279 and W280 – continuous cooling 20 °C s^{-1}.
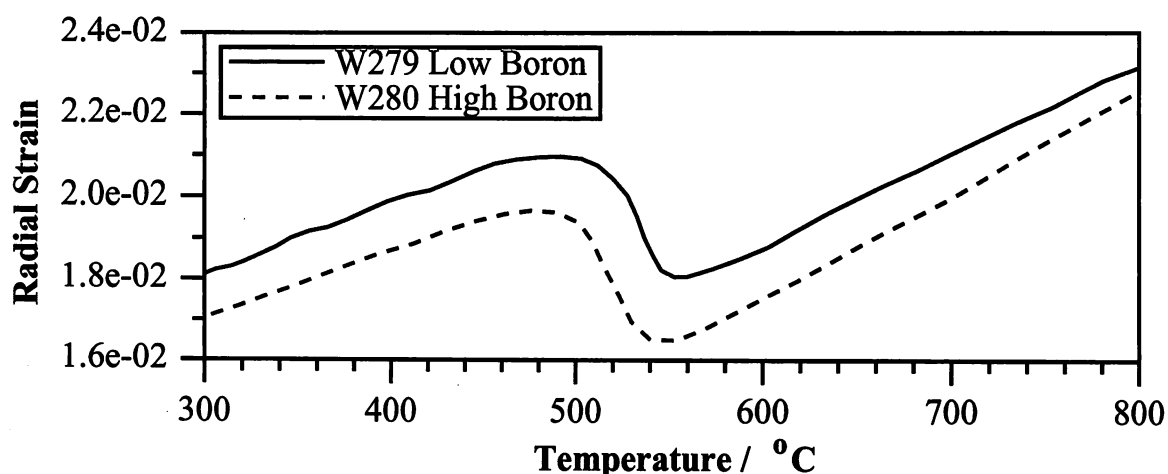
Figure 7.4 Dilatation curves for alloys W279 and W280 – continuous cooling 30 °C s^{-1}.

7.2.3 Discussion

It is apparent from the continuous cooling transformation curves shown in Figures 7.6 to 7.8 that boron may induce a slight retardation of the displacive transformation to acicular ferrite. The effect is small, approximately an order of magnitude less than the retardation of the transformation to allotriomorphic ferrite. However, caution must be exercised in the interpretation of these results because W280 contains significantly more titanium than weld W279 (Table 6.1). The titanium in W280 is required to protect the boron from oxygen and nitrogen. Titanium compounds are particularly effective nucleants of acicular ferrite (section 3.3.2), and it might be expected that the transformation would occur more rapidly in W280 if it were not for the high concentration of boron. It is therefore possible that boron may exert a greater retarding influence on the displacive transformation to acicular ferrite than suggested by the
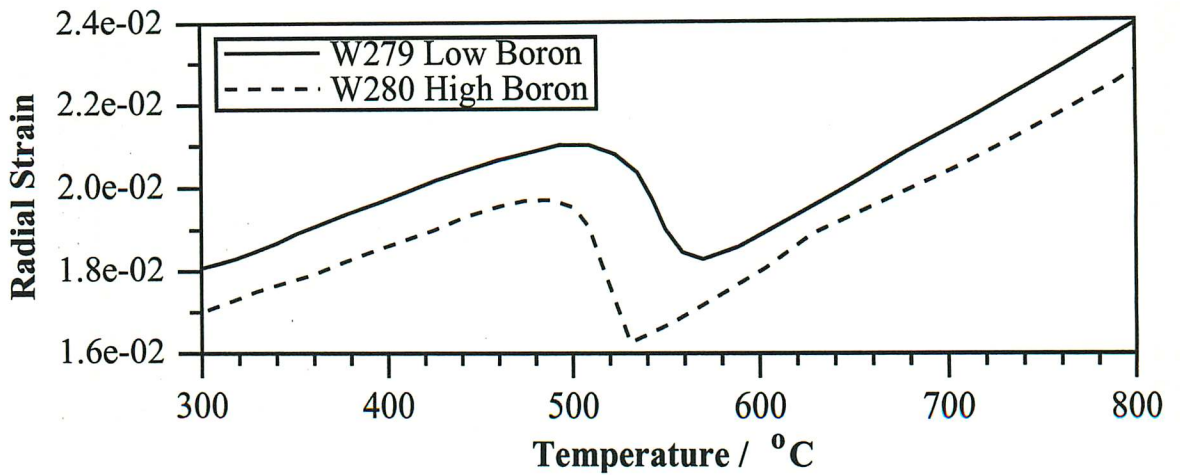
Figure 7.5 Dilatation curves for alloys W279 and W280 – continuous cooling 50 °C s^{-1}.
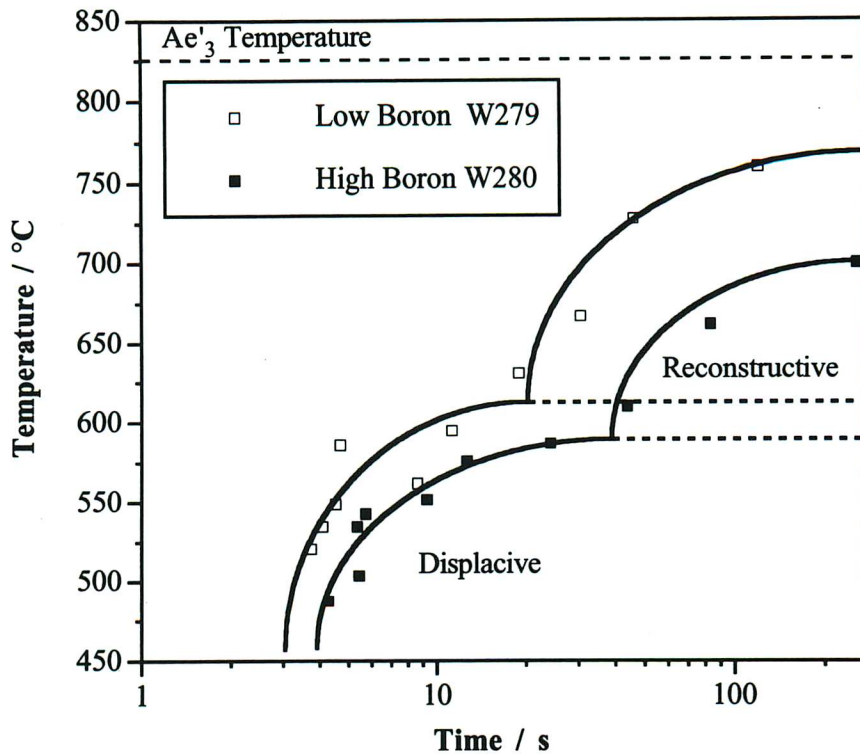
Figure 7.6 Continuous cooling 1 % transformation curves for alloys W279 and W280.

continuous cooling curves. This is considered to be unlikely, since previous work implies that both weld metals W279 and W280 contain sufficient inclusions capable of nucleating acicular ferrite during rapid cooling. It is also clear that boron does not significantly alter the flat top of the displacive transformation curve because trace additions of boron are unlikely to influence strongly the thermodynamics of the transformation to acicular ferrite. In conclusion,
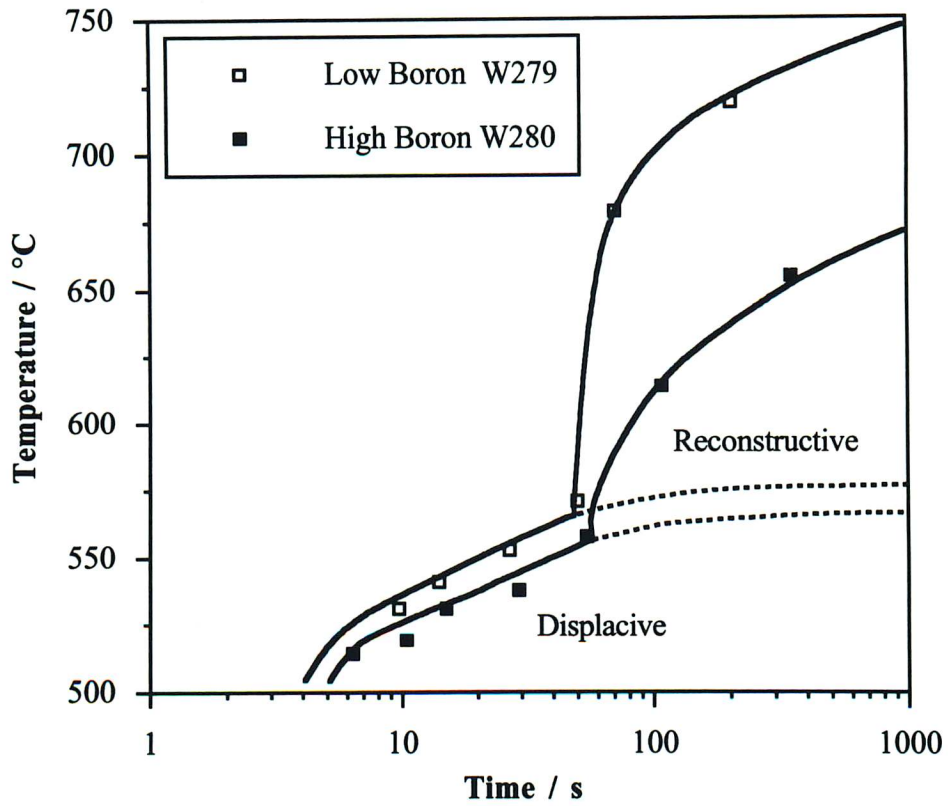
Figure 7.7 Continuous cooling 50 % transformation curves for alloys W279 and W280.
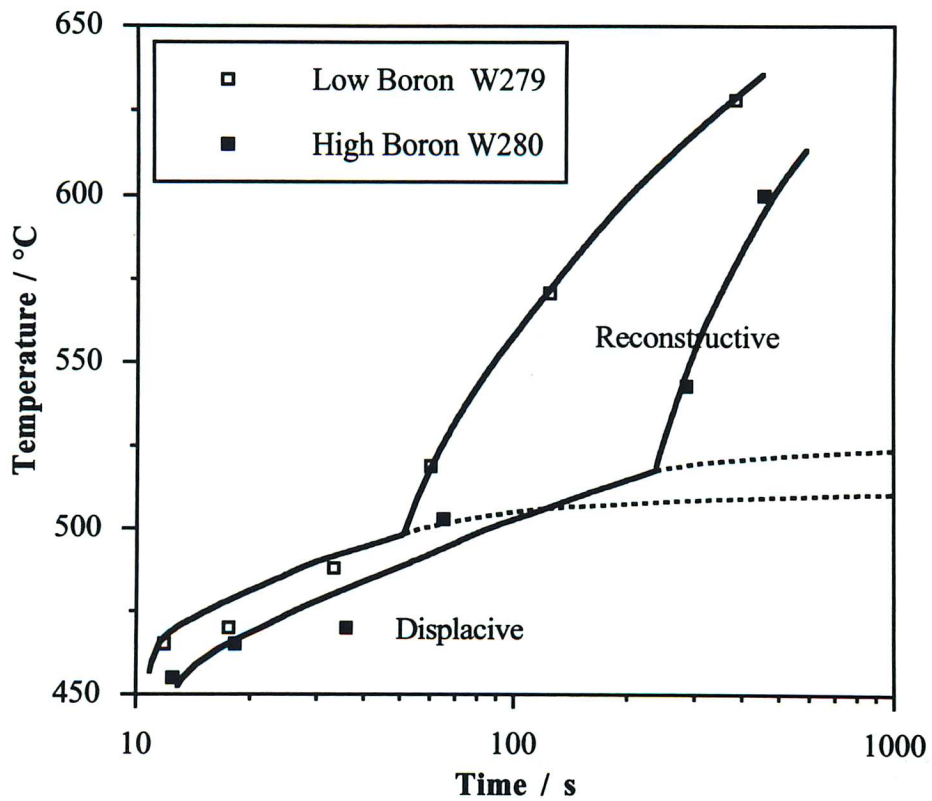
Figure 7.8 Continuous cooling 100 % transformation curves for alloys W279 and W280.

it appears that trace levels of boron do not significantly retard the displacive transformation to acicular ferrite during cooling. There are several possible explanations for this behaviour:

(1) Experiments (section 3.2.4) by Yamamoto *et al.* (1996) indicate that free boron atoms may be removed from the inclusion-austenite interface by absorption into the volume of the inclusion so that the activation energy barrier to nucleation remains unaffected despite the segregation of boron.

(2) Classical nucleation theory suggests that because acicular ferrite forms well below the Ae_3 temperature the nucleation rate is controlled by the activation energy for diffusion across the austenite-ferrite interface, not the activation energy barrier to nucleation which is a function of the inclusion–austenite interfacial energy.

(3) The nucleation rate of displacive acicular ferrite is not influenced by the inclusion-austenite interfacial energy and is instead controlled by the rate at which pre-existing embryos become unstable (section 3.2.3).

7.3 The Ferrite to Austenite Transformation

7.3.1 Introduction

The transformation of ferrite to austenite on heating is unlike that which occurs during the cooling of austenite. The classical kinetic behaviour described by the C-curve on the TTT diagram during cooling is not expected or found upon heating. The origins of the C-curve are in the opposing effects of an increasing thermodynamic driving force and decreasing diffusivity during cooling. Austenitisation occurs during *heating* causing the thermodynamic driving force and diffusivity to increase simultaneously. Therefore, the speed of transformation increases indefinitely and the kinetic response might best be described by a smooth L-shaped curve. Consequently, it is not possible to retain metastable ferrite by rapid heating.

Austenitisation can be a reconstructive process which strongly depends on the degree of superheating (Nehrenberg, 1952). Experimental evidence indicates that the kinetics of the nucleation and growth of austenite are also determined by the starting microstructure (Law and Edmonds, 1980). Two distinct modes of austenite nucleation and growth are observed during the austenitisation of bainitic and martensitic steels; a 'globular' form which nucleates along the prior-austenite boundaries and 'acicular' austenite observed to form intragranularly on the boundaries between individual martensitic or bainitic laths (Kimmins and Gooch, 1983). Coalescence of different austenite grains leads eventually to the regeneration of the original prior-austenite grain structure. This effect has been termed the austenite 'memory'. Kimmins

and Gooch further suggested that the intragranular formation of austenite occurs because of the retained austenite film between the individual martensitic or bainitic laths in the starting microstructure. The austenitisation heat treatment causes these grains to grow and eventually coalesce. Other intragranular nucleation may also contribute, if the superheating is large enough (Bhadeshia, 1992). By contrast the formation of globular austenite destroys the prior-austenite grain structure. The balance between globular and acicular austenite depends on the degree of superheating, the former being favoured at low driving forces. At larger driving forces intragranular austenite dominates the transformation (Law and Edmonds, 1980; Kimmins and Gooch, 1983). The austenite memory effect is not found if the starting microstructure is allotriomorphic ferrite because this reconstructive transformation product destroys the prior-austenite grain boundaries.

Experiments are reported here to establish whether trace additions of boron retard the formation of austenite upon heating.

7.3.2 Continuous Heating

Continuous heating transformation curves were measured for both the low boron alloy W279, and the high boron alloy W280. The starting microstructure in each case consisted of acicular ferrite formed by quenching ($\simeq 60$ °C s^{-1}) the specimen with helium gas from an austenitising treatment of 15 s at 1200 °C. Hollow samples of each alloy were heated at rates of 50, 40, 20, 10, 5 and 2 °C s^{-1} to 1200 °C.

The transformation to austenite was identified when the dilatation curve began to deviate significantly from that expected from thermal expansion alone. This method was used to determine the transformation start temperature for each heating rate. The Ae'_1 temperature was calculated for the alloys W279 and W280 as 689 and 693 °C respectively, according to a method due to Bhadeshia (1982c). Analysis revealed that constant heating rates were maintained for all experiments. Typical measurements are shown in Figures 7.9 and 7.10, which were used to construct continuous heating transformation curves (Figures 7.11).

The start of the transformation to austenite, as represented by the 1 % transformation curve (Figure 7.11), is retarded strongly by trace additions of boron. The extent of retardation is influenced by the heating rate (Figures 7.9 and 7.10). This is because both the driving force and kinetics of the transformation to austenite increase rapidly with rising temperature. Significant retardation by boron is therefore only possible at slow heating rates. The 100 % curves (Figure 7.11) are, within the limits of experimental error, identical for both alloys. This is because once transformation starts it is very rapid so that any initial differences are masked.

In conclusion, boron does retard the early stages of austenite formation during heating,
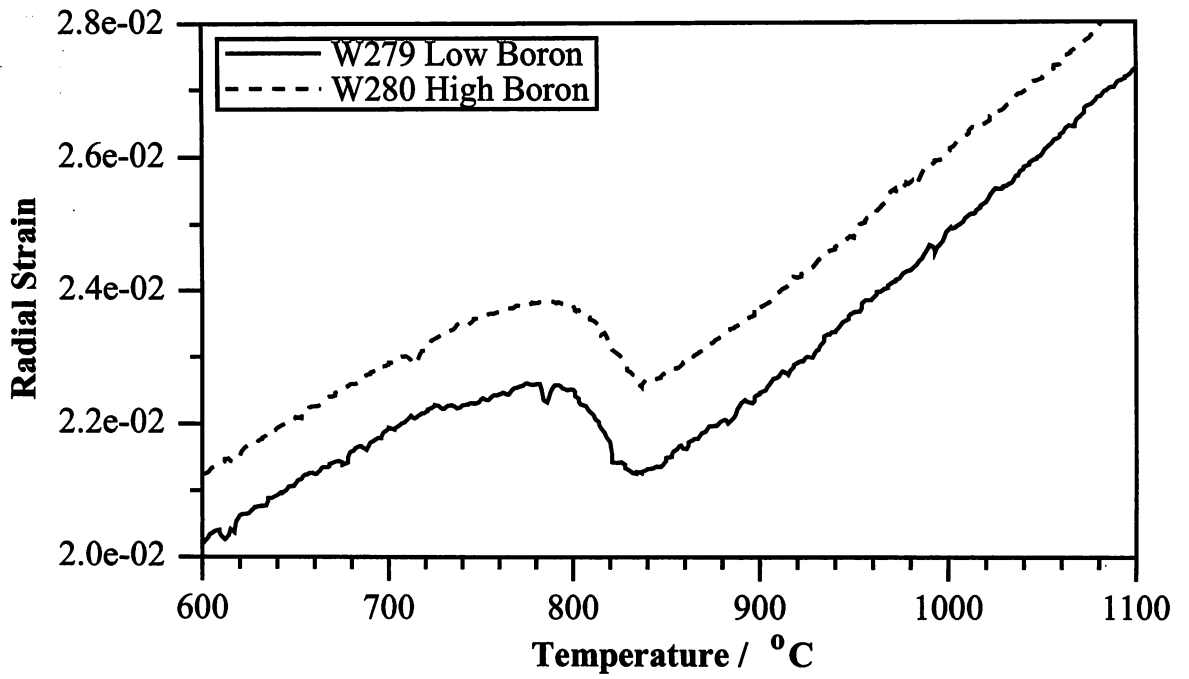
Figure 7.9 Dilatation curves for alloys W279 and W280 - continuous heating at 2 °C s^{-1}.
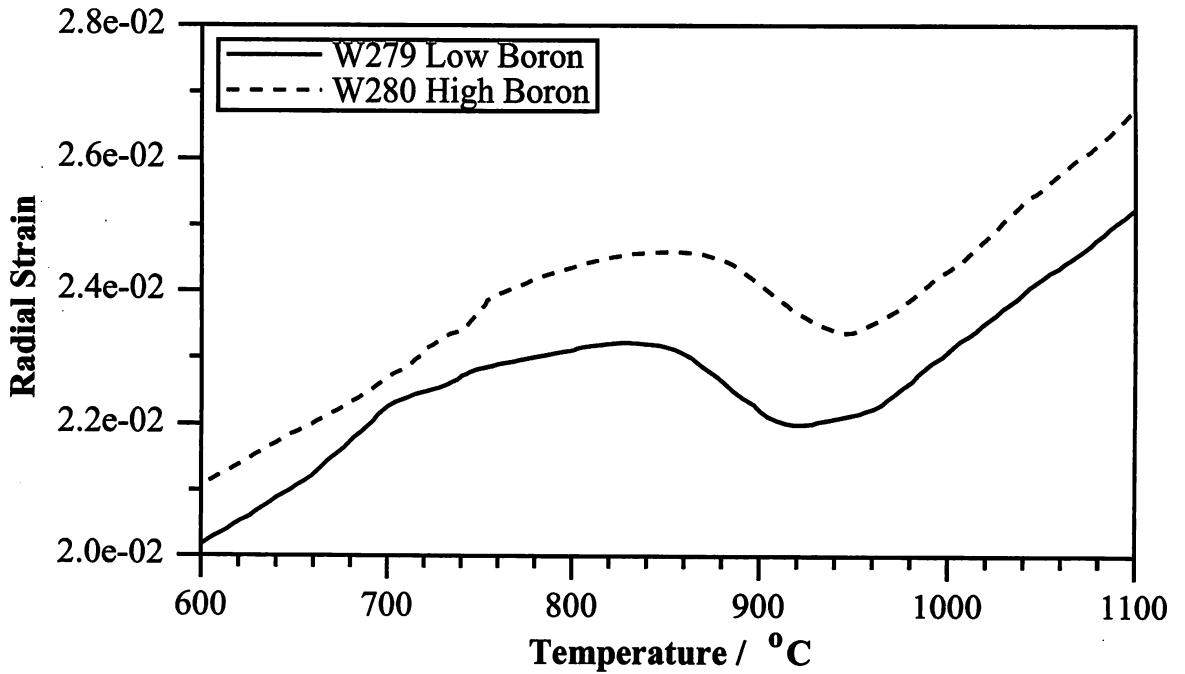
Figure 7.10 Dilatation curves for alloys W279 and W280 - continuous heating at 50 °C s^{-1}.
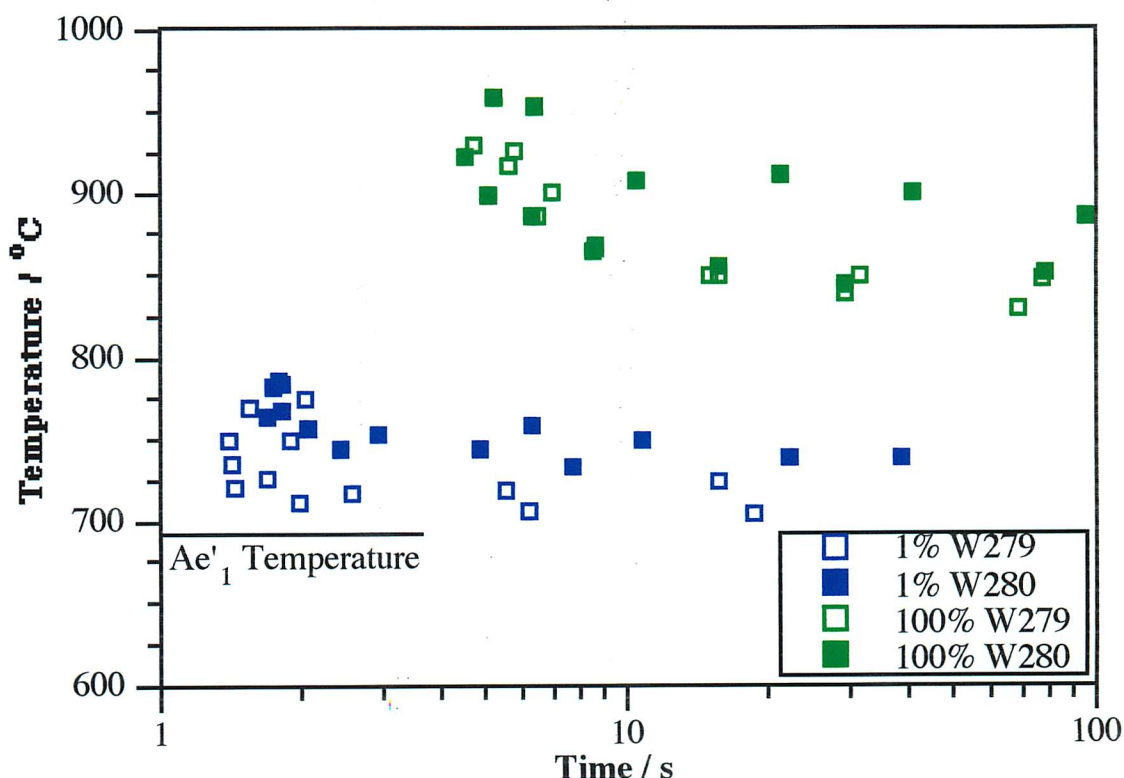
Figure 7.11 Continuous heating curves for alloys W279 and W280, 1 and 100 % transformation.

but only at relatively slow heating rates. Furthermore, any differences are reduced as transformation progresses.

7.3.3 Partial Austenitisation Experiments

Partial austenitisation experiments were conducted to understand the mechanism by which boron retards austenitisation. To provide a comparable starting microstructure, hollow samples from both weld metals were heated at 20 °C s^{-1} to an austenitising temperature of 1300 °C which was maintained for 240 s, prior to quenching ($\simeq$ 70 °C s^{-1}) with helium to a microstructure dominated by acicular ferrite. Each specimen was then reheated immediately from room temperature at 30 °C s^{-1} to a temperature of 770 °C and held for 18 s to allow partial austenitisation to occur prior to quenching ($\simeq$ 70 °C s^{-1}) with helium. Figure 7.12 shows, for both alloys, radial strain versus time during the isothermal austenitising stage at 770 °C. A much greater degree of austenitisation occurs in the low boron alloy W279 compared to the high boron alloy W280.

Scanning electron microscopy (SEM) revealed (Figures 7.13 and 7.14) that 'acicular' austenite formed intragranularly between the laths of acicular ferrite.[2] For comparison Fig-

---

[2] A CamScan S2 microscope was operated at a voltage of 20 kV. The photomicrographs

ure 7.15 shows the starting microstructure of W279 which was obtained in a similar experiment without the secondary reheating stage. It appears that the austenitisation is slightly more advanced in the low boron alloy W279 where impingement and coalescence between neighbouring austenite grains is more apparent.
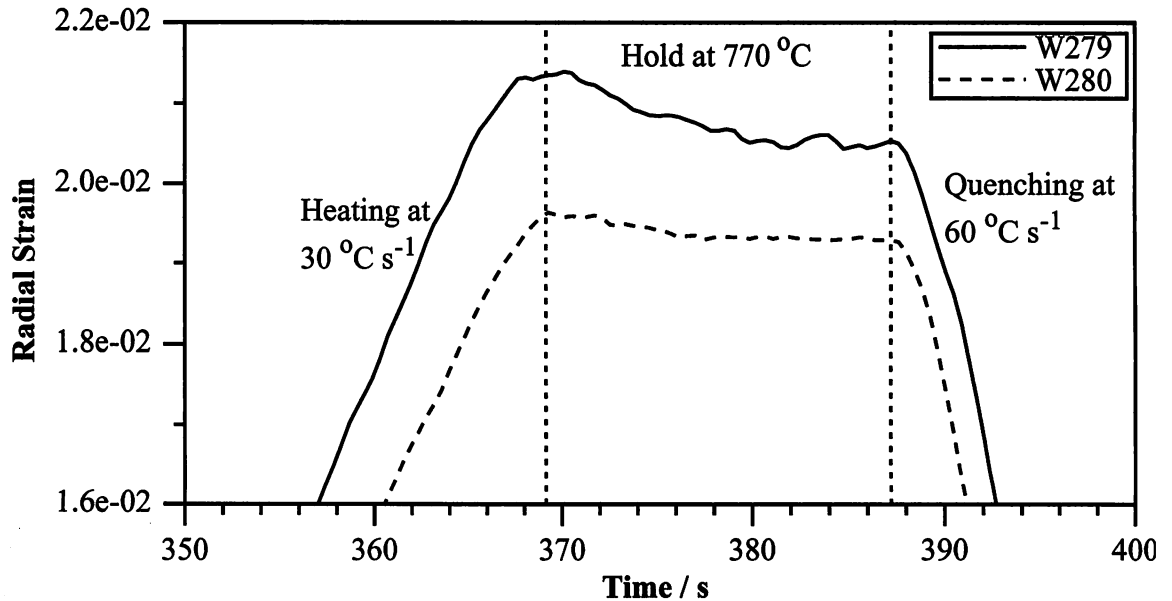
Figure 7.12 Radial strain versus time for alloys W279 and W280 during partial austenitisation experiments at 770 °C.

The effects observed are consistent with the retardation of austenite formation by the segregation of boron to intragranular transformation sites in the starting microstructure. It is speculated that this boron might stabilise any retained austenite grains present (Kimmins and Gooch, 1983). Alternatively, boron may decrease the surface energy of the intragranular laths and thereby reduce their nucleation potency.

7.4 Boron Segregation and Thermal Cycling

7.4.1 Introduction

During the study of transformations between austenite and ferrite as described above, a new phenomenon was observed; the transformation start temperature during cooling of fully austenitised samples of the weld metal W279 varied systematically with the number of successive austenitisation heat treatments. To investigate this three basic types of experimental thermal cycles were adopted:

---

shown were obtained using an image inversion technique.
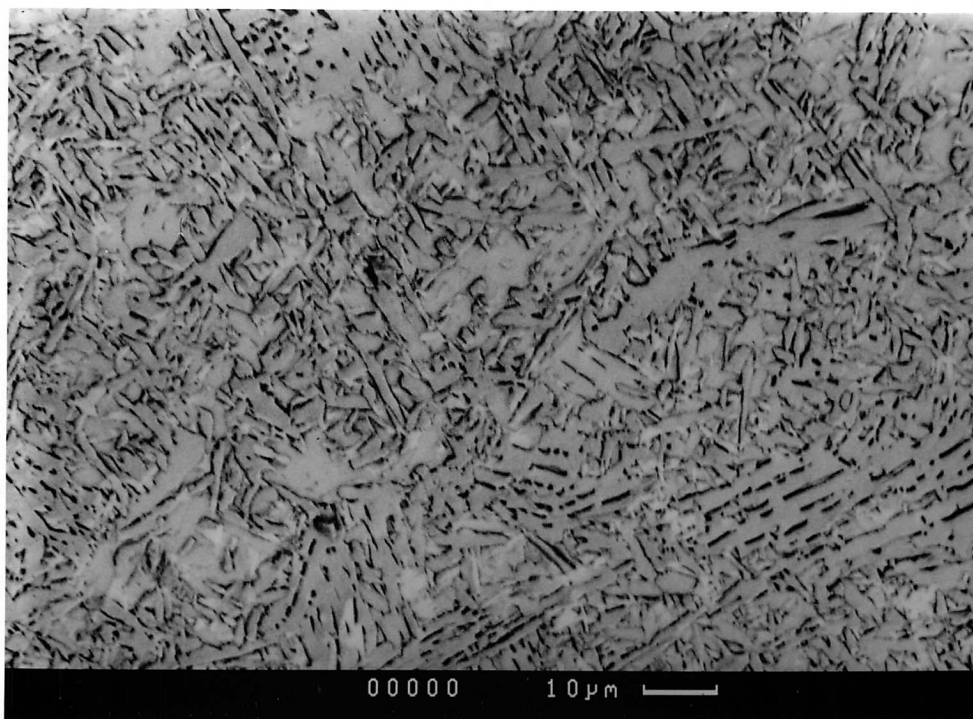
Figure 7.13 SEM image of the starting microstructure in alloy W279 as used in the partial austenitisation experiments at 790 °C.

'A' Heating at 20 °C s^{-1} to 1300 °C, hold for 300 s, cool at 7 °C s^{-1} to room temperature.

'B' Heating at 20 °C s^{-1} to 1300 °C, hold for 300 s, cool at 7 °C s^{-1} to 620 °C and quench at $\simeq$ 70 °C s^{-1} to room temperature.

'C' Heating at 20 °C s^{-1} to 1300 °C, hold for 300 s, cool at 7 °C s^{-1} to 860 °C, hold for 240 s, cool at 7 °C s^{-1} to room temperature.

7.4.2 Repeated Thermal Cycling of Low Boron Alloy

Weld W279 was subjected to five consecutive thermal cycles of type 'A', with an interval of approximately 10 minutes between each thermal cycle to allow for data acquisition and vacuum pumping. Figure 7.16 indicates that the transformation start temperature decreases by approximately 12 °C with each successive cycle, decreasing from 640 to 590 °C over five cycles. A separate experiment using another specimen of alloy W279 revealed identical results.

Figures 7.17 and 7.18 show the final microstructure of W279 after one (from a separate experiment) and five type 'A' thermal cycles respectively. More allotriomorphic ferrite formed along the austenite grain boundaries in the specimen subjected to only one thermal cycle, compared to that subjected to five thermal cycles in which the microstructure was dominated
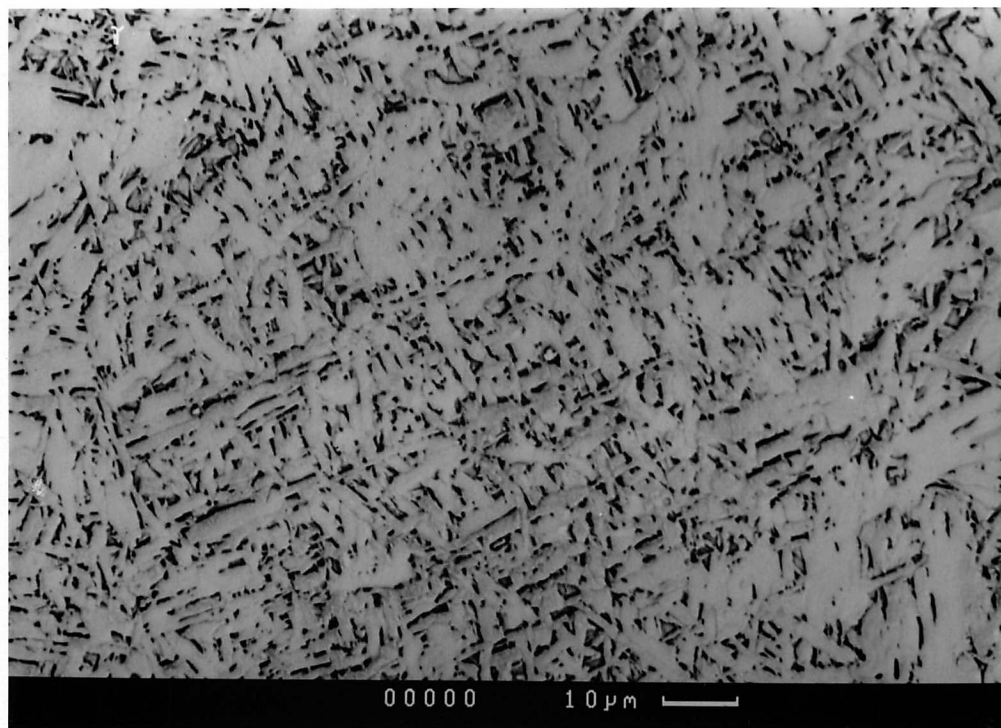
Figure 7.14 SEM image of the microstructure in alloy W279 after partial austenitisation experiments at 790 °C.

by displacive transformation products. The austenite grain size did not appear to vary significantly between the two specimens.[3] Indeed, repeated thermal cycling might be expected to refine the austenite grain size, which would tend to increase the transformation temperature (contrary to the measured trend). These results suggest that the retardation of transformation caused by repeated thermal cycling was due to a reduction in the ability of the austenite grain boundaries to act as heterogeneous nucleation sites.

7.4.3 Interrupted Thermal Cycles

To further demonstrate the reduction in the potency of the austenite grain boundaries, a specimen of weld W279 was subjected to a single thermal cycle of type 'B'. It is apparent from the dilatation data (Figure 7.19) that a significant amount of transformation occurred between 700 °C and the quench at 620 °C. Microstructural examination (Figure 7.20) confirms that allotriomorphic ferrite formed along the austenite grain boundary prior to the interrupting quench. The acicular ferrite found in the central regions of the prior-austenite grains was formed during the quench from 620 °C – other experiments have shown that it forms below

---

[3] Unfortunately attempts to measure the austenite grain size, using a thermal etching technique, as a function of the number of thermal cycles performed proved unsuccessful.
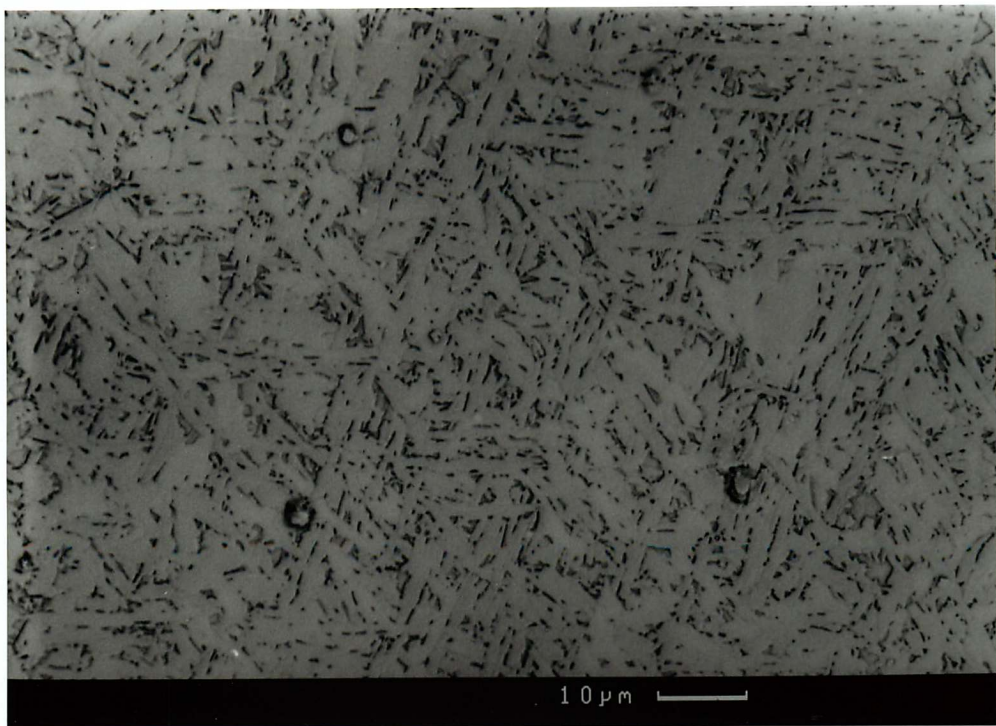
Figure 7.15 SEM image of the microstructure in alloy W280 after partial austenitisation experiments at 790 °C.

Figure 7.16 Radial strain versus temperature during cooling in the sample of alloy W279 subjected to five consecutive thermal cycles of type 'A'.

Figure 7.17 The microstructure of alloy W279 after one thermal cycle of type 'A'.
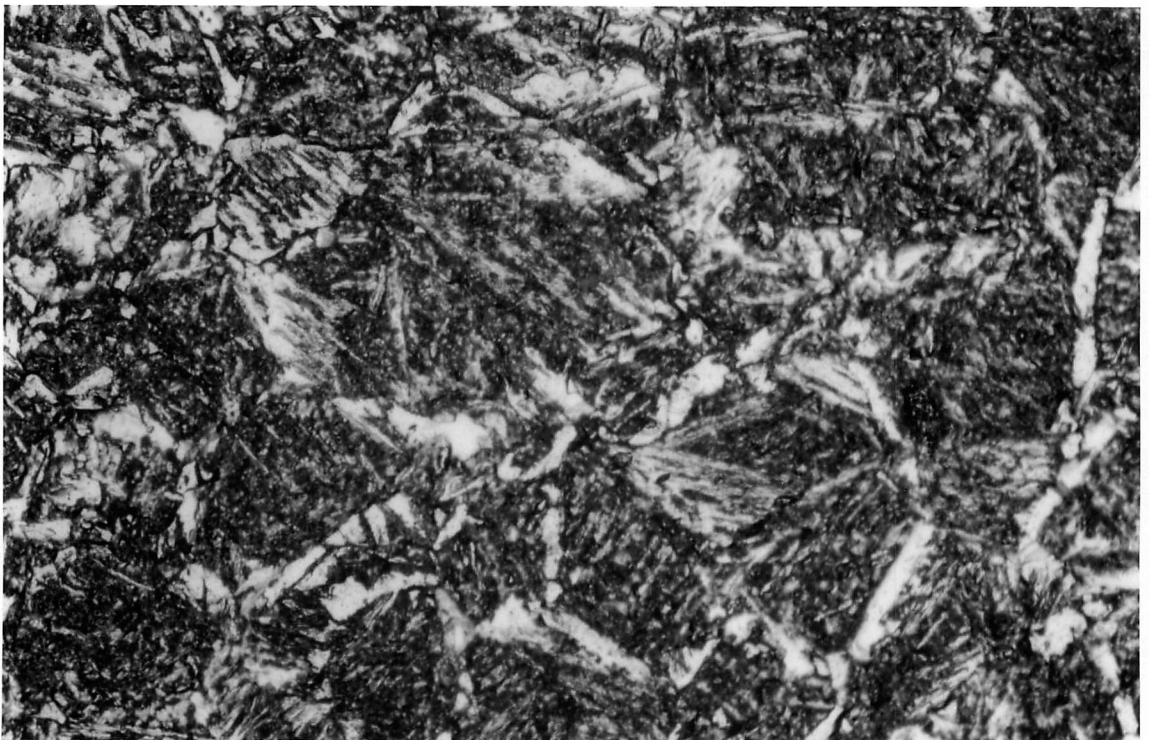
Figure 7.18 The microstructure of alloy W279 after five consecutive thermal cycles of type 'A'.

Figure 7.19 Radial strain versus temperature during cooling in the sample of alloy W279 subjected to one interrupted thermal cycle of type 'B'.

$\simeq$ 590 °C (section 6.3.2).

Another specimen of weld W279 was subjected to four thermal cycles of type 'A' followed by a single thermal cycle of type 'B'. The microstructure after the fifth run is shown in Figure 7.21. Dilatation versus temperature plots again demonstrated a cumulative decrease in the transformation start temperature with the number of thermal cycles. The microstructure found after the fifth interrupted run was dominated by acicular ferrite which had formed during the quench from 620 °C. Very little allotriomorphic ferrite had nucleated along the austenite grain boundaries. This was confirmed by the dilatation data for the fifth run (Figure 7.22) which demonstrate a lack of transformation prior to the helium gas quench.

7.4.4 Storage at Room Temperature

After storage for three days at room temperature the same specimen as used in the experiments described in section 7.4.2 was subjected to a further five thermal cycles of type 'A', again with an interval of approximately 10 minutes between each thermal cycle. The results were surprising (Figure 7.23). The transformation start temperature during the sixth run had increased to about 680 °C, compared with 570 °C found on the fifth run three days earlier. It then decreased successively to about 550 °C by the tenth cycle.

It appears that the full nucleation potency of the austenite grain boundaries had been

170
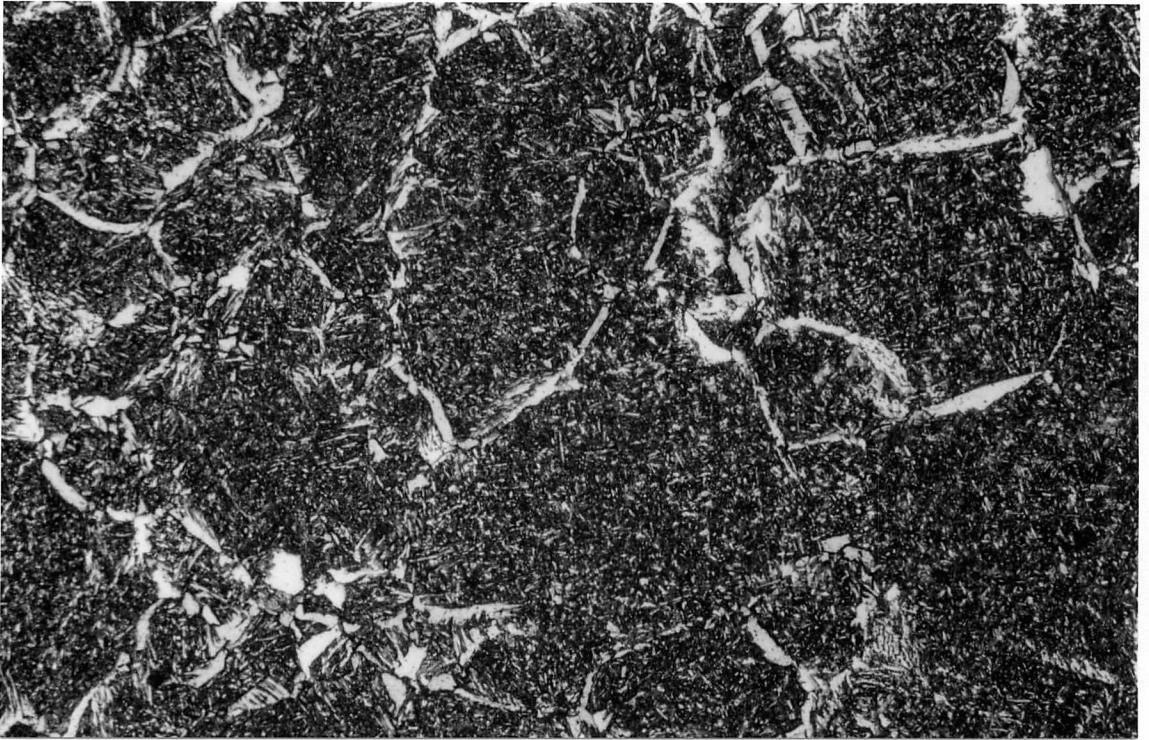
Figure 7.20 The microstructure of alloy W279 after one interrupted thermal cycle of type 'B'.

restored and even enhanced during three days storage at room temperature; an observation which cannot be rationalised by any variation in the austenite grain size which remains constant at ambient temperature.

7.4.5 Discussion

Boron segregates to the austenite grain boundaries in two ways, equilibrium and non-equilibrium segregation, depending on the cooling rate from high temperature (section 7.3.1). Although the details remain unclear, it is suggested that observations made during thermal cycling might be explained by the interaction of non-equilibrium segregation boron-vacancy complexes, the equilibrium segregation of free boron atoms, the precipitation of boron-rich phases and the reconstitution of the original austenite grains due to a memory effect (section 7.3.1). The following explanation is therefore tentatively proposed as a starting point for discussion.

During the first five thermal cycles the amount of boron at the reconstituted austenite grain boundaries increases after each cycle, eventually exceeding the equilibrium concentration. This is because the rapid cooling rate and the time interval between cycles does not allow significant precipitation of boron-rich phases or permit boron atoms to re-enter the matrix. The resulting cumulative increase in the boundary boron concentration causes the observed

171
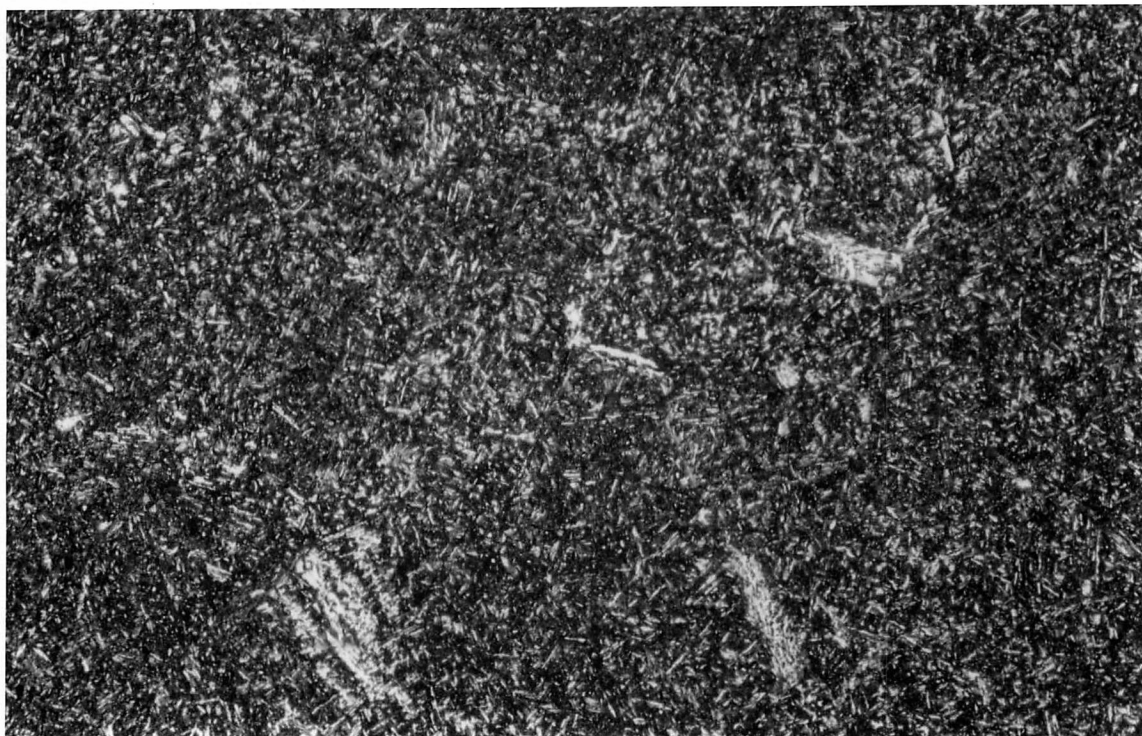
Figure 7.21 The microstructure of alloy W279 after four consecutive thermal cycles of type 'A' which were immediately followed by one interrupted thermal cycle of type 'B'.

increase in hardenability. However, if the time interval between thermal cycles is long then boron-rich phases may precipitate and some boron atoms may re-enter the matrix to reduce the supersaturation at the austenite grain boundaries. This increases the energy of the austenite grain boundaries and thereby restores their nucleation potency. The presence of boron-rich precipitates at the austenite grain boundaries should also raise their nucleation potency. In order to test this hypothesis the following experiments were undertaken.

7.4.6 Cycling of Welds with Different Concentrations of Boron

Weld 113 (Table 7.1) supplied by ESAB (Sweden) does not contain boron; it was subjected to five thermal cycles of type 'A'. Figure 7.24 reveals that the transformation start temperature did not decrease systematically with cycling, changing between 520 °C and 540 °C.[4] This indicates that it is boron which caused the hardenability effects observed in weld W279. However, because alloy 113 has in any case a high overall hardenability, this result may not be conclusive (the main transformation product is intragranularly nucleated acicular ferrite and

---

[4] The initial increase in the start temperature between the first and the second cycles is possibly due to variations in the austenite grain size because as-deposited weld metal usually has a relatively large austenite grain size compared to reheated weld metal.
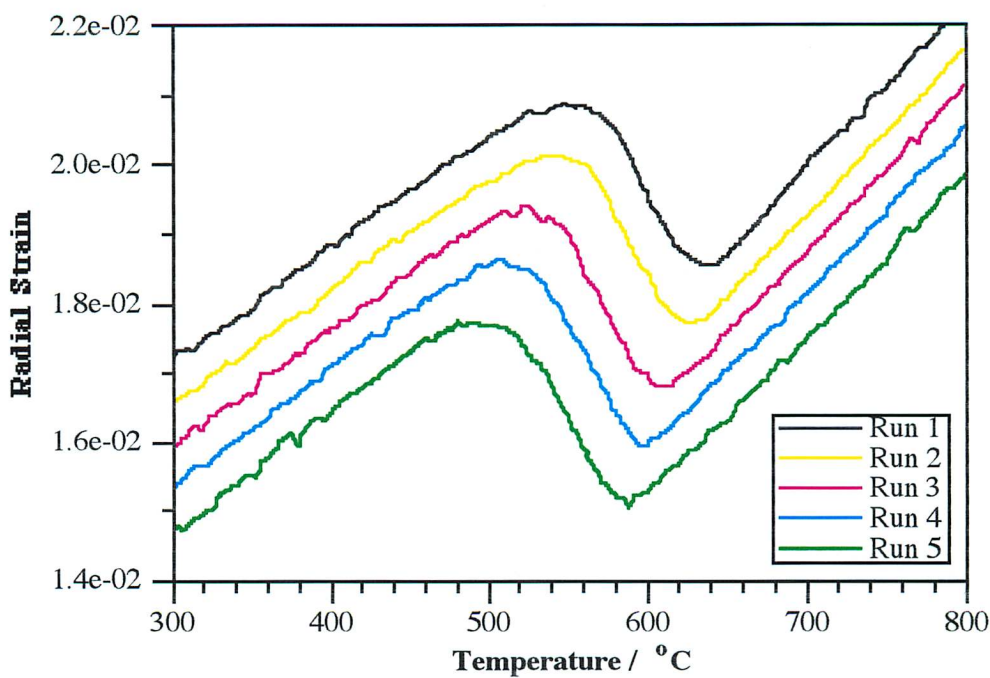
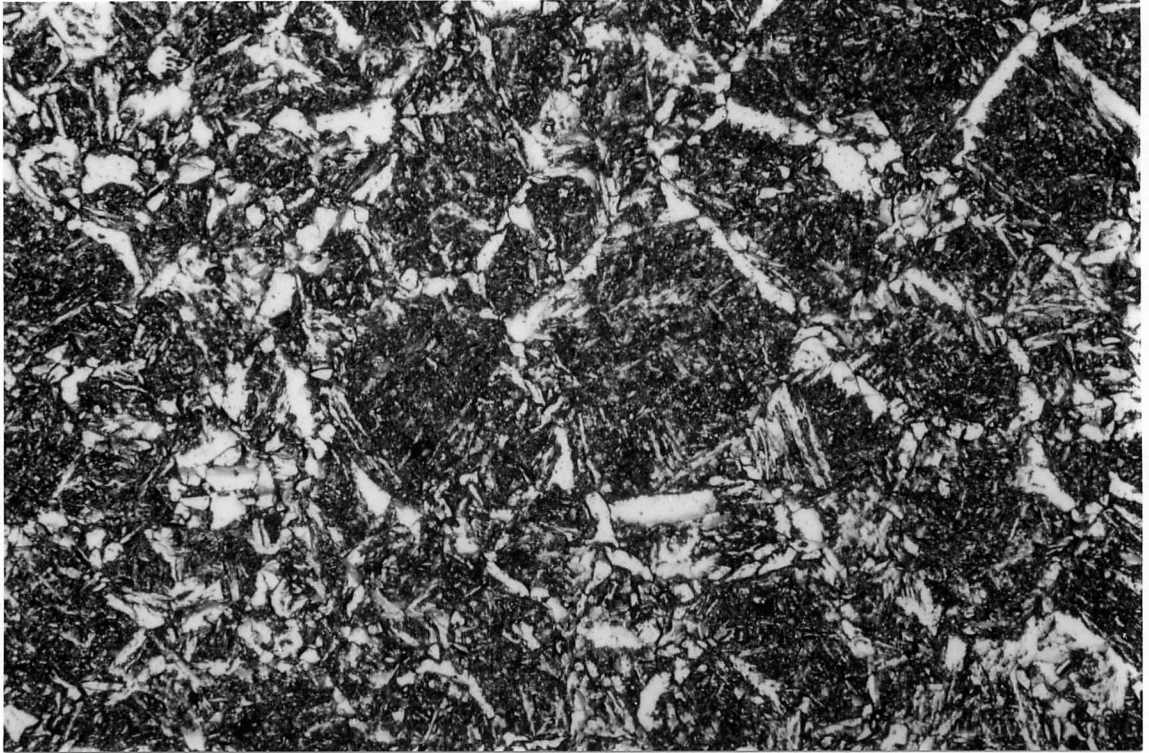Figure 7.22 Radial strain versus temperature during cooling in the sample of alloy W279 subjected to four consecutive thermal cycles of type 'A' which were immediately followed by one interrupted thermal cycle of type 'B'.
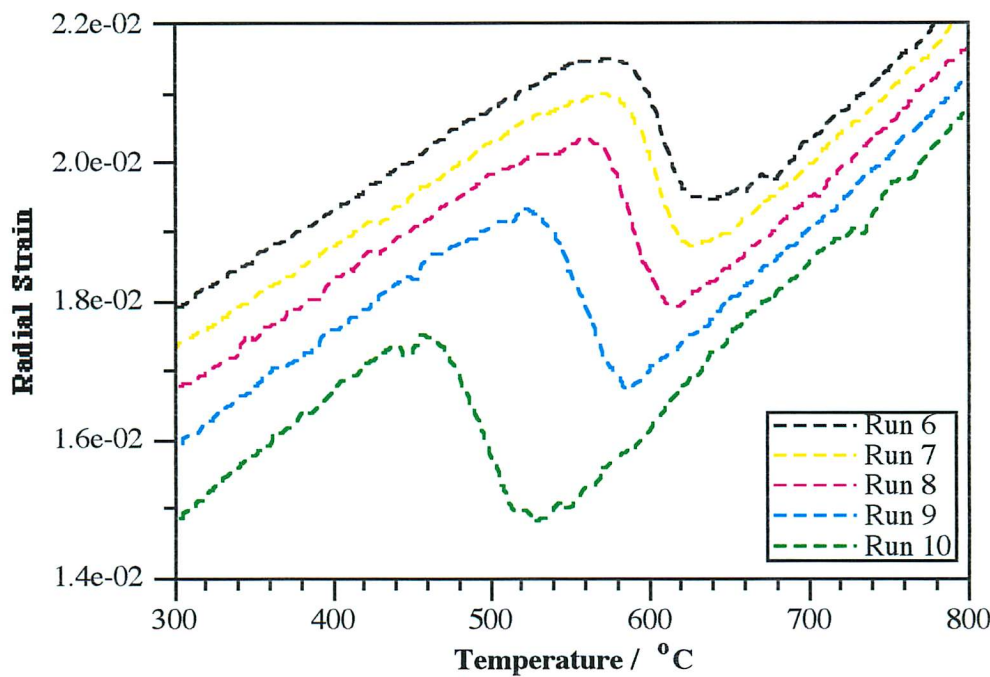
Figure 7.23 Radial strain versus temperature during cooling in the sample of alloy W279 stored at room temperature for three days before being subjected to a further five consecutive thermal cycles of type 'A'.

not allotriomorphic ferrite). The experiment was repeated with a low-alloy steel weld metal (Table 7.1) supplied by BHP Steel (Australia), containing less than 3 ppm wt boron. Figure 7.25 shows that the transformation start temperature decreased from about 630 to 580 °C over the five thermal cycles performed.

Alloy	C	Mn	Si	Ni	Mo	Cr	V	Al	Ti	S	O	N	B	Cu	P	Nb
113	0.059	1.48	0.47	2.0	0.37	0.63	–	0.022	0.006	–	0.0304	0.0055	–	–	–	–
BHP	0.07	1.08	0.09	0.026	0.19	0.016	0.003	0.032	0.014	0.004	–	0.0036	0.0003	0.01	0.014	0.04

Table 7.1 The compositions of the other two weld metals used in the thermal cycling experiments.

The high boron weld W280 was given three thermal cycles of type 'A' (experimental difficulties prevented further cycles). Figure 7.26 indicates that the transformation start temperature decreased as the number of runs increased, from about 615 °C during the first run to 600 °C.

If a weld, such as W280, contains a relatively high concentration of boron then this will cause a considerable reduction in the potency of the austenite grain boundaries during the first thermal cycle, subsequent cycles having a minor effect. It follows that welds with low concentrations of boron (*e.g.* the BHP alloy and W279) are more sensitive to repeated thermal cycling.
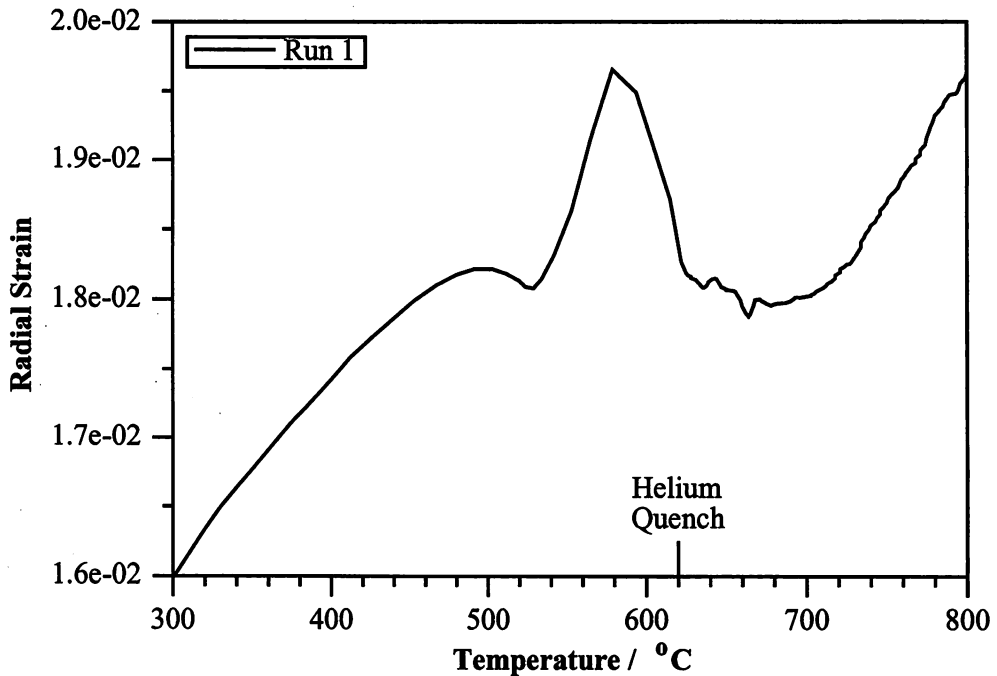

Figure 7.26 Radial strain versus temperature during cooling in the sample of alloy W280 subjected to three consecutive thermal cycles of type 'A'.

Figure 7.24 Radial strain versus temperature during cooling in the sample of alloy 113 subjected to five consecutive thermal cycles of type 'A'.

Figure 7.25 Radial strain versus temperature during cooling in the BHP alloy subjected to five consecutive thermal cycles of type 'A'.

7.4.7 Isothermal Equilibration above the Ae_3 Temperature

To distinguish non-equilibrium and equilibrium segregation effects, a series of six inter-rupted cooling cycles of type 'C' were performed using the low boron alloy W279. Thermal cycle 'C' is similar to 'A', but the cooling stage (7 °C s^{-1}) is interrupted with a four minute isothermal heat treatment at 860 °C. This temperature is 25 °C above the calculated Ae_3 temperature of this alloy and should allow any deviations from equilibrium to be removed. Four minutes is about ten times the period required [5] for boron diffusion across 100 μm. Thus, the boron concentration at the austenite grain boundary should remain constant during repeated thermal cycling.
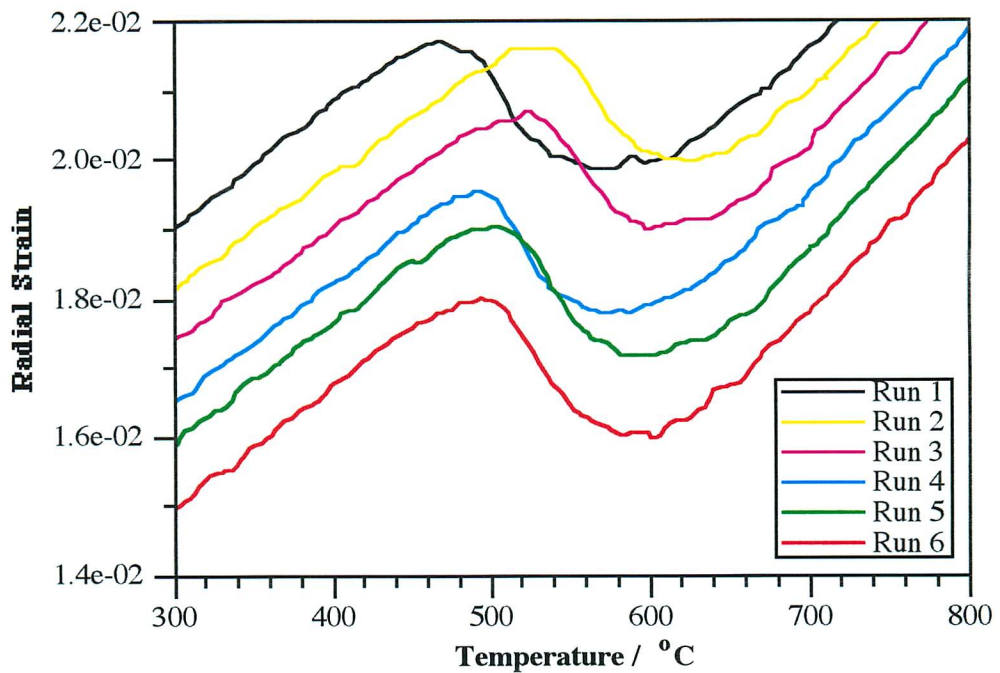
Figure 7.27 Radial strain versus temperature during cooling in the sample of alloy W279 subjected to six consecutive equilibrating thermal cycles of type 'C'.

Figure 7.27 demonstrates that the equilibrating isothermal treatment at 860 °C has a dramatic effect on the observed transformation start temperature, which did not decrease with cycling. Instead it increased after the first cycle from 620 to 665 °C and thereafter remained approximately constant. This indicates that it is the non-equilibrium segregation of boron–vacancy complexes during cooling that is responsible for the cumulative reduction in

---

[5] The diffusion distance (cm) of free boron in austenite was calculated as $2.4\sqrt{Dt}$ (Shewmon, 1963), where t is time and the diffusivity was evaluated according to Busby (1953) as $D = 2 \times 10^{-3} \exp(-87900/RT)$ (cm^2 s^{-1}), where R is the gas constant (J mole^{-1}) and T is the absolute temperature.

the nucleation potency of the austenite grain boundaries during repeated thermal cycling.

7.4.8 Storage in Liquid Nitrogen

Perhaps the most surprising experimental result was the complete restoration of the nucleation potency of the austenite grain boundaries during storage for three days at room temperature (section 7.4.4). It appears somewhat implausible that boron atoms could segregate away from the prior-austenite grain boundaries and/or boride precipitation could occur at room temperature. A specimen of weld W279 was given five consecutive thermal cycles of type 'A' and then stored at a temperature of -196 °C in liquid nitrogen for three days. Upon removal from the liquid the specimen was subjected to a further five thermal cycles of type 'A'. Figure 7.28 reveals that the transformation start temperature during cooling decreased from 640 to 590 °C during the first five consecutive cycles. However, the potency of the austenite grain boundaries was fully restored during the three day interval at -196 °C (Figure 7.29). During the second series of five cycles the transformation temperature dropped from 650 to 620 °C.

This rather enigmatic result appears to be inconsistent with the argument proposed earlier, that the precipitation of boron-rich phases and/or the segregation of free boron atoms away from the boundary region is responsible for the restoration of the nucleation potency of the austenite grain boundaries. However, it is tentatively suggested that 'quenching' the sample in liquid nitrogen for three days may have induced the formation of boron-rich phases local to the austenite boundary.

7.4.9 Storage at Room Temperature for One Hour

One final experiment involved subjecting a sample of weld W279 to five consecutive thermal cycles of type 'A' (Figure 7.30) before holding at room temperature for just one hour. After this period a further five consecutive thermal cycles of type 'A' were performed (Figure 7.30). It is apparent that one hour at room temperature does not allow the austenite grain boundaries to recover their nucleation potency, the transformation start temperature decreasing from 680 to 620 °C during the first five cycles and from 600 to 570 °C during the sixth to tenth cycles. Therefore, it is not yet possible to adequately explain the mechanism by which the nucleation potency of the austenite grain boundaries is restored during storage for three days at either room temperature or -196 °C.

7.5 Summary

Investigations into the effects of trace additions of boron on the austenite to ferrite transformation in steel weld metals have indicated that boron may induce a slight retardation of the
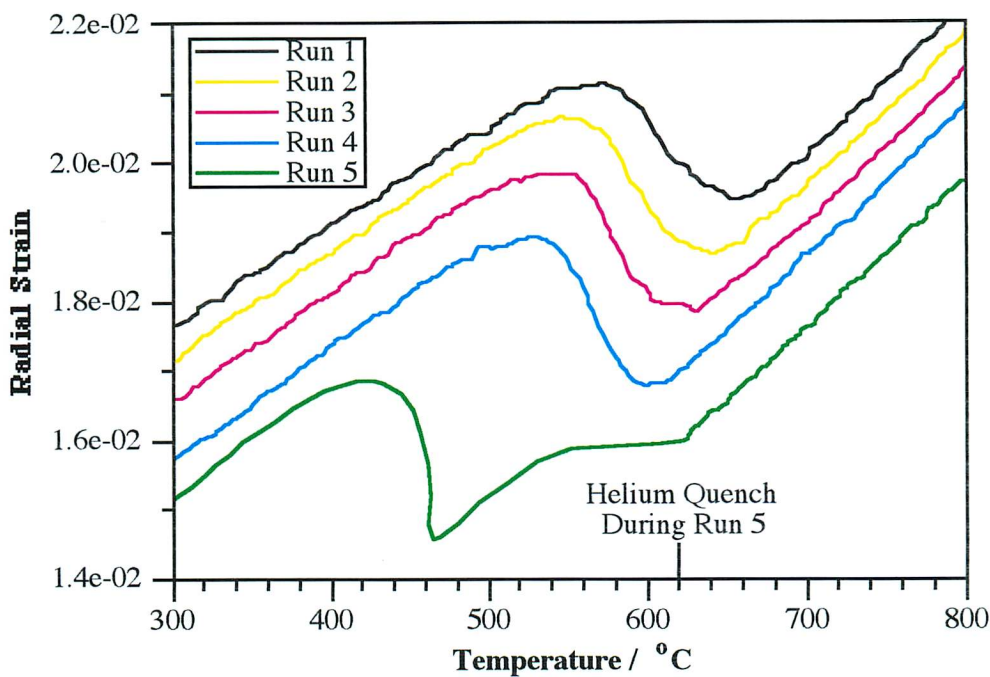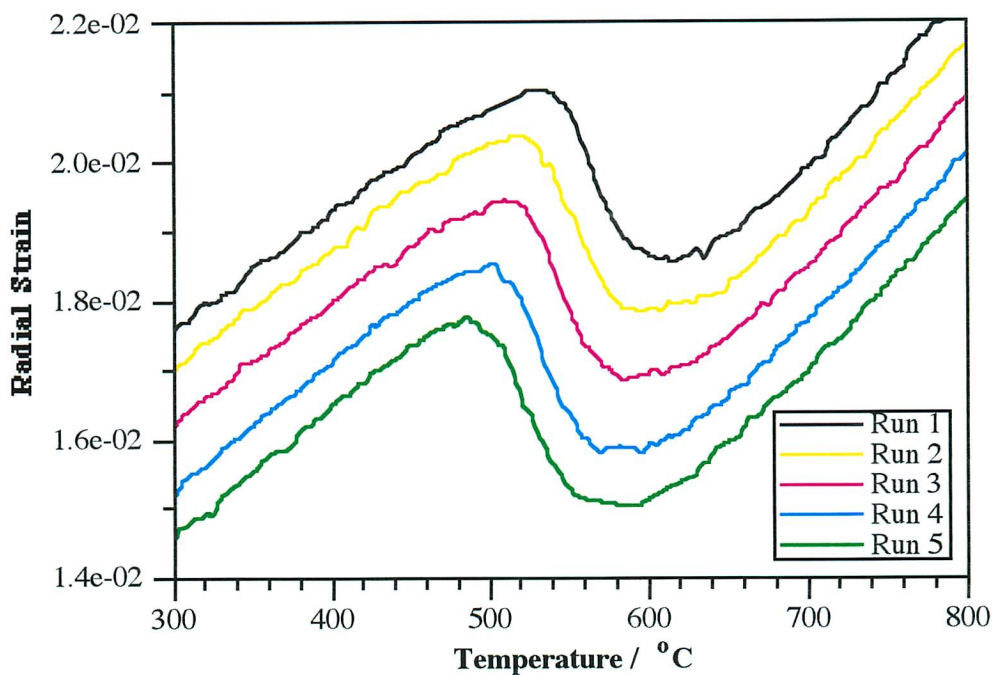
Figure 7.28 Radial strain versus temperature during cooling in the sample of alloy W279 subjected to five consecutive thermal cycles of type 'A' prior to storage in liquid nitrogen for three days.
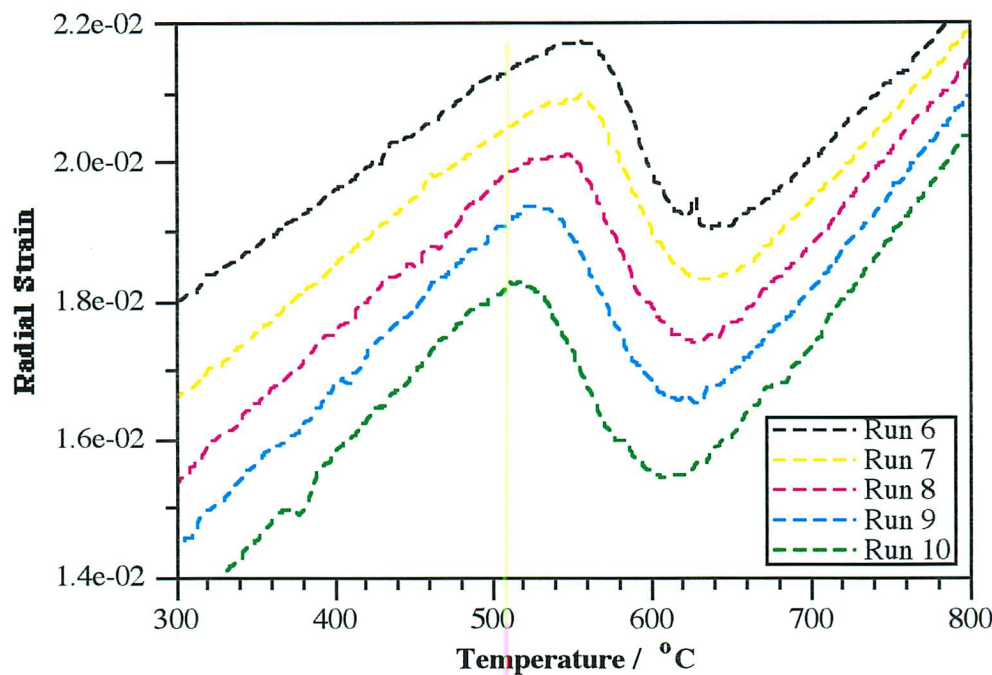
Figure 7.29 Radial strain versus temperature during cooling in the sample of alloy W279 subjected to an additional five thermal cycles of type 'A' after storage in liquid nitrogen for three days.
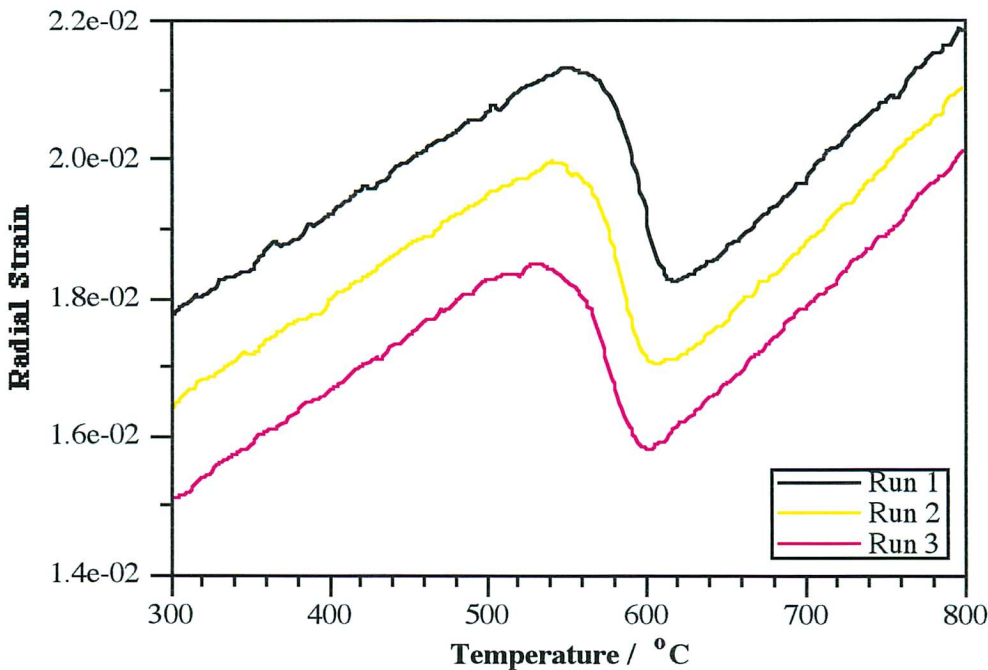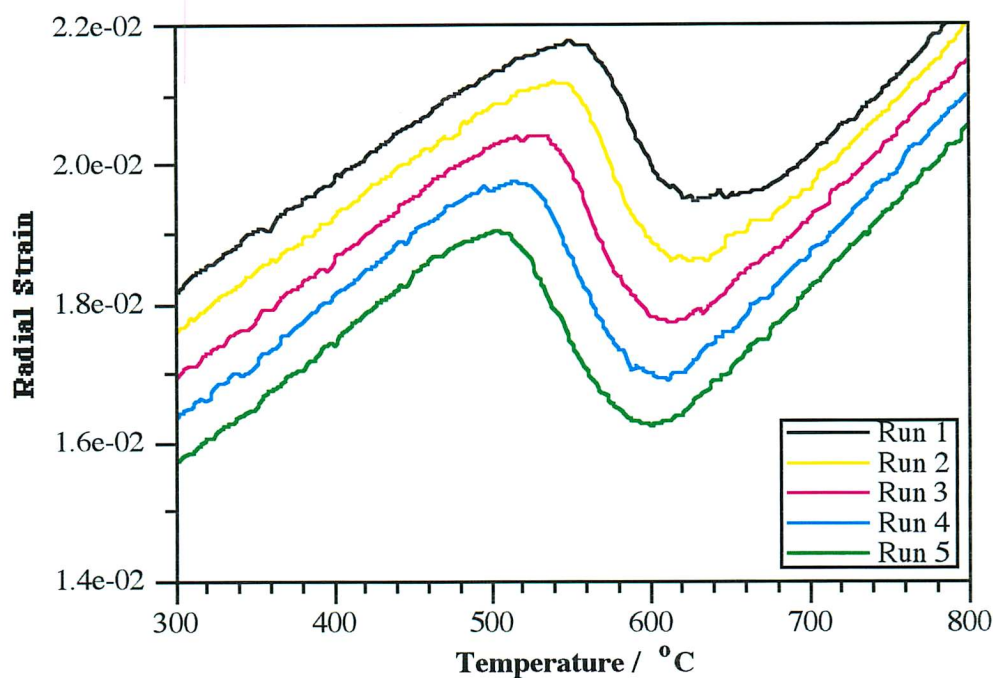
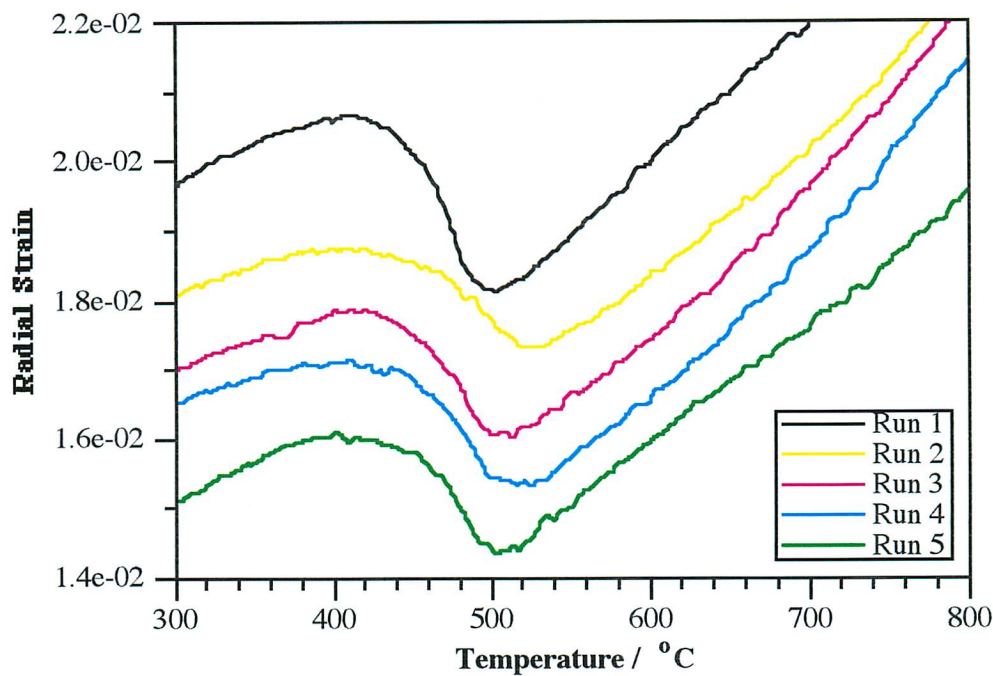Figure 7.30 Radial strain versus temperature during cooling in the sample of alloy W279 subjected to five consecutive thermal cycles of type 'A' prior to storage at room temperature for one hour.
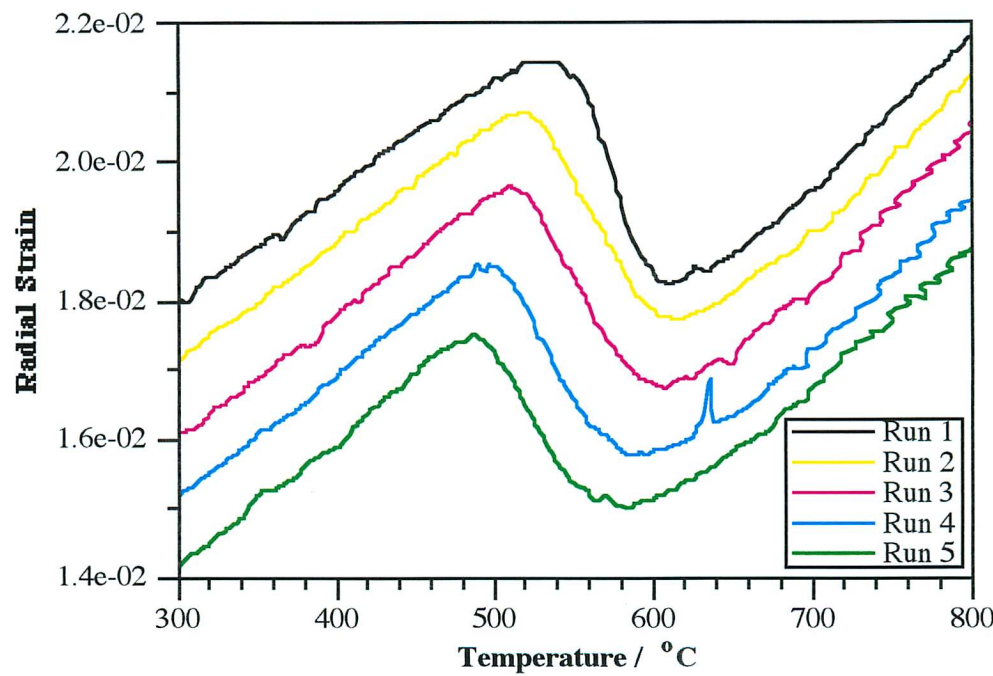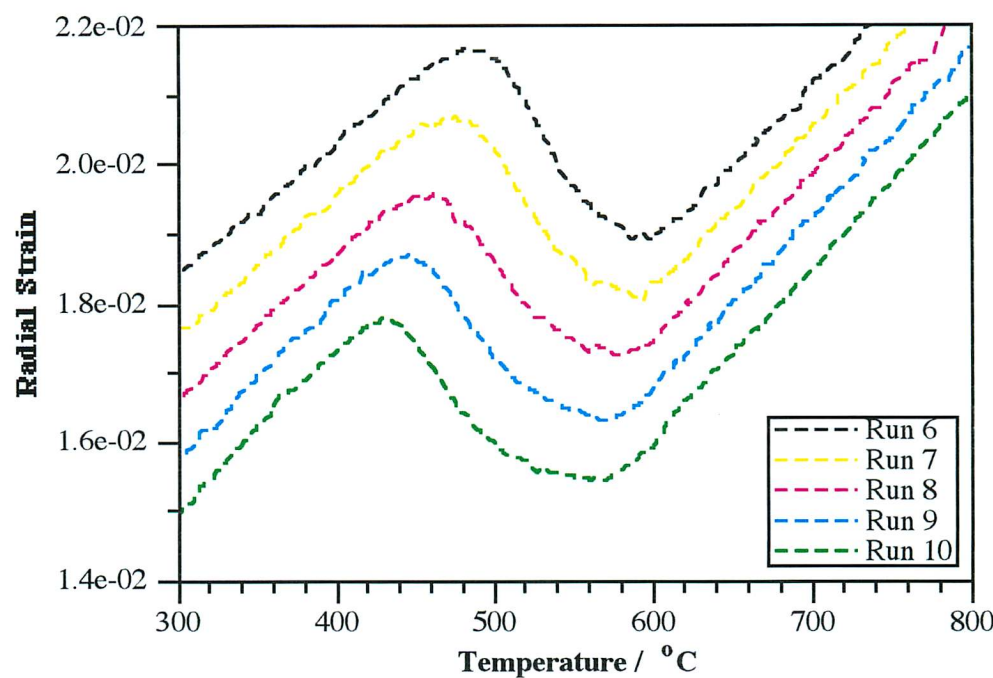

Figure 7.31 Radial strain versus temperature during cooling in the sample of alloy W279 subjected to an additional five thermal cycles of type 'A' after storage at room temperature for one hour.

179

transformation to acicular ferrite. However, the effect is small, much less than the pronounced retardation of the transformation to allotriomorphic ferrite. The influence of boron on the formation of austenite during heating has also been studied. As anticipated, the boron retards the transformation during heating, though the effects diminish as transformation progresses because the rate of transformation is extremely rapid at elevated temperatures.

The transformation from austenite in steels containing less than 5 ppm wt boron has revealed systematic variations during repeated experiments. These variations are not completely understood, but are believed to be related to the non-equilibrium segregation of boron-vacancy complexes and the austenite memory effect.

CHAPTER EIGHT

Suggestions for Future Research

8.1 Modelling Simultaneous Transformation Kinetics

It is suggested that the theory developed in chapter four to describe simultaneous transformation kinetics in steels could in the future be extended to allow for the intergranular nucleation of bainite and the intragranular nucleation of acicular ferrite. Such a 'complete' phase transformation model could be used to describe rigorously the competitive evolution of microstructure during rapid cooling from high temperatures in both wrought and welded steels. This model might be further enhanced by incorporating the theories outlined in chapter five which describe inclusion nucleation potency and the effects of soluble boron on transformation behaviour. Transformations in thermo-mechanically processed steels could also be represented if equivalent theory for nucleation and growth from linear defects such as dislocations were developed.

8.2 Modelling Inclusion Nucleation Potency

The strong influence of chemical depletion of the austenite matrix on the nucleation potency of inclusions was revealed in chapter five, therefore, it is considered that the various chemical interactions that might occur between the austenite and inclusion should be investigated using theoretical approaches. The interface between ferrite and various inclusion phases could be usefully characterised using the O-lattice method to provide a fresh insight into possible epitaxial relationships. This technique could then be used to establish how the relative interfacial energy of each system influences inclusion nucleation potency.

8.3 Boron – Effects in Steel Welds

It would be interesting to use an atom probe to study the interfaces between laths of acicular ferrite and retained austenite to ascertain whether a boron concentration exists there. If this is the case then other techniques could be used to investigate how this boron might delay the reverse transformation to austenite during heating. Particle tracking autoradiography or secondary ion mass spectroscopy could be employed to examine the segregation of boron to the austenite grain boundaries in an attempt to rationalise the enigmatic variation in transformation behaviour found during repeated thermal cycling.

APPENDIX ONE

Subroutine MAP_SIM_TRANS

0. Provenance of Source Code

S.J. Jones and H.K.D.H. Bhadeshia, Phase Transformations Group, Department of Materials Science and Metallurgy, University of Cambridge, Cambridge, UK.

1. Purpose

To calculate the volume fraction of various simultaneously nucleating phases (allotriomorphic, idiomorphic, Widmanstätten ferrite and pearlite) in steels where nucleation occurs randomly at non-metallic inclusions and at planar austenite grain boundaries.

2. Specification

```
    SUBROUTINE MAP_SIM_TRANS(I2,TIME,PRETIME,DTIME,PARA1,
&PARA3,DIFFUSY,GRWID,GRPEARL,AR,ARWID,ARPEARL,
&VIINCA,VIINCWID,VIINCPEARL,VIA,VIWID,VIPEARL,
&EQVOLFRAC,OBOUND,PERCENTRANS,VTOTTRANS,VAREAL,
&VWIDREAL,VPEARLREAL,VAREALINC,VWIDREALINC,
&VPEARLREALINC,IFLAG,SATTIME)
    IMPLICIT DOUBLE PRECISION(A-H,K-Z), INTEGER(I-J)
    DOUBLE PRECISION QA(1001),PREQA(1001),OREA(3000),PREOREA(3000),
&QWID(1001),PREQWID(1001),OREWID(3000),PREOREWID(3000),QPEARL(1001),
&PREQPEARL(1001),OREPEARL(3000),PREOREPEARL(3000),
&Y(3000),NOPARTINCA(1001),NOPARTINCWID(1001),NOPARTINCPEARL(1001),
&NOPARTGBA(1001),NOPARTGBWID(1001),NOPARTGBPEARL(1001),
&TIMEOFNUCL(1001),EXTTHICK(1001)
```

3. Description

The volume fraction of a number of simultaneously nucleating phases in a system is calculated using a new numerical approach which is based on the methods of Johnson, Mehl, Avrami and Cahn. Six possibilities are allowed for:

1. Parabolic reconstructive growth of spheres of idiomorphic ferrite from random nuclei.

2. Parabolic reconstructive growth of discs of allotriomorphic ferrite from boundary nuclei.

3. Linear growth of displacive plates of Widmanstätten ferrite from random nuclei.

4. Linear growth of displacive plates of Widmanstätten ferrite from boundary nuclei.

5. Linear reconstructive growth of spheres of pearlite from random nuclei.

6. Linear reconstructive growth of discs of pearlite from boundary nuclei.

The model may be modified to allow any number of phases to nucleate at any number of sites.

4. References

1. S.J. Jones, *PhD. thesis, University of Cambridge, UK*, (submitted in 1996).

2. S.J. Jones and H.K.D.H. Bhadeshia, *Acta. Metall.*, (submitted in 1996).

3. S.J. Jones and H.K.D.H. Bhadeshia, *Metall. Trans.*, (submitted in 1996).

4. J.W. Cahn, The kinetics of grain boundary nucleated reactions, *Acta. Metall.*, **4**, (1956), 449-459.

5. J.W. Christian, The theory of phase transformations in metals and alloys, Part 1, 2nd ed., *Permagon, Oxford, UK*, (1965).

5. Parameters

5.1 Input Parameters

I2 - integer
I2 represents the time interval.

TIME - real
TIME is the elapsed time from the start of the transformation to the end of the current time interval (s).

PRETIME - real
PRETIME is the elapsed time from the start of the transformation to the end of the previous time interval (s).

DTIME - real
DTIME is the current time interval (s).

PARA1 - real
PARA1 is the natural 1-dimensional parabolic thickening parameter of allotriomorphic ferrite.

PARA3 - real
PARA3 is the natural 3-dimensional parabolic thickening parameter of idiomorphic ferrite.

DIFFUSY - real
DIFFUSY is the diffusivity of carbon in austenite (m^2 s^{-1}).

GRWID - real
GRWID is the lengthening rate of the Widmanstätten ferrite plates (m s^{-1}).

GRPEARL - real
GRPEARL is the lengthening rate of the pearlite discs (m s^{-1}).

AR - real
AR is the aspect ratio of the allotriomorphic ferrite discs.

ARWID - real
ARWID is the aspect ratio of the plates of Widmanstätten ferrite.

ARPEARL - real
ARPEARL is the aspect ratio of the pearlite discs.

VIINCA - real

VIINCA is the nucleation rate per unit volume of idiomorphic ferrite which nucleates randomly throughout the parent phase (m^{-3} s^{-1}).

VIINCWID - real
VIINCWID is the nucleation rate per unit volume of Widmanstätten ferrite which nucleates randomly throughout the parent phase (m^{-3} s^{-1}).

VIINCPEARL - real
VIINCPEARL is the nucleation rate per unit volume of pearlite which nucleates randomly throughout the parent phase (m^{-3} s^{-1}).

VIA - real
VIA is the nucleation rate per unit area of grain boundary of allotriomorphic ferrite (m^{-2} s^{-1}).

VIWID - real
VIWID is the nucleation rate per unit area of grain boundary of Widmanstätten ferrite (m^{-2} s^{-1}).

VIPEARL - real
VIPEARL is the nucleation rate per unit area of grain boundary of pearlite (m^{-2} s^{-1}).

EQVOLFRAC - real
EQVOLFRAC is the total equilibrium volume fraction of the various product phases.

OBOUND - real
OBOUND is the grain boundary area per unit volume in the parent phase (m^{-1}).

5.2 Output Parameters

PERCENTRANS - real
PERCENTRANS represents the ratio of the total volume fraction of all the transformation products to the total equilibrium volume fraction, expressed as a percentage.

VTOTTRANS - real
VTOTTRANS is the total volume fraction of all the transformation products.

VAREALINC - real
VAREALINC is the real volume fraction of randomly nucleated idiomorphic ferrite.

VWIDREALINC - real
VWIDREALINC is the real volume fraction of randomly nucleated Widmanstätten ferrite.

VPEARLREALINC - real
VPEARLREALINC is the real volume fraction of randomly nucleated pearlite.

VAREAL - real
VAREAL is the real volume fraction of boundary nucleated allotriomorphic ferrite.

VWIDREAL - real
VWIDREAL is the real volume fraction of boundary nucleated Widmanstätten ferrite.

VPEARLREAL - real
VPEARLREAL is the real volume fraction of boundary nucleated pearlite.

IFLAG - integer
IFLAG is set to unity when 99 % of the grain boundary of the parent phase is saturated.

SATTIME - real

SATTIME is the time when 99 % of the grain boundary of the parent phase is saturated (s).

EXTTHICK - real

EXTTHICK is the mean *extended* thickness of all the phases which are boundary nucleated.

6. Error Indicators

If MAXHGT exceeds YEND then an error is reported and the program execution is stopped.

7. Accuracy

The accuracy achieved depends upon the time interval chosen. To minimise the computational effort required a variable time interval should be used. As the transformation proceeds the time interval may be gradually increased to allow the overall transformation kinetics to be represented.

8. Further Comments

1. The numerical approach used allows changes in the nucleation and growth characteristics of the various phases to be modelled according to changes in the degree of solute enrichment in the untransformed austenite and variations in temperature during anisothermal transformation.

2. Widmanstätten ferrite and pearlite can nucleate directly from the austenite grain surfaces or indirectly from the allotriomorphic ferrite–austenite interfaces. This model includes both of these scenarios because of an approximation made in the formulation of *extended* area. The result of the approximation is to allow Widmanstätten ferrite and pearlite to form even if the entire austenite grain surface is decorated with allotriomorphic ferrite. This is approximately equivalent to the secondary nucleation of Widmanstätten ferrite and pearlite on allotriomorphic ferrite. This is only reasonable if the growth rates of those phases which nucleate in a secondary fashion are relatively high compared to allotriomorphic ferrite which nucleates in a primary fashion on the austenite grain surface during the early stages of transformation. However, it is possible to introduce an additional approximation to allow for such cases. This involves determining the mean *extended* thickness h of an imaginary layer containing the total extended volume of all boundary nucleated phases which have formed by the time t. This extended thickness h is added to the extended length of particles which are nucleated during the next time interval t to $t + dt$.

9. Example

9.1 Program Text

```
IMPLICIT DOUBLE PRECISION(A-H,K-Z), INTEGER(I-J)
READ(*,*) DTIME,PARA1,PARA3,DIFFUSY,GRWID,GRPEARL,AR,ARWID,
&ARPEARL,VIA,VIWID,VIPEARL,VIINCA,VIINCWID,VIINCPEARL,
&OBOUND,EQVOLFRAC
TIME=0.0
DO 1 I1=1,10,1
PRETIME=TIME
```

```
      TIME=DTIME*I1
      CALL MAP_SIM_TRANS(I1,TIME,PRETIME,DTIME,PARA1,
     &PARA3,DIFFUSY,GRWID,GRPEARL,AR,ARWID,ARPEARL,
     &VIINCA,VIINCWID,VIINCPEARL,VIA,VIWID,VIPEARL,
     &EQVOLFRAC,OBOUND,PERCENTRANS,VTOTTRANS,VAREAL,
     &VWIDREAL,VPEARLREAL,VAREALINC,VWIDREALINC,
     &VPEARLREALINC,IFLAG,SATTIME)
      IF (PERCENTRANS.GE.100.0) GOTO 3
      WRITE(*,2) TIME,VTOTTRANS,VAREAL,VWIDREAL,VPEARLREAL,
     &VAREALINC,VWIDREALINC,VPEARLREALINC
1CONTINUE
2FORMAT(E10.3,1X,E10.3,1X,E10.3,1X,E10.3,1X,E10.3,1X,E10.3,
     &1X,E10.3,1X,E10.3)
3STOP
      END
```

9.2 Program Data

3.5 1.5 2.5 1.0E-13 1.0E-6 1.0E-7 3.0 0.02 1.0 1.0E9 1.0E9 1.0E9 4.0E13 4.0E13 4.0E13 4.0E4
0.85

9.3 Program Results

0.350E+01	0.772E-02	0.552E-02	0.120E-03	0.383E-04	0.190E-02	0.120E-03	0.251E-04
0.700E+01	0.304E-01	0.219E-01	0.950E-03	0.295E-03	0.660E-02	0.597E-03	0.125E-03
0.105E+02	0.706E-01	0.479E-01	0.355E-02	0.104E-02	0.151E-01	0.246E-02	0.515E-03
0.140E+02	0.127E+00	0.791E-01	0.903E-02	0.246E-02	0.278E-01	0.726E-02	0.152E-02
0.175E+02	0.199E+00	0.109E+00	0.202E-01	0.446E-02	0.448E-01	0.168E-01	0.352E-02
0.210E+02	0.281E+00	0.133E+00	0.364E-01	0.699E-02	0.654E-01	0.328E-01	0.686E-02
0.245E+02	0.379E+00	0.150E+00	0.618E-01	0.105E-01	0.889E-01	0.564E-01	0.118E-01
0.280E+02	0.486E+00	0.159E+00	0.912E-01	0.156E-01	0.114E+00	0.878E-01	0.184E-01
0.315E+02	0.604E+00	0.160E+00	0.129E+00	0.234E-01	0.139E+00	0.126E+00	0.263E-01
0.350E+02	0.719E+00	0.160E+00	0.164E+00	0.318E-01	0.161E+00	0.166E+00	0.348E-01

10. Auxiliary Routines

11. Keywords

simultaneous, phase, transformation, nucleation, growth, random, inclusion, boundary, reconstructive, displacive, numerical, anisothermal, enrichment, allotriomorphic, idiomorphic, Widmanstätten, ferrite, pearlite, austenite, primary, secondary.

12. FORTRAN 77 Code

```
C SUBROUTINE TO MODEL THE SIMULTANEOUS TRANSFORMATION KINETICS OF ALLOTRIOMORPHIC,
C IDIOMORPHIC AND WIDMANSTATTEN FERRITE AND PEARLITE. NUCLEATION IS ALLOWED TO
```

```
C OCCUR RANDOMLY ON INCLUSIONS AND ON THE AUSTENITE GRAIN BOUNDARIES. (BY SJ
C JONES AND HKDH BHADESHIA, UNIVERSITY OF CAMBRIDGE, UK, 1996)
        SUBROUTINE MAP_SIM_TRANS(I2,TIME,PRETIME,DTIME,PARA1,
     &  PARA3,DIFFUSY,GRWID,GRPEARL,AR,ARWID,ARPEARL,
     &  VIINCA,VIINCWID,VIINCPEARL,VIA,VIWID,VIPEARL,
     &  EQVOLFRAC,OBOUND,PERCENTRANS,VTOTTRANS,VAREAL,
     &  VWIDREAL,VPEARLREAL,VAREALINC,VWIDREALINC,
     &  VPEARLREALINC,IFLAG,SATTIME)
        IMPLICIT DOUBLE PRECISION (A-H,K-Z), INTEGER (I-J)
        DOUBLE PRECISION
     &  QA(1001),PREQA(1001),OREA(3000),PREOREA(3000),QWID(1001),
     &  PREQWID(1001),OREWID(3000),PREOREWID(3000),QPEARL(1001),
     &  PREQPEARL(1001),OREPEARL(3000),PREOREPEARL(3000),
     &  Y(3000),NOPARTINCA(1001),NOPARTINCWID(1001),NOPARTINCPEARL(1001),
     &  NOPARTGBA(1001),NOPARTGBWID(1001),NOPARTGBPEARL(1001),
     &  TIMEOFNUCL(1001),EXTTHICK(1001)
        PI=3.141592654
        IF (I2.EQ.1) THEN
        VOLTOT=1.0
C ASSIGN NUMERICAL VALUES TO ARBITRARY PLANES THAT ARE PARALLEL TO A PLANAR
C AUSTENITE GRAIN BOUNDARY. THREE SIZE INTERVALS ARE USED.
        INOSMA=1001
        INOMED=990
        INOLAR=900
        IYPLANE=INOSMA+INOMED+INOLAR
        YEND=10000.0D-6
        DYSMA=0.01D-6
        DYMED=1.0D-6
        DYLAR=10.0D-6
C VARY THE HEIGHT OF THE ARBITRARY PLANE TO BE CONSIDERED:
        DO 810 I810=1,IYPLANE,1
         IF (I810.LE.INOSMA) THEN
          Y(I810)=1.0*((I810-1)*DYSMA)
         ELSEIF ((I810.GT.INOSMA).AND.(I810.LE.(INOSMA+INOMED))) THEN
          Y(I810)=Y(INOSMA)+1.0*((I810-INOSMA)*DYMED)
         ELSE
          Y(I810)=Y(INOSMA+INOMED)+1.0*((I810-INOSMA-INOMED)*DYLAR)
         ENDIF
         IF (I810.EQ.INOSMA) THEN
          Y(I810)=Y(I810)
         ELSEIF (I810.EQ.(INOSMA+INOMED)) THEN
          Y(I810)=Y(I810)
         ELSEIF (I810.EQ.IYPLANE) THEN
          Y(I810)=Y(I810)
         ENDIF
810     CONTINUE
        IFLAG=0
        ENDIF
        TIMEOFNUCL(I2)=PRETIME
C CALCULATE THE CHANGES IN THE EXTENDED VOLUMES OF THE VARIOUS PHASES
C WHICH NUCLEATE RANDOMLY ON INCLUSIONS:
```

```
        NOPARTINCA(I2)=VIINCA*DTIME*VOLTOT
        NOPARTINCWID(I2)=VIINCWID*DTIME*VOLTOT
        NOPARTINCPEARL(I2)=VIINCPEARL*DTIME*VOLTOT
        SUMINCA=0.0
        SUMINCWID=0.0
        SUMINCPEARL=0.0
        DO 610 I610=1,I2,1
          TIMESNINC=PRETIME-TIMEOFNUCL(I610)
          IF (I610.EQ.I2) THEN
C PARTICLES JUST NUCLEATED:
          NEWCONINCA=NOPARTINCA(I610)*(4.0*PI/3.0)
     &      *(PARA3**3.0)
     &      *(DIFFUSY**1.5)*(DTIME**1.5)
          NEWCONINCWID=NOPARTINCWID(I610)
     &      *ARWID*(DTIME**3.0)*(GRWID**3.0)
          NEWCONINCPEARL=NOPARTINCPEARL(I610)*(4.0*PI/3.0)
     &      * (GRPEARL**3.0) * (DTIME**3.0)
          SUMINCA=SUMINCA+NEWCONINCA
          SUMINCWID=SUMINCWID+NEWCONINCWID
          SUMINCPEARL=SUMINCPEARL+NEWCONINCPEARL
        ELSE
C PARTICLES AREADY NUCLEATED:
          GROWCONINCA=NOPARTINCA(I610)*(4.0*PI/3.0)
     &      *(3.0/2.0)*(PARA3**3.0)
     &      *(DIFFUSY**1.5)*DTIME*(TIMESNINC**0.5)
          GROWCONINCWID=NOPARTINCWID(I610)
     &      *ARWID*3.0*(GRWID**3.0)
     &      *DTIME*(TIMESNINC**2.0)
          GROWCONINCPEARL=NOPARTINCPEARL(I610)*(4.0*PI/3.0)
     &      *(3.0)*(GRPEARL**3.0)*DTIME*(TIMESNINC**2.0)
          SUMINCA=SUMINCA+GROWCONINCA
          SUMINCWID=SUMINCWID+GROWCONINCWID
          SUMINCPEARL=SUMINCPEARL+GROWCONINCPEARL
        ENDIF
610     CONTINUE
        DVEXTAINC=SUMINCA
        DVEXTWIDINC=SUMINCWID
        DVEXTPEARLINC=SUMINCPEARL
C CALCULATION OF THE INCREMENTS IN THE EXTENDED VOLUMES OF THE VARIOUS
C BOUNDARY NUCLEATED PHASES:
        NOPARTGBA(I2)=VIA*DTIME*OBOUND
        NOPARTGBWID(I2)=VIWID*DTIME*OBOUND
        NOPARTGBPEARL(I2)=VIPEARL*DTIME*OBOUND
C TO ALLOW FOR THE SECONDARY NUCLEATION OF WIDMANSTATTEN FERRITE AND PEARLITE
C CALCULATE THE MEAN EXTENDED THICKNESS AT THE PLANAR BOUNDARY CONSIDERED.
        TOTBOUNDEXTV=VAEXT+VWIDEXT+VPEARLEXT
        EXTTHICK(I2)=TOTBOUNDEXTV/OBOUND
        DO 20 I20=1,I2,1
          TIMESN=PRETIME-TIMEOFNUCL(I20)
C DETERMINE THE HEIGHT OF THE VARIOUS EXTENDED PARTICLES:
          IF (TIMESN.LT.(0.000001*DTIME)) THEN
```

189

```
C PARTICLES JUST NUCLEATED:
        PREQA(I20)=0.0
        QA(I20)=PARA1*(DIFFUSY**0.5)*(DTIME**0.5)
        PREQWID(I20)=0.0
        QWID(I20)=(GRWID*DTIME)+EXTTHICK(I2)
        PREQPEARL(I20)=0.0
        QPEARL(I20)=(GRPEARL*DTIME)+EXTTHICK(I2)
       ELSE
C PARTICLES AREADY NUCLEATED:
        QAINCRE=0.5*PARA1*(DIFFUSY**0.5)
     &    *((TIMESN)**(-0.5))*DTIME
        PREQA(I20)=QA(I20)
        QA(I20)=QA(I20)+QAINCRE
        QWIDINCRE=GRWID*DTIME
        PREQWID(I20)=QWID(I20)
        QWID(I20)=QWID(I20)+QWIDINCRE
        QPEARLINCRE=GRPEARL*DTIME
        PREQPEARL(I20)=QPEARL(I20)
        QPEARL(I20)=QPEARL(I20)+QPEARLINCRE
       ENDIF
20     CONTINUE
C TEST THAT NO PARTICLES HAVE A HEIGHT GREATER THAN YEND:
        MAXHGTA=0.0
        MAXHGTWID=0.0
        MAXHGTPEARL=0.0
        DO 642 I642=1,I2,1
         IF (QA(I642).GT.MAXHGTA) THEN
          MAXHGTA=QA(I642)
         ENDIF
         IF (QPEARL(I642).GT.MAXHGTPEARL) THEN
          MAXHGTPEARL=QPEARL(I642)
         ENDIF
         IF (QWID(I642).GT.MAXHGTWID) THEN
          MAXHGTWID=QWID(I642)
         ENDIF
642    CONTINUE
        MAXHGT=MAXHGTWID
        IF (MAXHGTPEARL.GT.MAXHGT) THEN
         MAXHGT=MAXHGTPEARL
        ENDIF
        IF (MAXHGTA.GT.MAXHGT) THEN
         MAXHGT=MAXHGTA
        ENDIF
        IF (MAXHGT.GT.YEND) THEN
         WRITE(*,*) "YEND TOO SMALL - ERROR !"
         PAUSE
        ENDIF
C COMPARE PARTICLES WITH THE VARIOUS ARBITRARY PLANES THAT ARE PARALLEL TO THE BOUNDARY
C TO DETERMINE THE VARIOUS CHANGES IN THE EXTENDED AREAS OF INTERSECTION:
        DO 10 I10=1,IYPLANE,1
         ALLA=0.0
```

190

```
            ALLWID=0.0
            ALLPEARL=0.0
C ONLY CONSIDER THOSE PLANES THAT INTERSECT THE EXTENDED PARTICLES:
            IF (MAXHGT.GT.Y(I10)) THEN
             DO 400 I400=1,I2,1
              TIMESN=PRETIME-TIMEOFNUCL(I400)
C TEST IF THESE ALLOTRIMORPHIC FERRITE PARTICLES REACH THIS PLANE:
              IF (QA(I400).GE.Y(I10)) THEN
C THIS IS THE FIRST TIME THAT THESE PARTICLES HAVE REACHED THIS PLANE.
               IF ((PREQA(I400).LT.Y(I10)).OR.
     &         (TIMESN.LT.(0.000001*DTIME))) THEN
C ADD ALL OF THE AREA OF THESE PARTICLES TO THE INCREMENT IN THE EXTENDED AREA:
                ALLA=ALLA+(NOPARTGBA(I400))*(PI*((AR*QA(I400))**2))
               ELSE
C ACCOUNT FOR THE INCREASE IN THE EXTENDED AREA CONTRIBUTED BY THESE PARTICLES:
                ALLA=ALLA+
     &          NOPARTGBA(I400)*DTIME*((PARA1*AR)**2)*PI*DIFFUSY
               ENDIF
              ENDIF
C TEST IF THESE WIDMANSTATTEN FERRITE PARTICLES REACH THIS PLANE:
              IF (QWID(I400).GE.Y(I10)) THEN
C THIS IS THE FIRST TIME THAT THESE PARTICLES HAVE REACHED THIS PLANE.
               IF ((PREQWID(I400).LT.Y(I10)).OR.
     &         (TIMESN.LT.(0.000001*DTIME))) THEN
C ADD ALL OF THE AREA OF THESE PARTICLES TO THE INCREMENT IN THE EXTENDED AREA:
                ALLWID=ALLWID
     &          +( (NOPARTGBWID(I400))
     &          *(ARWID*((QWID(I400)-EXTTHICK(I400))**2.0)) )
               ELSE
C ACCOUNT FOR THE INCREASE IN THE EXTENDED AREA CONTRIBUTED BY THESE PARTICLES:
                ALLWID=ALLWID
     &          +( 2.0*(NOPARTGBWID(I400))*ARWID*(GRWID**2.0)
     &          * TIMESN * DTIME )
               ENDIF
              ENDIF
C TEST IF THESE PEARLITE PARTICLES REACH THIS PLANE:
              IF (QPEARL(I400).GE.Y(I10)) THEN
C THIS IS THE FIRST TIME THAT THESE PARTICLES HAVE REACHED THIS PLANE.
               IF ((PREQPEARL(I400).LT.Y(I10)).OR.
     &         (TIMESN.LT.(0.000001*DTIME))) THEN
C ADD ALL OF THE AREA OF THESE PARTICLES TO THE INCREMENT IN THE EXTENDED AREA:
                ALLPEARL=ALLPEARL
     &          + ( NOPARTGBPEARL(I400)*PI*
     &          (((QPEARL(I400)-EXTTHICK(I400)) * ARPEARL )**2.0) )
               ELSE
C ACCOUNT FOR THE INCREASE IN THE EXTENDED AREA CONTRIBUTED BY THESE PARTICLES:
                ALLPEARL=ALLPEARL
     &          + ( 2.0*PI*NOPARTGBPEARL(I400)*(ARPEARL*GRPEARL**2.0)
     &          * TIMESN * DTIME )
               ENDIF
              ENDIF
```

191

```
400      CONTINUE
         ELSE
C NO PARTICLES HAVE REACHED THIS PLANE:
         ALLA=0.0
         ALLWID=0.0
         ALLPEARL=0.0
         ENDIF
         DOEXA=ALLA
         DOEXWID=ALLWID
         DOEXPEARL=ALLPEARL
C CONVERT THESE INCREMENTS IN THE EXTENDED AREAS OF INTERSECTION TO THE CORRESPONDING
C INCREMENTS IN THE REAL AREAS OF INTERSECTION:
         IF (I2.EQ.1) THEN
           DOREA=DOEXA
           DOREWID=DOEXWID
           DOREPEARL=DOEXPEARL
         ELSE
           IF ((OREA(I10)+OREWID(I10)+OREPEARL(I10)).GE.OBOUND) THEN
             FRACOBUT=0.0
           ELSE
             FRACOBUT=(1.0-(OREA(I10)+OREWID(I10)+OREPEARL(I10))/OBOUND)
           ENDIF
           DOREA=DOEXA*FRACOBUT
           DOREWID=DOEXWID*FRACOBUT
           DOREPEARL=DOEXPEARL*FRACOBUT
         ENDIF
C SUM TO FIND THE TOTAL EXTENDED AREAS OF INTERSECTION:
         IF ((OREA(I10)+OREWID(I10)+OREPEARL(I10)).LE.OBOUND) THEN
           PREOREA(I10)=OREA(I10)
           PREOREWID(I10)=OREWID(I10)
           PREOREPEARL(I10)=OREPEARL(I10)
         ENDIF
         OREA(I10)=OREA(I10)+DOREA
         OREWID(I10)=OREWID(I10)+DOREWID
         OREPEARL(I10)=OREPEARL(I10)+DOREPEARL
C ENSURE THAT THE TOTAL EXTENDED AREA OF EACH PHASE DOES NOT EXCEED OBOUND:
         IF ((OREA(I10)+OREWID(I10)+OREPEARL(I10)).GT.OBOUND) THEN
           IF ((PREOREA(I10)+PREOREWID(I10)+PREOREPEARL(I10)).GT.0.0)
     &     THEN
             PORA=PREOREA(I10)/
     &         (PREOREA(I10)+PREOREPEARL(I10)+PREOREWID(I10))
             PORWID=PREOREWID(I10)/
     &         (PREOREA(I10)+PREOREPEARL(I10)+PREOREWID(I10))
             PORPEARL=PREOREPEARL(I10)/
     &         (PREOREA(I10)+PREOREPEARL(I10)+PREOREWID(I10))
           ELSE
             PORA=OREA(I10)/
     &         (OREA(I10)+OREPEARL(I10)+OREWID(I10))
             PORWID=OREWID(I10)/
     &         (OREA(I10)+OREPEARL(I10)+OREWID(I10))
             PORPEARL=OREPEARL(I10)/
```

```
     &      (OREA(I10)+OREPEARL(I10)+OREWID(I10))
            ENDIF
            OREA(I10)=PORA*OBOUND
            OREWID(I10)=PORWID*OBOUND
            OREPEARL(I10)=PORPEARL*OBOUND
          ENDIF
C NOTE THE TIME WHEN THE AUSTENITE GRAIN BOUNDARY IS SATURATED:
          IF ( (I10.EQ.1).AND.(IFLAG.EQ.0) ) THEN
          IF ( (OREA(I10)+OREWID(I10)+OREPEARL(I10))
     &      .GE. (0.99*OBOUND) ) THEN
           SATTIME=TIME
           IFLAG=1
          ENDIF
          ENDIF
10        CONTINUE
C CALCULATE THE TOTAL EXTENDED VOLUME OF EACH PHASE THAT ORIGINATES FROM THIS BOUNDARY:
888       PREVAEXT=VAEXT
          PREVWIDEXT=VWIDEXT
          PREVPEARLEXT=VPEARLEXT
          VAEXT=( 2.0*0.5*DYSMA*( OREA(1)
     &    +OREA(INOSMA) ) )
     &    +( 2.0*0.5*DYMED*( OREA(INOSMA+1)
     &    +OREA(INOSMA+INOMED) ) )
     &    +( 2.0*0.5*DYLAR*( OREA(INOSMA+INOMED+1)
     &    +OREA(IYPLANE) ) )
          VWIDEXT=( 1.0*0.5*DYSMA*( OREWID(1)
     &    +OREWID(INOSMA) ) )
     &    +( 1.0*0.5*DYMED*( OREWID(INOSMA+1)
     &    +OREWID(INOSMA+INOMED) ) )
     &    +( 1.0*0.5*DYLAR*( OREWID(INOSMA+INOMED+1)
     &    +OREWID(IYPLANE) ) )
          VPEARLEXT=( 2.0*0.5*DYSMA*( OREPEARL(1)
     &    +OREPEARL(INOSMA) ) )
     &    +( 2.0*0.5*DYMED*( OREPEARL(INOSMA+1)
     &    +OREPEARL(INOSMA+INOMED) ) )
     &    +( 2.0*0.5*DYLAR*( OREPEARL(INOSMA+INOMED+1)
     &    +OREPEARL(IYPLANE) ) )
          DO 500 I500=2,(IYPLANE-1),1
           IF ( (I500.GT.1).AND.(I500.LT.INOSMA) ) THEN
            VAEXT=VAEXT+(2.0*DYSMA*OREA(I500))
            VWIDEXT=VWIDEXT+(1.0*DYSMA*OREWID(I500))
            VPEARLEXT=VPEARLEXT+(2.0*DYSMA*OREPEARL(I500))
           ELSEIF ((I500.GT.(INOSMA+1)).AND.(I500.LT.(INOSMA+INOMED)))THEN
            VAEXT=VAEXT+(2.0*DYMED*OREA(I500))
            VWIDEXT=VWIDEXT+(1.0*DYMED*OREWID(I500))
            VPEARLEXT=VPEARLEXT+(2.0*DYMED*OREPEARL(I500))
           ELSEIF((I500.GT.(INOSMA+INOMED+1)).AND.(I500.LT.(IYPLANE)))THEN
            VAEXT=VAEXT+(2.0*DYLAR*OREA(I500))
            VWIDEXT=VWIDEXT+(1.0*DYLAR*OREWID(I500))
            VPEARLEXT=VPEARLEXT+(2.0*DYLAR*OREPEARL(I500))
           ENDIF
```

193

```
500      CONTINUE
C CALCULATE THE CHANGES IN THE VARIOUS EXTENDED VOLUMES DURING THE CURRENT TIME INTERVAL:
         IF (I2.EQ.1) THEN
           DVAEXT=VAEXT
           DVWIDEXT=VWIDEXT
           DVPEARLEXT=VPEARLEXT
         ELSE
           DVAEXT=VAEXT-PREVAEXT
           DVWIDEXT=VWIDEXT-PREVWIDEXT
           DVPEARLEXT=VPEARLEXT-PREVPEARLEXT
         ENDIF
C CONVERT THE CHANGES IN THE VARIOUS EXTENDED VOLUMES INTO THE CORRESPONDING REAL CHANGES.
         FRACUT=1.0-
      &  ( (VAREALINC+VAREAL+VPEARLREALINC+VPEARLREAL
      &  +VWIDREALINC+VWIDREAL) / VOLTOT )
         DVAREALINC=DVEXTAINC*FRACUT
         DVWIDREALINC=DVEXTWIDINC*FRACUT
         DVPEARLREALINC=DVEXTPEARLINC*FRACUT
         VAREALINC=VAREALINC+DVAREALINC
         VWIDREALINC=VWIDREALINC+DVWIDREALINC
         VPEARLREALINC=VPEARLREALINC+DVPEARLREALINC
         DVAREAL=DVAEXT*FRACUT
         DVWIDREAL=DVWIDEXT*FRACUT
         DVPEARLREAL=DVPEARLEXT*FRACUT
         VAREAL=VAREAL+DVAREAL
         VWIDREAL=VWIDREAL+DVWIDREAL
         VPEARLREAL=VPEARLREAL+DVPEARLREAL
C TOTAL VOLUME FRACTION OF ALLOTRIOMORPHIC AND IDIOMORPHIC FERRITE:
         VTOTAREAL=VAREAL+VAREALINC
C TOTAL VOLUME FRACTION OF WIDMANSTATTEN FERRITE:
         VTOTWIDREAL=VWIDREAL+VWIDREALINC
C TOTAL VOLUME FRACTION OF PEARLITE:
         VTOTPEARLREAL=VPEARLREAL+VPEARLREALINC
C TOTAL VOLUME FRACTION OF ALL PHASES:
         PREVTFERR=VTOTTRANS
         VTOTTRANS=VTOTWIDREAL+VTOTAREAL+VTOTPEARLREAL
         PERCENTRANS=(VTOTTRANS/EQVOLFRAC)*100.0
         RETURN
         END
```

APPENDIX TWO

Subroutine MAP_INC_POTENCY

0. Provenance of Source Code

S.J. Jones and H.K.D.H. Bhadeshia, Phase Transformations Group, Department of Materials Science and Metallurgy, University of Cambridge, Cambridge, UK.

1. Purpose

To calculate the heterogeneous activation energy barrier to ferrite nucleation on a spherical substrate, such as a non-metallic inclusion, using classical nucleation theory.

2. Specification

SUBROUTINE MAP_INC_POTENCY(INCGMAX1VOL,GMAX1VOL,
&RI,UFAFENERGY,FAFENERGY,FIENERGY,AIENERGY,AEB,
&AEBHOMOG,FRACHOMAEB)
  IMPLICIT DOUBLE PRECISION(A-H,K-Z), INTEGER(I-J)

3. Description

Barritte (1982) developed a model for the activation energy barrier to ferrite nucleation on a spherical substrate by assuming that the 'wetting' angle is 90°. This new model does not rely upon this assumption.

4. References

1. S.J. Jones, *PhD. thesis, University of Cambridge, UK*, (submitted in 1996).

2. G.S. Barritte, *PhD. thesis, University of Cambridge, UK*, (1982).

3. J.W. Christian, The theory of phase transformations in metals and alloys, Part 1, 2nd ed., *Permagon, Oxford, UK* (1965).

5. Parameters

5.1 Input Parameters

INCGMAX1VOL - real
INCGMAX1VOL is the thermodynamic driving force per unit volume for nucleation local to the spherical substrate (J m^{-3}).

GMAX1VOL - real
GMAX1VOL is the thermodynamic driving force per unit volume for nucleation remote from the spherical substrate (J m^{-3}).

UFAFENERGY - real
UFAFENERGY is the interfacial energy per unit area at a disordered boundary between ferrite and austenite (J m^{-2}).

FAFENERGY - real
FAFENERGY is the interfacial energy per unit area at a faceted (coherent) boundary between ferrite and austenite (J m^{-2}).

FIENERGY - real
FIENERGY is the interfacial energy per unit area between ferrite and the spherical substrate (J m^{-2}).

AIENERGY - real
AIENERGY is the interfacial energy per unit area between austenite and the spherical substrate (J m^{-2}).

RI - real
RI is the radius of the spherical substrate (m).

5.2 Output Parameters

AEB - real
AEB is the activation energy barrier to nucleation at the spherical substrate (J).

AEBHOMOG - real
AEBHOMOG is the activation energy barrier to homogeneous nucleation remote from the spherical substrate (J).

FRACHOMAEB - real
FRACHOMAEB is the ratio between AEB and AEBHOMOG. This is the effective 'shape' factor for ferrite nucleation on the spherical substrate.

6. Error Indicators

1. If FAFENERGY is greater than UFAFENERGY then an error is reported and the program execution is stopped.

2. If the absolute value of TESTIT is greater than unity then an error is reported and the program execution is stopped.

3. If YHGT is greater than XHGT then an error is reported and the program execution is stopped.

7. Accuracy

8. Further Comments

9. Example

9.1 Program Text

```
      IMPLICIT DOUBLE PRECISION(A-H,K-Z), INTEGER(I-J)
      READ(*,*) INCGMAX1VOL,GMAX1VOL,RI,UFAFENERGY,
     &FAFENERGY,FIENERGY,AIENERGY
      CALL MAP_INC_POTENCY(INCGMAX1VOL,GMAX1VOL,
     &RI,UFAFENERGY,FAFENERGY,FIENERGY,AIENERGY,AEB,
     &AEBHOMOG,FRACHOMAEB)
      WRITE(*,1) AEB,AEBHOMOG,FRACHOMAEB
    1 FORMAT (E10.3,1X,E10.3,1X,E10.3)
      STOP
      END
```

9.2 Program Data

-0.260E7 -0.260E7 0.270E-6 0.500E-1 0.363E-1 0.463E-1 0.623E-1

9.3 Program Results

0.814E-16 0.310E-15 0.263E0

10. Auxiliary Routines

11. Keywords

activation, energy, barrier, nucleation, classical, spherical, substrate, inclusion, heterogeneous, homogeneous, ferrite, austenite.

12. FORTRAN 77 Code

```
C SUBROUTINE TO CALCULATE THE CLASSICAL ACTIVATION ENERGY BARRIER TO FERRITE NUCLEATION
C ON A SPHERICAL SUBSTRATE (BY SJ JONES AND HKDH BHADESHIA, UNIVERSITY OF CAMBRIDGE, UK,
C 1995). BASED ON A MODEL BY G BARRITTE, PHD. THESIS, UNIVERSITY OF CAMBRIDGE, 1982.
      SUBROUTINE MAP_INC_POTENCY(INCGMAX1VOL,GMAX1VOL,RI,UFAFENERGY,
     & FAFENERGY,FIENERGY,AIENERGY,AEB,AEBHOMOG,FRACHOMAEB)
      IMPLICIT DOUBLE PRECISION (A-H,K-Z), INTEGER (I-J)
      PI=3.141592654
C PHI=WETTING ANGLE.
C PSI=ANGLE BETWEEN THE CHORD WHICH SEPARATES THE INCLUSION AND FERRITE AND THE TANGENT
C TO THE INCLUSION AT THE TRIPLE POINT.
C THETA=ANGLE BETWEEN THE CHORD WHICH SEPARATES THE INCLUSION AND THE FERRITE AND THE
C TANGENT TO THE FERRITE NUCLEUS AT THE TRIPLE POINT.
C BETA=ANGLE BETWEEN THE CHORD WHICH SEPARATES THE AUSTENITE AND THE FACETED FERRITE
C AND THE TANGENT TO THE UNFACETED FERRITE AT THE DOUBLE POINT.
```

```
C CALCULATE THE HOMOGENEOUS ACTIVATION ENERGY BARRIER:
      AEBHOMOG=(16.0*PI/3.0)*(UFAFENERGY**3)/(GMAX1VOL**2.0)
C CALCULATE THE RADIUS OF CURVATURE OF A NUCLEI IN THE VICINITY OF AN INCLUSION:
      RC=(-2.0*UFAFENERGY)/INCGMAX1VOL
      IF (FAFENERGY.GT.UFAFENERGY) THEN
        WRITE(*,*) "ERROR - INTERFACIAL ENERGY (1) !"
        PAUSE
      ENDIF
      TESTIT=(-1.0*(FIENERGY-AIENERGY)/UFAFENERGY)
      IF ( (TESTIT.GT.1.0).OR.(TESTIT.LT.-1.0) ) THEN
        WRITE(*,*) "ERROR - INTERFACIAL ENERGY (2) !"
        PAUSE
      ENDIF
      PHI=ACOS(-1.0*(FIENERGY-AIENERGY)/UFAFENERGY)
C SEPN=DISTANCE BETWEEN THE CENTRE OF THE INCLUSION AND THE REAL OR NOTIONAL NUCLEUS
C CENTRE:
      SEPN=((RC**2.0)+(RI**2.0)-(2.0*RC*RI*COS(PHI)))**0.5
      IF (RC.LE.RI) THEN
       PSI=ASIN(RC*SIN(PHI)/SEPN)
       THETA=(PI-PHI)-PSI
       THETA=THETA
       PSI=PSI
      ENDIF
      IF (RI.LT.RC) THEN
       THETA=ASIN(RI*SIN(PHI)/SEPN)
       PSI=(PI-PHI)-THETA
       THETA=THETA
       PSI=PSI
      ENDIF
      BETA=ACOS(FAFENERGY/UFAFENERGY)
      FUNCTHETA=2.0-(3.0*COS(THETA))+((COS(THETA))**3.0)
      FUNCPSI=2.0-(3.0*COS(PSI))+((COS(PSI))**3.0)
      FUNCBETA=2.0-(3.0*COS(BETA))+((COS(BETA))**3.0)
C VOLUME TERMS:
C VS=SPHERICAL NUCLEUS.
C VC1=SPHERICAL SEGMENT LOST DUE TO THE SECTIONING OF THE NUCLEUS.
C VC2=SPHERICAL SEGMENT LOST DUE TO INTRUSION INTO THE NUCLEUS.
C VC3=SPHERICAL SEGMENT LOST DUE TO THE FORMATION OF A FACET.
      VS=(4.0*PI/3.0)*(RC**3.0)
      VC1=(1.0*PI/3.0)*(RC**3.0)*FUNCTHETA
      VC2=(1.0*PI/3.0)*(RI**3.0)*FUNCPSI
      VC3=(1.0*PI/3.0)*(RC**3.0)*FUNCBETA
C CHECK IF THE FACET INTERSECTS THE INCLUSION SURFACE:
C XHGT=DISTANCE FROM THE TOP OF THE INCLUSION TO THE TOP OF THE UNFACETED NUCLEUS.
C YHGT=DISTANCE FROM THE TOP OF THE UNFACETED NUCLEUS TO THE FACET.
      XHGT=(RC*(1.0+COS(THETA)))-(RI*(1.0-COS(PSI)))
      YHGT=RC*(1.0-COS(BETA))
      IF (YHGT.GT.XHGT) THEN
       WRITE(*,*) 'ERROR  - FACET INTERSECTS INCLUSION !'
       PAUSE
      ENDIF
```

```
C AREA TERMS:
C AS=SPHERICAL NUCLEUS.
C AC1=AREA OF NUCLEUS LOST DUE TO SECTIONING.
C AC2=AREA OF FERRITTE/INCLUSION INTERFACE CREATED (EQUAL TO THE AUSTENITE/INCLUSION
C INTERFACE DESTROYED).
C AC4=AREA OF NUCLEUS LOST DUE TO FACET FORMATION.
C AF=AREA OF NUCLEUS CREATED DUE TO FACET FORMATION.
        AS=4.0*PI*(RC**2.0)
        AC1=2.0*PI*(RC**2.0)*(1.0-COS(THETA))
        AC2=2.0*PI*(RI**2.0)*(1.0-COS(PSI))
        AC4=2.0*PI*(RC**2.0)*(1.0-COS(BETA))
        AF=1.0*PI*(RC**2.0)*(1.0-((COS(BETA))**2.0))
        AEB=
     &  (INCGMAX1VOL*(VS-(VC1+VC2+VC3)) )
     &  +((AS-AC1-AC4)*UFAFENERGY)
     &  +((AF)*FAFENERGY)
     &  -((AC2)*AIENERGY)
     &  +((AC2)*FIENERGY)
C CALCULATE AN EFFECTIVE SHAPE FACTOR:
        FRACHOMAEB=AEB/AEBHOMOG
        RETURN
        END
```

APPENDIX THREE

Subroutine MAP_GB_POTENCY

0. Provenance of Source Code

S.J. Jones and H.K.D.H. Bhadeshia, Phase Transformations Group, Department of Materials Science and Metallurgy, University of Cambridge, Cambridge, UK.

1. Purpose

To calculate the heterogeneous activation energy barrier to ferrite nucleation on a planar austenite grain boundary using classical nucleation theory.

2. Specification

```
SUBROUTINE MAP_GB_POTENCY(GBGMAX1VOL,GMAX1VOL,
&UFAFENERGY,FAFENERGY,AGBENERGY,GBAEB,AEBHOMOG,
&GBFRACHOMAEB)
IMPLICIT DOUBLE PRECISION(A-H,K-Z), INTEGER(I-J)
```

3. Description

The activation energy barrier to ferrite nucleation on a planar austenite grain boundary is calculated using classical nucleation theory. The ferrite nucleus is assumed to exhibit a low-energy facet with respect to one of the adjacent austenite grains.

4. References

1. S.J. Jones, *PhD. thesis, University of Cambridge, UK*, (submitted in 1996).

2. W.C. Johnson *et al.*, *Met. Trans.*, **6A**, (1975) 911-919.

3. J.W. Christian, The theory of phase transformations in metals and alloys, Part 1, 2nd ed., *Permagon, Oxford, UK* (1965).

5. Parameters

5.1 Input Parameters

GBGMAX1VOL - real
GBGMAX1VOL is the thermodynamic driving force per unit volume for nucleation local to the boundary (J m^{-3}).

GMAX1VOL - real
GMAX1VOL is the thermodynamic driving force per unit volume for nucleation remote from the boundary (J m^{-3}).

UFAFENERGY - real
UFAFENERGY is the interfacial energy per unit area at a disordered boundary between ferrite and austenite (J m^{-2}).

FAFENERGY - real
FAFENERGY is the interfacial energy per unit area at a faceted (coherent) boundary between ferrite and austenite (J m^{-2}).

AGBENERGY - real
AGBENERGY is the interfacial energy per unit area at a planar boundary between two grains of austenite (J m^{-2}).

5.2 Output Parameters

GBAEB - real
GBAEB is the activation energy barrier to nucleation at the planar boundary (J).

AEBHOMOG - real
AEBHOMOG is the activation energy barrier to homogeneous nucleation remote from the planar boundary (J).

GBFRACHOMAEB - real
GBFRACHOMAEB is the ratio between GBAEB and AEBHOMOG. This is the effective 'shape' factor for ferrite nucleation at the boundary.

6. Error Indicators

1. If FAFENERGY is greater than UFAFENERGY then an error is reported and the program execution is stopped.

2. If the absolute value of TESTY is greater than unity then an error is reported and the program execution is stopped.

7. Accuracy

8. Further Comments

9. Example

9.1 Program Text

```
   IMPLICIT DOUBLE PRECISION(A-H,K-Z), INTEGER(I-J)
   READ(*,*) GBGMAX1VOL,GMAX1VOL,UFAFENERGY,
&FAFENERGY,AGBENERGY
   CALL MAP_GB_POTENCY(GBGMAX1VOL,GMAX1VOL,
&UFAFENERGY,FAFENERGY,AGBENERGY,GBAEB,AEBHOMOG,
&GBFRACHOMAEB)
   WRITE(*,1) GBAEB,AEBHOMOG,GBFRACHOMAEB
1FORMAT (E10.3,1X,E10.3,1X,E10.3)
```

```
        STOP
        END
```

9.2 Program Data

-0.260E7 -0.260E7 0.500E-1 0.363E-1 0.708E-1

9.3 Program Results

0.199E-16 0.310E-15 0.643E-1

10. Auxiliary Routines

11. Keywords

activation, energy, barrier, nucleation, classical, planar, boundary, facet, coherent, heterogeneous, homogeneous, ferrite, austenite.

12. FORTRAN 77 Code

```
C SUBROUTINE TO CALCULATE THE CLASSICAL ACTIVATION ENERGY BARRIER TO FERRITE NUCLEATION AT
C A PLANAR AUSTENITE GRAIN BOUNDARY (BY SJ JONES AND HKDH BHADESHIA, UNIVERSITY OF
C CAMBRIDGE, UK, 1995)
        SUBROUTINE MAP_GB_POTENCY(GBGMAX1VOL,GMAX1VOL,UFAFENERGY,
     &  FAFENERGY,AGBENERGY,GBAEB,AEBHOMOG,GBFRACHOMAEB)
        IMPLICIT DOUBLE PRECISION (A-H,K-Z), INTEGER (I-J)
        PI=3.141592654
C GBRC=RADIUS OF A NUCLEI AT THE BOUNDARY:
        GBRC=(-2.0*UFAFENERGY)/GBGMAX1VOL
C HOMOGENEOUS ACTIVATION ENERGY BARRIER TO NUCLEATION REMOTE FROM THE BOUNDARY:
        AEBHOMOG=(16.0*PI/3.0)*(UFAFENERGY**3)/(GMAX1VOL**2.0)
        IF (FAFENERGY.GT.UFAFENERGY) THEN
         WRITE(*,*) "ERROR - INTERFACIAL ENERGY (1) !"
         PAUSE
        ENDIF
C GBBETA=ANGLE BETWEEN THE CHORD WHICH SEPARATES THE AUSTENITE AND THE FACETED FERRITE
C INTERFACE AND THE TANGENT TO THE UNFACETED FERRITE AT THE DOUBLE POINT.
        GBBETA=ACOS(FAFENERGY/UFAFENERGY)
        GBFUNCBETA=2.0-(3.0*COS(GBBETA))+((COS(GBBETA))**3.0)
C GBSIGMA=WETTING ANGLE.
        TESTY=AGBENERGY/(2.0*UFAFENERGY)
        IF ((TESTY.GT.1.0).OR.(TESTY.LT.0.0)) THEN
         WRITE(*,*) "ERROR - INTERFACIAL ENERGY (2) !"
         PAUSE
        ENDIF
        GBSIGMA=ACOS(TESTY)
```

```
        GBFUNCSIGMA=2.0-(3.0*COS(GBSIGMA))+((COS(GBSIGMA))**3.0)
C VOLUME TERMS:
C GBVSEG=VOLUME OF THE UNFACETED NUCLEUS SEGMENT ON ONE SIDE OF THE BOUNDARY.
C GBVC3=VOLUME OF THE SEGMENT LOST DUE TO THE FORMATION OF A FACET.
        GBVSEG=(1.0*PI/3.0)*(GBRC**3.0)*GBFUNCSIGMA
        GBVC3=(1.0*PI/3.0)*(GBRC**3.0)*GBFUNCBETA
C AREA TERMS:
C GBASEG=CURVED SURFACE AREA OF THE UNFACETED SEGMENT ON ONE SIDE OF THE BOUNDARY.
C GBAC2=AREA OF THE AUSTENITE BOUNDARY DESTROYED (OR FERRITE/AUSTENITE INTERFACE CREATED).
C GBAC4=CURVED SURFACE AREA LOST DUE TO FACET FORMATION.
C GBAF=PLANAR AREA CREATED DUE TO FACET FORMATION.
        GBASEG=2.0*PI*(GBRC**2.0)*(1.0-COS(GBSIGMA))
        GBAC2=1.0*PI*(GBRC**2.0)*(1.0-(COS(GBSIGMA)**2.0))
        GBAC4=2.0*PI*(GBRC**2.0)*(1.0-COS(GBBETA))
        GBAF=1.0*PI*(GBRC**2.0)*(1.0-((COS(GBBETA))**2.0))
        IF (GBSIGMA.GT.GBBETA) THEN
C THE SEGMENT LOST DUE TO FACETING IS SMALLER THAN THE FERRITE NUCLEUS SEGMENT - NUCLEUS
C HAS VOLUME ON BOTH SIDES OF THE BOUNDARY.
        GBAEB=(((2.0*GBVSEG)-GBVC3)*GBGMAX1VOL)
     &     +(((2.0*GBASEG)-GBAC4)*UFAFENERGY)
     &     +(GBAF*FAFENERGY)
     &     -(GBAC2*AGBENERGY)
        ELSEIF (GBSIGMA.LE.GBBETA) THEN
C NUCLEUS ONLY HAS VOLUME ON ONE SIDE OF THE BOUNDARY.
        GBAEB=(GBVSEG*GBGMAX1VOL)
     &       +(GBASEG*UFAFENERGY)
     &       +(GBAC2*FAFENERGY)
     &       -(GBAC2*AGBENERGY)
        ENDIF
C CALCULATE AN EFFECTIVE SHAPE FACTOR.
        GBFRACHOMAEB=GBAEB/AEBHOMOG
        RETURN
        END
```

APPENDIX FOUR
Subroutine MAP_SOL_BOR

0. Provenance of Source Code

S.J. Jones and H.K.D.H. Bhadeshia, Phase Transformations Group, Department of Materials Science and Metallurgy, University of Cambridge, Cambridge, UK.

1. Purpose

To calculate the soluble boron, soluble nitrogen and boron nitride concentration in equilibrium with austenite at any temperature.

2. Specification

SUBROUTINE MAP_SOL_BOR(BATM,BWT,NITATM,NITWT,NIT2,
&TEMPC,BSOL,BWTSOL,NITSOL,NITWTSOL,NITB,BNIT)
IMPLICIT DOUBLE PRECISION(A-H,K-Z), INTEGER(I-J)

3. Description

If only boron is present then all of this is assumed to remain in solution, whilst if there is only residual nitrogen (that nitrogen present after reacting with titanium to form TiN) all of this is assumed to remain in solution.

If both residual nitrogen and boron are present then a solubility product is used to assess whether all of the boron and nitrogen can remain in solution. This is determined by assuming that all of the residual nitrogen enters solution and calculating the maximum possible soluble boron concentration. This is then compared with the actual boron concentration. If the actual boron concentration is less than this maximum then all of the boron and all of the residual nitrogen can remain in solution simultaneously. However, if the actual boron concentration is greater than the maximum calculated then all the boron and the residual nitrogen cannot remain in solution simultaneously and boron nitride will precipitate. By considering mass balance and assuming that the stoichiometry of boron nitride is represented exactly by BN then it is possible to calculate the soluble boron concentration using an analytical approach.

4. References

1. S.J. Jones, *PhD. thesis, University of Cambridge, UK*, (submitted in 1996).

2. Maitrepierre *et al.*, *Boron in Steels, Proc. Metall. Soc. A.I.M.E.*, eds S. K. Banerji and J. E. Morral, Milwaukee, USA, (1979) 1-19.

5. Parameters

5.1 Input Parameters

BATM - real
BATM is the total number of moles of boron per 100 grams of austenite.

BWT - real
BWT is the total boron concentration (wt %).

NITATM - real
NITATM is the total number of moles of nitrogen per 100 grams of austenite.

NITWT - real
NITWT is the total nitrogen concentration (wt %).

NIT2 - real
NIT2 is the number of moles of residual nitrogen (after TiN formation) per 100 grams of austenite.

TEMPC - real
TEMPC is the temperature at which the solubility product is evaluated (°C).

5.2 Output Parameters

BSOL - real
BSOL is the number of moles of soluble boron per 100 grams of austenite.

BWTSOL - real
BWTSOL is the soluble boron concentration (wt %).

NITSOL - real
NITSOL is the number of moles of soluble nitrogen per 100 grams of austenite.

NITWTSOL - real
NITWTSOL is the soluble nitrogen concentration (wt %).

BNIT - real
BNIT is the number of moles of boron combined with nitrogen per 100 grams of austenite.

NITB - real
NITB is the number of moles of nitrogen combined with boron per 100 grams of austenite.

6. Error Indicators

7. Accuracy

8. Further Comments

9. Example

9.1 Program Text

```
IMPLICIT DOUBLE PRECISION(A-H,K-Z), INTEGER(I-J)
READ(*,*) BATM,BWT,NITATM,NITWT,NIT2,TEMPC
CALL MAP_SOL_BOR(BATM,BWT,NITATM,NITWT,NIT2,
&TEMPC,BSOL,BWTSOL,NITSOL,NITWTSOL,NITB,BNIT)
&WRITE(*,1) BSOL,BWTSOL,NITSOL,NITWTSOL,NITB,BNIT
1FORMAT (E10.3,1X,E10.3,1X,E10.3,1X,E10.3,1X,E10.3,1X,E10.3)
STOP
END
```

9.2 Program Data

0.370E-5 0.400E-2 0.357E-5 0.500E-2 0.940E3

9.3 Program Results

0.184E-5 0.199E-2 0.171E-5 0.239E-2 0.186E-5 0.186E-5

10. Auxiliary Routines

11. Keywords

solubility, product, equilibrium, boron, nitrogen, austenite, steel, nitride, temperature.

12. FORTRAN 77 Code

```
C SUBROUTINE TO CALCULATE THE SOLUBLE BORON, SOLUBLE NITROGEN AND BORON NITRIDE
C CONCENTRATION IN EQUILIBRIUM WITH AUSTENITE AT ANY TEMPERATURE.
        SUBROUTINE MAP_SOL_BOR(BATM,BWT,NITATM,NITWT,NIT2,TEMPC,
     &  BSOL,BWTSOL,NITSOL,NITWTSOL,NITB,BNIT)
        IMPLICIT REAL*8 (A-H,L-Z),INTEGER (I-K)
        IF(BATM.EQ.0.0. AND. NIT2.EQ.0.0 ) THEN
          NITB=0.0
          BWTSOL=0.0
          BSOL=0.0
          NITWTSOL=0.0
          NIT3=0.0
          GOTO 2
        ENDIF
        IF(BATM.EQ.0.0) THEN
          NITB=0.0
          BWTSOL=0.0
          BSOL=0.0
```

```
          NITWTSOL=NIT2*NITWT/NITATM
          NIT3=NIT2
          GOTO 2
        ENDIF
        IF(NIT2.EQ.0.0) THEN
          NITB=0.0
          BWTSOL=BWT
          BSOL=BATM
          NITWTSOL=0.0
          NIT3=0.0
          GOTO 2
        ENDIF
C SET SOLUBLE NITROGEN NIT3 EQUAL TO NIT2 - ALL AVAILABLE AFTER TIN FORMATION:
        NIT3=NIT2
C SOLUBILITY PRODUCT DUE TO MAITREPIERRE ET AL. (1979):
        BWTSOLMAX=(10.0**(0.20 - (6700.0/(TEMPC+273.00))))/
     &    (NIT3*NITWT/NITATM)
C IF BWTSOLMAX IS GREATER THAN OR EQUAL TO BWT THEN ASSUME THAT ALL OF THE AVAILABLE
C NITROGEN AND ALL OF THE BORON CAN REMAIN IN SOLUTION AT THIS TEMPERATURE.
        IF (BWTSOLMAX.GE.BWT) THEN
          BWTSOL=BWT
          BSOL=BATM
          NITWTSOL=NIT2*NITWT/NITATM
          NIT3=NIT2
          NITB=0.0
          GOTO 2
        ENDIF
C OR IF BWTSOLMAX IS LESS THAN BWT THEN NIT2 AND BATM CANNOT ALL REMAIN IN SOLUTION AT
C THIS TEMPERATURE.
        CONST=(BWT/BATM)*(NITWT/NITATM)
        SOLPRODCON=(10.0**(0.20-(6700.0/(TEMPC+273.00))))/(CONST)
        DIFBATMNIT2=BATM-NIT2
        SQROOT=( (DIFBATMNIT2**2.0)+(4.0*SOLPRODCON) )**(0.5)
        NIT3A=( (-1.0*DIFBATMNIT2)+SQROOT )/2.0
        NIT3B=( (-1.0*DIFBATMNIT2)-SQROOT )/2.0
        IF (NIT3A.LT.0.0) THEN
          NIT3=NIT3B
        ELSE
          NIT3=NIT3A
        ENDIF
        BSOL=SOLPRODCON/NIT3
        BWTSOL=BSOL*BWT/BATM
        NITWTSOL=NIT3*NITWT/NITATM
        NITB=BATM-BSOL
        GOTO 2
2       NITSOL=NIT3
        BNIT=NITB
        RETURN
        END
```

APPENDIX FIVE
Subroutine MAP_TTT_TO_CCT

0. Provenance of Source Code

S.J. Jones and H.K.D.H. Bhadeshia, Phase Transformations Group, Department of Materials Science and Metallurgy, University of Cambridge, Cambridge, UK.

1. Purpose

To convert a known TTT (time-temperature-transformation) curve into a CCT (continuous-cooling-transformation) curve using Scheil's additive reaction rule.

2. Specification

SUBROUTINE MAP_TTT_TO_CCT(IINFORM,IPAIRS,THEQU,PAE3,
&MS,ISWITCH,TITTT,TMTTT,ITTTPT,TTIME,TTEMP,ICCTPT,TICCT,
&TMCCT)
IMPLICIT DOUBLE PRECISION(A-H,K-Z), INTEGER(I-J)

3. Description

An input TTT curve is converted into a CCT curve using Scheil's additive reaction rule. An arbitrary natural cooling curve is divided into an equivalent series of small isothermal steps. If $\tau(T)$ is the incubation time before the start of detectable transformation during an isothermal treatment at the temperature T, then transformation during continuous cooling is considered to begin when:

$$\int_{t=0}^{t} \frac{dt}{\tau(T)} = 1$$

where t is the time and dt is the duration of the small isothermal step at the temperature T. This procedure is repeated for a wide range of cooling curves to generate the complete CCT curve.

4. References

1. J.W. Christian, The theory of phase transformations in metals and alloys, Part 1, 2nd ed., *Permagon, Oxford, UK* (1965).

2. H.K.D.H. Bhadeshia *et al.*, *Scandinavian Journal of Metallurgy*, **15**, (1986) 97-103.

5. Parameters

5.1 Input Parameters

IINFORM - integer

IINFORM specifies the format of the input TTT curve.

IPAIRS - integer
IPAIRS specifies the number of points in the input TTT curve.

THEQU - real
THEQU is the temperature above which the product phase cannot form (°C).

PAE3 - real
PAE3 is the Ae_3' temperature above which ferrite cannot form under paraequilibrium conditions (°C).

MS - real
MS is the martensite start temperature (°C).

ISWITCH - integer
ISWITCH is a flag which if set to unity causes all the arrays in the subroutine to be initialised.

TITTT - real
TITTT is an array used to store transformation start times for the input TTT curve (s).

TMTTT - real
TMTTT is an array used to store temperature for the input TTT curve (°C).

5.2 Output Parameters

ITTTPT - integer
ITTTPT is the number of points in the output TTT curve.

TTIME- real
TTIME is an array used to store transformation start times for the output TTT curve (s).

TTEMP - real
TTEMP is an array used to store temperature for the output TTT curve (°C).

ICCTPT - integer
ICCTPT is the number of points in the output CCT curve.

TICCT- real

TICCT is an array used to store transformation start times for the output CCT curve (s).

TMCCT- real
TMCCT is an array used to store temperature for the output CCT curve (°C).

6. Error Indicators

1. If ISWITCH is incorrectly set then an error is reported and the program execution is stopped.

2. If the arrays used to store the calculated CCT curve are too small then an error is reported and the program execution is stopped.

7. Accuracy

8. Further Comments

1. This subroutine requires that the temperature intervals in the input TTT data are either 1 °C (IINFORM=1) or 20 °C (IINFORM=2).

2. The format of the input TTT data must be such that the highest temperature is read first.

9. Example

9.1 Program Text

```
   IMPLICIT DOUBLE PRECISION(A-H,K-Z), INTEGER(I-J)
   DOUBLE PRECISION TITTT(1000),TMTTT(1000),TTIME(1000),
&TTEMP(1000),TICCT(300),TMCCT(300)
   READ(*,*) IINFORM,IPAIRS,THEQU,PAE3,MS,ISWITCH
   DO 1 I1=1,IPAIRS,1
   READ(*,*) TMTTT(I1),TITTT(I1)
1CONTINUE
   CALL MAP_TTT_TO_CCT(IINFORM,IPAIRS,THEQU,PAE3,
&MS,ISWITCH,TITTT,TMTTT,ITTTPT,TTIME,TTEMP,ICCTPT,TICCT,
&TMCCT)
   DO 2 I2=1,30,1
   WRITE(*,3) TMCCT(I2),TICCT(I2)
2CONTINUE
3FORMAT (E10.4,1X,E10.4)
   STOP
   END
```

9.2 Program Data

```
1 29 0.8139E3 0.8139E3 0.4746E3 0
0.7600E+03 0.1675E+12
0.7400E+03 0.2112E+06
0.7200E+03 0.7462E+03
0.7000E+03 0.6394E+02
0.6800E+03 0.2026E+02
0.6600E+03 0.9643E+01
0.6400E+03 0.6796E+01
0.6200E+03 0.8430E+01
0.6000E+03 0.3299E+02
0.5800E+03 0.4692E+02
0.5600E+03 0.9134E+02
0.5400E+03 0.2300E+03
0.5200E+03 0.7192E+03
0.5000E+03 0.2730E+04
0.4800E+03 0.1234E+05
0.4600E+03 0.6583E+05
0.4400E+03 0.4225E+06
0.4200E+03 0.3220E+07
```

```
0.4000E+03 0.2945E+08
0.3800E+03 0.3262E+09
0.3600E+03 0.4437E+10
0.3400E+03 0.7165E+11
0.3200E+03 0.1487E+13
0.3000E+03 0.4106E+14
0.2800E+03 0.1507E+16
0.2600E+03 0.7929E+17
0.2400E+03 0.5942E+19
0.2200E+03 0.6672E+21
0.2000E+03 0.1192E+24
```

9.3 Program Results

```
0.6971E+03 0.7343E+03
0.6965E+03 0.6773E+03
0.6958E+03 0.6249E+03
0.6951E+03 0.5768E+03
0.6944E+03 0.5326E+03
0.6936E+03 0.4920E+03
0.6927E+03 0.4547E+03
0.6919E+03 0.4203E+03
0.6909E+03 0.3887E+03
0.6900E+03 0.3595E+03
0.6890E+03 0.3327E+03
0.6880E+03 0.3079E+03
0.6870E+03 0.2850E+03
0.6860E+03 0.2638E+03
0.6849E+03 0.2442E+03
0.6839E+03 0.2261E+03
0.6828E+03 0.2093E+03
0.6818E+03 0.1938E+03
0.6807E+03 0.1793E+03
0.6797E+03 0.1659E+03
0.6786E+03 0.1536E+03
0.6774E+03 0.1423E+03
0.6762E+03 0.1319E+03
0.6750E+03 0.1223E+03
0.6737E+03 0.1134E+03
0.6723E+03 0.1052E+03
0.6709E+03 0.9770E+02
0.6694E+03 0.9073E+02
0.6679E+03 0.8427E+02
0.6664E+03 0.7830E+02
```

10. Auxiliary Routines

11. Keywords

TTT, CCT, conversion, Scheil, additive, reaction, rule, incubation, time, temperature, isothermal, transformation, continuous, cooling.

12. FORTRAN 77 Code

```
C SUBROUTINE TO CALCULATE A CCT CURVE FROM A KNOWN TTT CURVE USING NATURAL COOLING CURVES.
C (BY SJ JONES AND HKDH BHADESHIA, UNIVERSITY OF CAMBRIDGE, 1996).
        SUBROUTINE MAP_TTT_TO_CCT(IINFORM,IPAIRS,THEQU,PAE3,MS,
     &  ISWITCH,TITTT,TMTTT,ITTTPT,TTIME,TTEMP,ICCTPT,TICCT,TMCCT)
        IMPLICIT DOUBLE PRECISION (A-H,K-Z),INTEGER(I,J)
        DOUBLE PRECISION TITTT(1000),TMTTT(1000),
     &  TMCCT(300),TICCT(300),TTEMP(1000),TTIME(1000)
C TMTTT AND TITTT CONTAIN THE INPUT TTT CURVE.
C TTEMP AND TTIME CONTAIN THE FULL TTT CURVE.
C TMCCT AND TICCT CONTAIN THE CALCULATED CCT CURVE.
        IF (ISWITCH.EQ.1) THEN
          DO 5 J5=1,300
            TICCT(J5)=0.0
            TMCCT(J5)=0.0
5         CONTINUE
          DO 10 J10=1,1000
            TITTT(J10)=0.0
            TMTTT(J10)=0.0
            TTEMP(J10)=0.0
            TTIME(J10)=0.0
10        CONTINUE
          PRETEMP=0.0
          TEMP=0.0
        ENDIF
        IF (IINFORM.EQ.1) THEN
C INTERPOLATE TO ONE DEGREE CENTIGRADE INTERVALS:
          IPLONE=IPAIRS-2
          DO 20 J20=0,IPLONE
            TTEMP(J20*20+1)=TMTTT(J20+1)
            TTIME(J20*20+1)=TITTT(J20+1)
            TTEMP(J20*20+21)=TMTTT(J20+2)
            TTIME(J20*20+21)=TITTT(J20+2)
            ANUM=(TTIME(J20*20+1)-TTIME(J20*20+21))
            BNUM=(TTEMP(J20*20+1)-TTEMP(J20*20+21))
            CONS=ANUM/BNUM
            DO 30 J30=2,20
              TTEMP(J20*20+J30)=TTEMP(J20*20+1)-1.0*(J30-1)
              AVAL=TTEMP(J20*20+1)-TTEMP(J20*20+21)
              BVAL=TTEMP(J20*20+1)-TTEMP(J20*20+J30)
              DELTA=(AVAL-BVAL)*CONS
              TTIME(J20*20+J30)=TTIME(J20*20+21)+DELTA
30          CONTINUE
20        CONTINUE
```

```
                ITTTPT=((IPAIRS-1)*20)+1
              ELSEIF (IINFORM.EQ.2) THEN
C COPY THE INPUT TTT DATA.
                DO 35 I35=1,IPAIRS,1
                  TTEMP(I35)=TMTTT(I35)
                  TTIME(I35)=TITTT(I35)
35              CONTINUE
                ITTTPT=IPAIRS
              ELSE
                WRITE(*,*) 'ERROR - INPUT TTT FORMAT NOT SPECIFIED !'
                PAUSE
              ENDIF
C COOLING PARAMETERS:
              C1=0.6208D-1
              C2=3.085
              A2=C1*(1-C2)
              A3=1-C2
              AFAC=(PAE3-20.0)**A3
              BFAC=(PAE3-10.0-20.0)**A3
              STARTEFFHT=50.0*A2/(AFAC-BFAC)
              ICCTPT=0
              DO 40 J40=1,ITTTPT
                IF (TTEMP(J40).LT.THEQU) THEN
C BEGIN SCHEILS SUM:
                  IBEGIN=J40
                  GOTO 50
                ENDIF
40            CONTINUE
C COOLING MODEL:
50            DO 80 J80=0,100
                IF (J80.EQ.0) THEN
                  IELOOP=150
                ELSE
                  IELOOP=29
                  NEW1EFFHT=PRE2EFFHT
                  NEW2EFFHT=EFFHT
                ENDIF
C VARY THE COOLING RATE:
                DO 70 J70=0,IELOOP
                  SUM=0.0
                  IF (J80.EQ.0) THEN
                    PRE2EFFHT=PREEFFHT
                    PREEFFHT=EFFHT
                    EFFHT=STARTEFFHT*(1/(2**((1.0*J70)*(19.0/150.0))))
                  ELSE
                    PRE2EFFHT=PREEFFHT
                    PREEFFHT=EFFHT
                    EFFHT=NEW1EFFHT-((NEW1EFFHT-NEW2EFFHT)*((1.0*J70)+1)/30.0)
                  ENDIF
                  IF ( THEQU.GT.TTEMP(1) ) THEN
                    TINTV=EFFHT*((THEQU-20.0)**A3-(TTEMP(1)-20.0)**A3)/A2
```

213

```fortran
        FRAC=TINTV/TTIME(1)
        SUM=FRAC
      ENDIF
C APPLY SCHEILS ADDITIVE REACTION RULE:
      IENDL=ITTTPT-1
      DO 60 J60=IBEGIN,IENDL
      TINTV=EFFHT*((TTEMP(J60)-20.0)**A3-(TTEMP(J60+1)-20.0)**A3)/A2
      FRAC=TINTV/((TTIME(J60)+TTIME(J60+1))/2.0)
      PRETEMP=TEMP
      TEMP=(TTEMP(J60)+TTEMP(J60+1))/2.0
      PRESUM=SUM
      SUM=SUM+FRAC
      IF (SUM.GE.1) THEN
        IF (J60.EQ.IBEGIN) THEN
         RTEMP=TEMP
        ELSE
         CONA=(1.0-PRESUM)/(SUM-PRESUM)
         CONB=(PRETEMP-TEMP)
         RTEMP=PRETEMP-(CONA*CONB)
        ENDIF
        IF (RTEMP.GT.(TTEMP(1)-5.0)) GOTO 70
C STOP WHEN BELOW THE MARTENSITE START TEMPERATURE:
        IF (RTEMP.LT.MS) GOTO 90
C CALCULATE THE TIME BEFORE THE TRANSFORMATION BEGINS:
        REAST=EFFHT*((PAE3-20.0)**A3-(RTEMP-20.0)**A3)/A2
C STORE THE CCT DATA:
        ICCTPT=ICCTPT+1
        IF (ICCTPT.GT.1000) THEN
         WRITE (*,*) "ERROR - CCT ARRAY TOO SMALL !"
         PAUSE
        ENDIF
        TMCCT(ICCTPT)=RTEMP
        TICCT(ICCTPT)=REAST
        GOTO 70
      ENDIF
C BELOW THE TTT CURVE - BUT SCHEILS SUM IS LESS THAN UNITY:
      IF (J60.EQ.IENDL) GOTO 80
60      CONTINUE
70      CONTINUE
80    CONTINUE
90    RETURN
      END
```

APPENDIX SIX

Boundary Nucleated Transformation Kinetics

This appendix contains two analytical models for isothermal phase transformations in which the nuclei form along the grain boundaries in the parent material. Both models are developed from methods originally due to Cahn (1956) which are described in section 2.1.2. Only the essential differences are given here.

Model for the Widmanstätten Ferrite Transformation

It is assumed that the Widmanstätten ferrite (β) plates grow in a linear fashion at a rate G. Each plate prior to site saturation is modelled as a tetragonal prism growing perpendicular to the grain boundary on which it nucleated. The longest dimension of each prism is $q = G(t - \tau)$ and the ratio of the length to thickness is η. The extended area O_{β}^{e} is defined as the sum of the areas of intersection of the plates of β with an arbitrary plane at y. The change dO_{β}^{e} in O_{β}^{e} due to those plates nucleated in the interval τ to $\tau + d\tau$ is:

$$dO_{\beta}^{e} = O_b I_B [\eta\, G^2 (t - \tau)^2]\, d\tau \qquad G(t - \tau) > y \qquad \text{(A6.1)}$$

$$dO_{\beta}^{e} = 0 \qquad G(t - \tau) < y \qquad \text{(A6.2)}$$

If the nucleation rate per unit area of boundary I_B remains constant during the transformation and noting that only those particles nucleated such that $\tau < t - (y/G)$ can contribute to the extended area of intersection at y, then the total extended area intersected at the time t is:

$$O_{\beta}^{e} = \int_{\tau=0}^{t-(y/G)} \eta\, G^2 O_b I_B (t^2 - 2t\tau + \tau^2)\, d\tau \qquad \text{(A6.3)}$$

Integration gives:

$$O_{\beta}^{e} = (1/3) O_b I_B \eta\, G^2 t^3 [1 - \theta^3] \qquad \text{(A6.4)}$$

where $\theta = y/(Gt)$. Assuming that there is no interference from other nucleating boundaries and noting that Widmanstätten ferrite plates never cross the austenite grain boundaries, the total volume V_{β}^{b} of material originating from this grain boundary is:

$$V_{\beta}^{b} = \int_{\theta=0}^{1} O_b Gt (1 - \exp\{-O_{\alpha}^{e}/O_b\})\, d\theta \qquad \text{(A6.5)}$$

or

$$V_{\beta}^{b} = O_b Gt f(\eta, G, I_B, t) \qquad \text{(A6.6)}$$

where:

$$f(\eta, G, I_B, t) = \int_{0}^{1} [1 - \exp\{-(1/3) I_B \eta\, G^2 t^3 (1 - \theta^3)\}]\, d\theta \qquad \text{(A6.7)}$$

The total extended volume V_{β}^{e} of material emanating from all of the grain boundaries in an assembly is:

$$V_{\beta}^{e} = S_V V Gt f(\eta, G, I_B, t) \qquad \text{(A6.8)}$$

If ϕ is the paraequilibrium volume fraction of Widmanstätten ferrite then the fraction of the paraequilibrium volume ϕV transformed at the time t is:

$$\zeta_{\beta} = \frac{V_{\beta}}{\phi V} = 1 - \exp[-(S_V/\phi) Gt f(\eta, G, I_B, t)] \qquad \text{(A6.9)}$$

If either G, I_B or t is large then the grain boundaries rapidly saturate so that the function $f(\eta, G, I_B, t)$ tends to unity. Therefore, equation A6.9 reduces to an equation which describes planar thickening:

$$\zeta_\beta = 1 - \exp[-(S_V/\phi)Gt] \qquad (A6.10)$$

Model for the Pearlite Transformation

The pearlite (β) nodules grow in a linear manner at a rate G. Each nodule prior to site saturation is modelled as a a disc whose face is parallel to the grain boundary on which it nucleated. The half-thickness of each nodule is $q = G(t - \tau)$ and the radius is ηq where η is the aspect ratio. The extended area O_β^e is defined as the sum of the areas of intersection of the nodules of β with an arbitrary plane at y. The change dO_β^e in O_β^e due to those nodules nucleated in the interval τ to $\tau + d\tau$ is:

$$dO_\beta^e = O_b I_B [\pi(\eta G)^2 (t - \tau)^2]\, d\tau \qquad G(t - \tau) > y \qquad (A6.11)$$

$$dO_\beta^e = 0 \qquad G(t - \tau) < y \qquad (A6.12)$$

If the nucleation rate per unit area of boundary I_B is invariant during the transformation and considering that only those nodules nucleated such that $\tau < t - (y/G)$ may contribute to the extended area of intersection at y, then the total extended area intersected at the time t is:

$$O_\beta^e = \int_{\tau=0}^{t-(y/G)} \pi(\eta G)^2 O_b I_B (t^2 - 2t\tau + \tau^2)\, d\tau \qquad (A6.13)$$

Integration yields:

$$O_\beta^e = (1/3) O_b I_B \pi(\eta G)^2 t^3 [1 - \theta^3] \qquad (A6.14)$$

where $\theta = y/(Gt)$. If there is no interference from other nucleating boundaries and noting that pearlite nodules may cross the austenite grain boundaries, the total volume V_β^b of material originating from this grain boundary is:

$$V_\beta^b = \int_{\theta=0}^{1} O_b Gt(1 - \exp\{-O_\alpha^e/O_b\})\, d\theta \qquad (A6.15)$$

or

$$V_\beta^b = 2 O_b Gt f(\eta, G, I_B, t) \qquad (A6.16)$$

where:

$$f(\eta, G, I_B, t) = \int_{0}^{1} [1 - \exp\{-(\pi/3)I_B(\eta G)^2 t^3 (1 - \theta^3)\}]\, d\theta \qquad (A6.17)$$

The total extended volume V_β^e of material emanating from all of the grain boundaries in an assembly is:

$$V_\beta^e = 2 S_V V Gt f(\eta, G, I_B, t) \qquad (A6.18)$$

If ϕ is the equilibrium volume fraction of pearlite then the fraction of the equilibrium volume ϕV transformed at the time t is:

$$\zeta_\beta = \frac{V_\beta}{\phi V} = 1 - \exp[-2(S_V/\phi)Gt f(\eta, G, I_B, t)] \qquad (A6.19)$$

If either G, I_B or t is large then the grain boundaries rapidly saturate so that the function $f(\eta, G, I_B, t)$ tends to unity. Equation A6.19 then reduces to an equation for planar thickening:

$$\zeta_\beta = 1 - \exp[-2(S_V/\phi)Gt] \qquad (A6.20)$$

APPENDIX SEVEN

Nucleation on a Grain Surface

The heterogeneous activation energy barrier to ferrite nucleation at a planar austenite grain boundary can be found (Appendix Three) by considering the nucleus shape illustrated in Figure A7.1, where $\sigma_{\gamma\gamma}$ is the interfacial energy per unit area of the incoherent austenite-austenite grain boundary (assumed to be 0.07 J m^{-2}). The ferrite nucleus is assumed to be truncated by a low-energy facet which forms with respect to one of the adjacent austenite grains. The critical radius of curvature of the ferrite nucleus R is obtained using classical nucleation theory (ignoring strain energy terms) as:

$$R = \frac{2\sigma_{\alpha\gamma}}{-\Delta G} \qquad (A7.1)$$

where $\sigma_{\alpha\gamma}$ is the interfacial energy of the incoherent ferrite-austenite surface per unit area and ΔG is the free energy change per unit volume driving the austenite to ferrite transformation (Christian, 1975). Assuming that those interfacial energies which have components in the plane of the austenite grain boundary balance allows the 'wetting' angle to be evaluated as:

$$\mu = \cos^{-1}\left(\frac{\sigma_{\gamma\gamma}}{2\sigma_{\alpha\gamma}}\right) \qquad (A7.2)$$

The angle β between the low-energy facet and the tangent to the ferrite nucleus at the edge between the faceted and unfaceted ferrite–austenite interfaces is given by (Johnson *et al.*, 1975):

$$\beta = \cos^{-1}\left(\frac{\varphi_{\alpha\gamma}}{\sigma_{\alpha\gamma}}\right) \qquad (A7.3)$$
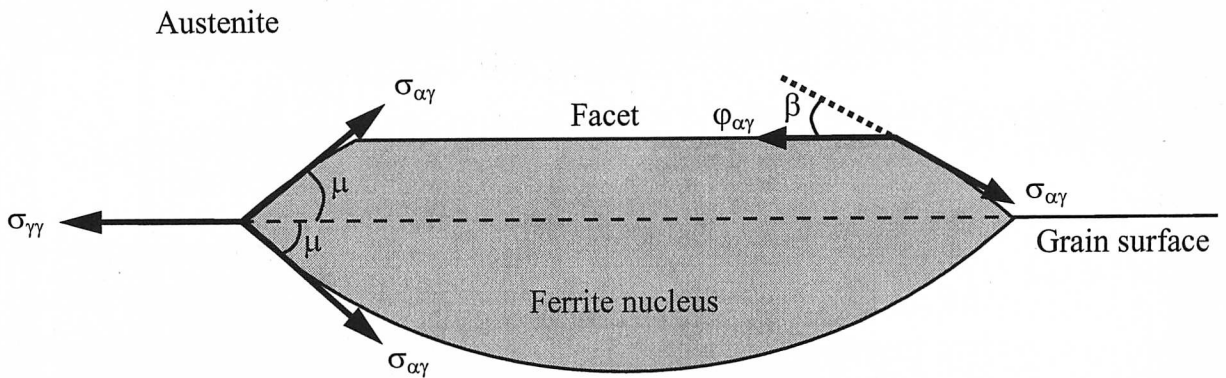
Figure A7.1   The nucleus geometry used to model the heterogeneous activation energy barrier to ferrite nucleation on a planar grain surface.

The following volumes and areas are required:

V_n = volume of the unfaceted nucleus on one side of the boundary.

217

$V_{c5}=$ volume lost due to the formation of a low-energy facet.

$A_n=$ curved surface area of the unfaceted nucleus on one side of the boundary.

$A_a=$ area of the austenite grain boundary lost to the nucleus.

$A_{c6}=$ curved surface area of the nucleus lost due to the formation of a facet.

$A_f=$ planar surface area of the facet.

These are calculated using:

$$V_n = \frac{1}{3}\pi R^3 f(\mu) \tag{A7.4}$$

$$V_{c5} = \frac{1}{3}\pi R^3 f(\beta) \tag{A7.5}$$

$$A_n = 2\pi R^2 (1 - \cos\mu) \tag{A7.6}$$

$$A_a = \pi R^2 (1 - \cos^2\mu) \tag{A7.7}$$

$$A_{c6} = 2\pi R^2 (1 - \cos\beta) \tag{A7.8}$$

$$A_f = \pi R^2 (1 - \cos^2\beta) \tag{A7.9}$$

where the functions $f(\mu)$ and $f(\beta)$ are:

$$f(\mu) = 2 - 3\cos\mu + \cos^3\mu \tag{A7.10}$$

$$f(\beta) = 2 - 3\cos\beta + \cos^3\beta \tag{A7.11}$$

If $\beta < \mu$ then the ferrite nucleus has volume on both sides of the boundary so that the activation energy barrier to nucleation is:

$$G_b^* = \Delta G(2V_n - V_{c5}) + \sigma_{\alpha\gamma}(2A_n - A_{C6}) - \sigma_{\gamma\gamma}A_a + \varphi_{\alpha\gamma}A_f \tag{A7.12}$$

However, if $\beta \geq \mu$ then the ferrite nucleus has volume on one side of the boundary and the activation energy barrier to nucleation is:

$$G_b^* = \Delta G V_n + \sigma_{\alpha\gamma}A_n + (\varphi_{\alpha\gamma} - \sigma_{\gamma\gamma})A_a \tag{A7.13}$$

REFERENCES

Aaronson, H.I., Eylon, D., Cooke, C.M., Enomoto, M. and Froes, F.H., The W_S temperature as affected by the matrix grain size. *Scripta Metallurgica et Materialia*, **23** (1989) 435-440.

Aaronson, H.I. and Lee, J.K., The kinetic equations of solid-solid nucleation theory. *Lectures on the Theory of Phase Transformations, ed. by Aaronson, H.I., American Institute of Mining, Metallurgical and Petroleum Engineering, New York, USA*, (1975) 83-115.

Abbruzzese, G., Computer simulated grain growth stagnation. *Acta Metallurgica*, **33** (1985) 1329-1337.

Abson, D.J., Non-metallic inclusions in ferritic steel weld metals - A review. *International Institute of Welding*, **IX-1486-87** (1987) .

Abson, D.J. and Dolby, R.E., *Welding Research Institute Bulletin*, (1978) 202-206.

Abson, D.J., Dolby, R.E. and Hart, P.H.M., Investigation into the role of non-metallic inclusions on ferrite nucleation in carbon steel weld metals. *Welding Institute*, **67/1978/M** (1978) .

Ali, A. and Bhadeshia, H.K.D.H., Growth rate data on bainite in alloy steels. *Materials Science and Technology*, **5** (1989) 398-402.

Andrews, K.W. and Brooksbank, D., Stresses associated with inclusions in steel: A photoelastic analogue and the effect of inclusions in proximity. *Journal of the Iron and Steel Institute*, (1972) 765-776.

Anelli, E., Amato, S. and Di Nunzio, P.E., Mathematical model of phase transformation of deformed austenite for predicting the microstructure of thermomechanically processed low-carbon steels. *Final report for the European Coal and Steel Community, Centro Sviluppo Materiali, Rome, Italy*, **Contract 7210-EA/418 (D 3.7/89)** (1991) .

Avrami, M., *Journal of Chemical Physics*, **7** (1939) 1103.

Avrami, M., *Journal of Chemical Physics*, **8** (1940) 212.

Avrami, M., *Journal of Chemical Physics*, **9** (1941) 177.

Babu, S.S., Acicular ferrite and bainite in Fe-Cr-C weld deposits. *Ph.D. thesis, University of Cambridge, UK*, (1991) .

Babu, S.S., David, S.A., Vitek, J.M., Mundra, K. and DebRoy, T., Development of macro- and microstructures of carbon-manganese low alloy steel welds: Inclusion formation. *Materials Science and Technology*, **11** (1995) 185-199.

Bailey, N., Titanium flux additions during submerged-arc welding of ferritic steels. *Welding Institute*, **7702.11/83/359.3** (1983) .

Bansal, P.P. and Ardell, A.J., Average nearest neighbour distances between uniformly distributed fine particles. *Metallography*, **5** (1972) 97-111.

Barbaro, F.J., The microstructural development, toughness and weldability of a new oxide dispersed steel. *Ph.D. thesis, University of New South Wales, Australia*, (1990) .

Barbaro, F.J., Edwards, R.H. and Easterling, K.E., The composition and morphology of non-metallic inclusions in HSLA steel. *7th International Conference of the Australian X-ray Analysis Association, Proc., University of Western Australia, Australia*, (1988) .

Barritte, G.S., The microstructure of weld metals in low alloy steels. *Ph.D. thesis, University of Cambridge, UK*, (1982) .

Barritte, G.S. and Edmonds, D.V., Microstructure and toughness of HSLA steel weld metals. *Advances in the Physical Metallurgy and Applications of steels, Proc. Metals Society, Liverpool, UK*, (1981) .

Barritte, G.S., Ricks, R.A. and Howell, P.R., Application of STEM/EDS to the study of microstructural development in HSLA steel weld metals. *Quantitative Microanalysis with High Spatial Resolution, Proc. of the Metals Society, Manchester, UK*, (1981) 112-118.

Bhadeshia, H.K.D.H., A rationalisation of shear transformations in steels. *Acta Metallurgica*, **29** (1981) 1117-1130.

Bhadeshia, H.K.D.H., Application of first-order quasichemical theory to transformations in steels. *Metal Science*, **16** (1982c) 167-169.

Bhadeshia, H.K.D.H., Bainite in steels. *Institute of Materials, London*, (1992) .

Bhadeshia, H.K.D.H, Bainite: Overall transformation kinetics. *Journal de Physique*, **43(2-C4)** (1982a) 443-448.

Bhadeshia, H.K.D.H., Diffusion controlled growth of ferrite plates in plain-carbon steels. *Materials Science and Technology*, **1** (1985) 497-504.

Bhadeshia, H.K.D.H., Diffusional formation of ferrite in iron and its alloys. *Progress in Materials Science*, **29** (1985b) 321-386.

Bhadeshia, H.K.D.H., Diffusion of carbon in austenite. *Metal Science*, **15** (1981a) 477-479.

Bhadeshia, H.K.D.H., Driving force for martensitic transformation in steels. *Metal Science*, **15** (1981b) 175-177.

Bhadeshia, H.K.D.H., Modelling the elementary mechanical properties of steel welds. *Mathematical Modelling of Weld Phenomena III, eds Cerjak, H., Buchmayer, B. and Bhadeshia, H.K.D.H., Institute of Materials*, (1996) 1-50.

Bhadeshia, H.K.D.H., Thermodynamic analysis of isothermal transformation diagrams. *Metal Science*, **16** (1982b) 159-165.

Bhadeshia, H.K.D.H., Thermodynamic extrapolation and martensite-start temperature of substitutionally alloyed steels. *Metal Science*, **15** (1981c) 178-180.

Bhadeshia, H.K.D.H. and Ali, A., Growth rate data on bainite in alloy steels. *Materials Science and Technology*, **5** (1989) 398-402.

Bhadeshia, H.K.D.H., David, S.A., Vitek, J.M. and Reed, R.W., Stress induced transformation to bainite in Fe-Cr-Mo-C pressure vessel steel. *Materials Science and Technology*, **7** (1991) 686-698.

Bhadeshia, H.K.D.H. and Edmonds, D.V., The bainite transformation in a silicon steel. *Metallurgical and Materials Transactions A*, **10A** (1979) 895-907.

Bhadeshia, H.K.D.H. and Edmonds, D.V., The mechanism of bainite formation in steels. *Acta Metallurgica*, **28** (1980) 1265-1273.

Bhadeshia, H.K.D.H., Gretoft, B. and Svensson, L.-E., An analysis of cooling curves from the fusion zone of steel weld deposits. *Scandinavian Journal of Metallurgy*, **15** (1986a) 97-103.

Bhadeshia, H.K.D.H., Svensson, L.-E. and Gretoft, B., A model for the development of microstructure in low-alloy steel (Fe-Mn-Si-C) weld deposit. *Acta Metallurgica*, **33** (1985) 1271-1283.

Bhadeshia, H.K.D.H. and Svensson, L.-E., Modelling the evolution of microstructure in steel

weld metals. *Mathematical Modelling of Weld Phenomena, eds Cerjak, H. and Easterling, K.E., Institute of Materials,* (1993) 109-180.

Bhadeshia, H.K.D.H. and Svensson, L.-E., Quantitative model for boron effects in steel welds. *Modelling and Control of Joining Processes, Proc. of American Welding Society, Orlando, USA,* (1993) .

Bhadeshia, H.K.D.H., Svensson, L.-E. and Gretoft, B., The austenite grain structure of low alloy steel weld deposits. *Journal of Materials Science,* **21(11)** (1986b) 3947-3951.

Bhadeshia, H.K.D.H., Svensson, L.-E. and Gretoft, B., Theory for allotriomorphic ferrite formation in steel weld deposits. *Welding and the Performance of Pipelines, Welding Institute, London, UK,* (1987) 517-529.

Bodnar, R.L. and Hansen, S.S., Effect of austenite grain size and cooling rate on Widmanstätten ferrite formation in low-alloy steels. *Metallurgical and Materials Transactions A,* **25A** (1994a) 665-675.

Bodnar, R.L. and Hansen, S.S., Effects of Widmanstätten ferrite formation on the mechanical properties of a 0.2 pct C - 0.7 pct Mn steel. *Metallurgical and Materials Transactions A,* **25A** (1994b) 763-773.

Bodnar, R.L., Ohhashi, T. and Jaffe, R.I., Effects of Mn, Si, and purity on the design of 3.5NiCrMoV, 1CroMoV and 2.25Cr-1Mo bainitic alloy steels. *Metallurgical and Materials Transactions A,* **20A** (1989) 1445-1460.

Bradley, J.R. and Aaronson, H.I., The stereology of grain boundary allotriomorphs. *Metallurgical Transactions A,* **8A** (1977) 317-322.

Bramfitt, B.L., The effect of carbide and nitride additions on the heterogeneous nucleation behaviour of liquid iron. *Metallurgical Transactions,* **1** (1970) 1987-1995.

Brooksbank, D. and Andrews, K.W., Stress fields around inclusions and their relation to mechanical properties. *Journal of the Iron and Steel Institute,* (1972) 246-255.

Brooksbank, D. and Andrews, K.W., Stresses associated with duplex oxide-sulphide inclusions in steel. *Journal of the Iron and Steel Institute,* (1970) 582-586.

Brooksbank, D. and Andrews, K.W., Tessellated stresses associated with some inclusions in steel. *Journal of the Iron and Steel Institute,* (1969) 474-483.

Busby, P.E., Warga, M.E. and Wells, C., Diffusion and solubility of boron in iron and steel. *Journal of Metals,* **5(11)** (1953) 1463-1468.

Cahn, J.W., The kinetics of grain boundary nucleated reactions. *Acta Metallurgica,* **4** (1956) 449-459.

Callister, W.D, Materials science and engineering: An introduction, 2nd edition. *John Wiley, USA,* (1991) .

Chijiiwa, R., Tamehiro, H., Hirai, M., Matsuda, H. and Mimura, H., Extra high toughness titanium-oxide steel plates for offshore structures and line pipe. *Offshore Mechanics and Arctic Engineering,, Proc., Houston, USA,* (1988) .

Christian, J.W., The theory of transformations in metals and alloys: Part I, 2nd edition. *Pergamon, Oxford, UK,* (1975) .

Cochrane, R.C. and Kirkwood, P.R., The effect of oxygen on weld metal microstructure. *Trends in Steels and Consumables for Welding, Proc. Welding Institute, London, UK,* (1978) 103-121.

Cochrane, R.C., Ward, J.L and Keville, B.R., The influence of deoxidation and/or desulphurisation practice on the weld metal toughness of high dilution welds. *Effects of Residual, Impurity and Microalloying Elements on Weldability and Weld Properties, Proc. Welding Institute, London, UK*, (1983).

Court, S.A. and Pollard, G., Inclusion chemistry and morphology in shielded metal arc (SMA) steel weld deposits. *Metallography*, **22** (1989) 219-243.

Court, S.A. and Pollard, G., Microanalysis of weld metal inclusions. *Journal of Material Science Letters*, **4** (1985) 427-430.

Crooks, M.J. and Chilton, J.M., The isothermal decomposition of austenite in hot-rolled microalloyed steels. *Metallurgical Transactions A*, **15A** (1984) 1137-1145.

Dallam, C.B. and Olson, D.L., Stress and grain size effects on weld metal ferrite formation. *Welding Research Supplement*, (1989) 198s-204s.

Devillers, L., Kaplan, D., Ribes, A. and Riboud, P.V., The effects of low level concentrations of some elements on the toughness of submerged arc weld metals. *Effects of Residual, Impurity and Microalloying Elements on Weldability and Weld Properties, Proc. Welding Institute, London, UK*, (1983).

Donnay, J.D.H. ed., Crystal data - Determinative tables, 2nd edition. *American Crystallographic Association, USA*, (1963).

Dowling, J.M., Corbett, J.M. and Kerr, H.W., Inclusion phases and the nucleation of acicular ferrite in submerged arc welds in high strength low alloy steels. *Metallurgical and Materials Transactions A*, **17A** (1986) 1611-1623.

Dunand, D.C. and Mortensen, A., On plastic relaxation of thermal stresses in reinforced metals. *Acta Metallurgica et Materialia*, **39(2)** (1991) 127-139.

Dyson, D.J. and Holmes, B., Effect of alloying additions on the lattice parameter of austenite. *Journal of the Iron and Steel Institute*, (1970) 469-474.

Eagar, T.W., *Welding Journal*, **57** (1978) 76s-80s.

Earmme, Y.Y., Johnson, W.C. and Lee, J.K., Plastic relaxation of the transformation strain energy of a misfitting spherical precipitate: Linear and power-law strain hardening. *Metallurgical Transactions A*, **12A** (1981) 1521-1530.

Easterling, K., Introduction to the physical metallurgy of welding, 2nd edition. *Butterworth Heinemann, Oxford, UK*, (1992).

Enomoto, M., Prediction of TTT-diagram of pro-eutectoid ferrite reaction in iron alloys from diffusion growth theory. *Iron and Steel Institute of Japan International*, **32(3)** (1992) 297-305.

Es-Souni, M. and Beaven, P.A., Microanalysis of inclusion / matrix interfaces in weld metals. *Surface and Interface Analysis*, **16** (1990) 504-509.

Evans, G.M., Microstructure and mechanical properties of Cu-bearing MMA C-Mn weld metal metal. *OERLIKON-Schweißmitt*, **48(123)** (1990a) 15-31.

Evans, G.M., The effect of titanium on the microstructure and properties of C-Mn all-weld metal deposits. *OERLIKON-Schweißmitt*, **49(125)** (1991) 22-33.

Evans, G.M., The effects of sulphur and phosphorus on the microstructure and properties of C-Mn all-weld metal deposits. *Metal Construction*, **18(9)** (1986) 631R-636R.

Evans, G.M., The influence of aluminium on the microstructure and properties of C-Mn all-weld metal deposits. *OERLIKON-Schweißmitt*, **48(124)** (1990b) 15-31.

Farrar, R.A. and Watson, M.N., Effect of oxygen and manganese on submerged arc weld metal microstructures. *Metal Construction,* (1979) 285-286.

Farrar, R.A., Zhang, Z., Bannister, S.R. and Barritte, G.S., The effect of prior-austenite grain size on the transformation behaviour C-Mn-Ni weld metal. *Journal of Materials Science,* **28** (1993) 1385-1390.

Ferrante, M. and Farrar, R.A., The role of oxygen rich inclusions in determining the microstructure of weld metal deposits. *Journal of Materials Science,* **17** (1982) 3293-3298.

Fleck, N.A., Grong, O., Edwards, G.R. and Matlock, D.K., The role of filler metal wire and flux composition in submerged arc weld metal transformation kinetics. *Welding Journal,* **65** (1986) 113s-121s.

Fountain, W. and Chipman, J., Solubility and precipitation of boron nitride in iron-boron alloys. *Transactions of the Metals Society – American Institute of Mechanical Engineers,* **224** (1962) 599-606.

Fox, A.G. and Brothers, D.G., The role of titanium in the non-metallic inclusions which nucleate acicular ferrite in submerged arc weld (SAW) fusion zones of navy HY-100 steel. *Scripta Metallurgica et Materialia,* **32(7)** (1995) 1061-1066.

Funakoshi, T., Tanka, T., Ueda, S., Ishikawa, M., Koshizuka, N. and Kobayashi, K., Improvement in microstructure and toughness of large heat-input weld bond of high strength steel due to addition of rare earth metals and boron. *Transactions of the Iron and Steel Institute of Japan,* **17** (1976) 419-427.

Gokhale, A.M., Application of microstructure modelling to the kinetics of proeutectoid ferrite transformation in hot-rolled micro-alloyed steels. *Metallurgical Transactions A,* **17A** (1986) 1625-1629.

Gregg, J.M., Ferrite nucleation on non-metallic inclusions in steel. *Ph.D. thesis, University of Cambridge, UK,* (1994) .

Gregg, J.M. and Bhadeshia, H.K.D.H., Bainite nucleation from mineral surfaces. *Acta Metallurgica et Materialia,* **42(10)** (1994a) 3321-3330.

Gregg, J.M. and Bhadeshia, H.K.D.H., Modelling of inclusion nucleation potency in steel welds. *Modelling and Control of Joining Processes, Proc. American Welding Society, Orlando, USA,* (1993) .

Gregg, J.M. and Bhadeshia, H.K.D.H., Titanium-rich mineral phases and the nucleation of bainite. *Metallurgical and Materials Transactions A,* **25A** (1994b) 1603-1611.

Grong, O., Metallurgical modelling of welding. *Institute of Materials, London, UK,* (1994) .

Grong, O., Kluken, A.O., Nylund, H.K., Dons, A.L. and Hjelen, J., Catalyst effects in heterogeneous nucleation of acicular ferrite. *Metallurgical and Materials Transactions A,* **26A** (1995) 525-534.

Grong, O., Siewert, T.A., Martins, G.P. and Olson, D.L., A model for silicon-manganese deoxidation of steel weld metals. *Metallurgical and Materials Transactions A,* **17A** (1986) 1797-1807.

Gutzow, I., Induced crystallization of glass-forming systems: A case of transient heterogeneous nucleation, part1. *Contemporary Physics,* **21(2)** (1980) 121-137.

Harbottle, J.E. and Fisher, S.B., Copper sulphide $Cu_{1.8}S$ (digenite I) precipitation in mild steel. *Nature,* **299** (1982) 139-140.

Harrison, P.L., Continuous cooling transformation kinetics and microstructure of mild and low alloy steel weld metals. *Ph.D. thesis, University of Southampton, UK*, (1983) .

Harrison, P.L., Influence of oxygen-rich inclusions on the $\gamma - \alpha$ phase transformation in high-strength low-alloy (HSLA) steel weld metals. *Journal of Materials Science*, **16** (1981) 2218-2226.

Harrison, P.L., The influence of calcium treatment on the submerged-arc weld metal and HAZ toughness of microalloyed C-Mn steel. *Metal Construction*, (1987) 84R-91R.

Hehemann, R.F., The bainite transformation. *Phase Transformations, American Metals Society, Metals Park, Ohio, USA*, (1970) 397-432.

Hehemann, R.F., Kinsman, K.R. and Aaronson, H.I., A debate on the bainite reaction. *Metallurgical and Materials Transactions A*, **3** (1972) 1077-1094.

Hillert, M., An improved model for discontinuous precipitation. *Acta Metallurgica*, **30** (1982) 1689-1696.

Hillert, M., Diffusion and interface control of reactions in alloys. *Metallurgical Transactions A*, **6A** (1975) 5-19.

Hillert, M., Role of interfacial energy during solid state phase transformations. *Jernkontorets Ann.*, **141** (1957) 757-789.

Hillert, M., The kinetics of the first stage of tempering. *Acta Metallurgica*, **7** (1959) 653-658.

Hillert, M., The uses of Gibbs free energy-composition diagrams. *Lectures on the Theory of Phase Transformations, ed. by Aaronson, H.I., American Institute of Mining, Metallurgical and Petroleum Engineering, New York, USA*, (1975) 1-50.

Homma, H., Ohkita, S., Matsuda, S. and Yamamoto, K., Improvement of HAZ toughness in HSLA steel by introducing finely dispersed Ti-oxide. *Welding Research Supplement*, (1987) 301s-309s.

Honeycombe, R.W.K. and Bhadeshia, H.K.D.H., Steels: Microstructure and properties, 2nd edition. *Edward Arnold, London, UK*, (1995) .

Horii, Y., Ichikawa, K., Ohkita, S., Funaki, S. and Yurioka, N., Chemical composition and crystal structure of oxide inclusions promoting acicular ferrite transformation in low alloy submerged arc weld metal. *Quarterly Journal of Japan Welding Society*, **13(4)** (1995) 500-507.

Imagumbai, M., Chijiiwa, R., Aikawa, N., Nagumo, M., Homma, H., Matsuda, S. and Mimura, H., Advanced steels for low-temperature service. *Proc. HSLA Steels: Metallurgy and Applications, eds Gray, J.M., Ko, T., Shouhua, Z., Baorong, W. and Xishan, X., American Society for Metals International, Ohio, USA*, (1985) 557-566.

Inoue, T., Nanba, S., Katsumata, M. and Anan, G., A mathematical model for a prediction of structures and properties of hot rolled steel and its application to the plates and long products. *Proc. Mathematical Modelling of Hot Rolling of Steel, Canadian Institute of Materials, Montreal, Canada*, (1990) 290-299.

Irvine, K.J., Pickering, F.B. and Gladman, T., Grain-refined C-Mn steels. *Journal of the Iron and Steel Institute*, **205** (1967) 161-182.

Ishikawa, F. and Takahashi, T., The formation of intragranular ferrite plates in medium-carbon steels for hot-forging and its effect on the toughness. *Iron and Steel Institute of Japan International*, **35(9)** (1995) 1128-1133.

Ishikawa, F., Takahashi, T. and Ochi, T., Intragranular ferrite nucleation in medium-carbon steels. *Metallurgical and Materials Transactions A*, **25A** (1994) 929-936.

Ito, Y. and Nakanishi, M., Study on charpy impact properties of weld metal with submerged arc welding. *The Sumitomo Search*, **15** (1976) 42-62.

Ito, Y., Nakanishi, M. and Komizo, Y., Effects of oxygen on low carbon steel weld metal. *Metal Construction*, (1982) 472-478.

Jang, J. and Indacochea, J.E., Inclusion effects on submerged-arc weld microstructure. *Journal of Materials Science*, **22** (1987) 689-700.

Johnson, W.A. and Mehl, R.F., *Transactions of the American Institute of Mining (Metall.) Engineers*, **135** (1939) 416.

Johnson, W.C., White, C.L., Marth, P.E., Ruf, P.K., Tuominen, S.M., Wade, K.D., Russell, K.C. and Aaronson, H.I., Influence of crystallography on aspects of solid-solid nucleation theory. *Metallurgical Transactions A*, **6A** (1975) 911-919.

Jones, S.J., Thewlis, G. and Bhadeshia, H.K.D.H., *Unpublished research, University of Cambridge, UK*, (1993) .

Karlsson, L., Norden, H. and Odelius, H., Non-equilibrium grain boundary segregation of boron in austenitic stainless steel – I. large scale segregation behaviour. *Acta Metallurgica*, **36** (1988) 1-12.

Kayali, E.S., Corbett, J.M. and Kerr, H.W., Observations on inclusions and acicular ferrite nucleation in submerged arc HSLA steel welds. *Journal of Material Science Letters*, **2** (1983) 123-128.

Kiessling, R., Non-metallic inclusions in steel. *Metals Society, London, UK, 2nd edition.*, (1978) .

Kim, C.T., Lee, J.K. and Plichta, M.R., Plastic relaxation of thermoelastic stress in aluminium / ceramic composites. *Metallurgical Transactions A*, **21A** (1990) 673-682.

Kimmins, S.T. and Gooch, D.J., Austenite memory effect in 1Cr-1Mo-0.75V(Ti,B) steel. *Metal Science*, **17** (1983) 519-532.

Kluken, A.O., Modelling of the reaction sequence during the deoxidation sequence and solidification of steel weld metals. *Ph.D. thesis, Trondheim University of Technology, Norway*, (1990) .

Kluken, A.O. and Grong O., Mechanisms of inclusion formation in Al-Ti-Si-Mn deoxidised steel weld metals. *Metallurgical and Materials Transactions A*, **20A** (1989) 1335-1349.

Kluken, A.O., Grong, O. and Hjelen, J., SEM based automatic image analysis of non-metallic inclusions in steel weld metals. *Materials Science and Technology*, **4** (1988) 649-654.

Kluken, A.O., Grong, O. and Hjelen, J., The origin of transformation textures in steel weld metals containing acicular ferrite. *Metallurgical and Materials Transactions A*, **22** (1991) 657-663.

Kluken, A.O., Grong, O. and Rorvik, G., Solidification microstructure and phase transformations in Al-Ti-Si-Mn Steels. *Metallurgical and Materials Transactions A*, **21** (1990) 2047-2058.

Ko, T. and Cottrell, S.A., The formation of bainite. *Journal of the Iron and Steel Institute*, (1952) 307-313.

Krahe, P.R., Kinsman, K.R. and Aaronson, H.I., Influence of austenite grain size on the

W_S temperature for the proeutectoid ferrite transformation. *Acta Metallurgica*, **20** (1972) 1109-1121.

Law, N.C. and Edmonds, D.V., The formation of austenite in a low-alloy steel. *Metallurgical Transactions A*, **11A** (1980) 33-46.

Lee, J.K., Earmme, Y.Y., Aaronson, H.I. and Russell, K.C., Plastic relaxation of the transformation strain energy of a misfitting spherical precipitate: Ideal plastic behaviour. *Metallurgical Transactions A*, **11A** (1980) 1837-1847.

Lee, J-L., Evaluation of the nucleation potential of intragranular acicular ferrite in steel weldments. *Acta Metallurgica et Materialia*, **42(10)** (1994) 3291-3298.

Lee, J-L. and Pan, Y-T., Effect of silicon content on the microstructure and toughness of simulated heat-affected zone in Ti-killed steels. *Materials Science and Technology*, **8** (1992) 236-244.

Lee, J-L. and Pan, Y-T., Effect of sulphur content on the microstructure and toughness of simulated heat-affected zone in Ti-killed steels. *Metallurgical Transactions A*, **24A** (1993) 1399-1408.

Liao, F.-C. and Liu, S., Effect of deoxidation sequence on carbon manganese steel weld metal microstructures. *Welding Research Supplement*, (1992) 94s-103s.

Lin, H-R. and Cheng, G-H., Analysis of hardenability effect of boron. *Materials Science and Technology*, **6** (1990) 724-729.

Linaza, M.A., Romero, J.L., Rodriguez-Ibabe, J.M. and Urcola, J.J., Improvement of fracture toughness of forging steels microalloyed with titanium by accelerated cooling after hot-working. *Scripta Metallurgica et Materialia*, **29(2)** (1993) 1217-1222.

Liu, S. and Olson, D.L., The role of inclusions in controlling HSLA steel weld microstructure. *Welding Research Supplement*, (1986) 139s-148s.

Llewellyn, D.T., Boron in steels. *Iron and Steelmaking*, **20(5)** (1993) 338-343.

Mabuchi, H., The effect of excess aluminium on low-temperature toughness in A302C steels. *Iron and Steel Institute of Japan International*, **21** (1981) 495-501.

Maitrepierre, Ph., Rofes-Vernis, J. and Thivellier, D., Structure-properties relationships in boron steels. *Boron in Steels, Proc. Metallurgical Society of American Institute of Mechanical Engineers, eds S. K. Banerji and J. E. Morral, Milwaukee, USA*, (1979) 1-19.

Mehl, R.F., Barrett, C.S. and Smith, D.W., Studies upon the Widmanstätten structure, IV, the Fe-C alloys. *Transactions of the American Institute of Mining and Metallurgical Engineering, Iron and Steel Division*, **105** (1933) 215-258.

Mills, A.R., Thewlis, G. and Whiteman, J.A., Nature of inclusions in steel weld metals and their influence on the formation of acicular ferrite. *Materials Science and Technology*, **3** (1987) 1051-1061.

Mori, N., Homma, H., Okita, S. and Asano, K., The behaviour of B and N in notch toughness improvement of Ti-B bearing weld metals. *Nippon Steel Corporation - Products Research and Development*, **IIW Doc. IX.1158.80** (1980) .

Mori, N., Homma, H., Okita, S. and Wakabayashi, M., Mechanism of notch toughness improvement in Ti-B bearing steels. *Nippon Steel Corporation - Products Research and Development*, **IIW Doc. IX.1196.81** (1981) .

Morral, J.E. and Cameron, T.B., Boron hardenability mechanisms. *Boron in Steels, Proc.*

Metallurgical Society of American Institute of Mechanical Engineers, eds S. K. Banerji and J. E. Morral, Milwaukee, USA, (1979) 19-32.

Morrogh, H., The neutralization of sulphur in cast iron by various alloying elements. *Journal of the Iron and Steel Institute,* **154** (1946) 399-408.

Mortimer, D.A., Boron segregation in iron and stainless steel. *Ph.D. thesis, Warwick University, UK,* (1973) .

Mortimer, D.A., Segregation of boron to grain boundaries in iron and AISI 316 stainless steel. *Grain Boundaries in Engineering Materials, Proc. 4th Bolton Landing Conference, New York, USA,* (1974) .

Mortimer, D.A. and Nicholas, M.G., Surface and grain-boundary energies of AISI 316 stainless steel in the presence of boron. *Metal Science,* **10** (1976) 326-332.

Mott, N.F. and Nabarro, F.R.N., An attempt to estimate the degree of precipitation hardening, with a simple model. *Proc. of the Physics Society,* (1940) 86-89.

Nehrenberg, A.E., *Transactions of the American Institute of Mechanical Engineers,* **194** (1952) 181.

Nuri, Y., Ohashi, T., Hiromoto,T. and Kitamura, O., Solidification microstructure of ingots and continuously cast slabs treated with rare earth metals. *Transactions of the Iron and Steel Institute of Japan,* **22** (1982) 399-407.

Ochi, T., Takahashi T. and Takada, H., Improvement of the toughness of hot forged products through intragranular ferrite formation. *30th Mechanical Working and Steel Processing, Proc. Iron and Steel Society, Warrendale, PA, USA,* (1988) 1-12.

Oh, D.W., Olson, D.L. and Frost, R.H., The influence of boron and titanium on low-carbon steel weld metal. *Welding Research Supplement,* (1989) 151s-158s.

Olson, G.B. and Cohen, M., A general mechanism of martensitic nucleation: Parts I, II and III. *Metallurgical Transactions A,* **7A** (1976) 1897-1923.

Pakrasi, S., Just, E., Betzold, J. and Höllrigl-Rosta, F., How boron affects the hardenability of low carbon steel. *Boron in Steels, Proc. Metallurgical Society of American Institute of Mechanical Engineers eds S. K. Banerji and J. E. Morral, Milwaukee, USA,* (1979) 147-164.

Pargeter, R.J., Acicular ferrite and inclusions in C-Mn steel weld metals. *Welding Institute Research Bulletin,* (1983) 215-220.

Pargeter, R.J., Investigation of submerged arc weld metal inclusions. *Welding Institute,* **7702.01/81/260.3** (1981) .

Pickering, F.B., Inclusions. *Institute of Metallurgists, London, UK,* (1979) .

Pickering, F.B., Physical metallurgy and the design of steels. *Applied Science Publishers, Essex, UK,* (1978) .

Porter, L.F., The present status and future of boron steels. *Boron in Steels, Proc. Metallurgical Society of American Institute of Mechanical Engineers eds S. K. Banerji and J. E. Morral, Milwaukee, USA,* (1979) 199-211.

Press, W.H., Flannery, B.P., Teukolsky, S.A. and Vetterling W.T., Numerical recipes - The art of scientific computing. *Cambridge University Press, Cambridge, UK,* (1986) 251-254.

Read, R.C., The characterisation and modelling of multi-pass steel weld heat-affected zones. *Ph.D. thesis, University of Cambridge, UK,* (1990) .

Reed, R.C. and Bhadeshia, H.K.D.H., Kinetics of the reconstructive austenite to ferrite transformation in low alloy steels. *Materials Science and Technology*, **8** (1992) 421-435.

Rees, G.I. and Bhadeshia, H.K.D.H., Bainite transformation kinetics. *Materials Science and Technology*, **8** (1992) 985-996.

Rees, G.I. and Bhadeshia, H.K.D.H., Thermodynamics of acicular ferrite formation. *Materials Science and Technology*, **10** (1994) 353-358.

Ricks, R.A., Barritte, G.S. and Howell, P.R., Influence of second phase particles on diffusional transformations in steels. *Solid State Phase Transformations, Proc. Metallurgical Society of American Institute of Mechanical Engineers, Pittsburgh, USA*, (1981) .

Sadovskii, V.D., The kinetics and structural mechanisms of phase transformations when heating steel, Translated by the Central Electricity Generating Board, UK, C.E. translation 7648. *Probl Mettaloverskie Term Obrab*, (1956) 31-52.

Saeki, M., Kurosawa, F. and Masuo, M., Micro and state analysis as the basis for microalloying techniques. *Transactions of the Iron and Steel Institute of Japan*, **26** (1986) 1017-1035.

Saggese, M.E., Bhatti, A.R., Hawkins, D.N., and Whiteman, J.A., Factors influencing inclusion chemistry and microstructure in submerged-arc welds. *Effects of Residual, Impurity and Microalloying Elements on Weldability and Weld Properties, Proc. Welding Institute, London, UK*, (1983) .

Saito, Y., Modelling of microstructural evolution in thermomechanical processing of high strength low alloy steel plates. *Computer-assisted Materials Design and Process Simulation, Proc. Iron and Steel Institute of Japan, Tokyo, Japan*, (1993) 147-153.

Saito, Y. and Shiga, C., Computer simulation of microstructural evolution in thermomechanical processing of steel plates. *Iron and Steel Institute of Japan International*, **32(3)** (1992) 414-422.

Salmon Cox P.H. and Charles J.A., Further observations on the analysis and distribution of non-metallic inclusions in a 0.2 % C steel ingot. *Journal of the Iron and Steel Institute*, **203** (1965) 493-499.

Samsonov, G.V., The oxide handbook, Translated. *IFI / Plenum, USA*, (1973) .

Shewmon, P.G., Diffusion in solids. *McGraw-Hill, New York, USA*, (1963) .

Shinada, K., Horii, Y. and Yurioka, N., Development of weld metal with high toughness and low hardenability. *Welding Research Supplement*, (1992) 253s-262s.

Steven, W. and Haynes, A.J., The temperature of formation of martensite and bainite in low-alloy steels. *Journal of the Iron and Steel Institute*, (1956) 349-359.

St-Laurent, S. and L'Espérance, G., Effects of chemistry and size distribution of inclusions on the nucleation of acicular ferrite in C-Mn steel shielded-metal-arc weldments. *Materials Science and Engineering*, **A149** (1992) 203-216.

Strangwood, M. and Bhadeshia, H.K.D.H., Nucleation of ferrite at ceramic / steel interfaces. *Solid to Solid Phase Transformations, Proc. Institute of Metals, London, UK*, (1988) 467-474.

Suzuki, S., Weatherly, G.C. and Houghton, D.C., The response of carbo-nitride particles in HSLA steels to weld thermal cycles. *Acta Metallurgica*, **35** (1987) 341-352.

Svensson, L.-E., Control of microstructures and properties in steel arc welds. *CRC Press, Boca Raton, Florida, USA*, (1994) .

Takahashi, M., Reaustenitisation from bainite in steels. *Ph.D. thesis, University of Cambridge, UK*, (1992) .

Terashima, H. and Hart, P.H.M., Effect of flux TiO_2 and wire Ti content on tolerance to high Al content of submerged-arc welds made with basic fluxes. *The Effects of Residual, Impurity and Microalloying Elements on Weldability and Weld Properties, Proc. Welding Institute, London, UK*, (1983) .

Thewlis, G., Pipeline welds - Effects of pipe material and consumables composition. 1 - Experimental investigation and results. *Joining and Materials*, (1989a) 25-32.

Thewlis, G., Pipeline welds - Effects of pipe material and consumables composition. 2 - Discussion and conclusions. *Joining and Materials*, (1989b) 125-129.

Thewlis, G., The influence of pipe plate and consumable chemistry on the composition, microstructure and toughness of weld metal. *Welding and Performance of Pipelines, Proc. Welding Institute, London, UK*, (1986) .

Thewlis, G., Transformation kinetics of ferrous weld metals. *Materials Science and Technology*, **10** (1994) 110-125.

Titchener, A.L. and Bever, M.B., The stored energy of cold work. *Progress in Metal Physics*, **7** (1958) 247-338.

Tomita, Y., Saito, N., Tsuzuki T., Tokunaga, Y. and Okamoto, K., Improvement in HAZ toughness of steel by TiN-MnS addition. *Iron and Steel Institute of Japan International*, **34(10)** (1994) 829-835.

Trivedi, R., The role of interfacial free energy and interface kinetics during the growth of precipitate plates and needles. *Metallurgical Transactions*, **1** (1970) 921-927.

Trivedi, R. and Pound, G.R., Effect of concentration dependent diffusion coefficient on the migration of interphase boundaries. *Journal of Applied Physics*, **38** (1967) 3569-3576.

Turkdogan, E.T., Causes and effects of nitride and carbonitride precipitation during continuous casting. *Iron and Steel Maker*, (1989) 61-75.

Turnbull, D. and Vonnegut, R., Nucleation catalysis. *Industrial and Engineering Chemistry*, **44** (1952) 1292-1298.

Ueda, S., Ishikawa, M. and Ohashi, N., Enhanced nucleation of polygonal ferrite grain in the interior of austenite grain in boron bearing steel. *Boron in Steels, Proc. Metallurgical Society of American Institute of Mechanical Engineers, eds S. K. Banerji and J. E. Morral, Milwaukee, USA*, (1979) 181-198.

Umemoto, M., Hiramatsu, A., Moriya, A., Watanabe, T., Nanba, S., Nakajima, N., Anan, G. and Higo, Y., Computer modelling of phase transformation from work-hardened austenite. *Transactions of the Iron and Steel Institute of Japan*, **32(3)** (1992) 306-315.

Wantanabe, I. and Kojima, T., Effects of titanium, boron and oxygen on notch toughness (Report 1). *Journal of Japan Welding Society*, **49(11)** (1980a) 772-780.

Wantanabe, I. and Kojima, T., Role of titanium and boron in refinement of microstructure (Report 2). *Journal of Japan Welding Society*, **50(7)** (1980b) 702-709.

Watson, J.D. and McDougall, P.G., Crystallography of Widmanstätten ferrite. *Acta Metallurgica*, **21** (1973) 961-973.

Weatherly, G.C., A determination of the punching stress at the interface of particles during rapid quenching. *Metal Science Journal*, **2** (1968) 237-240.

Weisman, C. ed., Welding handbook, 7th edition. *American Welding Society, Florida, USA*, **1** (1981) 79.

Weiss I. *et al.*, *Process Modelling Tools, ed. Thomas, J.F., American Society for Metals*, (1981) 97.

Westbrook, J.H. and Aust, K.T., Solute hardening at interfaces - I. *Acta Metallurgica*, **11** (1963) 1151-1168.

Widgery, D.J., Deoxidation practice for mild steel weld metal. *Welding Research Supplement*, (1976) 57s-68s.

Williams, T.M., Stoneham, A.M. and Harries, D.R., The segregation of boron to grain boundaries in solution-treated type 316 austenitic stainless steel. *Metal Science*, (1976) 14-19.

Yamamoto, K., Hasegawa, T. and Takamura, J., Effect of B on intra-granular ferrite formation in Ti-oxide bearing steels. *Iron and Steel Institute of Japan International*, **36(1)** (1996) 80-86.

Yamamoto, K., Matsuda, S., Haze, T., Chijiiwa, R. and Mimura, H., Newly developed Ti-oxide bearing steel having high HAZ toughness. *Residuals and Unspecified Elements in Steels, Proc. American Society for Testing and Materials, Ohio, USA*, (1987) .

Yamanaka, K. and Ohmori, Y., Effect of boron on the transformation of low-carbon low-alloy steels. *Transactions of the Iron and Steel Institute of Japan*, **17(2)** (1977) 92-101.

Zener, C., *Journal of Applied Physics*, **20** (1949) 950.

Zhang, Z. and Farrar, R.A., Role of non-metallic inclusions in formation of acicular ferrite in low-alloy weld metals. *Materials Science and Technology*, **12** (1996) 237-260.